ADVANCED MANPACK RADIO CONCEPT FOR UHF DAMA SATELLITE COMMUNICATIONS

By

ComFocus Corporation

29 March 1992

NOTICE:

Much of the information presented in this technical report is proprietary in nature, having been developed prior to contract award. Material falling into this category is so denoted by "ComFocus Proprietary" in the lower left hand corner of each page. Pages marked "ComFocus Corporation" are free of this restriction.

ADVANCED MANPACK RADIO CONCEPT FOR UHF DAMA SATELLITE COMMUNICATIONS

By

ComFocus Corporation

29 March 1992

Principle Investigator: James A. Crawford

Report Type: SBIR Phase I Final Technical Report
Topic AF91-030

Sponsoring Organization: Electronic Systems Division
Air Force Systems Command, USAF
Hanscom AFB, MA 017305320

Contract Number: F19628-91-C-0154

ABSTRACT:

A new manpack radio concept is presented which supports UHF satellite and U.S. cellular telephone communications. At UHF, 5 kHz and 25 kHz DAMA standards are supported as well as a new multi-channel DAMA which provides greater network capacity and connectivity. A nonconventional radio architecture is proposed employing distributed signal processing for enhanced capabilities, lower power consumption, and reduced internal electromagnetic interference.

Cosite communications issue are specifically addressed for UHF. New algorithms for 5 kHz DAMA signal acquisition and tracking are presented as well as for other communication modes of operation. A complete radio architecture is presented and discussed in depth.

Table of Contents

Technical Appendices

Appendix I	5 kHz DAMA Spectral Occupancy
Appendix II	AMST Link Margin Analysis
Appendix III	Bandpass Sampling Fundamentals
Appendix IV	5 kHz DAMA Signal Detection and Acquisition
Appendix V	Digital Signal Processing for 5 kHz DAMA Services
Appendix VI	AMST Frequency Plan Considerations
Appendix VII	Frequency Synthesis for the AMST
Appendix VIII	Fractional-N Frequency Synthesis Fundamentals
Appendix IX	Advanced Modulation Waveforms
Appendix X	AMST DAMA Operation and COMSEC
Appendix XI	CDMA Cellular and GPS Interoperability
Appendix XII	Cosite Operation
Appendix XIII	Advanced Digital Signal Processing

1.0 Summary of Principle Findings and Introduction:

Advanced Manpack Satellite Terminal (AMST)

The findings presented in this Phase I SBIR report describe a manpack radio concept which should substantially outperform existing manpack UHF radios while keeping cost elements comparable to or lower than existing hardware solutions. This has been accomplished in part by utilizing existing component technology from the cellular industry combined with proper architectural choices as initially described in our Phase I SBIR proposal [2]. Some of the most important findings are summarized here:

1). Link margin analysis for inter-AMST communication via UHF satellite revealed that substantial battery power savings is possible by having power level control at the AMST transmitter since 10 watts or less is generally sufficient for communications. In cases where 10 watts was insufficient, 20 watts was insufficient for reliable communications as well (Appendix II).

2) Receiver preselection filtering is mandatory for simultaneous cosite operation of multiple AMSTs. Simple calculations showed that LST-5 vintage radios must utilize physical separations on the order of 400 feet worst case in order to communicate simultaneously without interference. In sharp contrast, inter-radio distances on the order of only 20 feet would be adequate for the AMST (Appendix XII).

3) Moderate transmitter waveform shaping can reduce the modulation sidebands of the 5 kHz DAMA waveform from roughly 12 dB per octave to more than 50 dB per octave with fairly negligible E_b/N_o performance degradation (Appendix I). This improved sidelobe performance is mandatory for stringent cosite operation (Appendix I,XII) and can also be extended to SBPSK which is used in 25 kHz DAMA operation.

4) Inclusion of interoperability with the U.S. cellular telephone band is highly advocated. Not only is the TDMA waveform ($\pi/4$-DQPSK) being used for TDMA digital cellular, it is also being advocated for future military radios to realize improved spectral efficiency [14]. Providing cellular interoperability would greatly enhance the AMST, and its inclusion can be accomodated with only moderate hardware impact.

These findings alone when addressed in the AMST would dramatically relieve present-day user constraints for UHF SATCOM and line-of-sight (LOS) operation. Before diving into our additional findings further however, we will first examine the mechanical concept developed for the AMST.

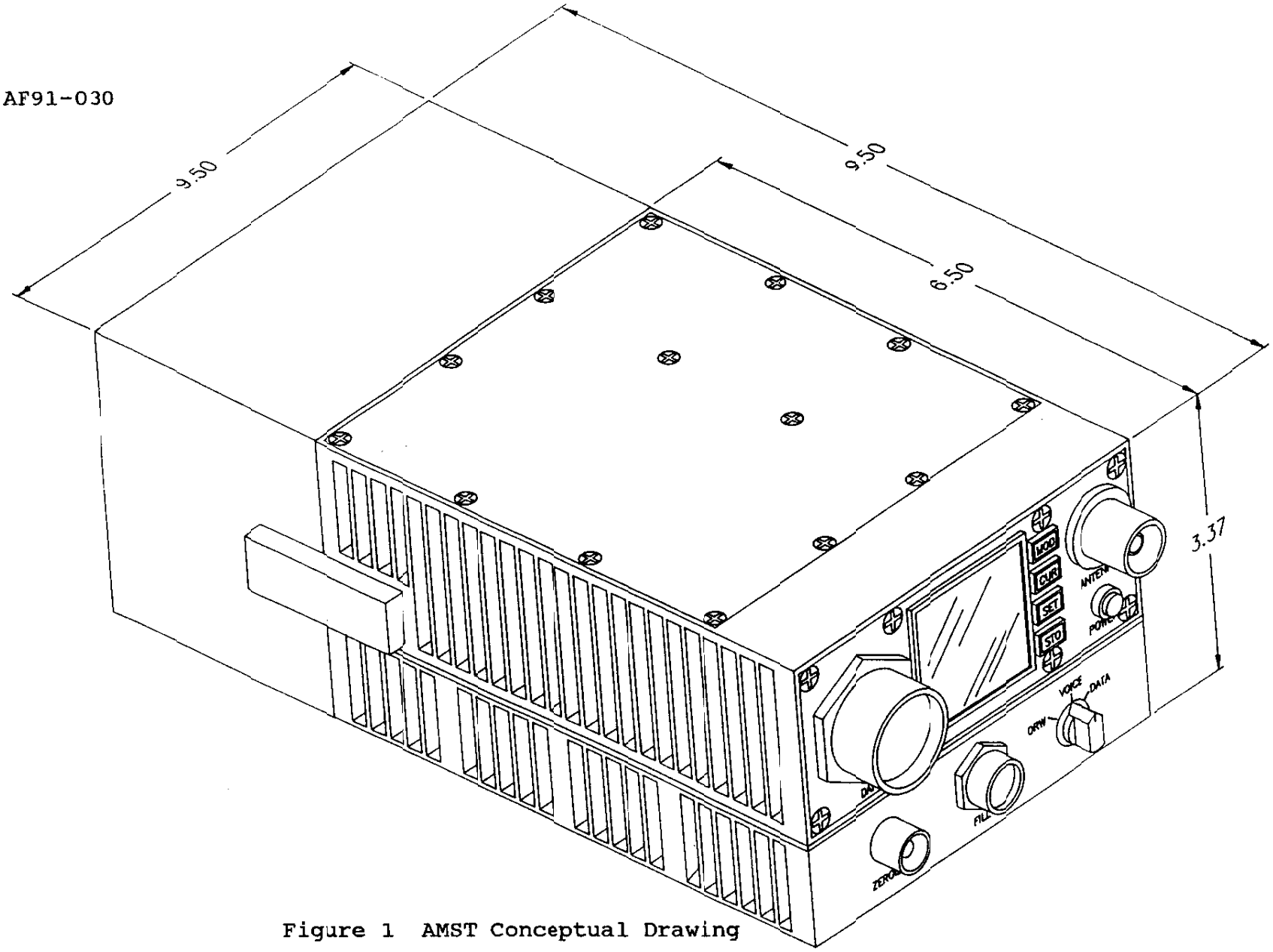

Figure 1 AMST Conceptual Drawing

An artist's conceptual drawing of the AMST with attatched battery is shown in Figure 1. The dimensions of the AMST are equivalent to those of the Motorola LST-5 radio. A front view of the operator's control panel is shown in Figure 2 where the front panel is purposely void of numerous switches and control knobs. The user interface envisioned for the AMST utilizes a panel mounted alpha-numeric display (with additional icons) as shown in order to (i) provide a completely reconfigurable user interface for multiple armed services usage, (ii) permit user alterations without costly mechanical alterations, and (iii) simplify keystroke operations by guiding a user through a logically oriented window tree. Attention has been given to the needed COMSEC interface in the lower portion of the front panel where mechanical switches are used rather relying upon operation via the software radio interface.

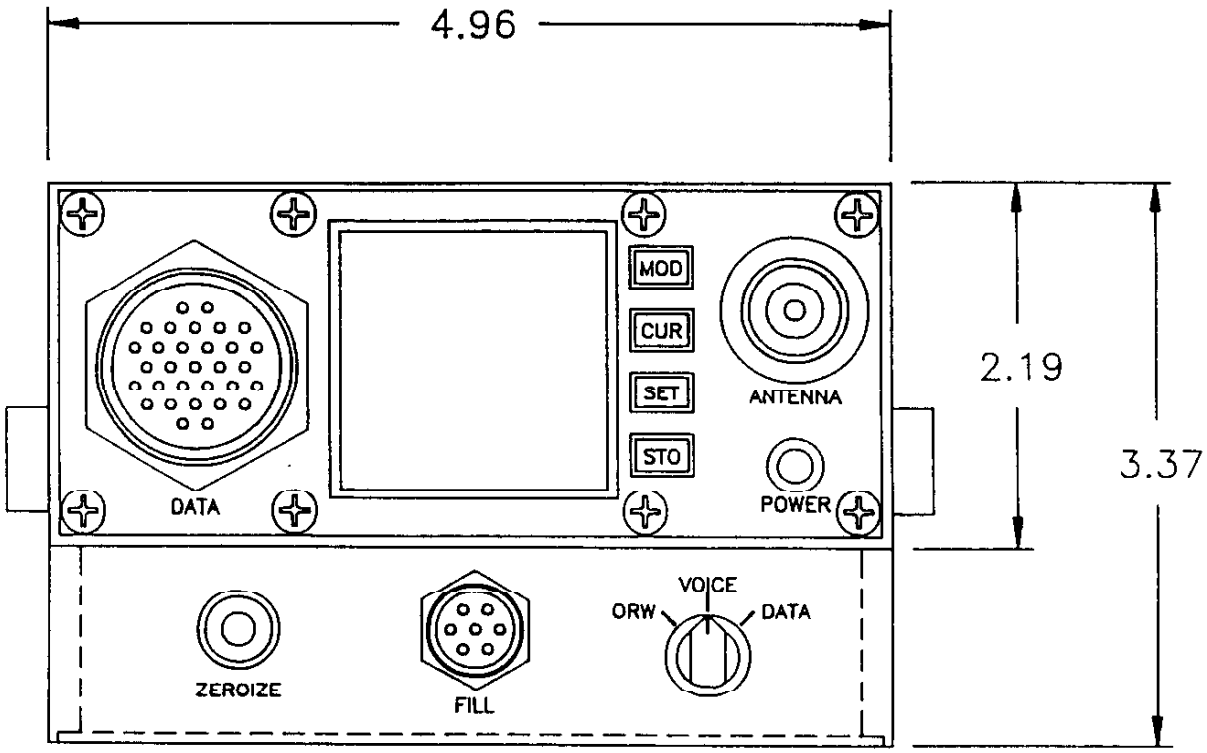

Figure 2 AMST Front Panel Concept

This Phase I SBIR report has been organized in a structured manner in order to enhance readability as much as possible. Most of the highly technical discussions have been puposely placed in the technical appendices and only the key findings are reported on in the main body of the report. Many other findings were also obtained during this research which are worthy of mention in this introduction:

5) The need for sophisticated digital filter implementations within the AMST even in the presence of severe adjacent channel interference should not be required. Although more complicated digital filters may be required for interoperability with emerging digital cellular systems, simple integrate-and-dump matched filters should suffice for the AMST (Appendix XIII). Although some digital filtering is required for transmitter waveshaping, this occurs only during transmit operation when 50 mA more current drain for this function is less an issue.

6) Although the desire to include a GPS capability within the AMST admits a despreading capability for spread spectrum within the AMST, this fact does not lend itself to an easy implementation of CDMA digital cellular or full GPS within the AMST since both waveforms are inherently multi-channel in nature. A more conventional spread-spectrum approach is however possible in the AMST which retains the narrowband channel features of the UHF SATCOM modes while accomodating the inherently wideband features of spread spectrum communications as discussed in Appendix XI.

7) Bandpass sampling techniques were developed which permit the AMST to receive all of the normal military communication data rates plus the data rates to be used by future TDMA and CDMA digital cellular systems. A new Hilbert transforming technique was developed which permits this operation to be performed with strictly shift and add operations (Appendix III) if desired.

8) New techniques for 5 kHz DAMA signal detection and acquisition are proposed which are very robust and can lead to net entry times 50% shorter than presently specified (i.e., 45 seconds rather than 90 seconds) as discussed in Appendix IV. These same techniques may be extended to 25 kHz DAMA as well.

9) New error metrics for simultaneous symbol timing and carrier phase recovery operations were developed to further enhance acquisition performance for the 5 kHz DAMA modes as discussed in depth in Appendix V.

10) The detailed hardware design makes use of standard device

technologies readily available thereby shortening design times and lowering unit cost (Appendix VI,VII).

11) Inclusion of TDMA digital cellular capability within the AMST is possible with only minor additions to the overall radio (Appendix VI,XIII).

12) Advanced waveforms such as trellis coded modulation are not advantageous for E_b/N_o-limited communication links such as those generally used in AMST communications (Appendix IX). Therefore, further consideration was deferred.

Of the technical items cited above, the cosite and link margin related results carry potentially the most significant weight in dictating design elements for the AMST. This is largely true because cosite performance dictates a different design philosophy be adopted for virtually the entire radio. As contended in [2], these considerations must be placed at the forefront of the design effort.

Many other low-level conclusions are drawn throughout the technical appendices which are too numerous to mention here. Sufficient detail has been included wherever possible to provide insight into these findings as well.

The first discussions of this report pertain to interoperability with other non-military communication systems which may be very desirable for inclusion within the AMST. The main body of our report then follows.

2.0 Interoperability with a World of Communications

"Over the past three years, the interest in wireless communications has been nothing less than spectacular," to quote Dr. Theodore Rappaport writing in IEEE Communications Magazine November, 1991 [1]. Fueled by the military communications research of the 1970s and 1980s, emerging systems promise to have sophistication and performance rivaling even some of the most complicated military systems in existence today. This is particularly true in the UHF SATCOM arena where communications have not been hardened using exotic anti-jam (AJ) and low-probability intercept (LPI) techniques.

With declining defense budgets and what is perceived as a safer world, the need for sophisticated military communication systems which anticipate a sophisticated threat have diminished greatly. Furthermore, economic factors combined with the explosion in commercial communications have resulted in tremendous innovation also occuring outside military circles. As we saw in Desert Storm, the ability to supplement normal military communications with commercial equipment (e.g., GPS receivers, cellular telephones, etc.) provided a cost effective, rapid response alternative which due to simple economics will no doubt occur in the future if necessary. Therefore, compatibility with emerging commercial systems where feasible is viewed as a necessary requirement for the Advanced Manpack Satellite Terminal, AMST.

Aside from coverage of the traditional military UHF SATCOM band 225-400 MHz, deciding what other capabilities should be included within the AMST has been one of the most difficult issues to address. This report therefore begins with a discussion of the some of the options available.

A Proliferation of Communications

Even though it is desirable to include overlap with commercial systems in the AMST, it is imperative that the prime objectives of the AMST not be compromised in attainment of that goal. Borrowing from our SBIR proposal submission [2], we maintain that

> "the AMST effort must be focused to i) provide maximum satellite throughput at a reasonable cost thereby supporting a proliferation of users, ii) consume little power to support extended missions, and iii) be based upon architectural choices which do not render it obsolete overnight as newer technologies and requirements emerge."

The next decade promises to be one of tremendous change for wireless communications. Potentially large redistributions of spectrum resources may well accompany these changes and military users will have to accomodate the changing times also. In 1989, Congressmen Dingell and Markey proposed the Emerging Telecommunications Technology Act (HR-2965) which proposed to reallocate 200 MHz of the spectrum presently allocated to government use [5] for instance. In many respects, this should not come as a surprise given that roughly 40% of the spectral resources from 10 kHz through 10.5 GHz are presently allocated for exclusive use by the United States government [5]. Therefore, it is reasonable to assume that the utility of the AMST can only benefit if it overlaps existing communication services which will unquestionably grow during the next decade (e.g., cellular telephone).

In the next few paragraphs, we will briefly review some of the most promising emerging commercial communication systems with an eye toward inclusion within the AMST.

Land Mobile Radio (LMR)

Since its first use in the early 1920s, LMR has expanded and evolved steadily, and today it is estimated that there are several tens of millions of LMR users in the U.S. alone [14]. It should be noted that LMR excludes cellular radio telephone as well as military combat radio systems from this terminology even though they operate within the same VHF and UHF bands.

In September 1989, the National Communications System (NCS) Office of Technology and Standards approved Fed Std 1023 which defined interoperability requirements for one category of encrypted 12 kbps CVSD voice digitizers operating with 25 kHz channel FM radios at frequencies above 30 MHz [15]. This standard was regarded as an interim standard only. In June 1988, GTE Government Systems began providing technical support to the DoD in their development of a future digital LMR standard to be designated as Fed Std 1024. The principle objectives for Fed Std 1024 include:

1) a modulation technique permitting operation with 12.5 kHz or 6.25 kHz channel spacings,

2) inclusion of the government standard 4800 bps voice digitization technique know as Code Excited Linear Predictive (CELP) coding,

3) reliable initial and late-entry synchronization in the fading/multipath environment typical of VHF/UHF radio channels.

Although Fed Std 1024 goes a long way to modernize LMR systems, since the standard can only apply to new systems, equipment availability given the shrinking defense budget is at best questionable in the near future. Therefore, a explicit AMST interoperability with LMR at this time is not advocated.

A number of the components of Fed Std 1024 are however noteworthy in that they appear in a number of other systems which will be discussed momentarily. Specifically, the standard calls for 12.5 to 6.25 kHz channel spacings and the $\pi/4$-QPSK waveform which is planned for the next generation of (digital) cellular phones in the United States. The real issues of interoperability then remain in the transmission modes and formats.

Personal Communication Networks (PCN) and Personal Communication Services (PCS)

PCNs and PCSs promise to show the most dramatic worldwide growth during the next decade of any of the emerging communication technologies. Analysts put annual U.S. revenues at somewhere between $33 and $55 billion by the year 2000. Even with this recognized world market potential, the United States has not allocated any spectrum for these services to date [1]. The United Kingdom is viewed by many as the leading country for PCS initiatives. They see users using 10 mW portable terminals to provide communications.

The pervasiveness of PCNs will be made available by an immense infrastructure of low-power suitcase sized base stations which will access the local telephone loop in populated areas. The low-power element has a natural appeal for portable communications and is also advantageous in that the system capacity can be increased by making each cell smaller [4] (When the radius decreases to less than one mile, a cell is commonly called a microcell.)

Due to the very nature of PCNs, communications will be limited to areas having the forementioned immense infra-structure to support such communications, e.g. metropolitan areas of highly developed countries. Given the additional spectrum issues which have yet to be legislated in the United States, and many other technical issues, AMST interoperability with emerging PCNs is not advocated at this time.

Mobile Satellite Communications

Until late in the last decade, mobile satellite communications were only provided by Inmarsat-A. Over the next few decades, it is anticipated that mobile satellite communications will experience dramatic growth [8].

At present, all communications between satellites and mobiles are at L-band, specifically:

Satellite to Mobile	1530.0 - 1559.0
Mobile to Satellite	1631.5 - 1660.5

These bands were further divided by the 1987 WARC to service a number of different user groups [8].

Table I.
L-Band Frequency Bands Allocated to Mobile Satellite Communications at the 1987 WARC

DownLink, MHz	UpLink, MHz	Services
1530 - 1533	1631.5 - 1634.5	Maritime mobile and land mobile
1533 - 1544	1634.5 - 1645.5	Maritime mobile and land mobile
1544 - 1545	1645.5 - 1646.5	Emergency and distress
1545 - 1555	1646.5 - 1656.5	Aeronautical mobile and safety services
1555 - 1559	1656.5 - 1660.5	Land mobile; airborne and marine

Most of the currently used satellites merely amplify and frequency translate the received signal from the uplink prior to transmission over the downlink. Almost all satellites are geosynchronous at 42,162 km which implies certain time delay and antenna issues which must be addressed. Inmarsat is the only organization providing satellite communications services worldwide to all modes of transportation by air, land, and sea [9].

Most mobile satellite services which offer voice and data capabilities are future and to a large degree tenative.

Table II.
Mobile Satellie Systems Offering Voice and Data Services
(Future initial services dates are only tenative.)

Mobile System	Region	Available
Inmarsat-A	Global	1976
Inmarsat Aeronautical	Global	1990
Inmarsat-M	Global	1993
Inmarsat-B	Global	1993
MOBILESAT	Australia	1993
MSAT	North Am.	1994

Table III.
Summary of Voice Transmission Characteristics

System	Voice Coding Rate	Data Rate	Modulation	RF BW
Inmarsat-A	Not Applicable	Not Appl.	FM	50 kHz
Inmarsat Aero.	9.6 kbps	19.2 kbps	OQPSK	17.5 kHz
Inmarsat-M	4.2 kbps	6.4 kbps	OQPSK	10 kHz
Inmarsat-B1	16 kbps	21.33 kbps	OQPSK	20 kHz
MOBILESAT	4.2 kbps	6.4 kbps	$\pi/4$ QPSK	7.5 kHz
MSAT	4.2 kbps	6.4 kbps OOPSK	$\pi/4$ QPSK	7.5 kHz

Several companies have embarked upon very aggressive plans to provide mobile satellite communications over the next decade. RadioSat[1] is developing a mobile satellite system which will provide integrated services to consumers including communications and navigation [6]. The broadcasts will include nationwide digital audio broadcasts, data broadcasts and 2-way communications. This system will use the MSAT satellites which are scheduled for launch in 1994.

The Iridium[2] satellite-based personal communications system being developed by Motorola will bring cellular telephone service to virtually every point on the globe [10]. It will use a constellation of 77 satellites in low polar orbit at an altitude of 420 nautical miles resulting in at least one satellite in radio line of sight from every point on the earth. Iridium is still in development and the satellite design will not be frozen until early 1992. The system will not be operational before 1997. The satellites are interconnected via microwave crosslinks. The radio links between users and satellites will operate somewhere in the 1600-1700 MHz region of L-band.

Given that most of the mobile satellite systems are only now in their planning stages, AMST interoperability is not advised at this time. Other important issues such as system capacity remain to be studied and evaluated as well. The time table for the SBIR Phase II effort further precludes including an AMST interoperability at this time.

---

[1]RadioSat is a trademark of Radio Satellite Corporation

[2]Iridium is a trademark and service mark of Motorola, Inc.

Cellular Telephone

Cellular telephone technology is perhaps the most mature wireless communication form which is part of the emerging communications explosion. Even so, the industry is bantering standards back and forth at this moment for a next generation cellular telephone standard. An excellent current overview of mobile radio can be found in [11].

In early 1990, the Cellular Telephone Industry Association (CTIA) and Telecommunications Industry Association (TIA) approved Interim Standard 54 (IS-54) which specified a dual-mode cellular radio transciever that uses both the analog FM (the present day United Stated Advanced Mobile Phone System or AMPS standard) and a linearized $\pi/4$-Differential QPSK modulation format with a Code Excided Linear Predictive (CELP) speech coder (called the U.S. Digital Cellular or USDC standard) [3]. USDC utilizes TDMA and advanced speech coding techniques to increase system capacity roughly 3-fold over existing analog system capacity. Even though work has been in progress several years for this next generation cellular system, no dual-mode systems are operational at this time.

In February of 1990 just after the CTIA adopted IS-54, Qualcomm put forth its proposal for CDMA. This action caused quite a stir in the industry and over time, almost every major cellular radio service provider has since been conducting their own field trials to evaluate competing standards. It is therefore unclear if the United States digital cellular radio systems will be completely compatible throughout the country or not [1]. In contrast to the dual-mode system approach, Qualcomm has demonstrated a full-up working system in several cities within the U.S. and similar trials will be conducted globally over the next several months. The CDMA field results released in December, 1991 and January, 1992 showed dramatic capacity increases compared with the dual-mode system projections. These results will unquestionably shake the cellular industry, the implications upon IS-54 being of course unknown at this time.

In contrast to the USDC standard, the European digital cellular system (called Group Special Mobile or GSM) was developed for a brand new spectrum allocation in the 900 MHz band. It was developed to ensure that a single access and equipment standard would be used throughout the European continent. GSM is the world's first TDMA cellular system standard, and uses a constant envelope modulation format to gain power efficiency (class C amps) over spectral efficiency (constant envelope modulation has a smaller bits per hertz of RF occupancy than does linear modulation). GSM uses an equalizer and slow frequency hopping to combat multipath. GSM requires a large RF bandwidth (200 kHz) in order to support its high data rate of approximately 271 kbps. A comparison of the major cellular mobile radio systems in service and being developed is provided below.

Table IV.

Comparison of Cellular Mobile Radio Systems

Parameter	AMPS	MCS-L1/L2	NMT	C450	TACS	GSM	PCN	IS-54
Tx Freq, MHz								
Base	869-894	870-885	935-960	461-466	935-960	890-915	1710-1785	869-894
Mobile	824-849	925-940	890-915	451-456	890-915	935-960	1805-1880	824-849
Multiple Access	FDMA	FDMA	FDMA	FDMA	FDMA	TDMA	TDMA	TDMA
Duplexing Method	FDD	FDD	FDD	FDD	FDD	FDD	FDD	FDD
Channel BW, kHz	30.0	25.0 12.5	12.5	20.0 10.0	25.0	200.0	200.0	30.0
Voice	Analog	Analog	Analog	Analog	Analog	RELP	RELP	VSELP
Modulation Type	PM	PM	PM	PM	PM	GMSK	GMSK	$\pi/4$
Peak Dev, kHz	±12	±5	±5	±4	±9.5	-	-	-
Channel Rate, kbps	-	-	-	-	-	270.8	270.8	48.6
Channel Coding	BCH	BCH	B1	BCH	BCH	RS	RS	Conv.

Although this overview of cellular systems has been very brief, there is substantial evidence to support inclusion of an AMST interoperability with cellular systems. Only a question of which cellular system(s) to include remain.

Aside from the GSM European standard, the maximum RF bandwidth required with any of the cellular technologies listed above is 30 kHz. Given the 25 kHz UHF TDMA/DAMA Waveform [16] requirements for UHF SATCOM operation, accomodating a 30 kHz bandwidth in the IF processing portion of the AMST should not pose any major difficulties. It is therefore quite reasonable for the AMST to accomodate at least a portion of the receive band (869-960 MHz) and the transmit band (824-940 MHz) based upon Table IV permitting potential operation with all of the major cellular systems excluding GSM. Due to the shere processing bandwidths required for GSM, it will not be considered further.

Within the cellular services, there are (i) analog, (ii) TDMA digital, and (iii) CDMA digital waveforms to consider. Analog cellular presents no specific challenges for inclusion in the AMST. The latter two waveforms deserve individual attention.

TDMA digital refers to the USDC or IS-54 standard mentioned earlier and utilizes the $\pi/4$-DQPSK waveform, almost the same waveform stipulated in Fed Std 1024 for LMR. The TDMA approach requires fairly substantial adaptive equalization within the receiver for good performance, this factor no doubt contributing to the fact that no dual-mode systems are operational to date. The linear (nonconstant envelope) modulation further requires the transmitter power amplifier to be linear which is generally less efficient than the nonlinear class-C variety which is normally used with constant envelope waveforms.

Thus far, little detail has been given about the Code Division Multiple Access (CDMA) approach being developed by Qualcomm. Although this approach is substantially more complex than the IS-54 standard, it offers substantially higher system capacity as well as several other desirable features. These additional features include:

- inherent immunity to multipath (and limited jamming) due to the spread-spectrum nature of the waveform,
- operation with substantially lower C/N ratios which translate into less required transmitter power,
- an automatically built-in degree of privacy,
- dramatically smaller cell site hardware installations,
- a soft programmable tradeoff between power consumption (C/N) and voice quality.

At the time of this writing, the competition between CDMA and TDMA digital cellular is only beginning. Most experts agree that the market will decide which technology is favored in the future. Although Qualcomm is developing the chip set for CDMA, no advance information is yet available on these devices. One positive note here is that Qualcomm is under contract to NYNEX to develop a handheld CDMA phone using this chip set. This factor will virtually guarantee that the implementation will be as low in power consumption as possible.

Even though very good power level control must be maintained for the CDMA approach to be successful (typically 80 dB dynamic range), from a power amplifier point of view, this task is probably no less difficult to achieve than is the linearity requirement for $\pi/4$-DQPSK for the IS-54 standard. While it is true that PN code spreading and de-spreading must also be provided in the CDMA radio, if we assume that the AMST also includes a GPS receive capability, the additional impact is conceivably minimal. As discussed in Appendix XI however, detailed elements of the CDMA approach make interoperability impractical for the AMST and a full implementation of Qualcomm CDMA will therefore not be considered further at this time.

Summary of Desired Interoperability

Based upon the foregoing discussions, the interoperability goals being adopted for the AMST include the following systems:

1) standard military UHF SATCOM and line of sight
2) GPS L_1 (single-channel)
3) cellular telephone
   - analog
   - TDMA $\pi/4$-DQPSK

The degree to which these objectives can be achieved within the AMST and the tradeoffs which must be made consume the balance of this SBIR Phase I investigation. Although a number of necessary technical requirements concerning (2) and (3) above are considered in this report, UHF SATCOM remains the primary emphasis.

3.0 Cornerstone Concepts

The Phase I SBIR proposal submitted [2] advocated a number of cornerstone architectural concepts which were to guide the entire AMST effort. This perspective has not changed as a result of the studies reported on here, but has in fact been strengthed. It is worthwhile to discuss our findings in the context of these pronounced architectural choices here in some detail.

The first key cornerstone which was given in [2] was that

> "The unavoidable EMI problems present within a small envelope such as the AMST, combined with the need for a robust receiver front-end to cope with other users in close physical proximity can most effectively be met using an up-conversion receiver architecture."

The need for an upconversion receiver has been adhered to throughout this investigation, the receiver frequency plan clearly showing this choice in Figure 3. Compared to the original frequency plan in [2] which advocated a first IF of 2101.5 MHz as shown in Figure 4, the proposed first IF for the AMST has been lowered to 1054 MHz in order to take advantage of the dielectric filter technology available at that frequency range in connection with the cellular marketplace. As shown in the more detailed analysis presented in Appendix VI, this change still delivers excellent spurious performance with the added advantage that component and material cost (as well as test equipment cost) will be substantially lower at this frequency.

The problems associated with cosite operation which were recognized in the proposal phase are substantiated in Appendix XII. Using fairly simple models, it can be shown that substantial receiver desensitization occurs in cosite operation with radios such as the LST-5 (which do not have receiver preselection or transmit post-driver filtering) unless new design choices are made for both the receiver and transmitter portions of the radio. Additional spectral shaping as developed in Appendix I also leads to much better cosite performance. In command post operations, the AMST should be capable of operation within 20 feet of another AMST unit as compared to more like a minimum of 400 feet with more conventional radios (Appendix XII).

Part of our attention to the internal radio EMI issues is represented by the forementioned receiver frequency plan shown in Figure 3. Although the use of multiple IFs may at first seem undesirable, they are ideally suited for the AMST. The high first IF (1054 MHz) is necessary as advocated earlier for good spurious performance. The second IF (71.2075 MHz) is adequately high so as to ease the stopband requirements upon the first IF filter and is also a very good choice for receiving the cellular telephone band as shown in Figure 5. While it is true that the downconversion from

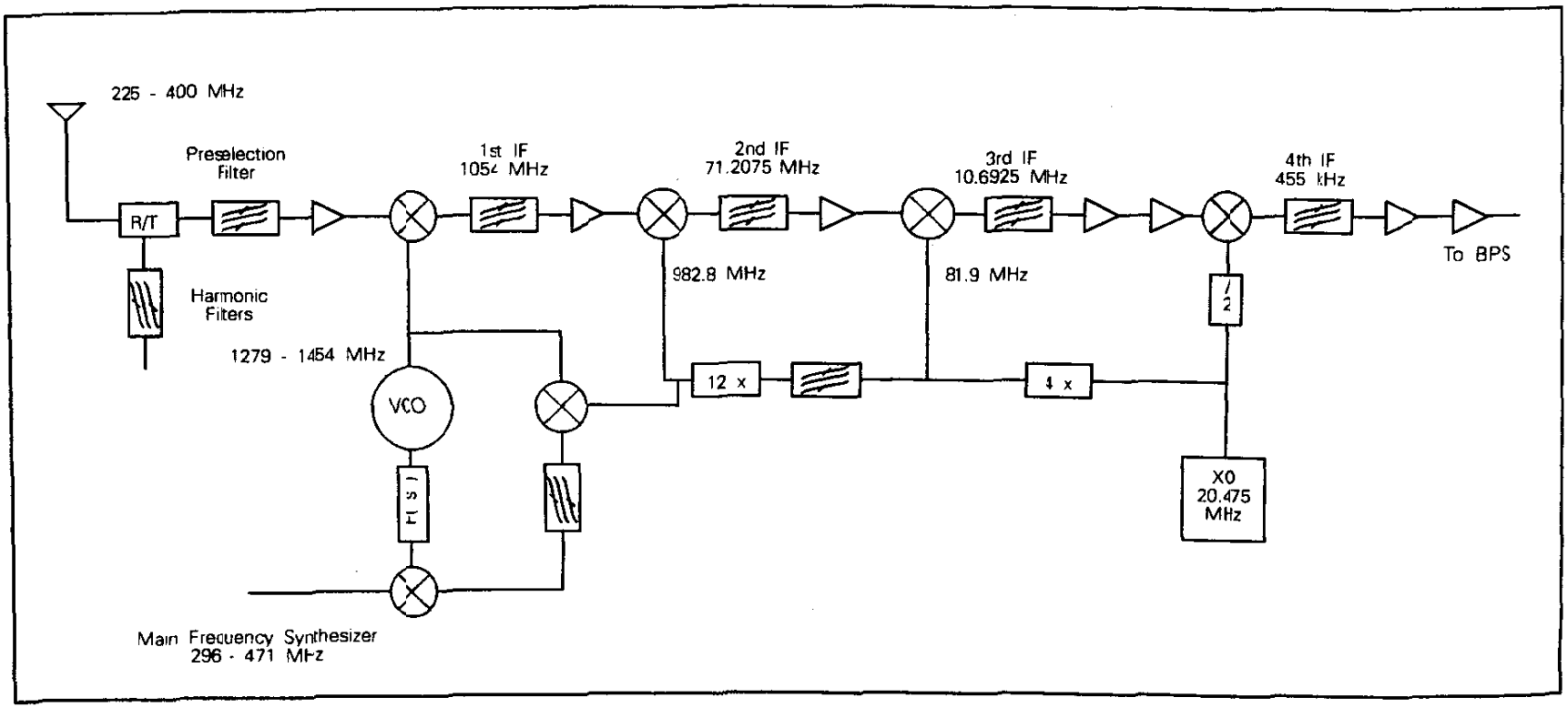

Figure 3 AMST Receiver Frequency Plan for UHF Receive Band

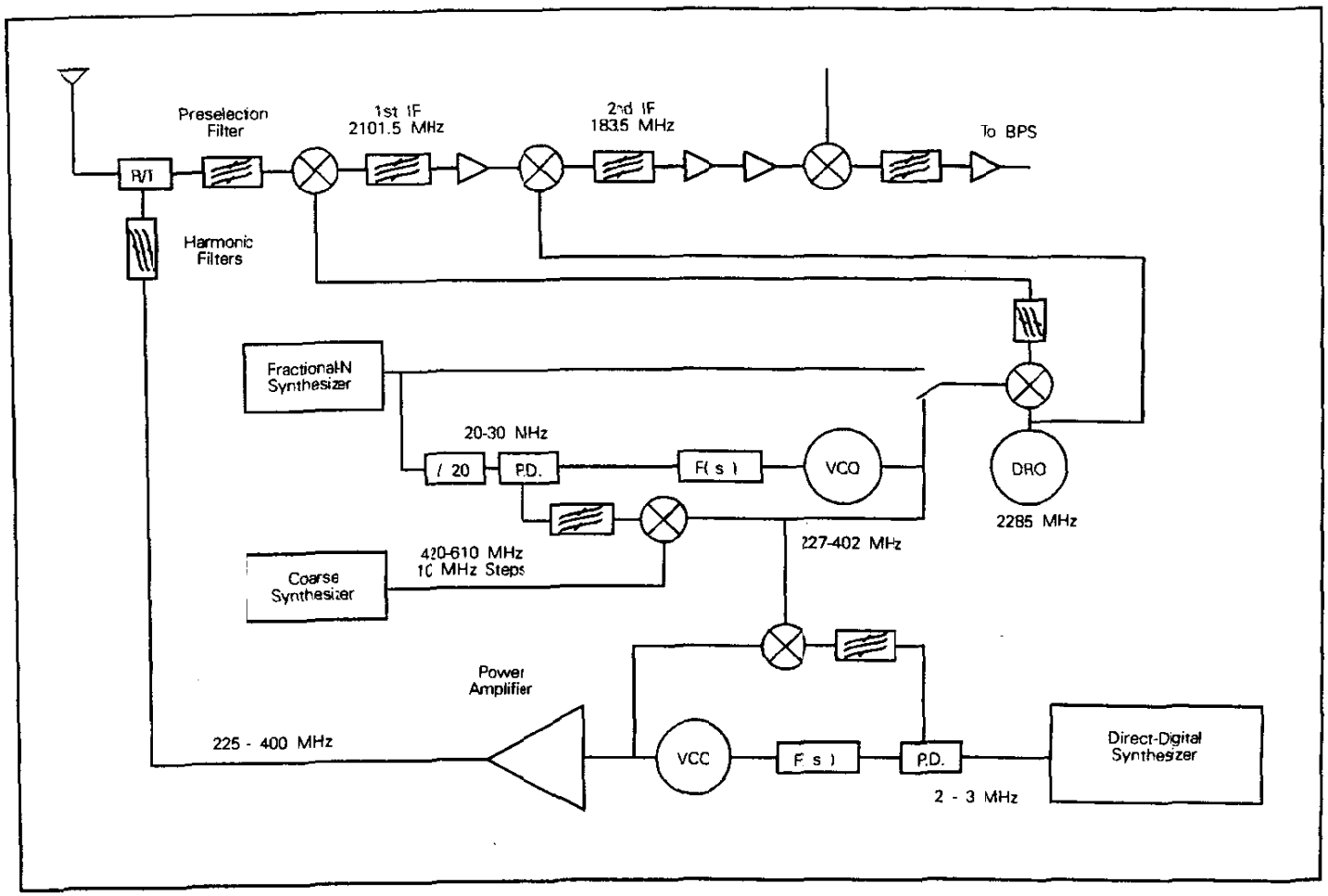

Figure 4 Proposed Radio Architecture from SBIR Phase I Proposal

this IF to 455 kHz could have been done directly, this choice would have resulted in almost all of the receiver gain being placed at one low IF which could easily result in stability problems as well as EMI problems. Instead, the gain is distributed fairly equally between the last two IFs thereby mitigating these concerns. As shown in Figure 3, these choices result in very standard filter frequencies for 2 of the 3 final IFs and creation of the local oscillator (LO) frequencies is very straight forward. Only the US cellular band portion of the 869-960 MHz band is covered in the AMST in order to keep complexity low.

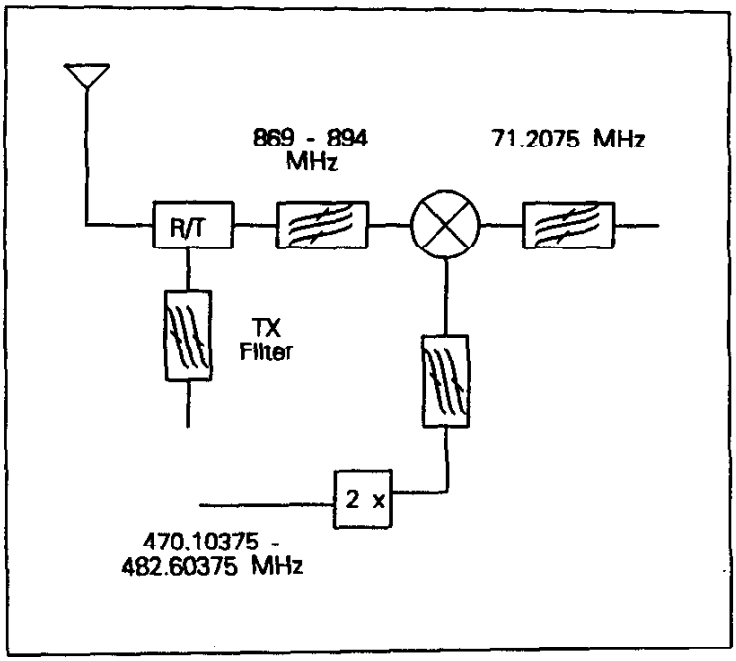

Figure 5 AMST Downconversion for Reception of the US Cellular Telephone Band (869-894 MHz)

The second key cornerstone we presented in [2] was

"The frequency synthesis function which is needed for both the receive and transmit operations should be tailored separately and specifically for each mode respectively in order to reduce power consumption while not sacrificing the attainment of superior transmit spectral purity and accomodating future advanced modulation waveforms."

One of the key ingredients proposed in [2] to achieve this objective was the use of a single-loop fractional-N frequency synthesizer which could provide the needed receiver LO with very low power consumption while tolerating somewhat degraded performance. In situations where better phase noise and spurious

performance was required, the fractional-N loop was to be combined in a three-loop configuration. This approach has been retained as shown in Figure 6. A number of the concepts planned for the fractional-N synthesizer are ComFocus Proprietary, but are nonetheless discussed in considerable detail in Appendices VII and VIII.

Originally in [2], a direct-digital synthesizer (DDS) approach was advocated for the transmit function as shown in Figure 2. Although this approach is quite adequate for the shaped QPSK and BPSK waveforms required for UHF SATCOM operation, this is not true for unshaped waveforms and for linear modulation such as the $\pi/4$-DQPSK waveform utilized in the American and Japanese digital cellular telephone equipment. Therefore, no DDS is used to create the modulation waveform in the AMST.

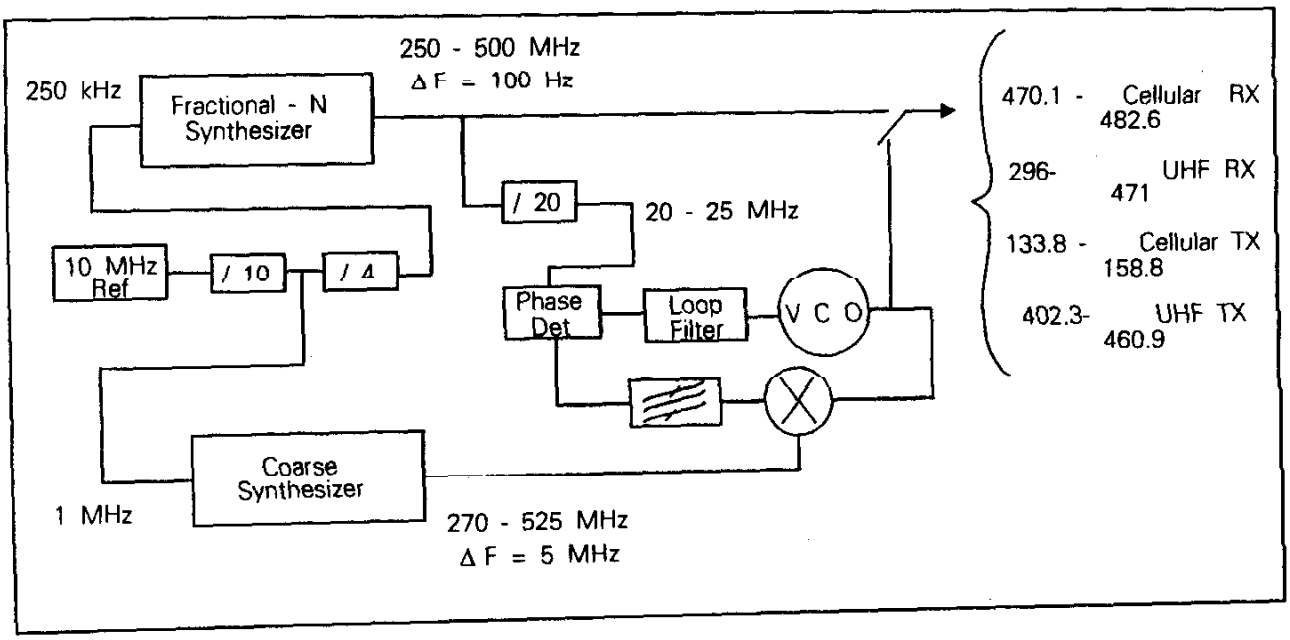

Figure 6 Top Level Block Diagram of the AMST Frequency Synthesis Function

The third cornerstone concept identified in [2] was that

"The latest algorithmic advances in demodulation, carrier recovery, synchronization, etc. should be researched to provide the best overall system implementation possible."

Considerable effort was spent in addressing the necessary signal processing algorithims required within the AMST and the results are detailed across six of the technical appendices provided. As advocated in [2], dedicated hardware will be used to perform most of the numerically intensive calculations within the AMST and digital signal processors will only operate at sampling rates no higher than the baud rate.

Several new signal processing concepts were identified through the course of this effort. One of the more important results found was that the transmitter waveform TOQPSK used in the 5 kHz DAMA mode (and 25 kHz DAMA shaped) could have its spectral sidelobes reduced substantially by angular filtering (Appendix I). A fairly modest amount of filtering substantially reduced the sidelobe spectral content. The smoothing temporarily adopted in this study was that of an N=4 Butterworth filter having BT= 0.8. The transmit spectrum with and without this shaping is shown in Figure 7. Not only is the spectral containment improved, the asymptotic rolloff rate which is really more important for UHF SATCOM cosite operation is improved considerably. The effects of finite numerical precision are evidenced in curve B for normalized offset frequencies exceeding approximately 3.2.

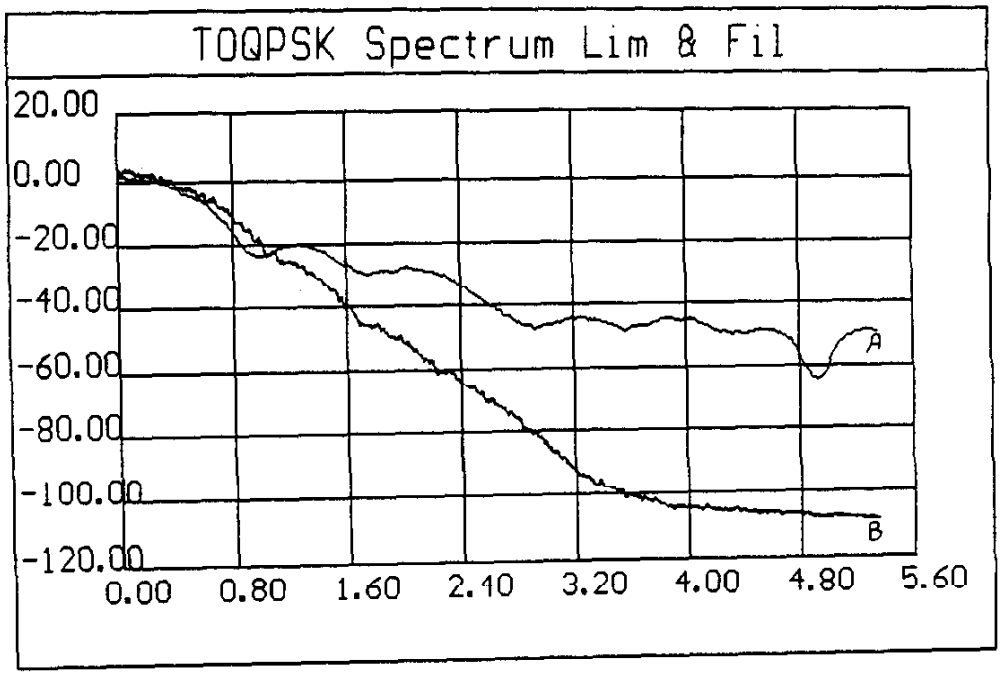

Figure 7 TOQPSK Spectrum with Phase Filtering
Power Spectral Density, dBc Versus Normalized Bandwidth. (A) TOQPSK with No Filtering
(B) N=4 Butterworth, BT= 0.80

Fairly minor eye closure resulted from the additional transmit waveform shaping as shown here in Figure 8. Although some additional intersymbol interference results from this approach, as shown in Appendix V, the impact is not severe.

The AMST utilizes bandpass sampling techniques in order to convert from the final radio IF signal to in-phase (I) and quadrature-phase (Q) samples as introduced in [2]. This technique was refined considerably in Appendix III where a sampling rate of 96 kHz was found which nicely meets all of the required symbol rates and also resulted in a very convenient final IF (456 kHz). The low sampling rate is ideal for low power consumption and 10 to 11 bit A/D converter components. A new algorithm was also derived for performing the necessary Hilbert transform operation using only simple shift and add binary operations and its performance was evaluated in detail. If adopted within the AMST, interpolation errors using this new approach result in an output signal to noise ratio floor of approximately 20-25 dB which is still certainly adequate. Detailed analysis of the sampling rate used compared to the analog-to-digital (A/D) device technology available showed that aperture jitter effects in the A/D converter will not be an issue in the AMST configuration being advocated. Since the bandpass sampling rate is fairly low (<100 kHz), many digital signal processing alternatives are possible.

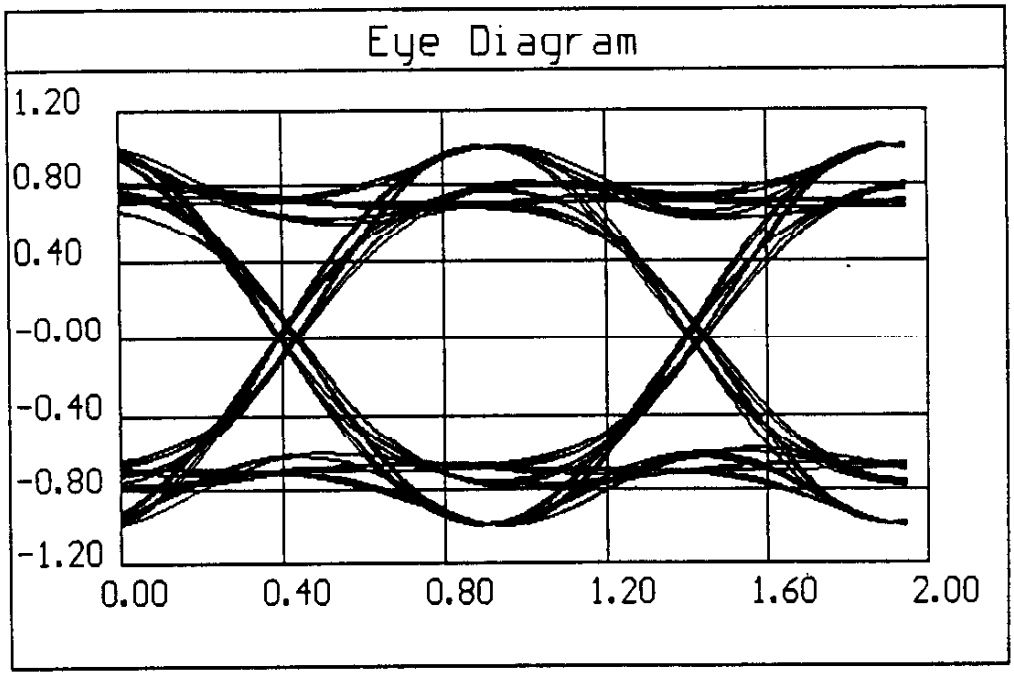

Figure 8 Data Eye Pattern for Phase Argument Filtering N=4 Butterworth, BT= 0.80

Some of the signal processing alternatives possible are discussed in Appendix XIII. Several ComFocus proprietary techniques for AM and FM reception are discussed there. Arbitrary filtering functions and use of the residue number system (RNS) are also considered. Owing to the low sampling rate used within the AMST, the Kenyan double and halve algorithm is proposed for implementing multiplication operations within the AMST with or without using RNS techniques. Finally, a standard integrate-and-dump matched filter receiver is considered for TOQPSK reception and it is shown that immediately adjacent channel interference can be tolerated quite well without resorting to more sophisticated digitally implemented receiver filtering.

Fairly extensive work was performed in connection with the initial acquisition of the 5 kHz DAMA waveform in Appendix IV. As pointed out there, initial acquisition is one of the most difficult problems facing the AMST. Stochastic process methods were developed in detail which show excellent initial frequency error estimation capability. They were further compared with traditional frequency discriminator techniques which have been used in the past as well as the more optimal Bellini method. The initial signal detection issue was also considered and a sufficient test statistic closely related to the frequency estimation process was identified for assessing signal presence.

The results from Appendix IV were then carried over into Appendix V where extensive investigations of the signal processing for 5 kHz DAMA are presented. Using the previous appendix results, the net entry performance for the AMST was examined and guidelines developed whereby the mean-time to net entry can be reduced by as much as 50%. This improvement is possible primarily due to the improved signal acquisition algorithms presented. New algorithms were then derived for carrier phase recovery and symbol timing recovery which are mutually independent of eachother. This mutual independence allows the carrier phase recovery and symbol timing recovery processes to start in parallel rather than necessarily be performed in a serial manner and leads to much more robust initial signal acquisition. Although similar algorithms have been presented in the past for BPSK signalling, the presented results are new and applicable specifically to the TOQPSK preamble used in 5 kHz DAMA. Additional algorithms for steady-state tracking were then addressed and the results used with first-order Markov methods to assess the steady-state performance. Finally, detailed simulation was done to assess the bit error rate performance for 5 kHz DAMA operation at a symbol rate of 3000 sps. Assuming that the N=4 Butterworth transmit filtering is used, the recovered signal constellation at the receiver integrate-and-dump filter outputs in the absence of noise is as shown in Figure 9 where elements of intersymbol interference are clearly visible. The recovered constellation at a carrier to noise ratio of 3 dB is shown in Figure 10 which corresponds to operation of the AMST at the specified sensitivity level for 5 kHz DAMA operation.

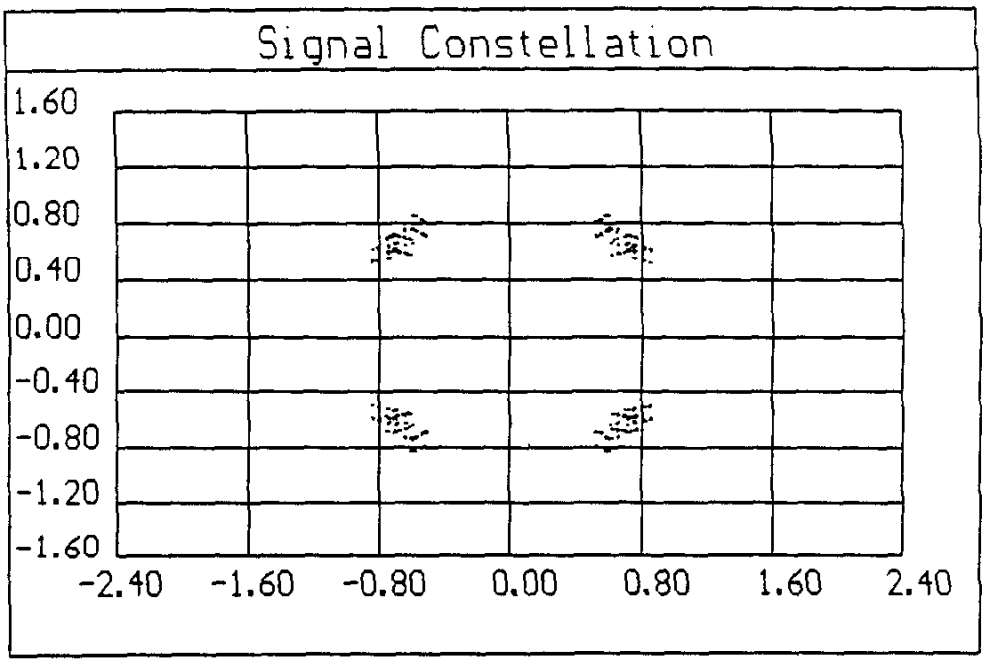

Figure 9 Recovered Signal Constellation at Receiver Output in the Absence of noise

Although considerably more optimization of AMST design parameters has yet to be completed, the (uncoded) bit error rate performance was assessed under the assumptions given in Appendix V for 5 kHz DAMA operation using computer simulation as shown in Figure 10.

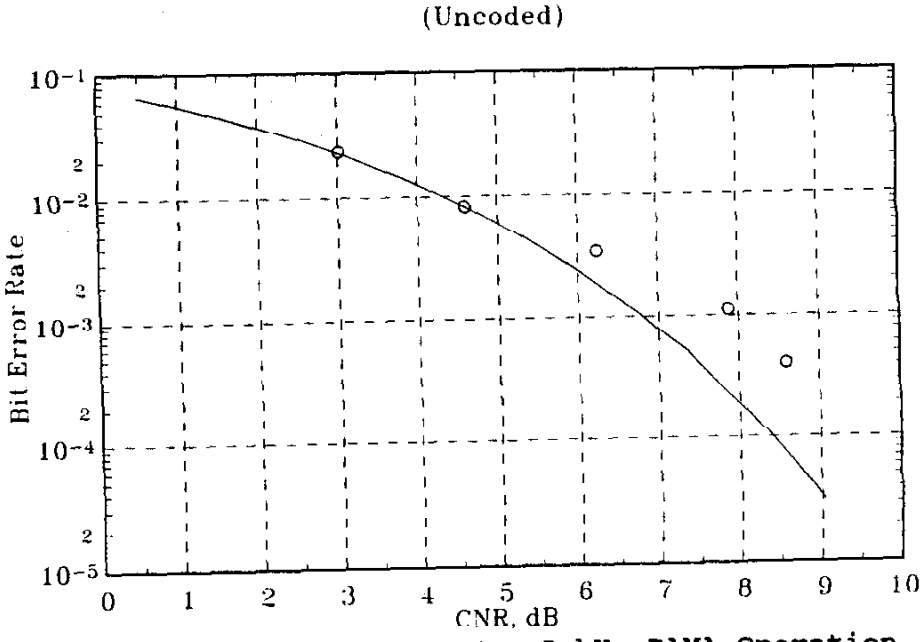

Figure 10 BER Performance for 5 kHz DAMA Operation

The fourth and final cornerstone concept presented in [2] was that

> " Digital signal processing functions should be performed utilizing distributed processing techniques in the form of application-specific-integrated-circuit (ASIC) gate array type technologies in order to maximize the information bandwidth through the radio. Microprocessor elements should only be used for control functions in order to avoid processor bottlenecks. Each ASIC should be configured with a "high-level" command interface with the controlling microprocessor thereby delivering a maximum degree of modularity within the digital portion of the radio."

Conceptually, the algorithms developed in this report support this move toward more distributed processing. However, the scope of this present effort and the funding in Phase II preclude any direct path to gate array implementations, custom or semi-custom. Some of these issues were discussed in Appendix XIII. Actual implementation of the major functions is addressed in more detail in the next section of this report, but in general, the Phase II effort will necessarily make use of much less dense FPGA device technologies.

A substantial amount of information pertaining to DAMA and COMSEC signal processing is contained in Appendix X where the intensive signal processing elements required for signal reception and demodulation have been lumped into the DSP block immediately following the RF front-end electronics. Since the AMST effort will certainly not be developing COMSEC devices even in Phase III, the highly integrated ASIC solutions for COMSEC presently available have been adopted for the AMST. COMSEC related hardware is discussed at length in this appendix. The remaining digital signal processing areas involved with signal demodulation are shown as functional areas in the detailed AMST block diagram which follows, Figure 11.

4.0 AMST Hardware Details

A detailed block diagram of the complete AMST is shown in Figure 11 where the primary emphasis has been placed upon the non-RED hardware elements of the radio. In this section, a detailed discussion of the proposed AMST approach is outlined drawing upon the technical findings which are reported in the technical appendices.

The RED portion of the radio is discussed at length in Appendix X and will not be addressed here. In that appendix, power estimates and real estate estimates for all of the RED signal processing is provided. It is shown that the circuitry fits within the radio volume allocated for this group of functions. Since all of the COMSEC functionality is essentially pre-defined by NSA, this portion of the AMST is quite straight forward and estimates on size and power consumption are only needed in order to assist in budgeting the other radio functionality across the remainder of the radio volume available.

UHF Portion of the AMST

The UHF RF portion of the AMST is shown in substantial detail in Figure 11A. Although all of the details may be found in the appendices, an abbreviated discussion will be presented here to illustrate the key elements of our approach.

The first evidence of cosite considerations in our approach is the inclusion of the pre-selection filtering at the front-end of the radio (upper left hand corner). As discussed in Appendix XII, this filtering is crucial in order to permit multiple AMST units to operate in reasonably close proximity to one another. The same filtering path is used in the transmit mode between the driver and power amplifier stages in order to reduce the noise floor for similar reasons. This filtering element represents a very key element in the AMST concept.

Focusing upon the receive path first, the desired signal is first up-converted to a high IF of 1054 MHz in order to achieve very good spurious performance, and then down-converted to a much lower IF of 71.2075 MHz. A summing loop is used to combine the frequency synthesizer output with the second local oscillator as shown for the first mixing operation. An auxiliary IF input port is shown to support reception of the cellular band, or other frequency bands if so desired. The 71.2075 MHz IF signal can then be despread if necessary for spread-spectrum reception. The chip rate supported must be less than approximately 1.5 MHz. Following this operation, the IF signal is downconverted once more to 10.6925 MHz and finally to a final IF of 456 kHz for UHF reception, 461.7 kHz for US digital cellular $\pi/4$-DQPSK.

The multiple IF approach used in the receive path is instrumental in supporting excellent spurious performance for both

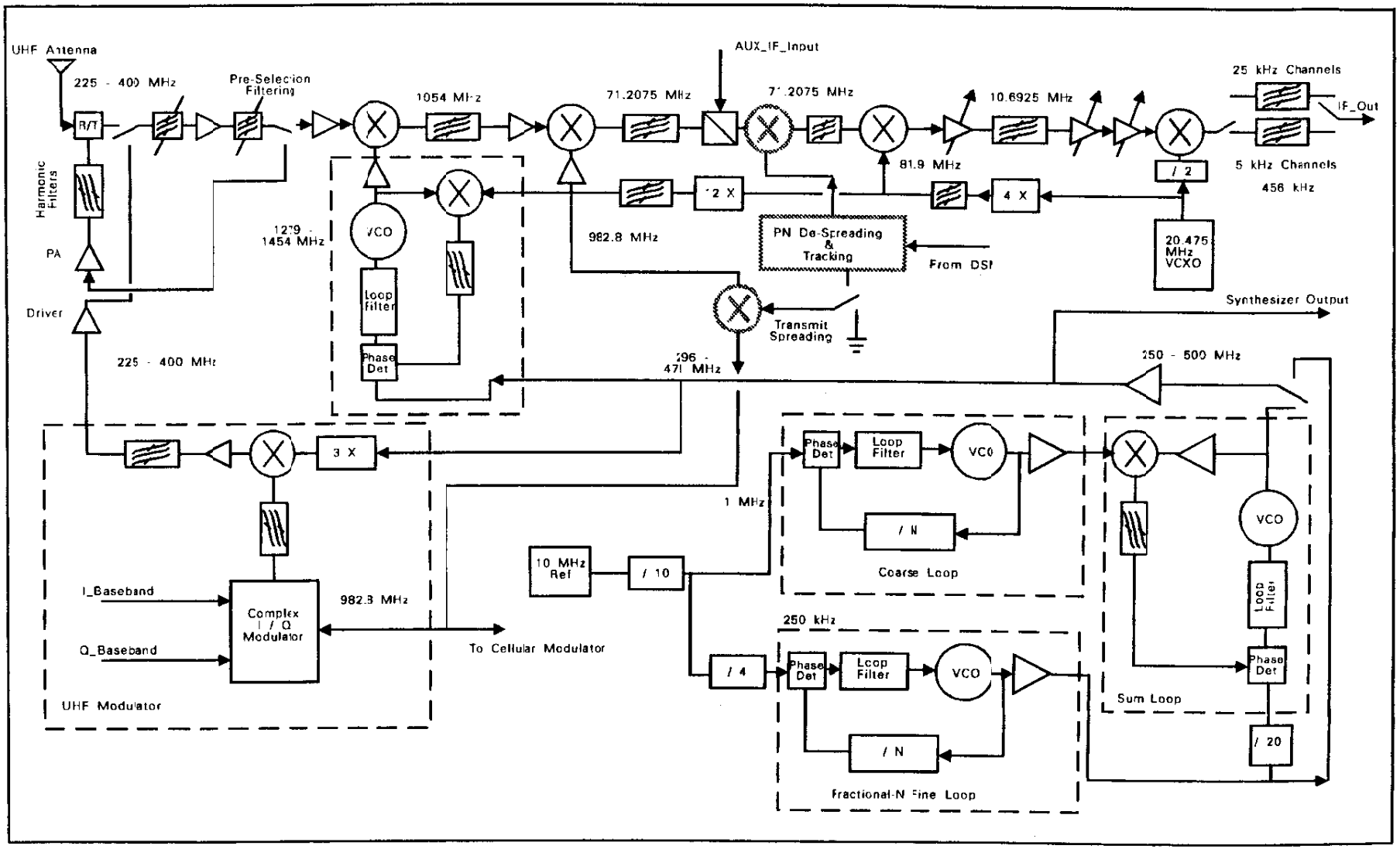

Figure 11A UHF RF Portion of the AMST Radio

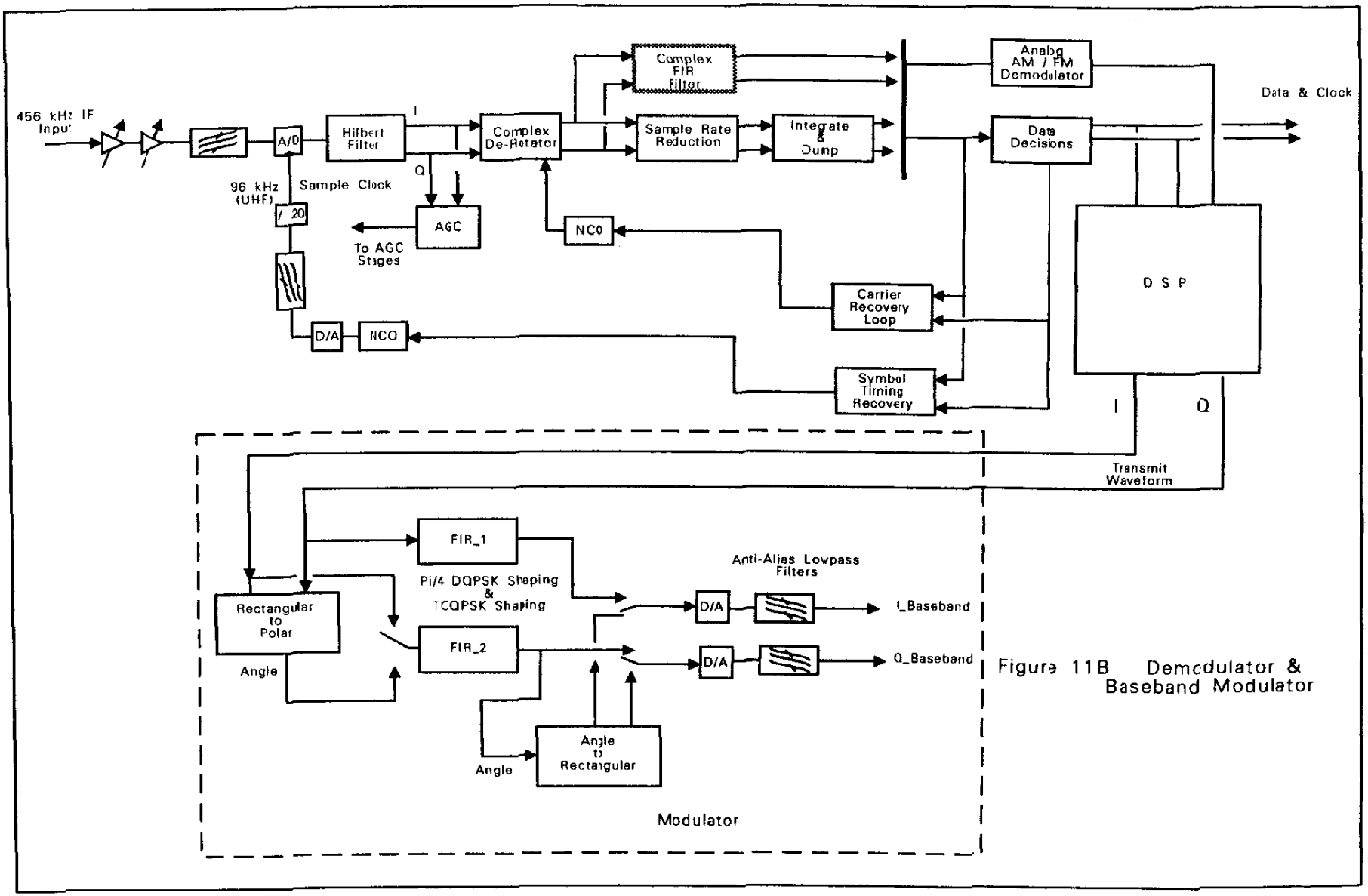

Figure 11B Demodulator & Baseband Modulator

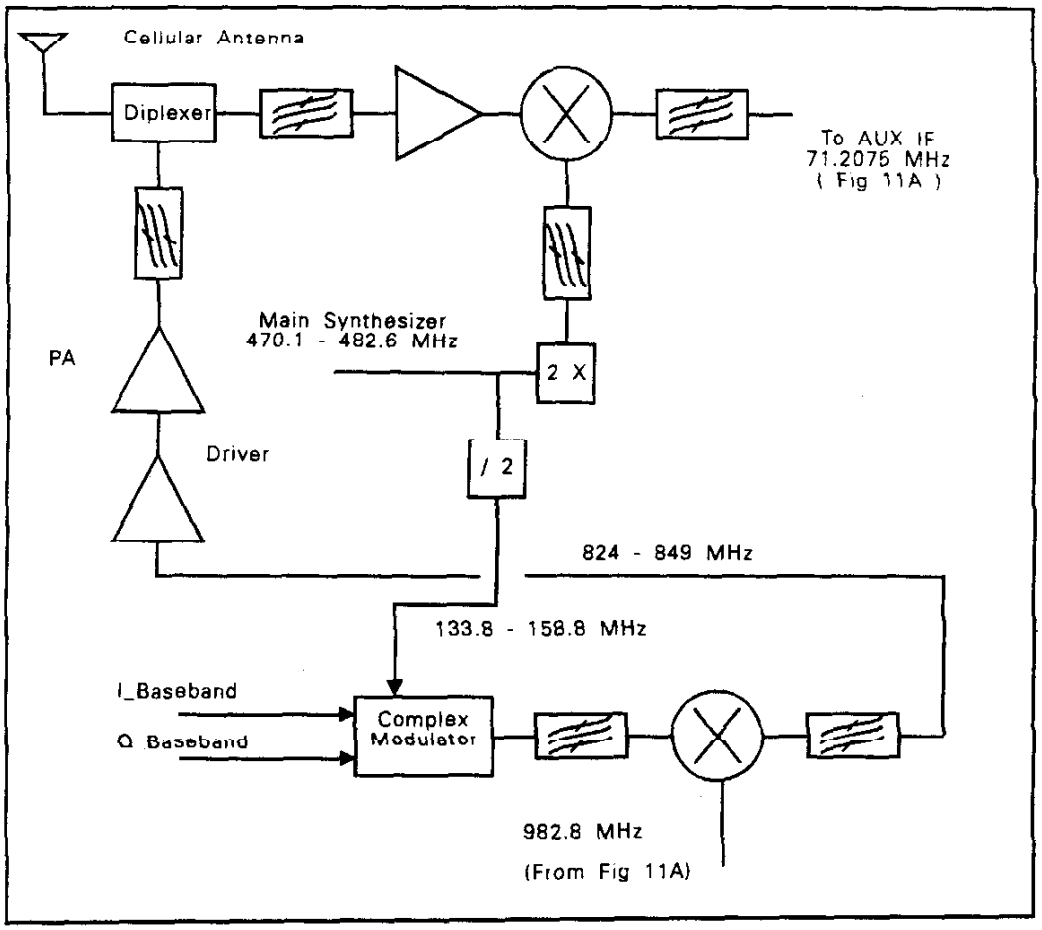

Figure 11C Cellular Portion Front-End Portion of the AMST

UHF and cellular receive bands. The use of two fairly low IFs in the radio (10.6925 MHz and 456 kHz) permits the necessary gain to be evenly distributed between these two frequencies which eliminates the need for intricate shielding. The entire receive chain portion will be able to be built on one surface mount card with no shielding for this very reason. Shielding will only be present to separate the frequency synthesizer portion of the RF receive electronics from the receive chain.

Although not explicitely shown, the 20.475 MHz VCXO is phase-locked to the precision 10 MHz reference source. This guarantees excellent frequency accuracy for the complete receive chain. The VCXO is first multiplied by 4 in order to obtain the needed tone at 81.9 MHz which is used for the frequency conversion from 71.2075 MHz to 10.6925 MHz. The 81.9 MHz signal is then multiplied up to 982.8 MHz and used directly as the local oscillator for the second mix operation. This frequency is also used in the cellular transmitter portion as shown in Figure 11C.

Provisions are shown for two switchable final IF filters which are intended to support 5 kHz and 25 kHz channel operations. Best

intermodulation performance is obtained when the electronics must process the minimum input bandwidth possible.

The primary automatic gain controlled (AGC) amplifiers are those at the two lowest IFs where most of the receive gain is located. Other gain elements within the receive path are only present to preserve the noise figure at the front end of the radio. These stages will require very little AGC control.

The first receiver mixing operation is particularly critical for preserving the large-signal performance of the radio. This component often determines the intermodulation performance of the radio, and hence what is commonly called the receiver's 3rd-order intercept. In [2], we proposed a first mixing stage which had an adjustable local oscillator power level to deal with this issue. A high power local oscillator signal (e.g., +17 dBm) would be used in cosite intensive situations whereas otherwise, a nominal lower power local oscillator signal (e.g., +7 dBm or lower) would be used in order to conserve battery power. The higher mixer insertion loss would be made up by increasing the radio front end low-noise amplifier gain in order to retain a good receiver noise figure. Due to the limited scope of Phase I, we have not taken this concept further, but we have retained it for planned inclusion in our Phase II effort.

One potential area for additional research in the mixer area surfaced during our investigations pertaining to the use of FET devices in a passive mixer configuration. This interest has been motivated by an expired patent [17] and comments by some authors [18] about the extremely high intercept performance achievable with this concept. One of the additional virtues of this approach as far as the AMST is concerned is that the local oscillator signal in this approach is applied to the fairly high impedance FET gate terminals thereby resulting in low power requirements. Since the first LO must only cover 12.8% tuning range for UHF reception, it should be possible to construct a Fano matching network which would be capable of delivering the necessary gate voltage swing with very little actual oscillator power required. Research is continuing with FET devices in mixers, but most of the work has continued to be done at frequencies in excess of 10 GHz [19-22]. A careful examination of these concepts for use in the AMST first IF is advised.

The frequency synthesizer used in AMST utilizes a triple loop configuration for high spectral performance, but can be scaled back to a single fractional-N loop when power consumption is critical during receive operations. The frequency synthesizer portion of the AMST is shown in the lower right hand portion of Figure 11A. As discussed in Appendix VII, the coarse loop steps in increments of 5 MHz whereas the fine loop provides the remainder of the frequency precision. The loop designs support a worst-case switching time of less than 100 microseconds. Phase noise issues were treated at length in this appendix also. Since the frequency synthesizer covers a complete octave in frequency, all of the variable local

oscillator requirements elsewhere in the AMST are easily met by either directly dividing down or multiplying up the basic synthesizer output.

The modulator portion of the AMST UHF radio is shown in the lower left hand corner of Figure 11A. It makes use of a new monolithic complex modulator available from Hewlett-Packard to directly impress I and Q channel modulation on the 982.8 MHz carrier. This carrier may also be spread using a multiplicative PN sequence as shown to support limited spread-spectrum transmission. The modulator fixed output frequency is then translated in frequency as shown using the main frequency synthesizer to cover the entire UHF band. As shown in Appendix VI, this frequency plan is virtually spurious free.

Little research was done in the power amplifier area during this phase owing to the limited resources available, but this is not intended to undermine the importance of this function in the AMST. Some applicable comments are given in Appendix VI. In general, the PA will require careful consideration given that (i) ideally it will efficiently support linear modulation types such as $\pi/4$-DQPSK and (ii) also be capable of power level control per our findings concerning SATCOM link margins. A total dynamic range of 10 dB should be sufficient for SATCOM power level control whereas a greater linear dynamic range will of course be required to support high quality linear modulation waveforms.

Baseband Demodulation and Modulation Functions

The baseband elements necessary to support modulation and demodulation within the AMST are shown in Figure 11B. The architecture represents the findings contained across roughly six separate appendices. In the upper left hand corner of this figure, the 456 kHz IF signal appears and is amplified. It is filtered once more following the gain stages prior to being converted into digital form via the A/D converter. Bandpass sampling techniques are utilized here as developed in Appendix III. As described there, the actual RF center frequency for all of the UHF operations is 456 kHz whereas cellular operations will be done using an IF frequency of 461.7 kHz with a sampling rate of 97.2 kHz. Ten and eleven bit A/D converters with low power consumption are obtainable at this sampling rate. A Hilbert transform filter operates on the serial sample stream and creates pairs of I and Q samples at its output. Although a new approach for this transform was developed in Appendix III, more than likely, the more exact approach shown in A3.2 will be adopted for the AMST. The I and Q sample pairs are then de-rotated numerically as shown and this same mechanism serves in the carrier recovery process to correct the local phase estimate. After de-rotation, sample-rate reduction and integrate-

and-dump operations may be done as for QPSK,TOQPSK, etc., or in the case of $\pi/4$-DQPSK, the de-rotated samples must be put through the more sophisticated sqare-root raised cosine matched filter. At this point in the radio, data decisions may be formed, or the filtered samples are passed to numerical AM/FM demodulators where analog demodulation is effectively implemented. Carrier phase recovery and symbol timing recovery loops are closed back through numerically controlled oscillators (NCO) as shown. Although explicit linking with the DSP has not been shown, all of the major distributed processing functions are initialized and controlled via the DSP.

On the transmit side of this figure, the DSP outputs I and Q data samples which are effectively up-sampled by the FIR filters shown with typically 4 samples per symbol. The rectangular-to-angle path/FIR filter/angle-to-rectangular path is taken when constant envelope modulation with angular filtering is desired, such as for TOQPSK as discussed in Appendix I. In most cases, the I and Q data paths simply undergo waveshaping and up-rate sampling in the pair of FIR filters and are then converted to baseband analog signals which are feed to either the UHF or cellular complex modulators. The modulator and frequency translation blocks for the UHF transmit function are shown in Figure 11A.

The cellular front-end portion of the AMST is shown in Figure A11C where the frequency translation down to an IF of 71.2075 MHz is shown along with the cellular modulator and upconversion to the cellular transmit band. As discussed in Appendix VI, both frequency translations are essentially void of spurious products. The main frequency synthesizer output is again used to provide the needed agile local oscillator signals. Only half-duple operation is supported, the justifications given in Appendix VI.

Much more could be said about the detailed AMST design but most of the applicable comments are available in the technical appendices. The details to support antenna diversity or adaptive equalization for cellular reception have not been included in Figure 11 in order to keep the level of detail reasonable and the fact that these areas remain open research areas as discussed in Appendix XIII.

and-dump operations may be done as for QPSK,TOQPSK, etc., or in the case of $\pi/4$-DQPSK, the de-rotated samples must be put through the more sophisticated sqare-root raised cosine matched filter. At this point in the radio, data decisions may be formed, or the filtered samples are passed to numerical AM/FM demodulators where analog demodulation is effectively implemented. Carrier phase recovery and symbol timing recovery loops are closed back through numerically controlled oscillators (NCO) as shown. Although explicit linking with the DSP has not been shown, all of the major distributed processing functions are initialized and controlled via the DSP.

The DSP operations are limited to baud-rate calculations at most, all of the numerically intensive calculations involved with signal detection, carrier tracking and symbol timing recovery, etc. delegated to dedicated distributed hardware. Ideally, these functions would be architected in one or two custom gate arrays. In the context of Phase II however, the functions will be distributed across a number of Actel or Xylinx devices in all probability due simply to cost constraints.

On the transmit side of this figure, the DSP outputs I and Q data samples which are effectively up-sampled by the FIR filters shown with typically 4 samples per symbol. The rectangular-to-angle path/FIR filter/angle-to-rectangular path is taken when constant envelope modulation with angular filtering is desired, such as for TOQPSK as discussed in Appendix I. In most cases, the I and Q data paths simply undergo waveshaping and up-rate sampling in the pair of FIR filters and are then converted to baseband analog signals which are feed to either the UHF or cellular complex modulators. The modulator and frequency translation blocks for the UHF transmit function are shown in Figure 11A.

The cellular front-end portion of the AMST is shown in Figure A11C where the frequency translation down to an IF of 71.2075 MHz is shown along with the cellular modulator and upconversion to the cellular transmit band. As discussed in Appendix VI, both frequency translations are essentially void of spurious products. The main frequency synthesizer output is again used to provide the needed agile local oscillator signals. Only half-duple operation is supported, the justifications given in Appendix VI.

Much more could be said about the detailed AMST design but most of the applicable comments are available in the technical appendices. The details to support antenna diversity or adaptive equalization for cellular reception have not been included in Figure 11 in order to keep the level of detail reasonable and the fact that these areas remain open research areas as discussed in Appendix XIII.

5.0 Conclusions

A large span of topics have been addressed during this SBIR as shown by the breadth and detail of the technical appendices which follow. The primary findings which were presented at the beginning of this report generally summarize our most important conclusions. Summarizing these findings in three final conclusions, we present that

1) Cosite issues are a very severe consideration which can only be addressed by a top-level down systems approach as initiated here. Our findings show that virtually every element of the RF portion of the AMST is affected by any attempts to deal with cosite interference. Generic radios not designed or equipped as the AMST will generally interfere with eachother unless placed hundreds of feet apart.

2) Interoperability with civilian communication systems such as the U.S. cellular telephone system is tactically important for a radio such as the AMST. As shown in this report, modifications to support a cellular capability within the AMST are quite modest.

3) Distributed signal processing techniques are invaluable for providing superior computational throughput and upgradeability within the AMST. Even in functional areas where details have not been fully defined, allocation of an ASIC place holder for those spots permit the detailed design to continue, providing avenues for later refinements to be inserted at reasonable cost.

6.0 Recommendations

A dedicated attempt has been made to include as much "bang for the buck" as possible in the AMST architecture proposed herein. Significant performance improvement opportunities have been an additional by-product of this effort as well. We believe that even if the present AMST concept did not go beyond a 19 inch rack mount version, it would be a valuable communication asset to the Air Force.

The shere mass required to develop a complete AMST radio must be sized with respect to the Phase II resources available. Rather than come out with a Phase II piece of hardware that only proves a concept but is otherwise useless, we advocate that the magnitude of the Phase II effort be tailored such that valuable concepts are proven while also delivering a genuine usable product to the U.S. Air Force. Therefore, we advocate the following recommendations for the Phase II prototype effort:

1) The AMST should be built in order to demonstrate and refine the technical findings reported hereing, noteably those pertaining to cosite, multi-channel DAMA, distributed signal processing, and interoperability with civilian communication services.

2) In order to keep the Phase II objectives reasonably proportioned with respect to the funding resources available, the AMST should be built having the necessary RED/BLACK interface, but excluding the COMSEC elements discussed in Appendix X. Efforts would be focused upon the remainder of the AMST. The remainder of the AMST could be emulated by an outboard computer and/or additional hardware.

3) Since custom gate arrays will not be possible for the Phase II effort, the digital portion of the AMST will be fairly large. Customization of some RF components may also be prevented by cost constraints and therefore physically larger than desired. Even so, the AMST prototype should be made as physically small as possible, particularly the RF electronics areas. Implementation approaches should be adopted which lend themselves easily to miniaturization.

We believe that the AMST architecture proposed represents a very good compromise between RF and digital technologies, as well as between centralized and distributed digital signal processing. *We belive it could serve the U.S. Air Force very well.*

References

1] Rappaport, T.S., "The Wireless Revolution," IEEE Communications Magazine, November 1991, pp. 52-71

2] ComFocus Corporation, "Advanced Manpack Radio Concept for UHF DAMA Satellite Communications," SBIR Proposal AF91-030, 7 January 1991

3] Electronics Industry Association/Telecommunications Industry Association Interim Standard IS-54, "Cellular System Dual-Mode Mobile Station-Base Station Compatibility Specification," May 1990

4] Lee, W.C.Y., "Smaller Cells for Greater Performance," IEEE Communications Magazine, November 1991, pp. 19-23

5] Schilling, D.L., et al., "Spread Spectrum for Commercial Communications," IEEE Communications Magazine, April 1991, pp. 66-79

6] Noreen, Gary K., "Mobile Satellite Communications for Consumers," Microwave Journal, November 1991, pp. 24-34

7] Pisano, J.J., "Using GPS to Calibrate Loran-C", IEEE AES-27, July 1991, pp. 696-707

8] Lodge, J.H., "Mobile Satellite Communications Systems: Toward Global Personal Communications," IEEE Communications Magazine, November 1991, pp. 24-30

9] Wood, P., "Mobile Satellite Services for Travellers," IEEE Communications Magazine, November 1991, pp. 32-35

10] Grubb, J.L., "The Traveller's Dream Come True," IEEE Communications Magazine, November 1991, pp. 48-51

11] Kucar, A.D., "Mobile Radio: An Overview," IEEE Communications Magazine, November 1991, pp. 72-85

12] Schilling, D.L., "Broadband CDMA for Personal Communications Systems," IEEE Communications Magazine, November 1991, pp. 86-93

13] Cox, D.C., "Universal Digital Portable Radio Communications," IEEE Proc. Vol. 75, April 1987, pp. 436-477

14] Levesque, A.H., et al., "A Proposed Federal Standard for Narrowband Digital Land Mobile Radio," Milcom 1990, pp. 23.1.1-23.1.5

15] Federal Standard 1023, "Telecommunications: Interoperability Requirements for Encrypted, Digitized Voice Utilized with 25 kHz Channel FM Radios Operating Above 30 MHz,", Sept. 25, 1989

16] Defense Communications Agency, "Technical Interface Specification: 25 kHz UHF TDMA/DAMA Waveform," JTC3A Specification 9128, 31 July 1989

17] Squires, W.K., "Mixer Circuit Employing Linear Resistive Elements," U.S. Patent 3,383,601, May 14, 1968

18] Rohde, U., "Performance Capability of Active Mixers," Professional Program Session Record, Wescon 1981

19] Maas, S.A., "Analysis and Design of GaAs MESFET Mixers," IEEE MTT-S Digest, 1984

20] Ohnishi, H., S. Yamashita, "S- and X-Band GaAs FET Mixers with Thin-Film Lumped Elements," IEEE MTT, January 1984

21] Hayward, W., "Experiments with Primitive FET Mixers," RF Design, November 1990

22] Maas, S.A., "A GaAs MESFET with Very Low Intermodulation," IEEE MTT, April 1987

Appendix I

5 kHz DAMA Spectral Occupancy

Spectrum considerations for UHF SATCOM and LOS communications is becoming an increasingly important issue as demands for frequency spectrum increase worldwide. Efforts are well underway to insure that future U.S. military communication systems are as spectrally efficient as possible [A1.1].

In generalized waveform design, spectral occupancy issues cannot be considered independently from the waveform's bit error rate (BER) performance versus signal-to-noise ratio (E_b/N_o) and receiver complexity. The receiver complexity issue is particularly acute for portable operation where low power consumption is critical.

In the present context, we have a very constrained problem where the 25 kHz and 5 kHz modulation waveforms have largely been defined [A1.2,A1.2]. Only minor implementation modifications can even be considered. In this appendix, several approaches are considered for improving the transmit spectrum occupancy for TOQPSK which is presently specified for the 5 kHz DAMA waveform. As the following analysis supports, substantial improvement over existing methods is possible with negligible impact to existing user equipments.

5 kHz Waveform

The 5 kHz DAMA waveform utilizes shaped offset quadrature phase-shift keying (SOQPSK). The ideal SOQPSK signal can be represented as [A1.3]

$$\begin{aligned} s(t) &= A \sin[\, \omega_o t + \varphi(t) \,] \\ &= \frac{A}{2}\, a_I(t)\, \cos\left[\omega_o t + \frac{\pi}{4}\right] + \frac{A}{2}\, a_Q(t) \sin\left[\omega_o t + \frac{\pi}{4}\right] \end{aligned} \qquad (1)$$

where

$$\varphi(t) = 0,\ \frac{\pi}{2},\ \pi,\ \frac{3\pi}{2}$$

with $a_I(t)$ and $a_Q(t)$ being the in-phase and quadrature-phase data modulation signals (±1) respectively. The quantity T is the symbol period.

A representative example of SOQPSK signaling is shown in Figure A1.1. The smoothing is accomplished by allowing 50 percent of a symbol time for the transition between alternating channel bits as shown. In principle, this percentage could be made arbitrary.

The modulation and demodulation processes are required to introduce no more than 1.0 dB of performance degradation from the theoretical performance of the 25 percent trapezoidal waveform shown in Figure 1 [A1.3]. This specific waveform will be refered to as Trapezoidal Offset QPSK (TOQPSK) throughout the remainder of this appendix.

The intention behind the TOQPSK waveform is to provide as much spectral confinement as possible while presenting a nearly constant-envelope signal to the satellite. The constant-envelope attribute is desirable because any amplitude variations of the signal are generally transformed into phase modulation via Am to PM conversion in the nonlinear satellite transponder which causes undesirable spectral broadening.

The issue of spectral broadening has received considerable attention of late in the commercial marketplace where service providers are delivering in excess of 30 Mbps to high-end users via satellite. Researchers have strayed away from offset QPSK waveforms back to normal QPSK waveforms utilizing Nyquist shaping (e.g., seperate raised-cosine filtering on I and Q channels prior to transmission) because they have found that any channel phase irregularities translate into substantial cross-coupling of the I and Q channels at the receiver thereby degrading performance. Although equalization or maximum likelihood sequence estimation (MLSE) techniques could be used to alleviate the problems observed, this would add substantial cost to the receiver unit which is unacceptable. The situation with AMST is substantially different since data rates are substantially less, an offset waveforms has already been selected as the 5 kHz DAMA standard to date, and there is not a substantial cost issue for transmitter versus receiver aside from power consumption issues.

With this information as background, we will examine possible modifications to the TOQPSK waveform in the balance of this appendix which result in improved spectral performance with negligible BER performance loss.

Approach

Intuitively, there is little doubt that improvements can be made to the TOQPSK spectral confinement because

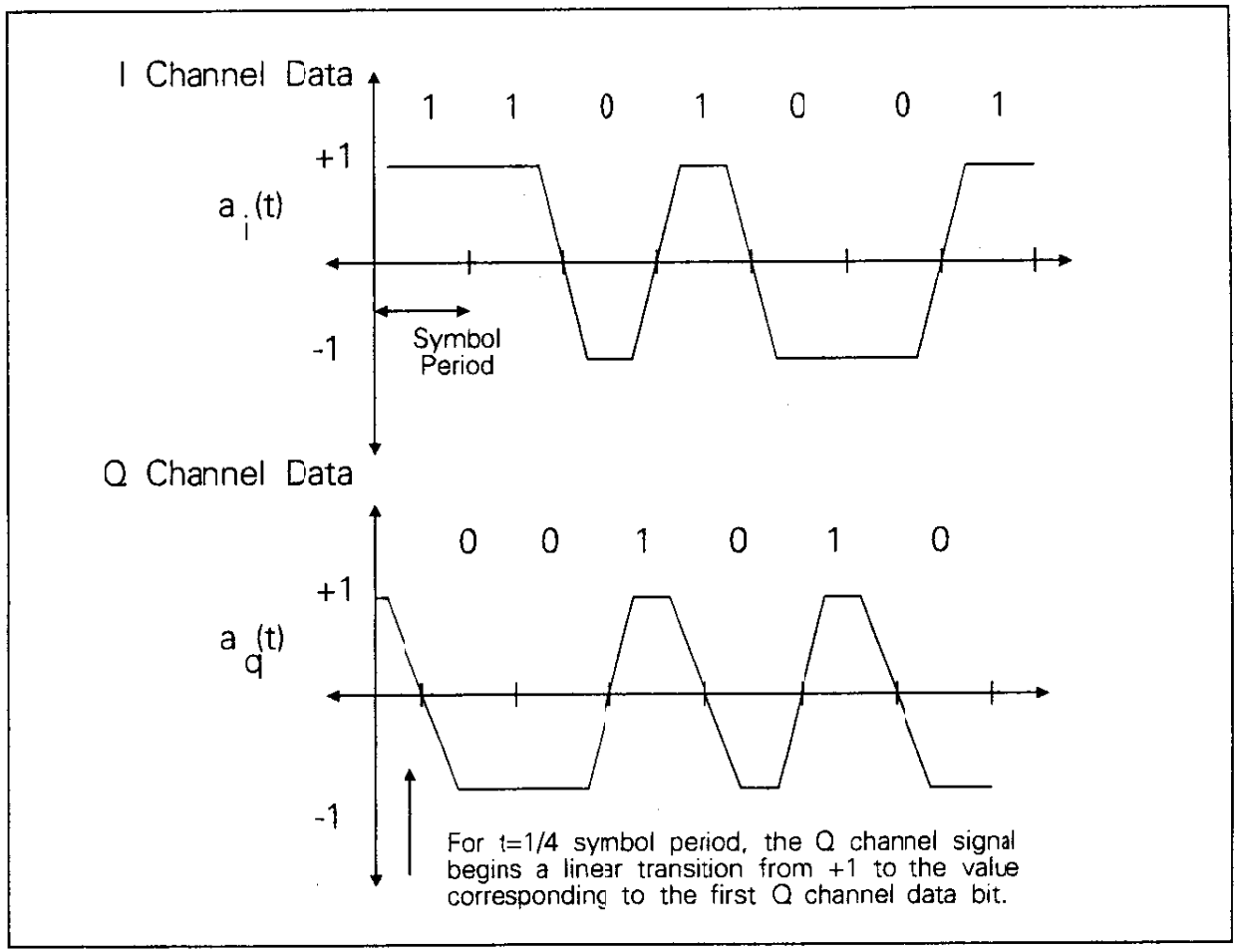

Figure A1.1 Example SOQPSK Modulator Waveforms.

i) TOQPSK as shown in Figure A1.1 is not constant-envelope,

ii) when I and Q signals in Figure A1.1 are expressed in polar form, the angular argument is a discontinuous function of time.

Exploitation of this second factor is important because it can be shown that if the phase response g(t) corresponding to a transmitted symbol has m continuous derivatives, then the power spectral density asymptotically falls off as $1/f^{(2m+4)}$ [A1.4].

Three separate approaches will be considered for improving the TOQPSK waveform for spectral containment, specifically (i) filtering of the hard-limited TOQPSK waveform using a phase-locked loop, (ii) explicit filtering of the forementioned phase function of the TOQPSK polar signal representation, and (iii) a nearly optimal method which is only included for academic interest.

Filtered TOQPSK Using a Phase-Locked Loop

This approach automatically came to mind because of its simplicity and possible inclusion in other radio elements without additional complexity. Although the phase-locked loop (PLL) is guaranteed to add at least one dominant pole due to the embedded voltage-controlled oscillator (VCO), loop stability issues prevent arbitrary filtering functions to be realized as a rule.

As an aside, a simple Markov model for the TOQPSK waveform can be found by considering the waveforms shown in Figure A1.2. The top trace is for the I or Q signal rail showing trapezoidal shaping whereas the second trace represents the time derivative of the first. Clearly, +1 and -1 pulses are sufficient to describe the modulation in the derivative context with the added constraint that consecutive +1s or -1s are disallowed. For purely random data, the Markov diagram shown in Figure A1.3 applies.

Prior to hard-limiting of the TOQPSK waveform shown in Figure A1.1, the waveform does not have a constant-envelope as stated earlier. The envelope when viewed over a period of two symbol periods would appear as shown in Figure A1.4. The peak-to-valley power ratio is $20.0\ \mathrm{Log}_{10}(\sqrt{2})$ or 3 dB.

Although completely analytical techniques could be used to compute the power spectral density PSD for unfiltered TOQPSK, a numerical approach was taken here, anticipating the need for this approach in subsequent analyses. The formal definition used for the PSD here, based upon ergodicity, has the discrete time form [A1.5]

$$P_{xx}(f) = \lim_{N\to\infty} \mathbf{E}\left\{ \frac{1}{(2N+1)\,T} \left| T \sum_{n=-N}^{N} x[n]\; e^{-j2\pi fnT} \right|^2 \right\} \qquad (2)$$

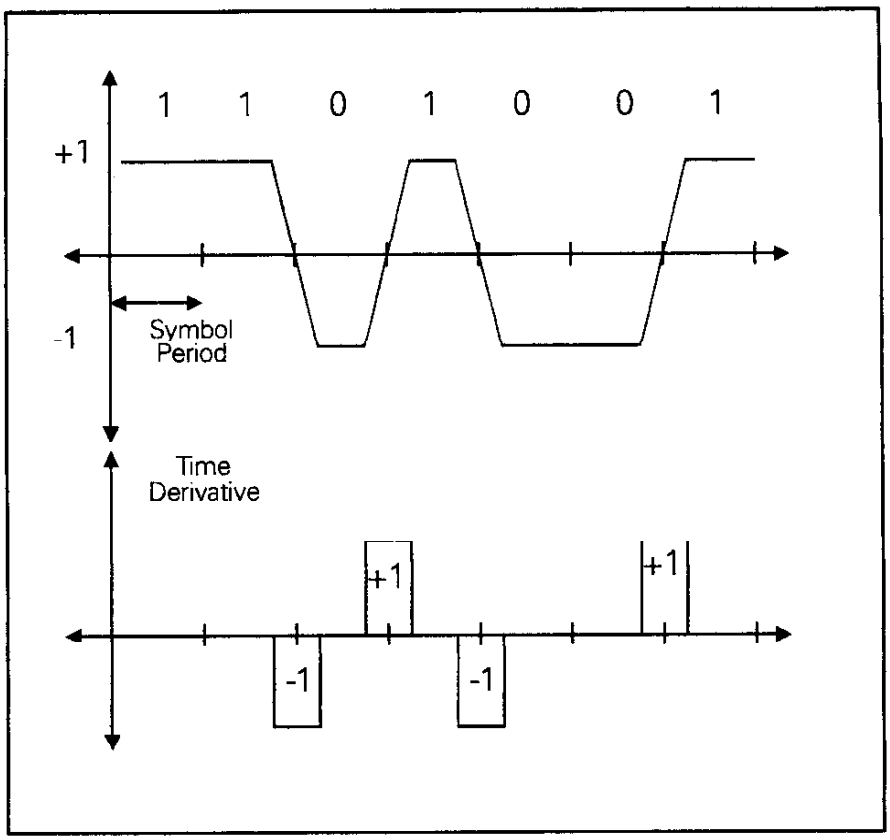

Figure A1.2a I (or Q) channel modulator signal and its time derivative.

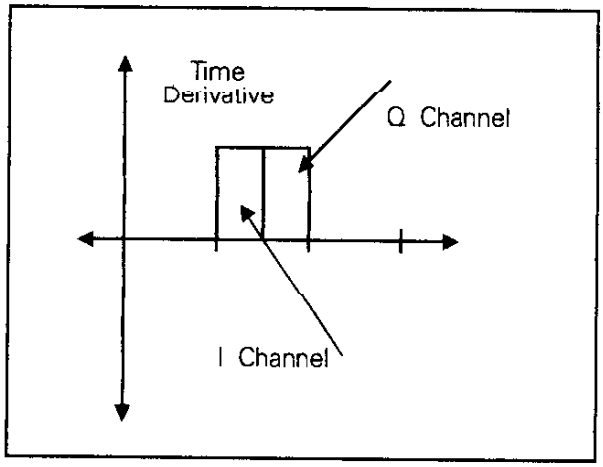

Figure A1.2b Positive-going basic units for I and Q channel time function derivatives.

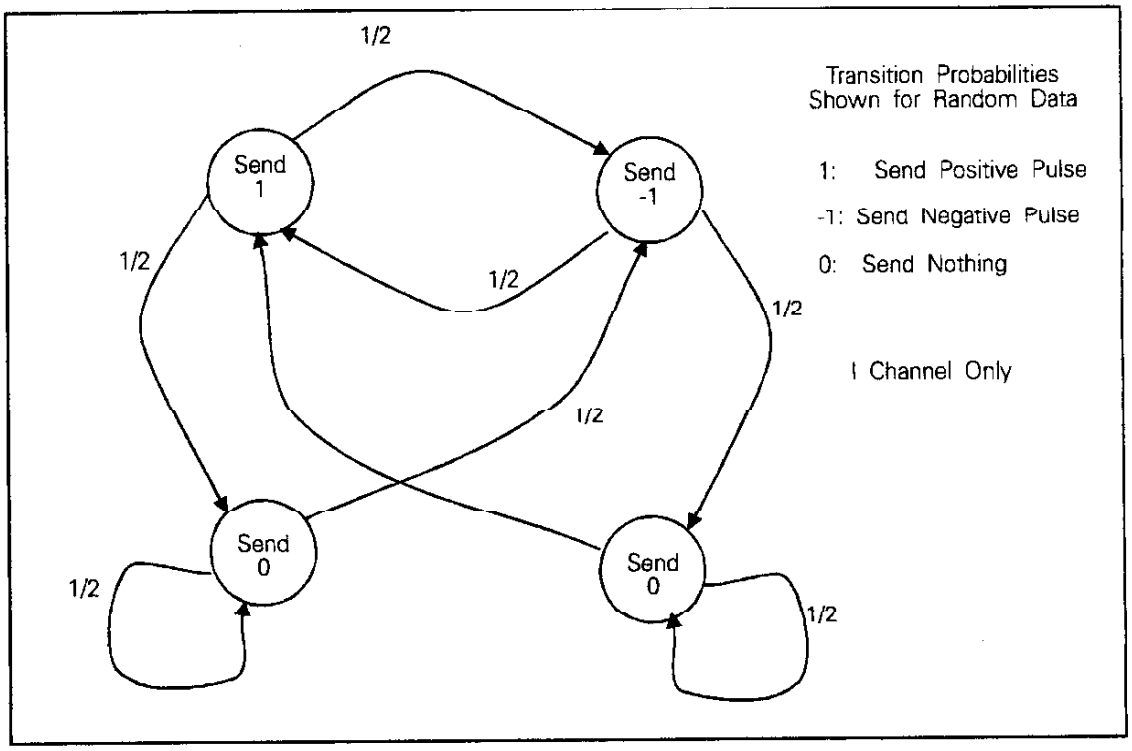

Figure A1.3 Markov model for random I-channel modulation waveform corresponding to Figure A1.2a.

where the bold E represents statistical expectation. Assuming a finite data set x[0],...,x[N-1], multiple sample spectrums were computed random TOQPSK signal segments and simply averaged to compute the PSD. Each sample spectrum was computed as

$$\tilde{P}_{xx}(f) = \frac{T}{N}\left|\sum_{n=0}^{N-1} y[n]\; e^{-j2\pi fnT}\right|^2 \qquad (3)$$

where N= 4096, 16 complex samples per symbol period were used, and a triangular window function was applied on each finite data set x[] as

$$y[k] = \left[\,1 - \frac{|\,k-N/2\,|}{N/2}\,\right] x[k] \qquad (4)$$

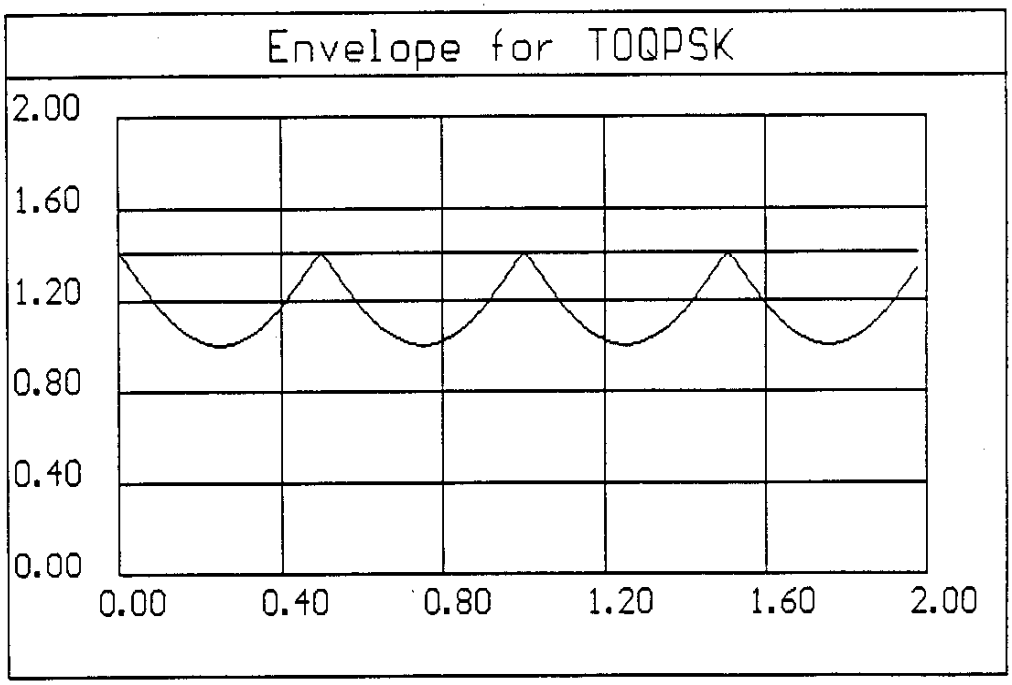

Figure A1.4 Instantaneous signal envelope for TOQPSK prior to hard-limiting.

Following this procedure, the PSD for TOQPSK after hard-limiting was computed and plotted in Figure A1.5. The result shown here is virtually identical to the PSD shown in [A1.6] for TOQPSK. The eye diagram for hard-limited TOQPSK is shown in Figure A1.6. These two figures will be used as a baseline for comparisons throughout this appendix.

Given a classic type-2 analog phase-locked loop and linear operation, the transfer function relationship between the output phase and input phase expressed as a Laplace transform is given as

$$\theta_o(s) = \frac{\omega_n^2 \left(1 + 2\zeta s/\omega_n \right)}{s^2 + 2\zeta\omega_n s + \omega_n^2} \qquad (5)$$

where ζ is the damping factor and ω_n is the loop natural frequency in radians per second. The standard bilinear transformation may be applied to this result in order to translate the continuous system description into a discrete system model suitable for computer simulation. This transformation is given by

$$s = \frac{2}{T}\,\frac{z-1}{z+1} \tag{6}$$

Since the analysis assumes 16 samples per symbol period which is on the order of 8 times the required Nyquist rate, the bilinear transform method will display negligible frequency domain warping leading to very accurate results. Substituting (6) into (5) and collecting terms, the discrete model representing the PLL filtering is given by

$$\theta_o[n] = C_1\,\theta_o[n-1] + C_2\,\theta_o[n-2] + C_3\,\theta_i[n] + C_4\,\theta_i[n-1] + C_5\,\theta_i[n-2] \tag{7}$$

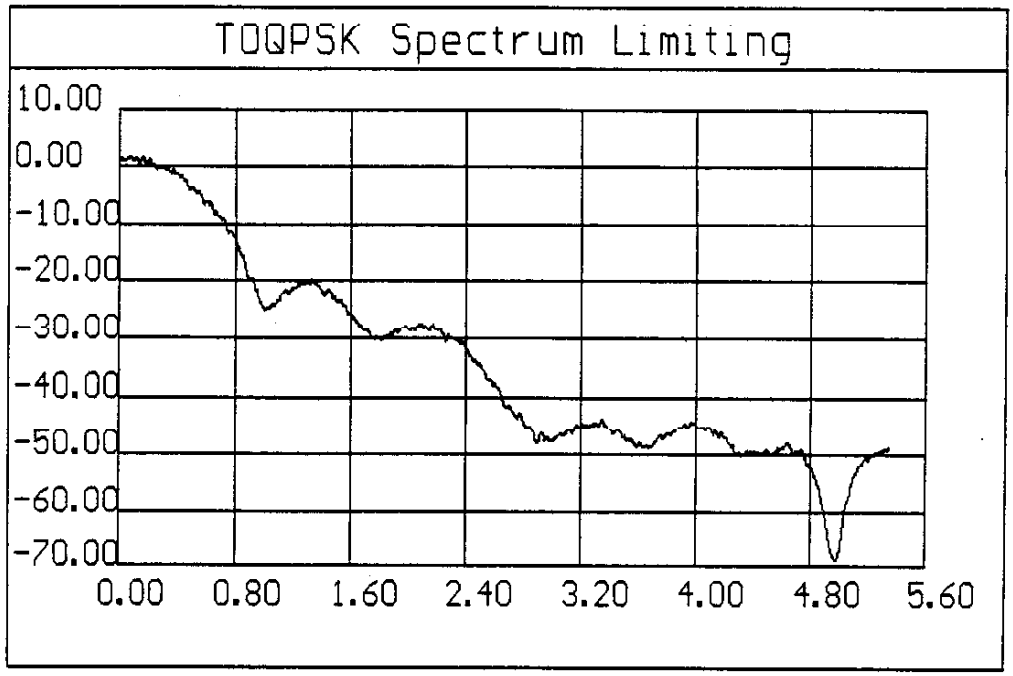

Figure A1.5 Power spectral density for normal TOQPSK after hard-limiting. Units are dBc versus normalized frequency offset, fT.

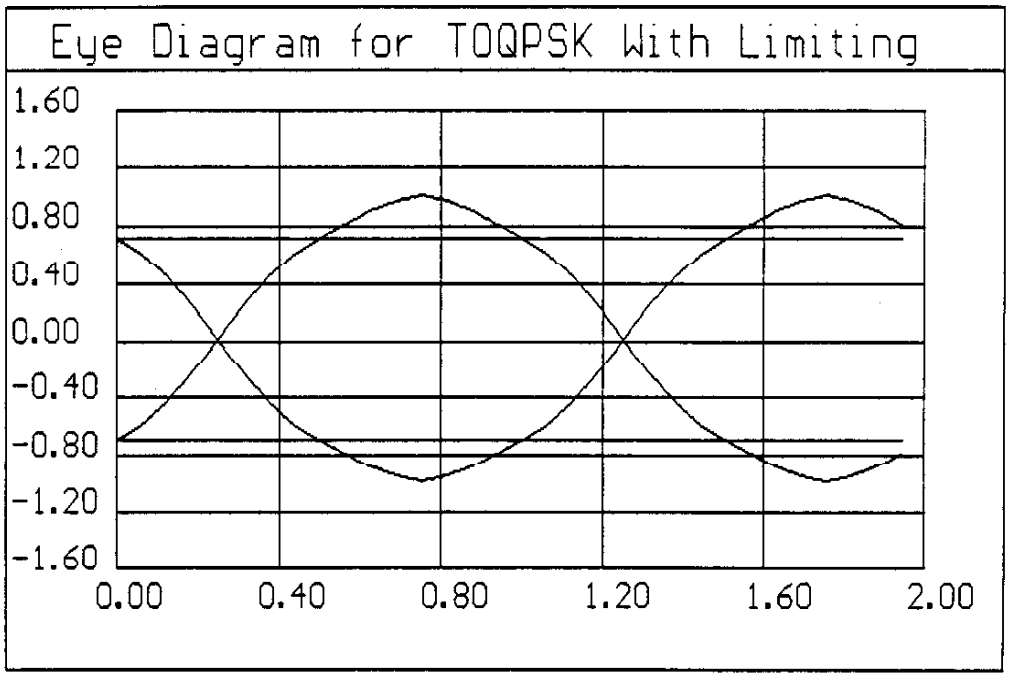

Figure A1.6 Eye diagram for normal TOQPSK after hard-limiting.

where

$$C_1 = \frac{8 - 2(\omega_n T)^2}{4 + 4\zeta\omega_n T + (\omega_n T)^2}$$

$$C_2 = \frac{4\zeta\omega_n T - 4 - (\omega_n T)^2}{4 + 4\zeta\omega_n T + (\omega_n T)^2}$$

$$C_3 = \frac{(\omega_n T)^2\left(1 + \frac{4\zeta}{\omega_n T}\right)}{4 + 4\zeta\omega_n T + (\omega_n T)^2} \qquad (10)$$

$$C_4 = \frac{2(\omega_n T)^2}{4 + 4\zeta\omega_n T + (\omega_n T)^2)}$$

$$C_5 = \frac{(\omega_n T)^2\left(1 - \frac{4\zeta}{\omega_n T}\right)}{4 + 4\zeta\omega_n T + (\omega_n T)^2}$$

In order to avoid modulo-2π problems in the simulation with the input phase function, it is much easier to convert the phase signal input to an equivalent sequence of phase increments with a known starting phase. In order to illustrate this, assume that the calculated I and Q values at time steps t and t+h are given by I_1+jQ_1 and I_2+jQ_2 where clearly

$$\begin{aligned} e^{j\theta_1} &= I_1 + jQ_1 \\ e^{j\theta_2} &= I_2 + jQ_2 \end{aligned} \tag{9}$$

The phase increment between these two complex sample pairs is (assuming h << T) given by

$$\begin{aligned} \Delta\theta &= \theta_2 - \theta_1 \\ &= Arg\left[(I_2 + jQ_2)(I_1 - jQ_1) \right] \\ &= Tan^{-1}\left[\frac{Q_2 I_1 - I_2 Q_1}{I_2 I_1 + Q_2 Q_1} \right] \end{aligned} \tag{10}$$

As seen in the following figures, the PLL filtering action was effective in reducing the spectral sidelobes somewhat, but in general, substantial intersymbol interference (ISI) was also introduced and the minimal received benefit is overshadowed by the increased complexity this approach represents. The loop parameter cases which are included in this report are summarized in Table I.

Table A1.1 Phase-Locked Loop Parameter Cases

Figure Number	Loop Damping, ζ	Normalized BW, $\omega_n T$
A1.7	1.0	0.15
A1.8	0.75	0.20
A1.9	1.0	0.20
A1.10	1.5	0.20
A1.11	2.0	0.2
A1.12	0.75	0.30
A1.13	0.85	0.30
A1.14	1.0	0.30
A1.15	2.0	0.30

In conclusion, the phase-locked loop approach for spectral sidelobe reduction is not recommended.

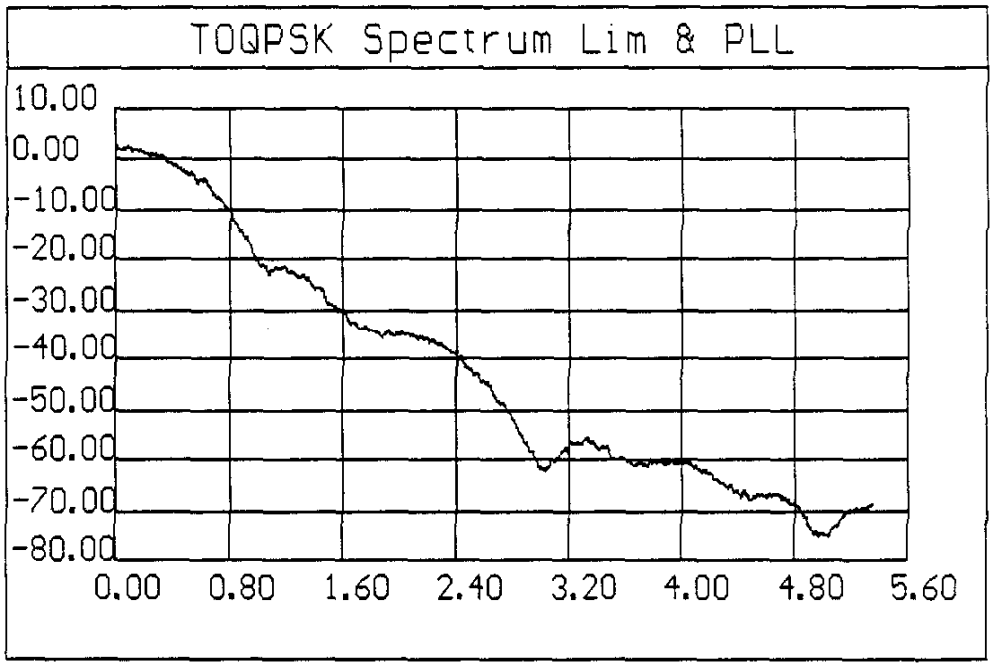

Figure A1.7a TOQPSK with PLL Post-Filtering.
Power Spectral Density vs. Offset, fT.
Loop parameters are $\omega_n T = 0.15$, $\zeta = 1.0$

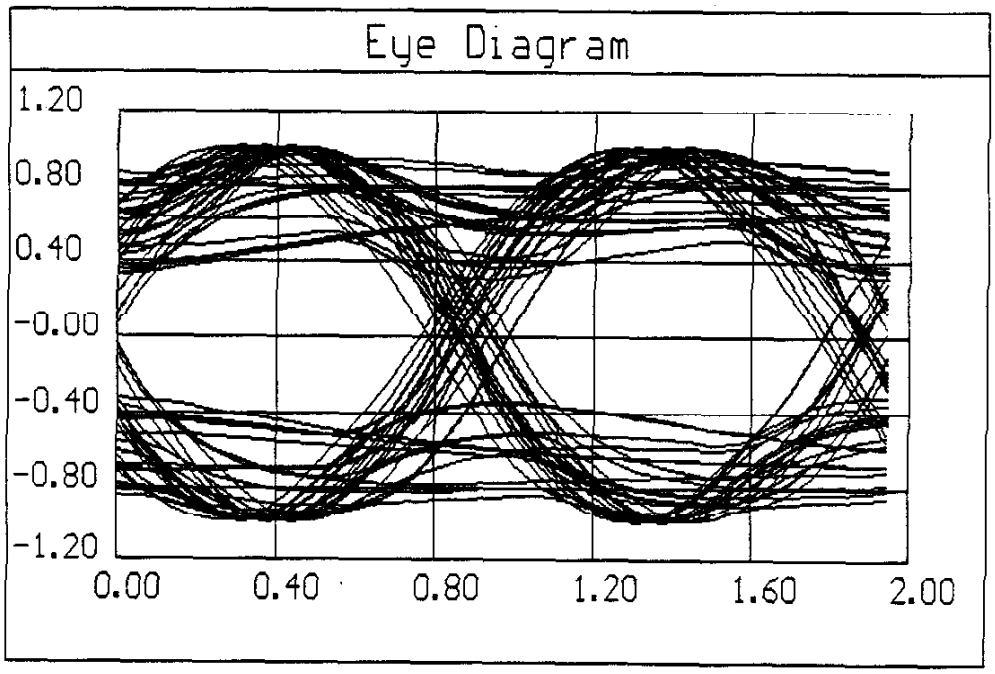

Figure A1.7b TOQPSK with PLL Post-Filtering.
Loop Parameters $\omega_n T = 0.15$, $\zeta = 1.0$

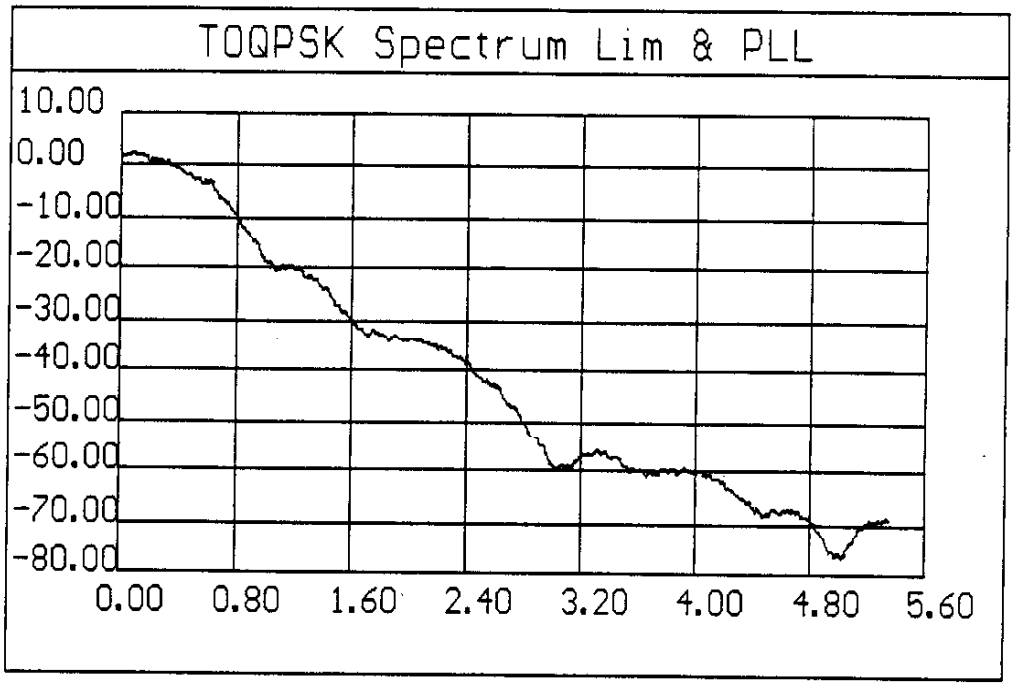

Figure A1.8a TOQPSK with PLL Post-Filtering.
Power Spectral Density Vs. Offset, fT.
Loop parameters are $\omega_n T = 0.20$, $\zeta = 0.75$

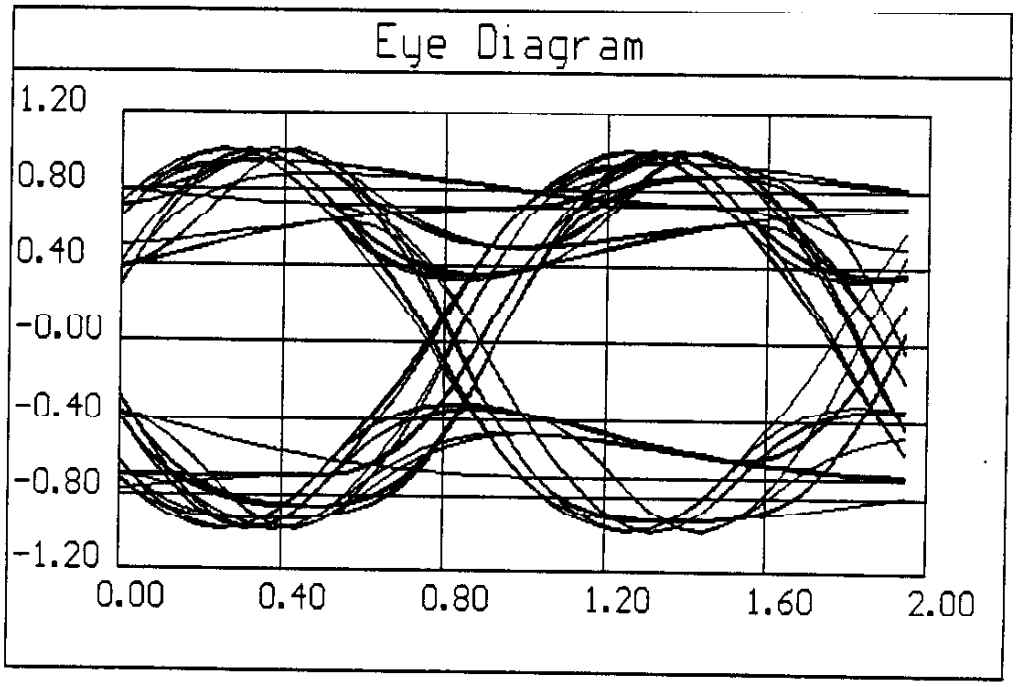

Figure A1.8b TOQPSK with PLL Post-Filtering.
Loop Parameters $\omega_n T = 0.20$, $\zeta = 0.75$

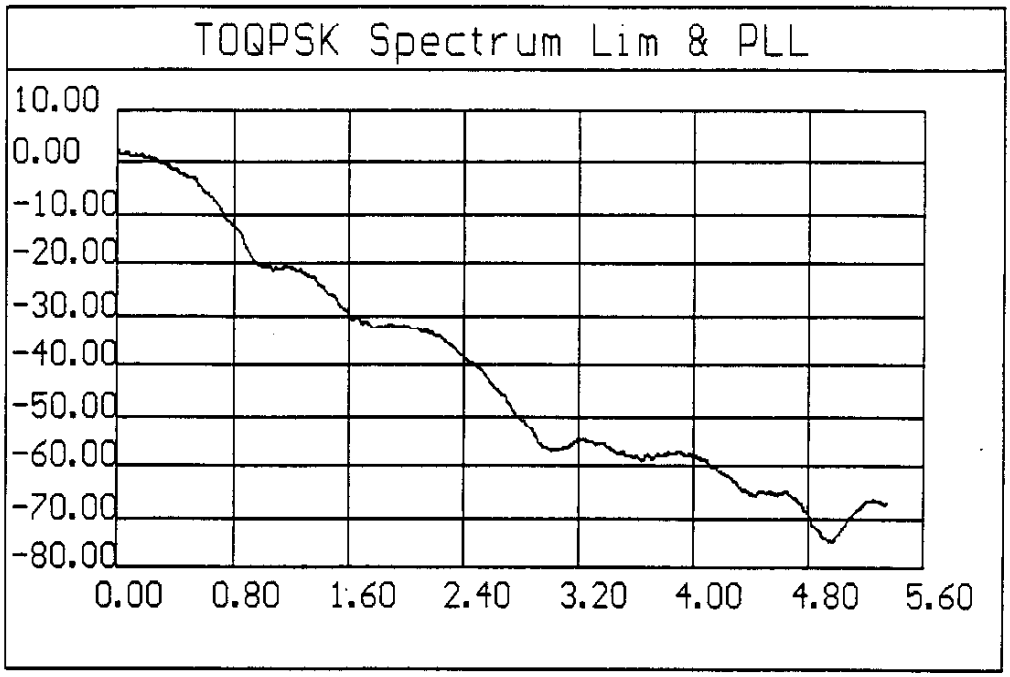

Figure A1.9a TOQPSK with PLL Post-Filtering.
Power Spectral Density Vs. Offset, fT.
Loop parameters are $\omega_n T = 0.20$, $\zeta = 1.0$

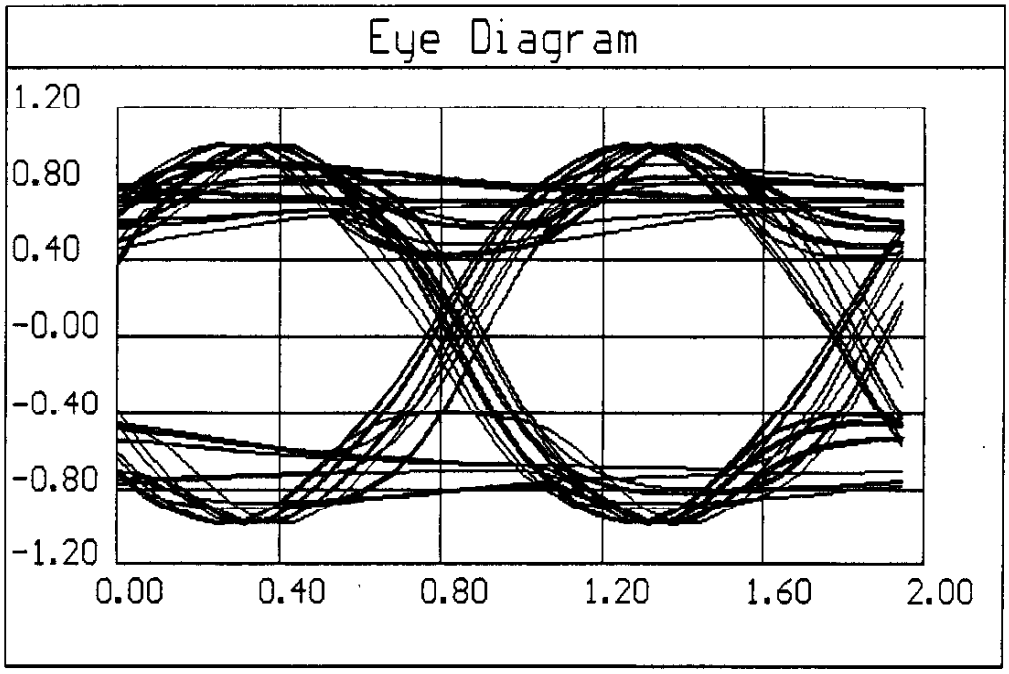

Figure A1.9b TOQPSK with PLL Post-Filtering.
Loop Parameters $\omega_n T = 0.20$, $\zeta = 1.0$

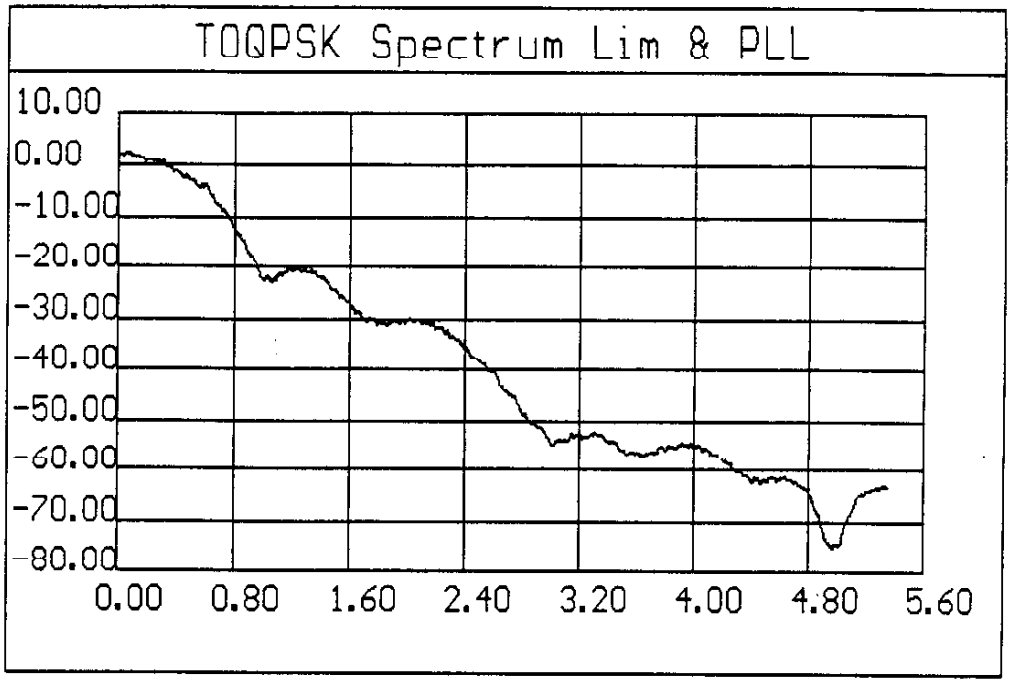

Figure A1.10a TOQPSK with PLL Post-Filtering.
Power Spectral Density Vs. Offset, fT.
Loop parameters are $\omega_n T = 0.20$, $\zeta = 1.5$

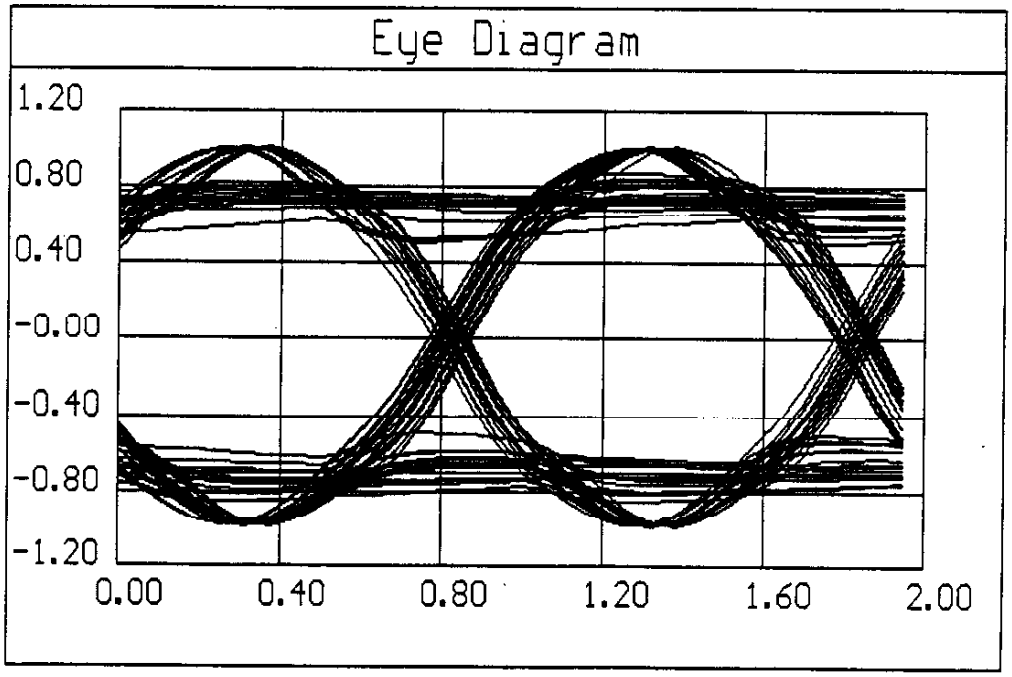

Figure A1.10b TOQPSK with PLL Post-Filtering.
Loop Parameters $\omega_n T = 0.20$, $\zeta = 1.5$

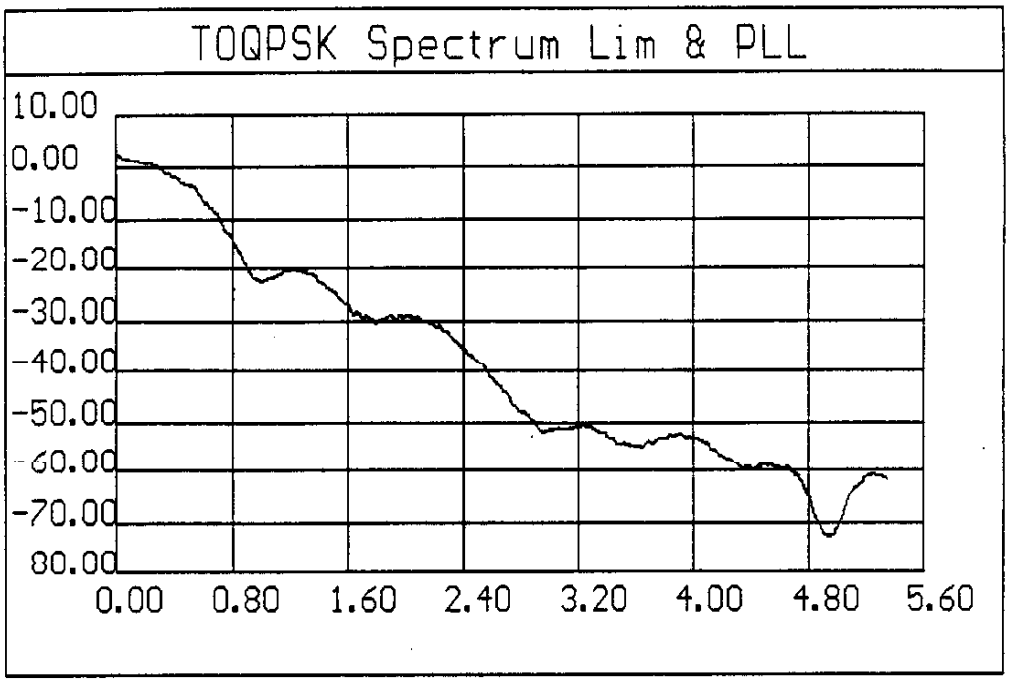

Figure A1.11a TOQPSK with PLL Post-Filtering.
Power Spectral Density Vs. Offset, fT.
Loop parameters are $\omega_n T$= 0.20, ζ= 2.0

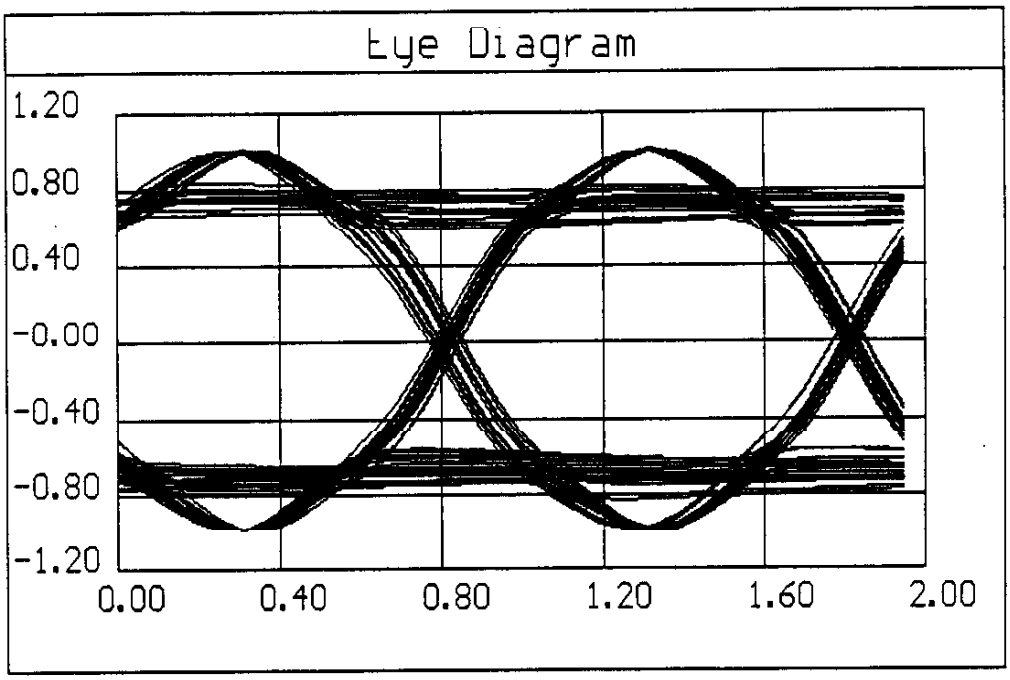

Figure A1.11b TOQPSK with PLL Post-Filtering.
Loop Parameters $\omega_n T$= 0.20, ζ= 2.0

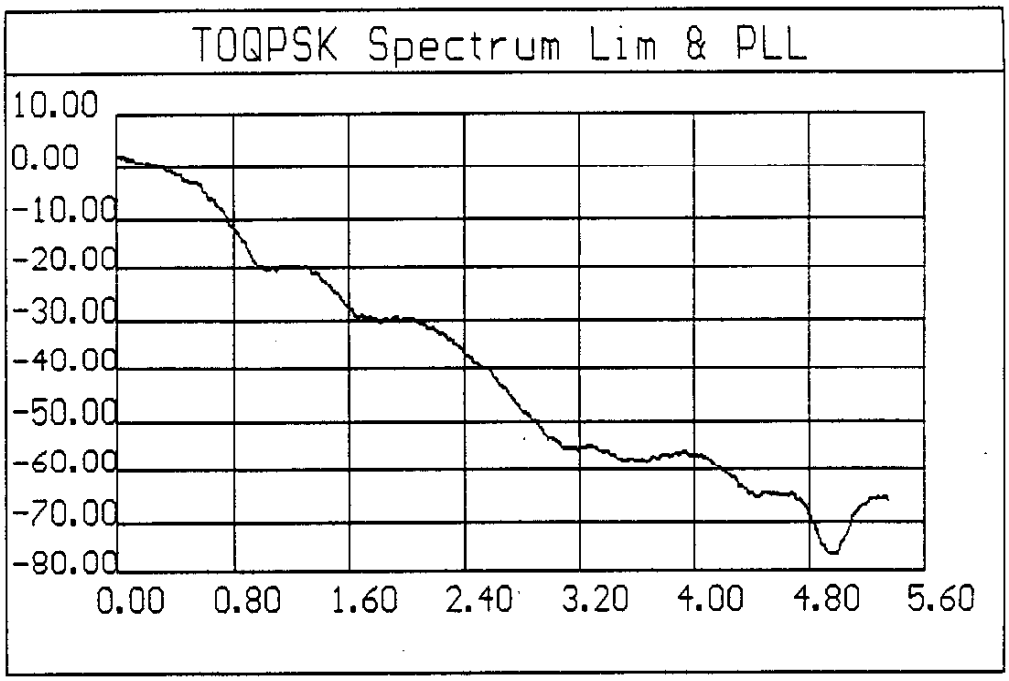

Figure A1.12a TOQPSK with PLL Post-Filtering.
Power Spectral Density Vs. Offset, fT.
Loop parameters are $\omega_n T = 0.30$, $\zeta = 0.75$

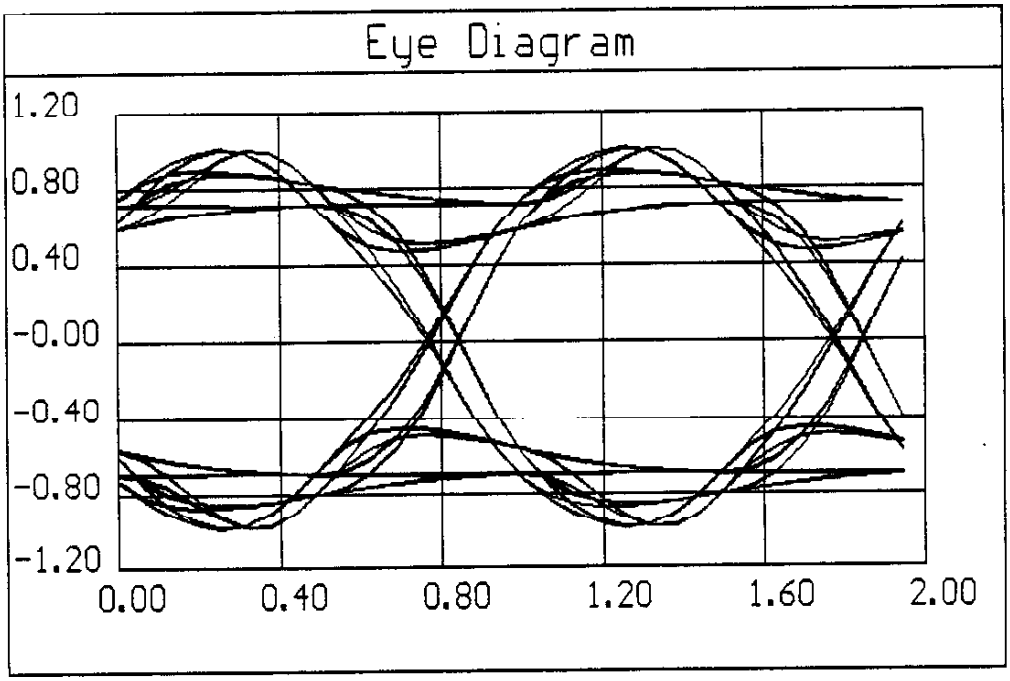

Figure A1.12b TOQPSK with PLL Post-Filtering.
Loop Parameters $\omega_n T = 0.30$, $\zeta = 0.75$

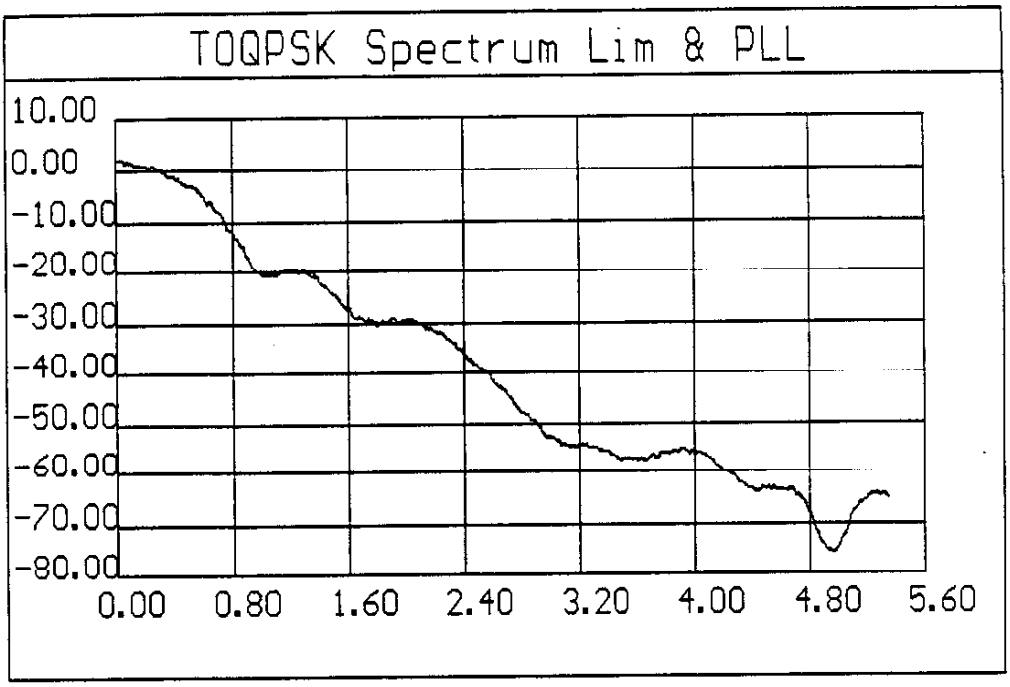

Figure A1.13a TOQPSK with PLL Post-Filtering.
Power Spectral Density Vs. Offset, fT.
Loop parameters are $\omega_n T = 0.30$, $\zeta = 0.85$

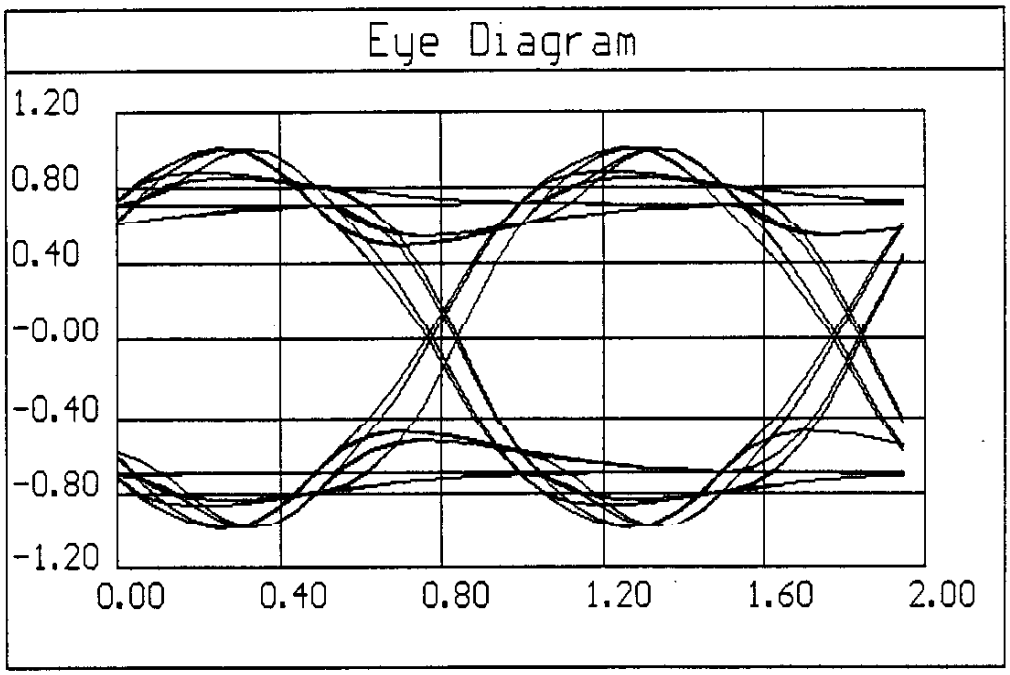

Figure A1.13b TOQPSK with PLL Post-Filtering.
Loop Parameters $\omega_n T = 0.30$, $\zeta = 0.85$

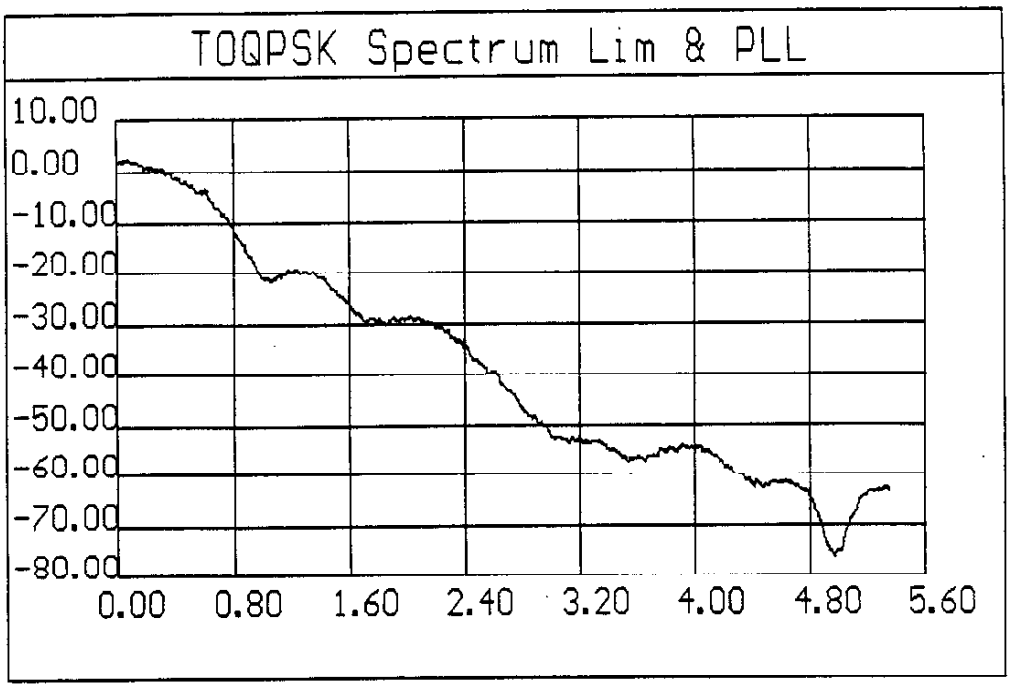

Figure A1.14a TOQPSK with PLL Post-Filtering.
Power Spectral Density Vs. Offset, fT.
Loop parameters are $\omega_n T = 0.30$, $\zeta = 1.0$

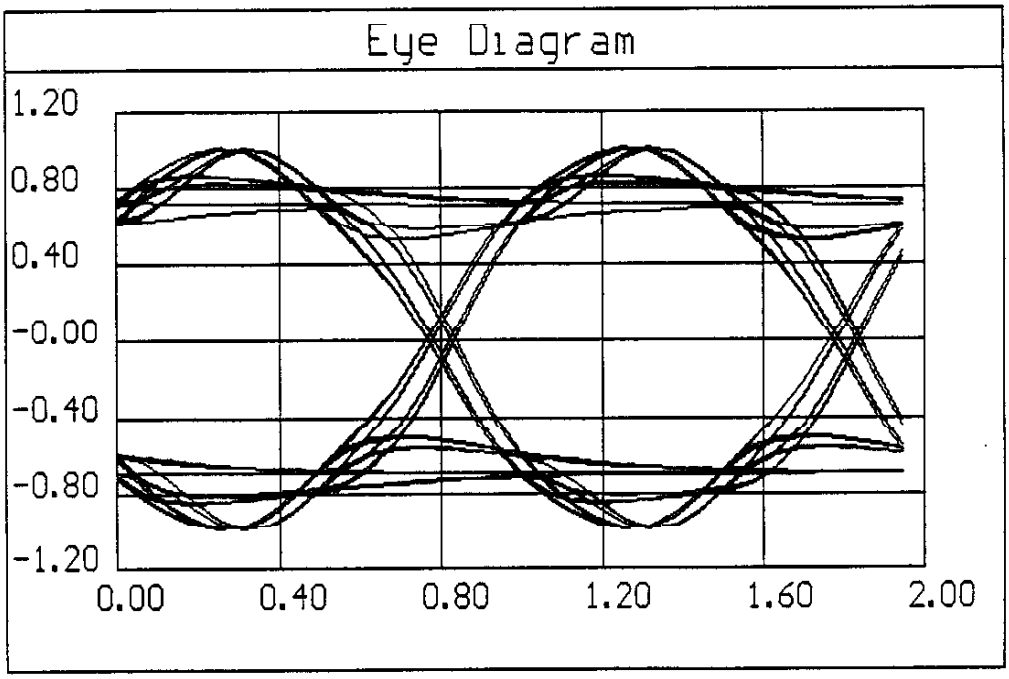

Figure A1.14b TOQPSK with PLL Post-Filtering.
Loop Parameters $\omega_n T = 0.30$, $\zeta = 1.0$

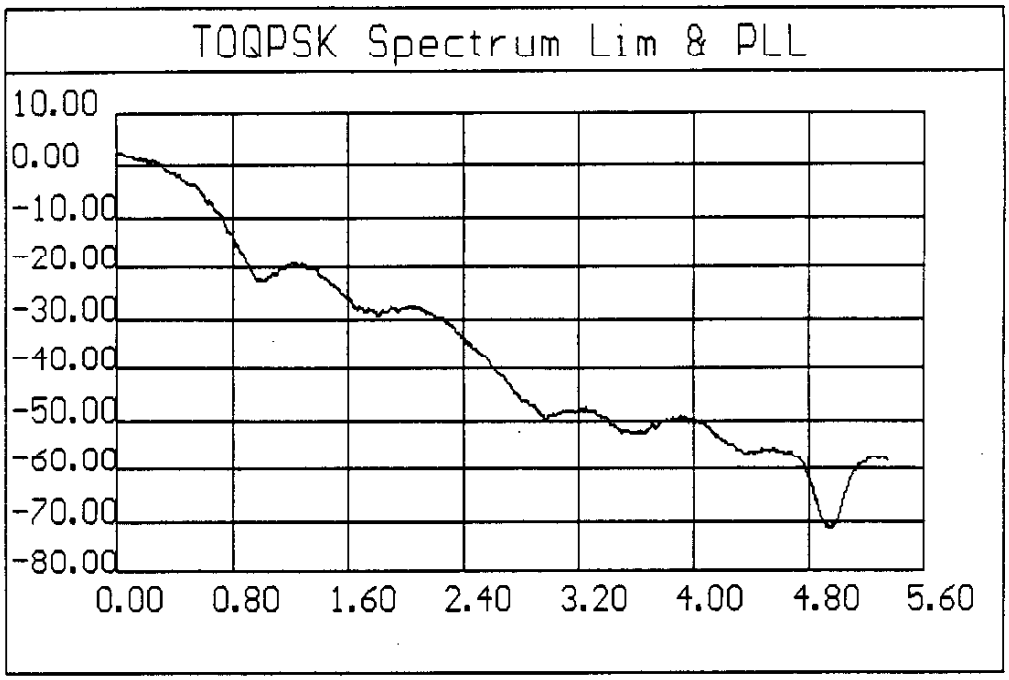

Figure A1.15a TOQPSK with PLL Post-Filtering.
Power Spectral Density Vs. Offset, fT.
Loop parameters are $\omega_n T = 0.30$, $\zeta = 2.0$

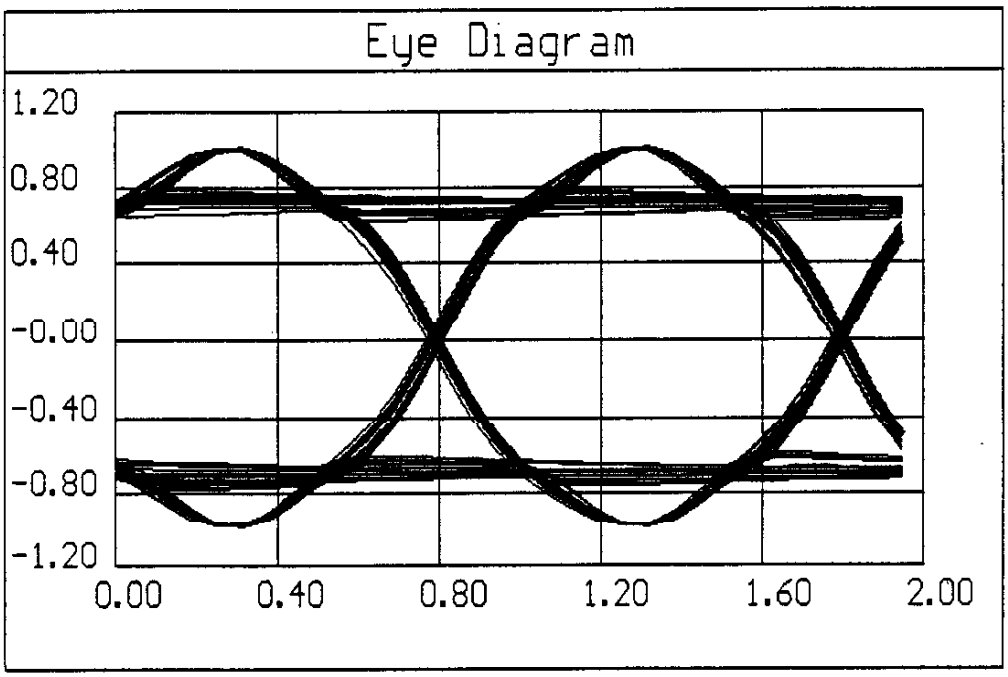

Figure A1.15b TOQPSK with PLL Post-Filtering.
Loop Parameters $\omega_n T = 0.30$, $\zeta = 2.0$

Filtered TOQPSK Using Phase Argument Filters

Only modest improvements in sidelobe reduction were possible with the PLL filtering approach because control system stability issues prevented using higher degrees of filtering to be performed. If instead, the phase function $\varphi(t)$ in equation (1) is explicitely filtered with a traditional lowpass filter (e.g., Butterworth, Gaussian, etc.), this restriction is removed.

The analysis performed in this section was based upon hard-limiting the same random TOQPSK waveform which was considered earlier. The instantaneous phase at the hard-limiter output was computed and then passed through a Butterworth lowpass filter before being re-inserted into equation (1) for $\varphi(t)$.

Rather than employ the same bilinear transformation which was used earlier, a more sophisticated approach was taken using a second-order Gear numerical integration algorithm [A1.7] for improved accuracy. Each filter which was considered was simulated as a cascade of first- and second-order filter sections, each based upon standard analog lowpass LC-filters.

Only the Butterworth family of classical all-pole filters was considered, partly due to time constraints, but also because the Butterworth family is a good compromise between flat group delay and stopband attenuation.

The spectral sidelobe improvements which can be achieved with this fairly simple approach are impressive as the following figures demonstrate. Although a final filtering choice canot be made without assessing the E_b/N_o performance impact at the receiver, processing the modulation waveform at the transmitter in this manner is very advantageous.

The angular filtering cases which are included for comparison in this appendix are summarized in Table II.

Table A1.2 Explicit Angle Filtering Cases

Figure	Order	Bandwidth, $B_{3db}T$	dBc at 2.4/T Offset
A1.5	No Filtering		-31
A1.16	2	1.0	-46
A1.17	2	0.80	-49
A1.18	2	0.70	-52
A1.19	2	0.60	-55
A1.20	2	0.50	-58
A1.21	3	1.0	-52
A1.22	3	0.80	-57
A1.23	3	0.60	-65
A1.24	4	1.0	-55
A1.25	4	0.80	-64

As seen from Table II and the accompanying figures, even with fairly modest filtering, the sidelobe level at 2.4 times the symbol rate can be reduced 15 to 20 dB with fairly minimal ISI being introduced. The BER performance degradation resulting from the ISI is quantified in a separate appendix.

The N=2 Butterworth filter choice is attractive in that the main spectral lobe is actually reduced in width as shown in Figure A1.16. On the other hand, usually the most severe impact of poor spectral containment is cosite operation where it is mandatory that the sidelobe roll-off be as rapid as possible. In this case, the spectral performance of the N=4 Butterworth choice shown in Figures A1.25 and A1.26 is very impressive compared to the nonfiltered TOQPSK baseline. The numerical precision floor is clearly visible in these two figures near -100 dBc. Proper filtering in the phase domain can clearly result in fairly dramatic improvements in spectral containment.

Generalized Digital Phase Modulation (DPM)

The third and final method considered here for spectral sidelobe improvement is digital phase modulation (DPM). It is slightly simpler than continuous phase modulation (CPM) in that it has phase pulses of finite length, but retains some of the advantages of CPM [A1.8]. Optimization of the pulse-shaping filter for the minimization of the signal bandwidth has been considered by several authors, but generally under fairly restrictive assumptions [A1.9]. Even so, the optimization approach is numerically intensive and impact upon the receiver is often downplayed. Since any adopted scheme must retain interoperability with already fielded equipments, a rigorous optimization effort will not be undertaken at this time.

References [A1.8-13] provide a solid foundation for follow-on work in this area.

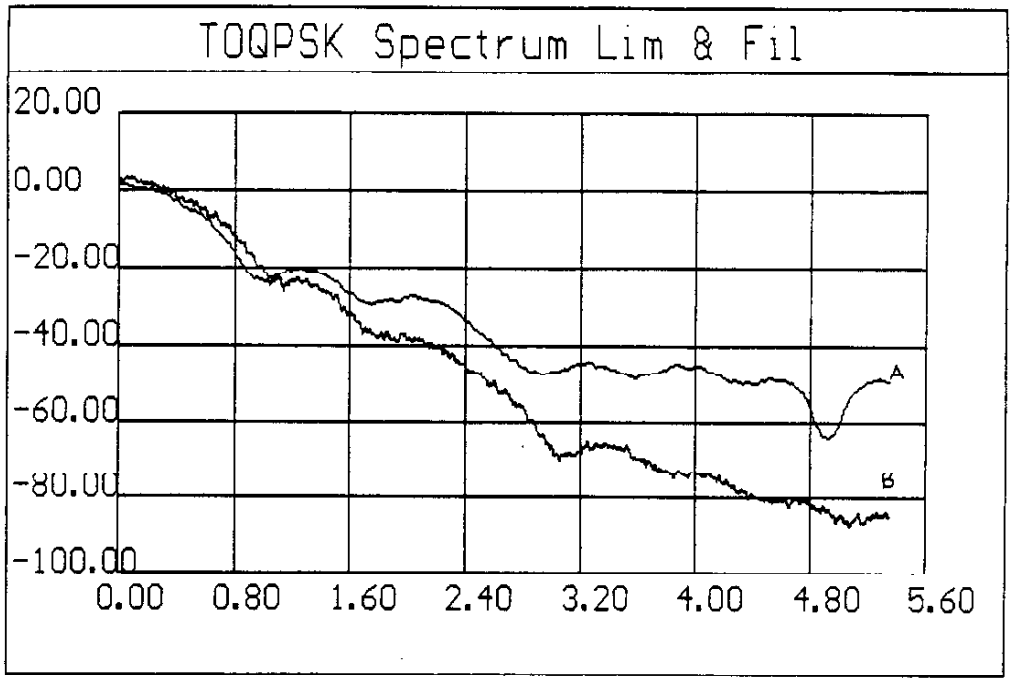

Figure A1.16a TOQPSK Spectrum with Phase Filtering
PSD dBc versus norm. bandwidth, fT
(A) TOQPSK with No Filtering
(B) N=2 Butterworth, BT= 1.0

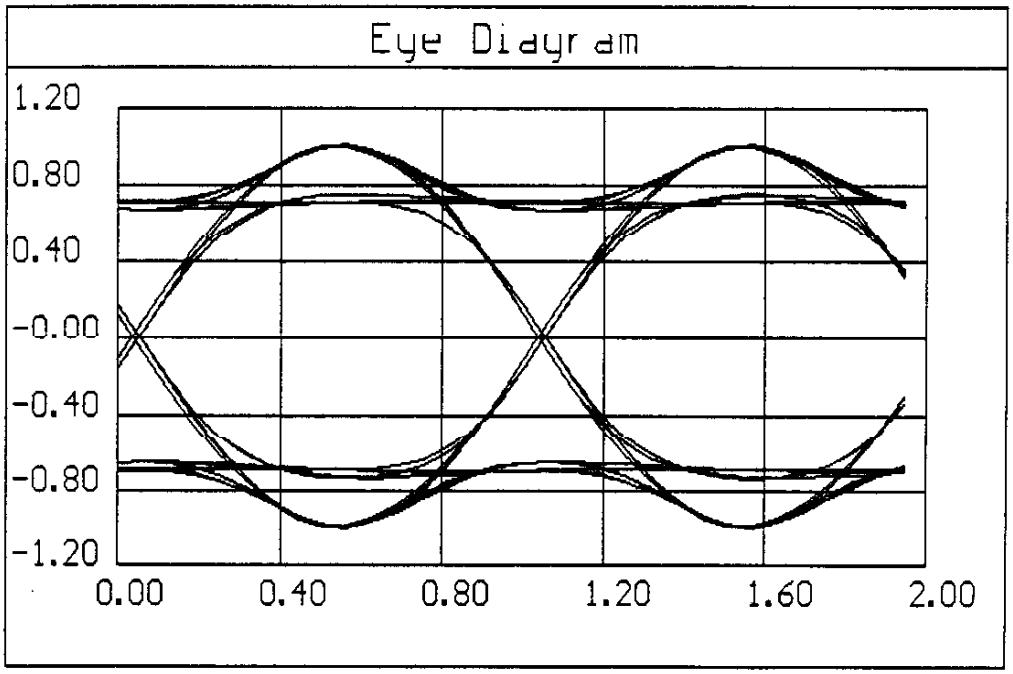

Figure A1.16b Phase Angle Filtering
(A) TOQPSK with No Filtering
(B) N=2 Butterworth, BT= 1.0

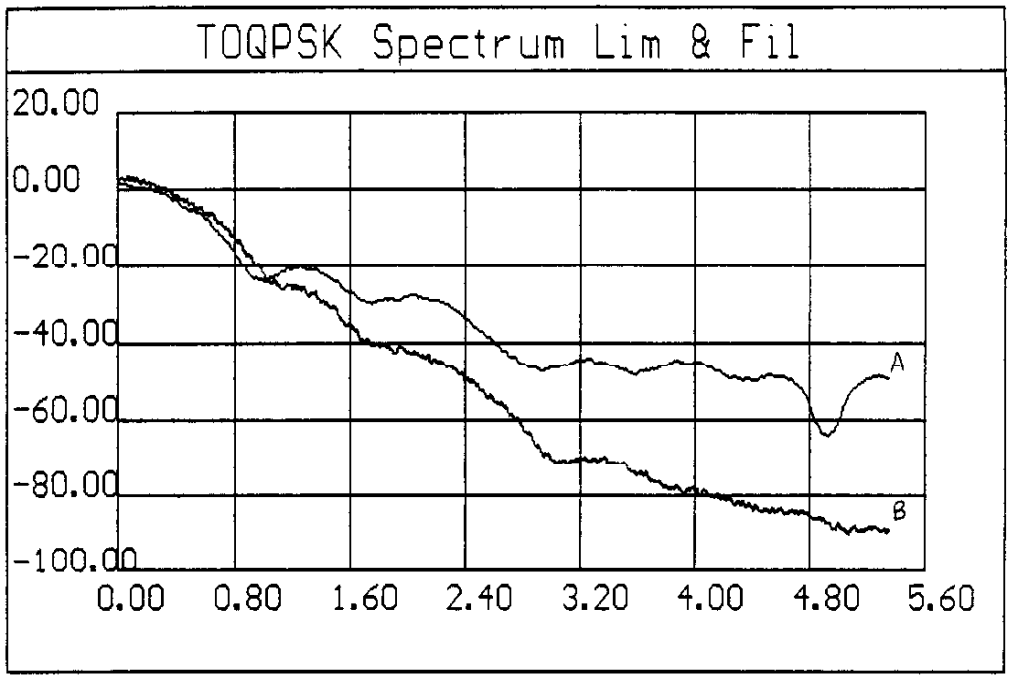

Figure A1.17a TOQPSK Spectrum with Phase Filtering
PSD dBc versus norm. bandwidth, fT
(A) TOQPSK with No Filtering
(B) N=2 Butterworth, BT= 0.80

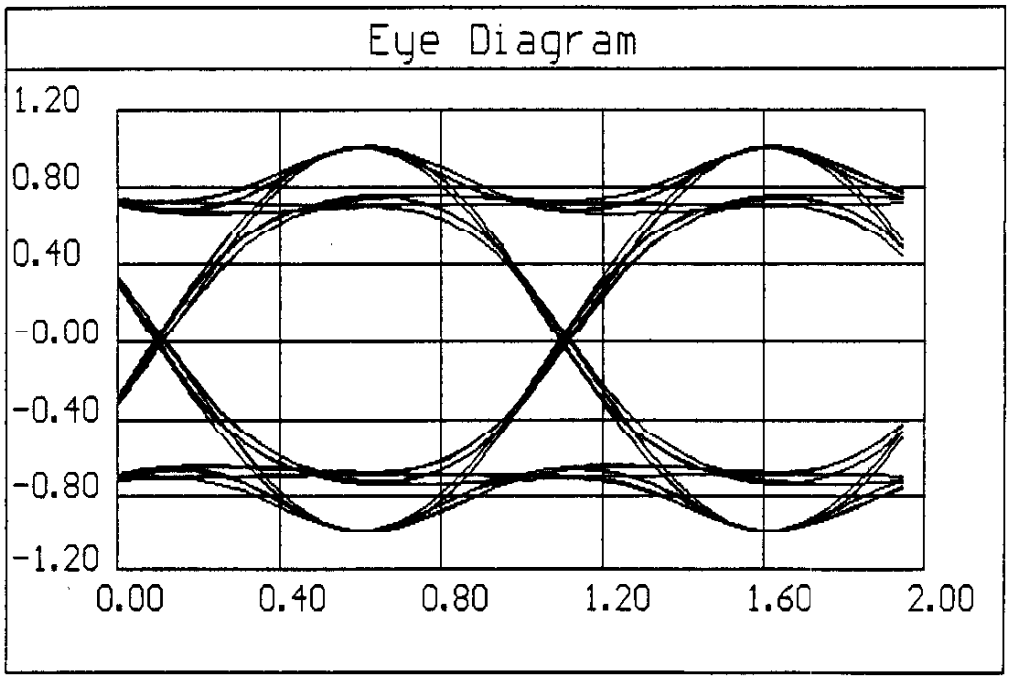

Figure A1.17b Phase Angle Filtering
(A) TOQPSK with No Filtering
(B) N=2 Butterworth, BT= 0.80

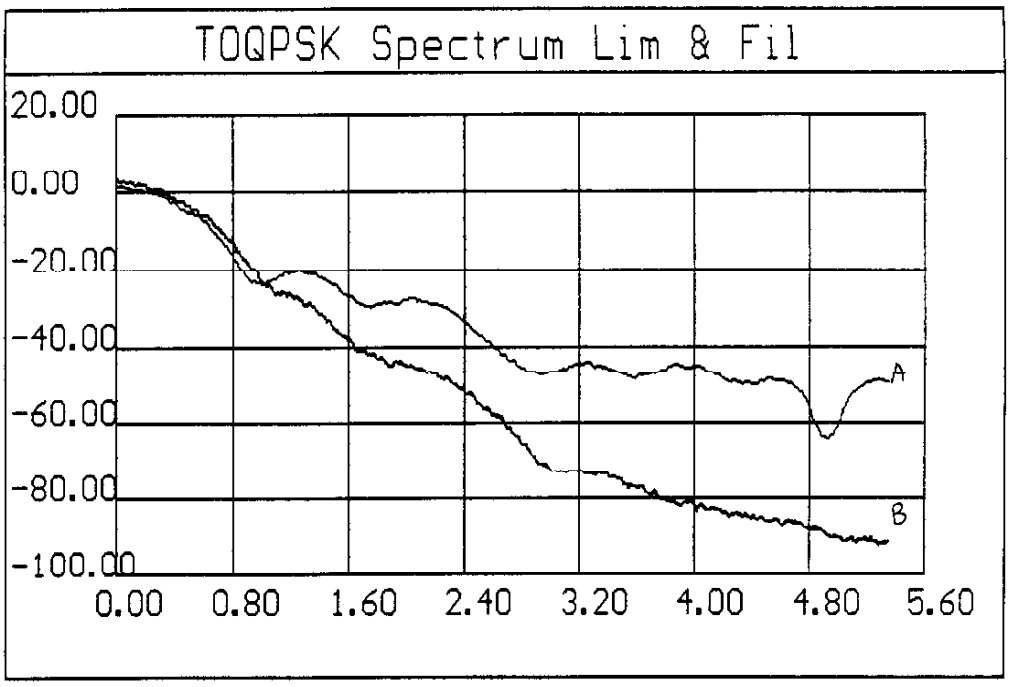

Figure A1.18a TOQPSK Spectrum with Phase Filtering
PSD dBc versus norm. bandwidth, fT
(A) TOQPSK with No Filtering
(B) N=2 Butterworth, BT= 0.70

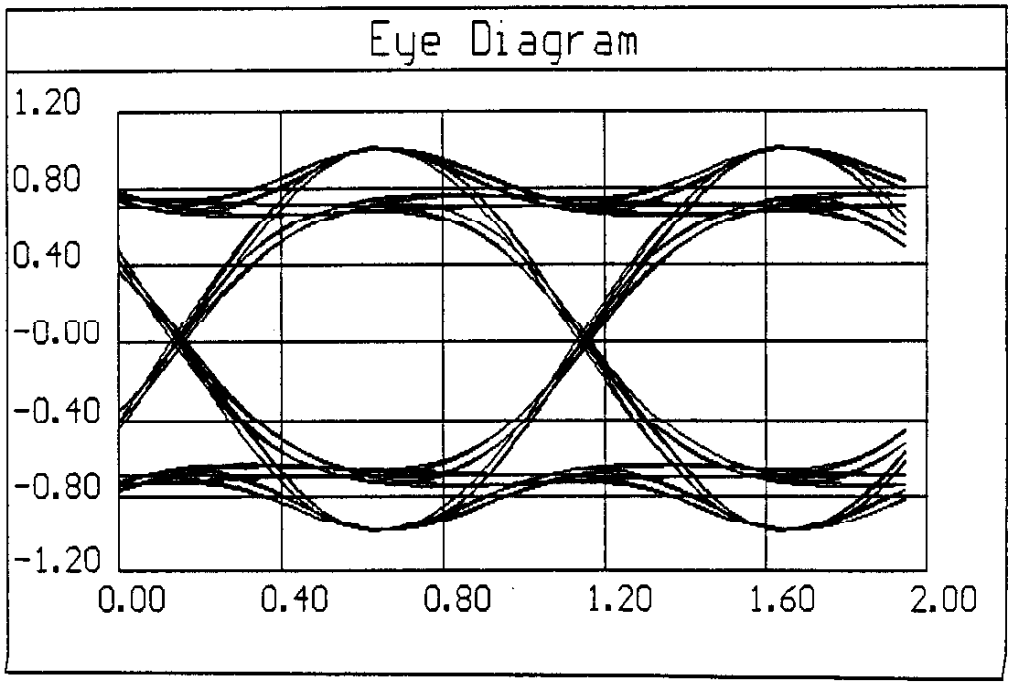

Figure A1.18b Phase Angle Filtering
(A) TOQPSK with No Filtering
(B) N=2 Butterworth, BT= 0.70

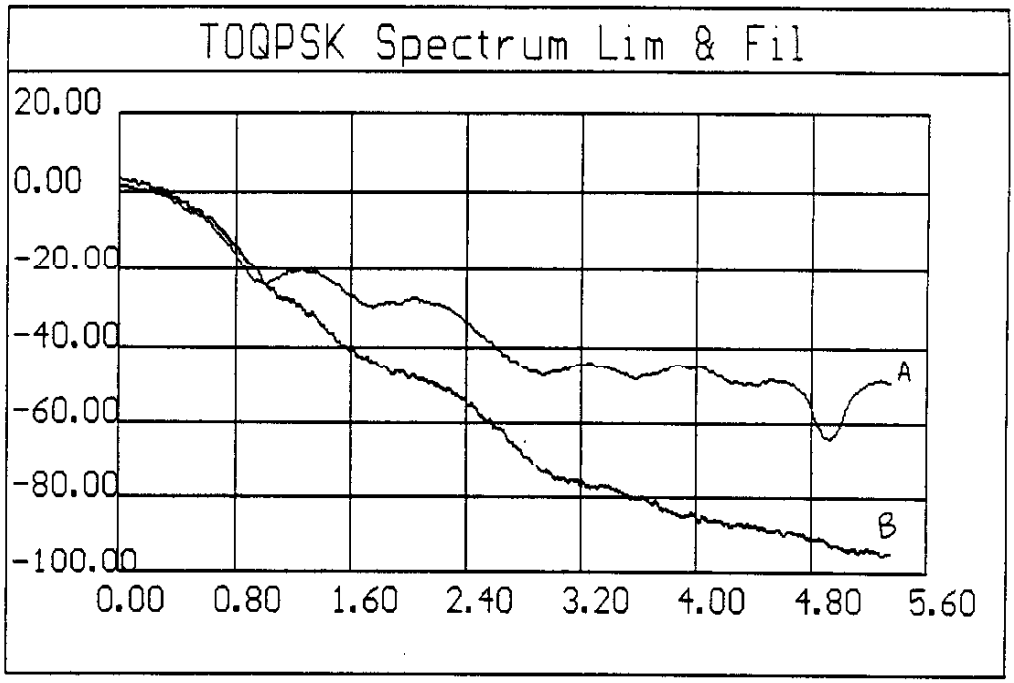

Figure A1.19a TOQPSK Spectrum with Phase Filtering
PSD dBc versus norm. bandwidth, fT
(A) TOQPSK with No Filtering
(B) N=2 Butterworth, BT= 0.60

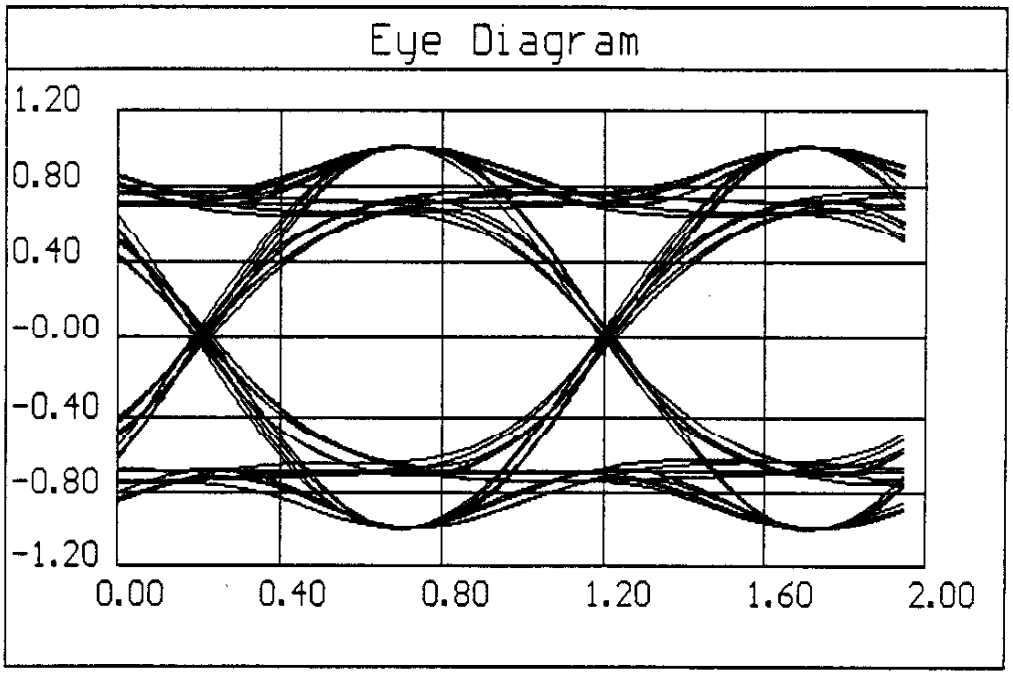

Figure A1.19b Phase Angle Filtering
(A) TOQPSK with No Filtering
(B) N=2 Butterworth, BT= 0.60

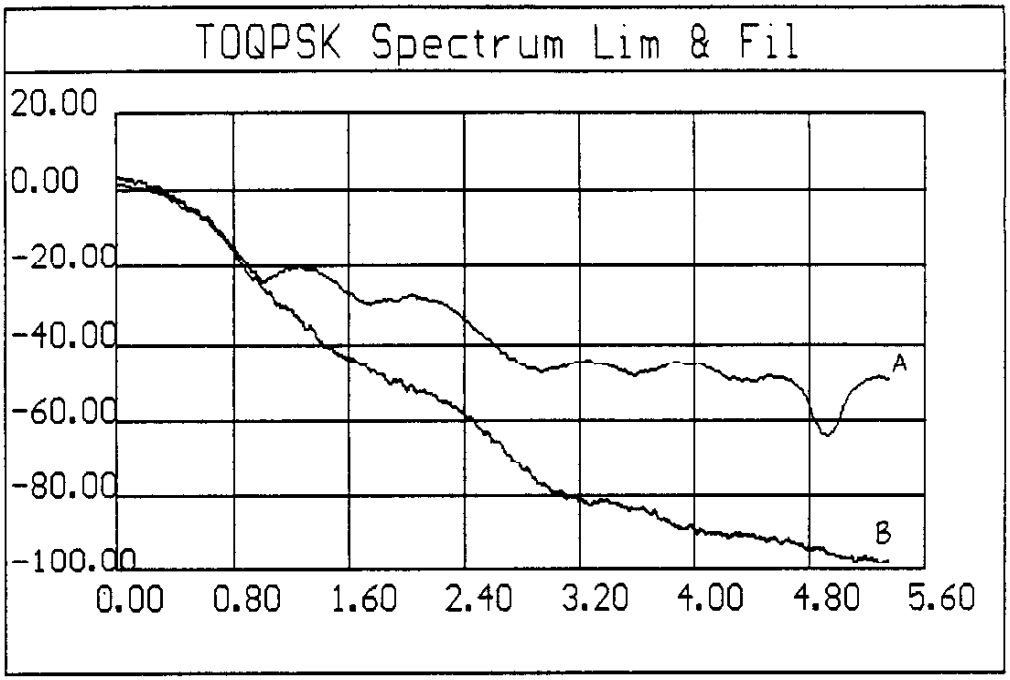

Figure A1.20a TOQPSK Spectrum with Phase Filtering
PSD dBc versus norm. bandwidth, fT
(A) TOQPSK with No Filtering
(B) N=2 Butterworth, BT= 0.50

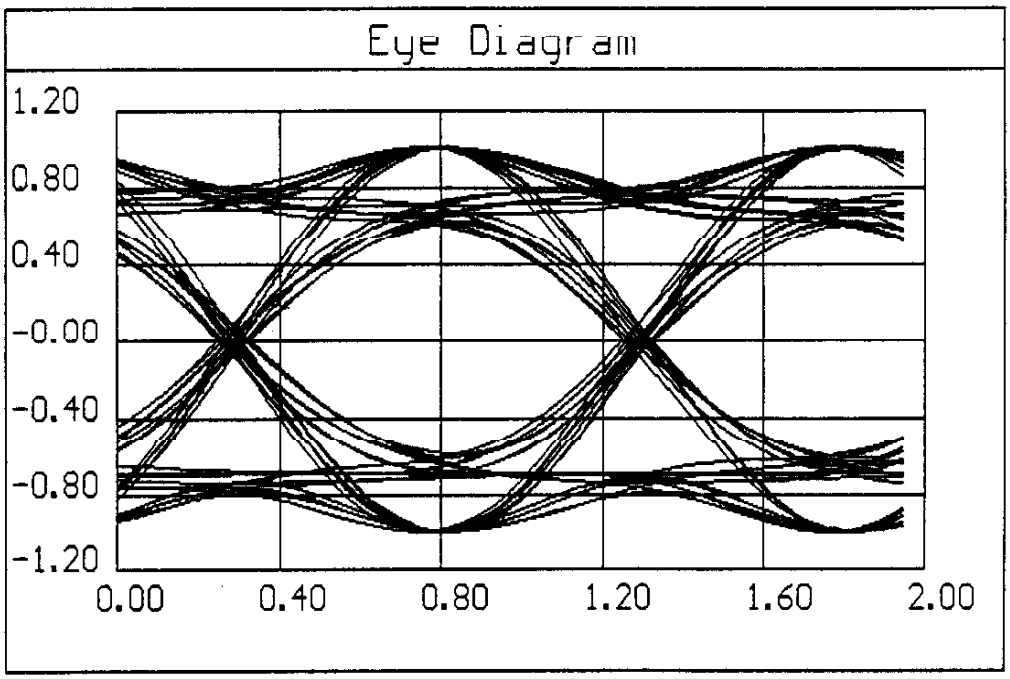

Figure A1.20b Phase Angle Filtering
(A) TOQPSK with No Filtering
(B) N=2 Butterworth, BT= 0.50

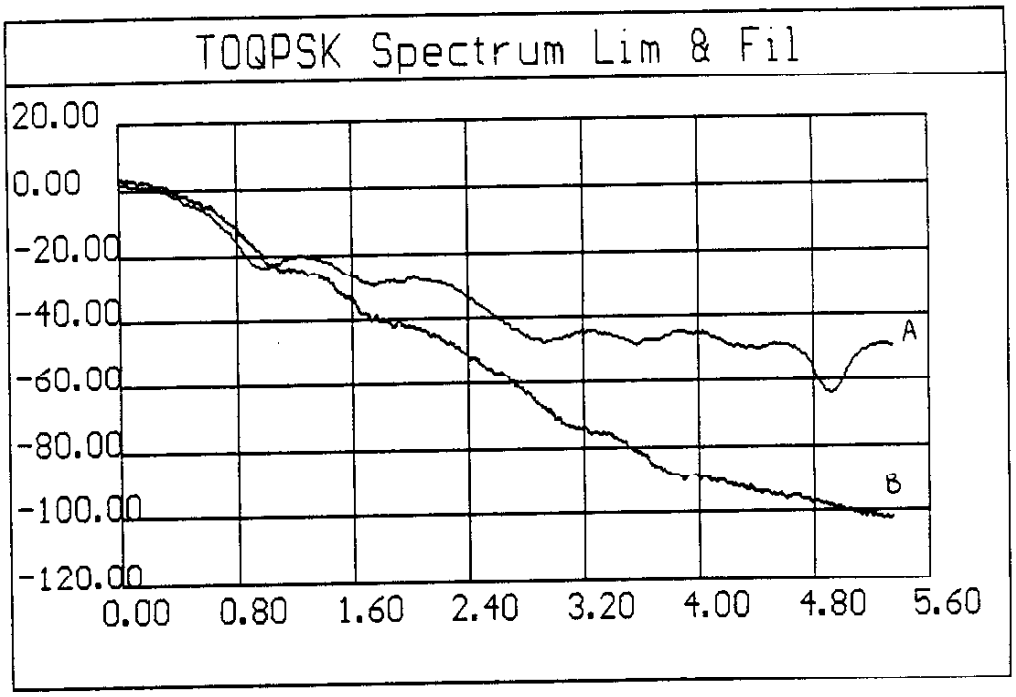

Figure A1.21a TOQPSK Spectrum with Phase Filtering
PSD dBc versus norm. bandwidth, fT
(A) TOQPSK with No Filtering
(B) N=3 Butterworth, BT= 1.0

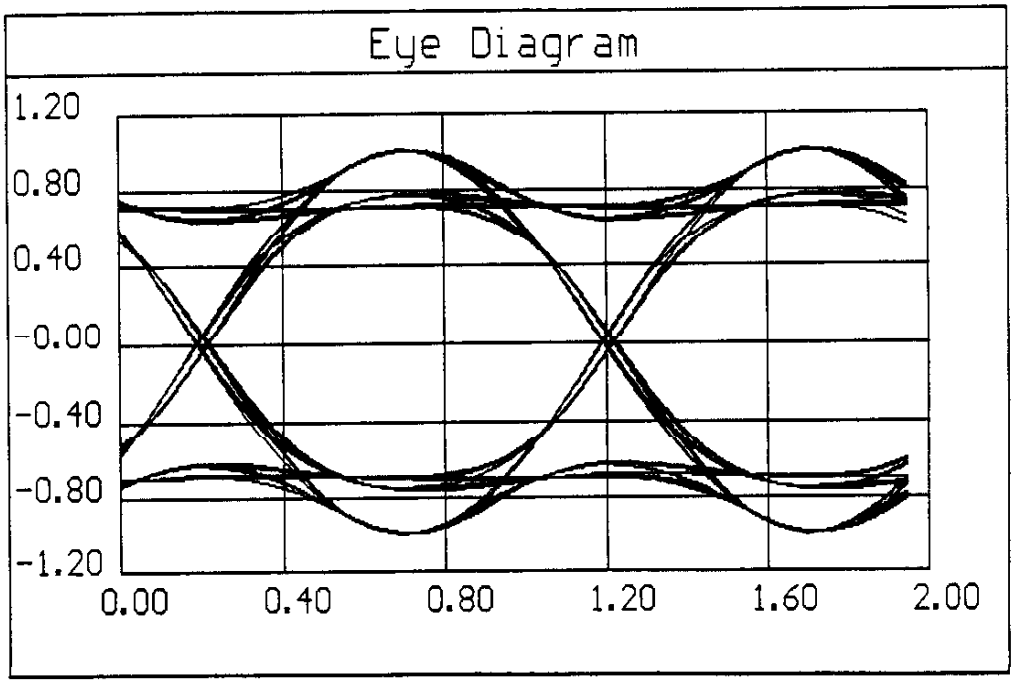

Figure A1.21b Phase Angle Filtering
(A) TOQPSK with No Filtering
(B) N=3 Butterworth, BT= 1.0.

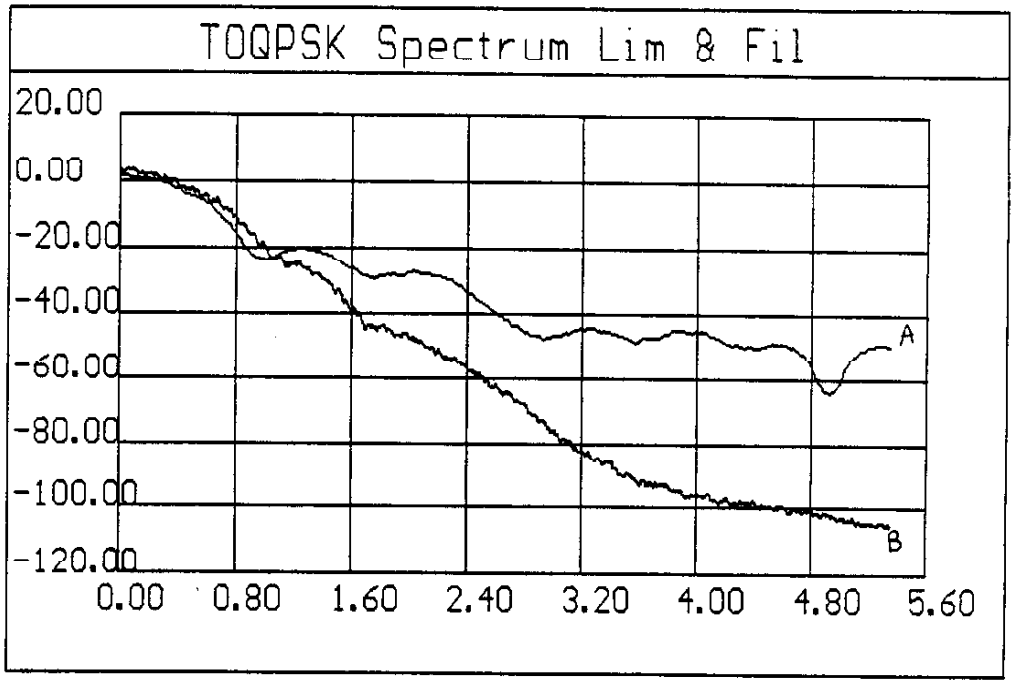

Figure A1.22a TOQPSK Spectrum with Phase Filtering
PSD dBc versus norm. bandwidth, fT
(A) TOQPSK with No Filtering
(B) N=3 Butterworth, BT= 0.80

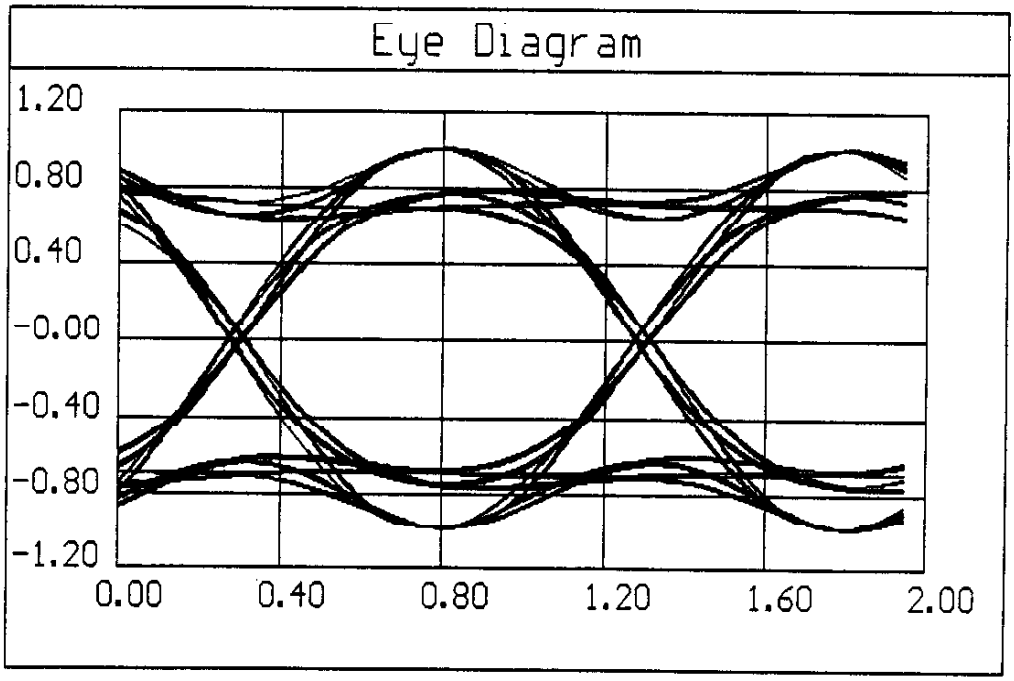

Figure A1.22b Phase Angle Filtering
(A) TOQPSK with No Filtering
(B) N=3 Butterworth, BT= 0.80

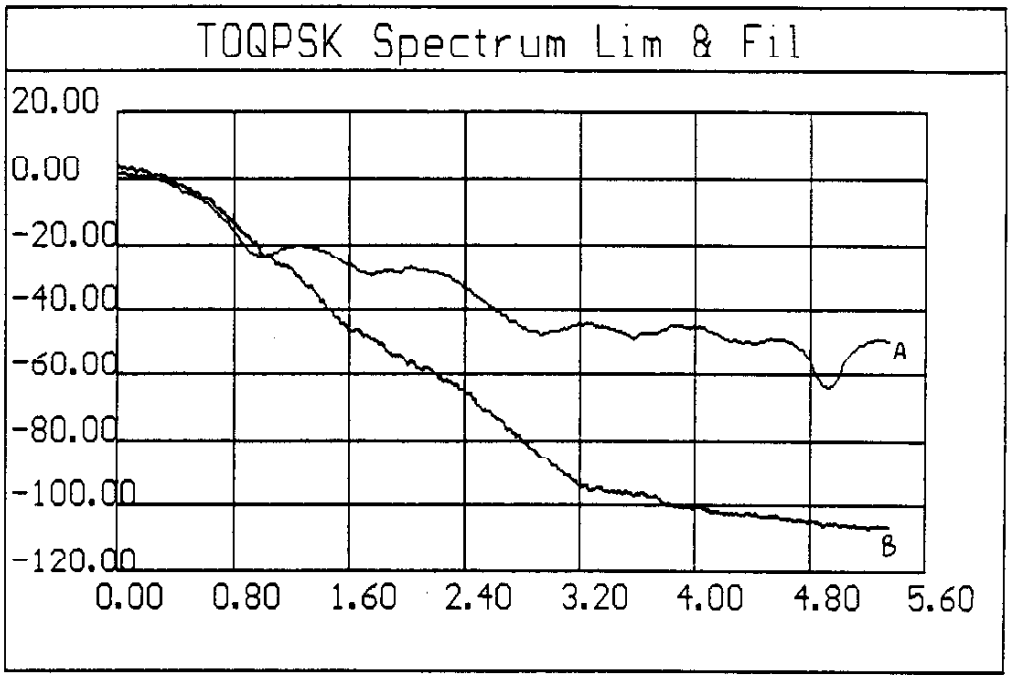

Figure A1.23a TOQPSK Spectrum with Phase Filtering
PSD dBc versus norm. bandwidth, fT
(A) TOQPSK with No Filtering
(B) N=3 Butterworth, BT= 0.60

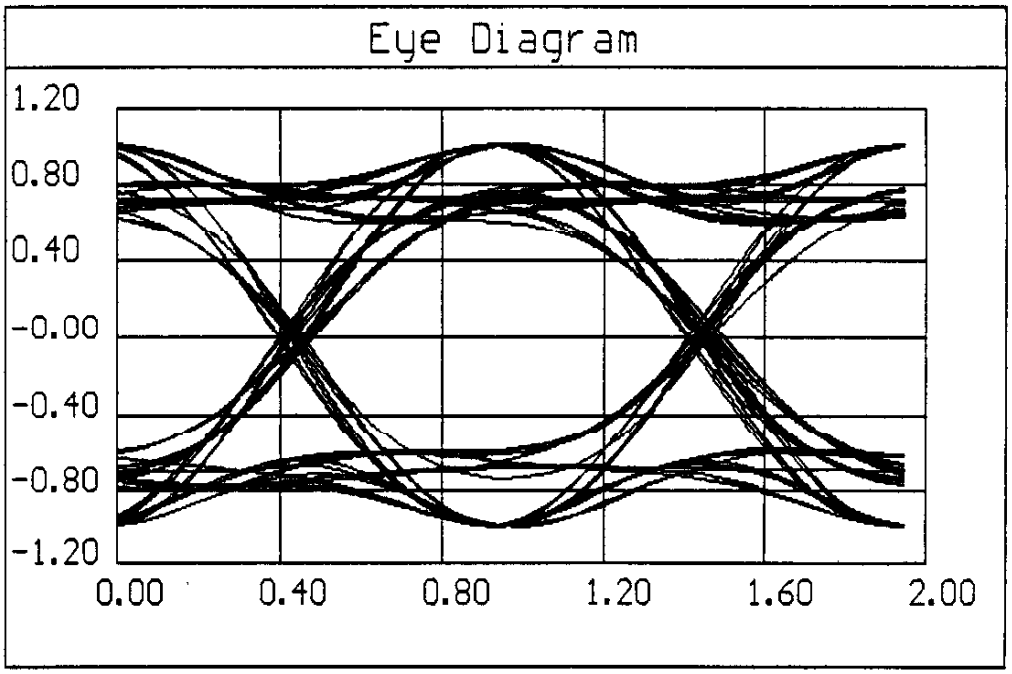

Figure A1.23b Phase Angle Filtering
(A) TOQPSK with No Filtering
(B) N=3 Butterworth, BT= 0.60

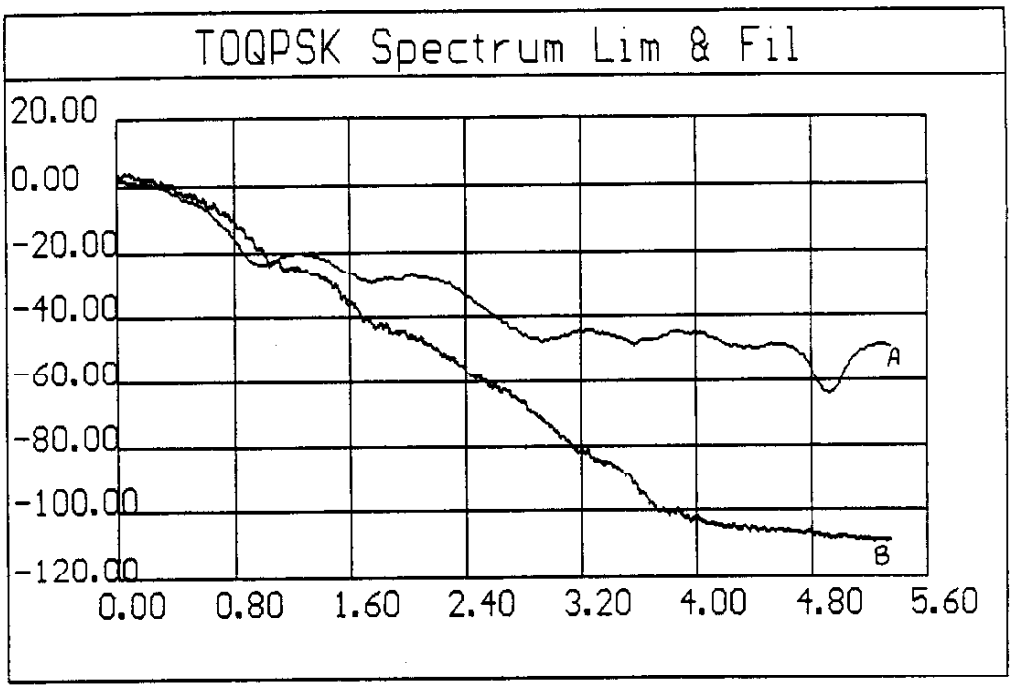

Figure A1.24a TOQPSK Spectrum with Phase Filtering
PSD dBc versus norm. bandwidth, fT
(A) TOQPSK with No Filtering
(B) N=4 Butterworth, BT= 1.0

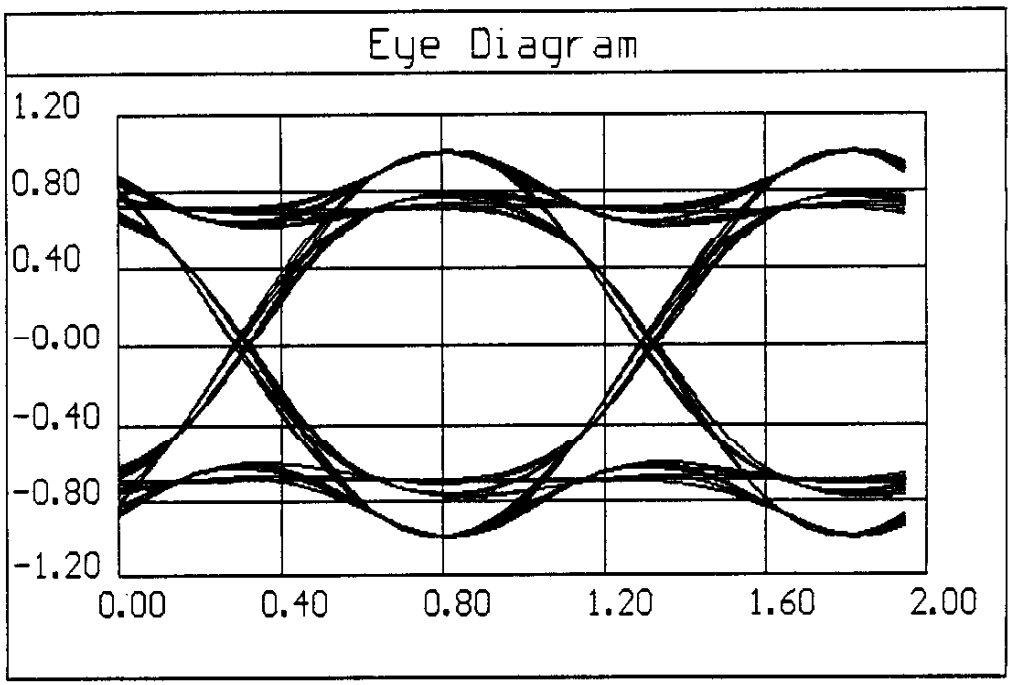

Figure A1.24b Phase Angle Filtering
(A) TOQPSK with No Filtering
(B) N=4 Butterworth, BT= 1.0

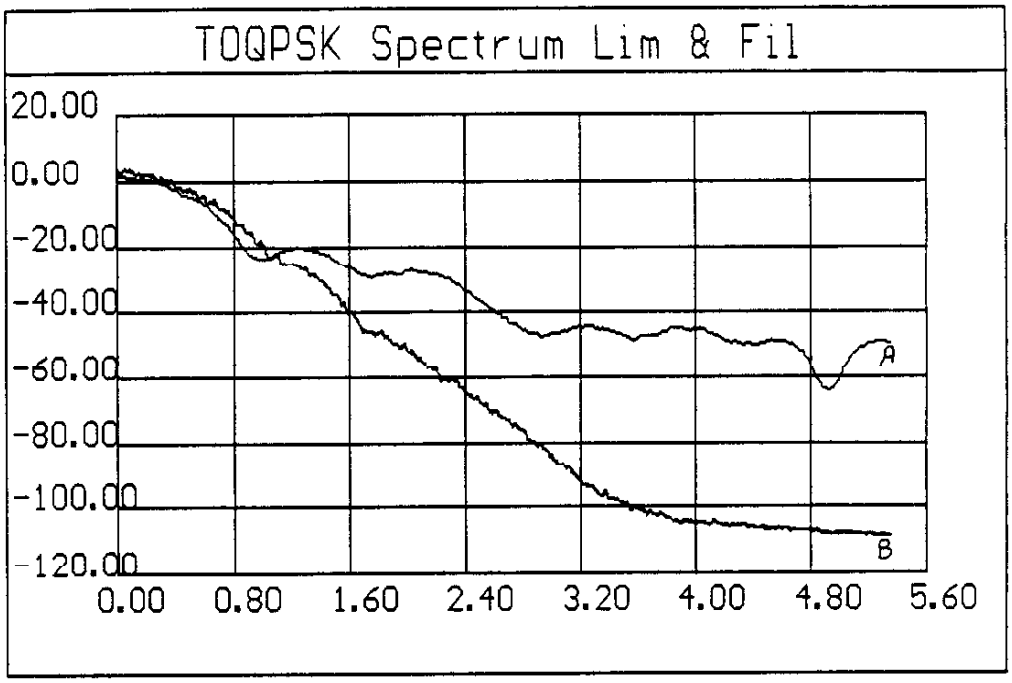

Figure A1.25a TOQPSK Spectrum with Phase Filtering
PSD dBc versus norm. bandwidth, fT
(A) TOQPSK with No Filtering
(B) N=4 Butterworth, BT= 0.80

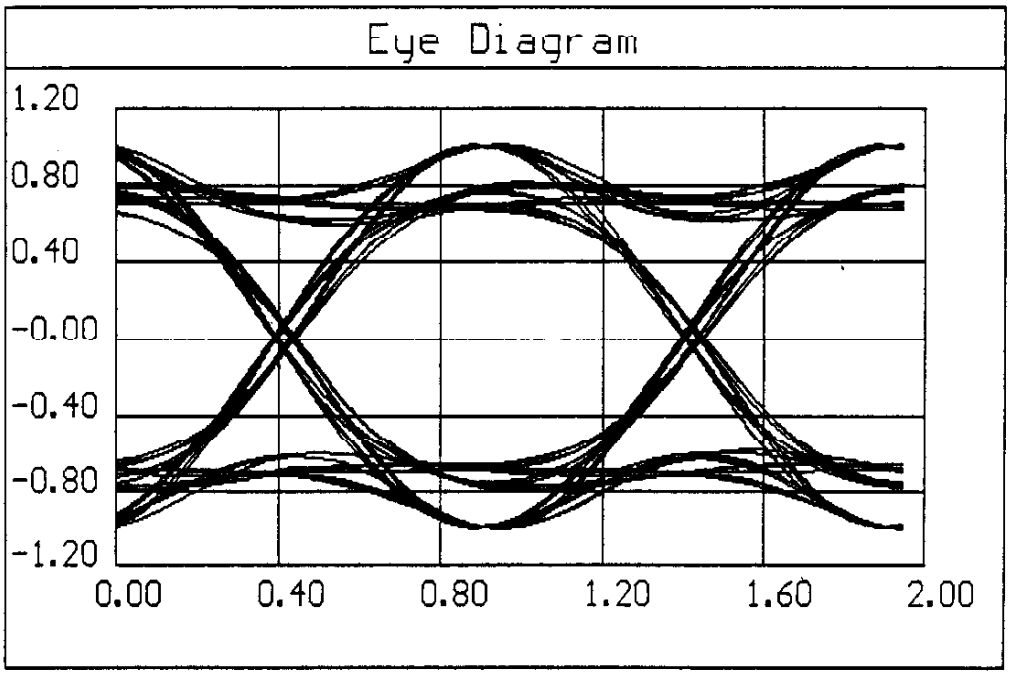

Figure A1.25b Phase Angle Filtering
(A) TOQPSK with No Filtering
(B) N=4 Butterworth, BT= 0.80

Appendix I References

A1.1] Levesque, A.H., et al., "A Proposed Federal Standard for Narrowband Digital Land Mobile Radio," MILCOM 1990, pp. 497-501

A1.2] Defense Communications Agency, "Technical Interface Specification 25 kHz UHF TDMA/DAMA Waveform," JTC3A Specification 9128, 31 July 1989

A1.3] Defense Communications Agency, "Technical Interface Specification for 5 kHz DAMA Waveform," JTC3A Specification 9129, 14 October 1990

A1.4] Baker, T., "Asymptotic Behavior of Digital FM Spectra," IEEE Trans. Commun., Vol. COM-22, Oct. 1974, pp. 1585-1594

A1.5] Marple, S.L., Digital Spectral Analysis, Prentice-Hall, 1987, Chapter 5

A1.6] Chandler, E.W., et al., "An Efficient Narrowband UHF DAMA Protocol and Waveform Developed for USTS", MILCOM 1990, pp. 922-928

A1.7] Chua, L.O., Pen-Min Lin, Computer-Aided Analysis of Electronic Circuits: Algorithms and Computational Techniques, Prentice-Hall, 1975

A1.8] Dzung, D., W.R. Braun, "Generalized CPM and DPM: Digital Angle Modulation Schemes with Improved Bandwidth Efficiency," IEEE Trans. Comm., Nov. 1990, pp. 1971-1979

A1.9] Prabhu, V.K., "Spectral Occupancy of Digital Angle-Modulated Signals," Bell Syst. Tech. J., Vol. 55, pp. 429-453, April 1976

A1.10] Asakawa, S. F. Sugiyama, "A Compact Spectrum Constant Envelope Digital Phase Modulation," IEEE Trans. Veh. Tech., Vol. VT-30, August 1981, pp. 102-111

A1.11] Deshpande, G.S., P.H. Wittke, "Optimum Pulse Shaping in Digital Angle Modulation," IEEE Trans. Comm., Vol. COM-29, Feb. 1981, pp. 162-168

A1.12] Maseng, T., "Digitally Phase Modulated (DPM) Signals," IEEE Trans. Comm., Vol. COM-33, Sept. 1985, pp. 911-918

A1.13] Anderson, J.B., et al., "Power-Bandwidth Performance of Smoothed Phase Modulation Codes," IEEE Trans. Comm., Vol. COM-29, March 1981, pp. 187-195

Appendix V
Digital Signal Processing for 5 kHz DAMA Services

Introduction

Although a number of important issues pertaining to 5 kHz DAMA have been addressed elsewhere in this study, this appendix will address many of the remaining details which have not been covered (e.g., bit synchronization). Simulation results are also provided which assess the overall end-to-end radio performance for this operational mode.

Sequence of Operations

Proper entry into the 5 kHz DAMA network can only be achieved by first reading the forward order wire (FOW) from the net controller (NC) which is transmitted at a burst rate of 600 sps [A5.1]. Some of the pertinent details concerning the FOW message are provided separately in Appendix IV.

The burst rates for the return order wire (ROW) and the ROW ranging are 2400 sps and 800 sps respectively. The burst rate for general communications may be any one of 600, 1200, 2400, or 3000 sps [A5.1]. Although many baseband protocol items make up the 5 kHz standard, only frame synchronization and steady-state data reception will be examined in this appendix.

During the preamble portion of each message burst, signal detection, initial frequency error estimation, symbol timing synchronization, and carrier phase synchronization must all be achieved prior to correctly receiving the start of message (SOM) unique word. The signal preamble duration prior to the appearance of the SOM word is given for each burst rate in Appendix IV. Each of the acquisition steps will be examined now in detail.

Frame Acquisition Probability

The terminal receiver system is required to provide an error-free reception of the FOW burst for at least 99 out of 100 FOW bursts with a confidence level of 98 percent [A5.1]. Since this standard does not specify the E_b/N_o value under which this measure is required, the best design guidelines remain those of Table A4.2.

The initial FOW frame acquisition operation is required to occur in less than 90 seconds with a probability of 0.95 assuming

an $E_b/N_o \geq 6$ dB. Given that p_d is the single frame probability of detection (achieving frame lock), and that one frame occurs every 8.96 seconds, the probability of detecting a frame in less than 90 seconds is given by

$$P_{FL} = \sum_{i=1}^{10} p_d \left(1 - p_d \right)^{i-1} = 1 - \left(1 - p_d \right)^{10} \quad (1)$$

This formula assumes that the system false frame detection probability is very small making this contribution completely negligible. From (1), the 90 second frame lock criteria can be achieved with a p_d as low as 0.2589. Stated in another manner, given a specified p_d, the number of frames required to achieve frame lock with a probability of 0.95 is given by

$$N_{Lock} = SIGTE\left[\frac{Log(0.05)}{Log(1 - p_d)} \right] + 1 \quad (2)$$

where SIGTE represents "smallest integer greater than or equal to". Due to the random initial starting point for the DAMA frame preamble boundary, the minimum frame count required to acquire lock is 2. Equation (2) is evaluated for a range of p_d values in Table A5.1.

Table A5.1 Worst-Case Net Entry Times Vs. P_d

Single Frame Detection Probability, p_d	Worst-Case Time to Net Entry (95% Prob), sec.
0.10	268.8
0.20	134.4
0.30	89.6
0.40	62.7
0.50	53.8
0.60	44.8
0.70	35.8
0.80	26.9
0.90	26.9
0.95	17.9

Based upon Table A5.1, a 0.70 single frame probability of detection, if achievable with a low false alarm rate, is very

desirable because it would lower the acquisition time from 90 seconds to roughly 30 seconds. The frame false alarm rate of 10^{-5}, if based upon 8.96 second frames, translates into one false frame detection every 10.4 days.

The SOM unique word consists of a total of 42 bits for the I and Q channels. A valid SOM must be observed before frame lock can be declared. Although the standard [A5.1] does not specify how many bits may be in error while still declaring a valid SOM, it does stipulate that up to one-fourth of the burst type indicator bits in the FOW message can be error. This bit error rate will be adopted for the SOM acceptance criterion as well.

Based upon this premise, up to 11 bits out of the 42 bits in the SOM word can be in error before the message is not recognized. Under noise-only conditions then, 42 - 11= 31 bits must happen to match with the SOM bit pattern in order for the random noise to be mistaken for a SOM word. The probability that ≥31 of the 42 random bits will be correct for random noise is given by

$$p_{sf} = \left(\frac{1}{2}\right)^{42} \sum_{i=31}^{42} \binom{42}{i} \qquad (3)$$

Evaluation of (3) gives p_{sf}= 0.00144 which is not a negligible false alarm probability per frame. Assuming that each group of 42 input bit values is an independent quantity, at 600 sps, this translates into an erroneously recognized SOM word once every 24.3 seconds which is clearly not acceptable. The overall system false alarm rate can only be improved by either allowing fewer bit errors in the SOM word, or by also requiring the cross-product (CP) ratio test outlined in Appendix IV to indicate a valid signal detection before declaring a valid frame lock. The latter approach is clearly more desirable since the alternative method would adversely impact the SOM detection probability, p_{sd}. Therefore, in order to have an adequate system level frame false alarm rate, the CP ratio test single frame false alarm rate p_{rf} should be less than (10.4 days/24.3 sec)$^{-1}$ = 2.7 10^{-5}.

The SOM probability of detection assuming a bit error rate of 0.25 is given by

$$p_{sd} = \sum_{i=31}^{42} \binom{42}{i} \left(\frac{3}{4}\right)^{i} \left(\frac{1}{4}\right)^{42-i} \qquad (4)$$

which equals 0.6486. This detection probability limits the single frame probability of detection p_d to 0.6486 at this bit error rate. Therefore, even if the CP ratio test probability of detection p_{rd} is 0.95, the overall system single frame probability of detection p_d is reduced to 0.6162 which increases the worst case time to frame acquisition to approximately 45 seconds. Based upon this value of p_{sd}, the CP ratio test probability p_{rd} must be at least 0.40 where $p_d = p_{rd}p_{sd}$.

Neglecting the finite frame false detection probability, the overall frame acquisition process may be described by the Markov process shown in Figure A5.1. Each state in this diagram represents a necessary step which must be accomplished in the frame acquisition process. State transition probabilities have been assigned to each branch indicative of the success and failure of each process step. The probability of sucecssfully obtaining carrier recovery lock is denoted by p_{cl} and the probability of successfully achieving symbol synchronization is denoted by p_{bl}. Both of these probabilities are difficult to ascertain in practice [A5.2] but are nevertheless equally important for ascertaining system performance.

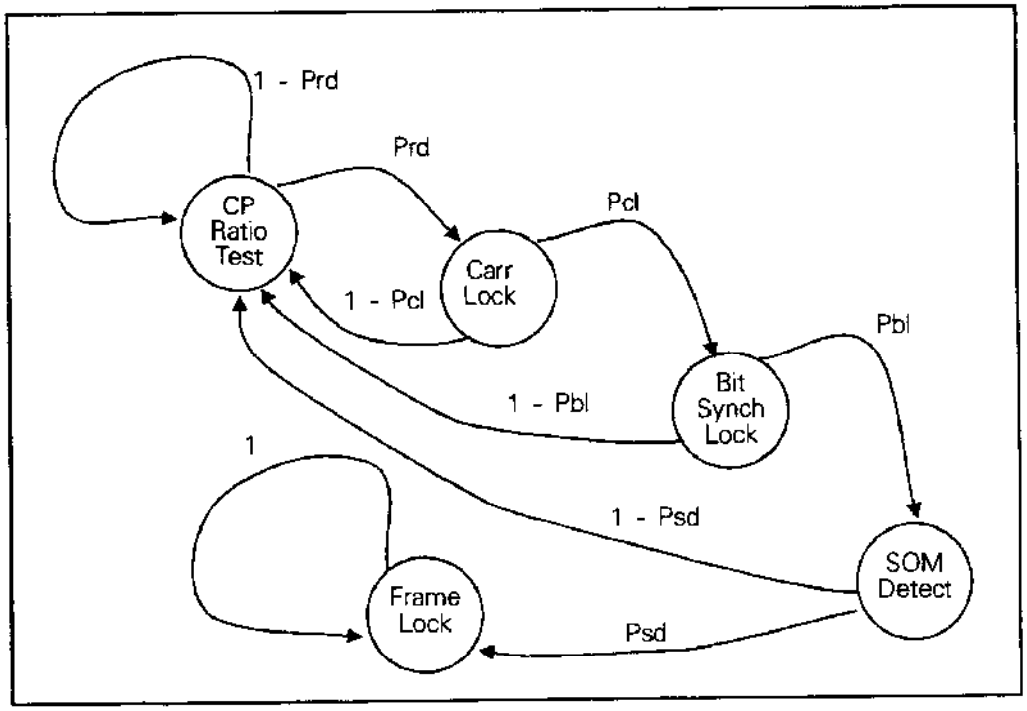

Figure A5.1 Markov Process Describing Initial FOW Frame Acquisition.

Directed graph techniques from classical control theory may be used to determine the average number of frames required in order to achieve frame lock.

The Markov process shown in Figure A5.1 may be state-reduced to Figure A5.2 where the carrier and bit synchronizer lock functions have been grouped into one state rather than two. A 'z' has been appended to each return path in Figure A5.2 in order to facilitate computing the mean number of frames required to achieve frame lock. Using Mason's Gain Rule, the transfer function from the

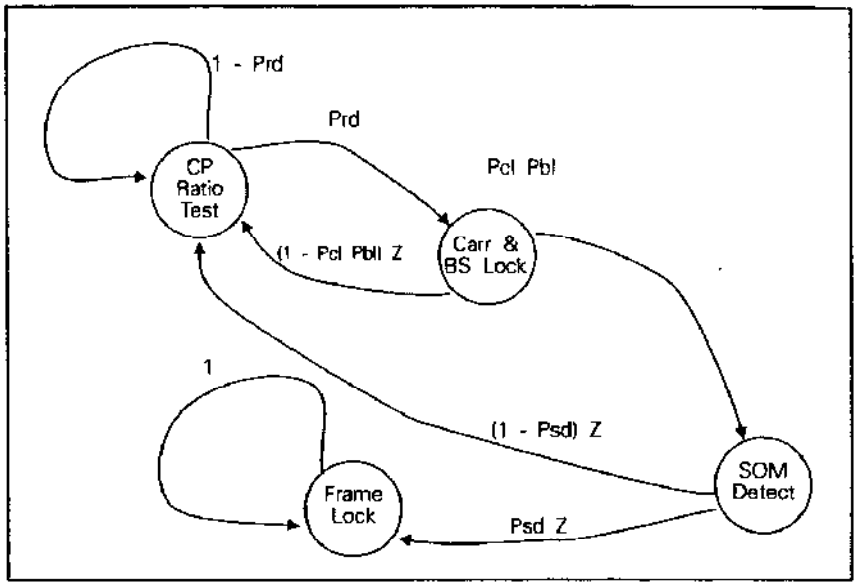

Figure A5.2 Reduced Markov State Diagram for Initial FOW Frame Acquisition.

initial search state to the fully absorbing state is given by

$$H(z) = \frac{p_{rt}p_{cl}p_{bl}p_{sd}\,z}{1 - (1-p_{rt})z - p_{rt}(1-p_{cl}p_{bl})z - p_{rt}p_{cl}p_{bl}(1-p_{sd})z} \qquad (5)$$

The average number of frames required to reach the absorbing state from the initial search state can be calculated as

$$\mu = \left[\frac{d\,H(z)}{dz} \right]_{z=1} \qquad (6)$$

Applying (6) to (5) with $p_{rt}p_{c1}p_{b1}p_{sd} = \alpha$,

$$H(z) = \frac{\alpha z}{1 - (1-\alpha)\, z} \tag{7}$$

and

$$\mu = \frac{1}{\alpha} \tag{8}$$

Therefore, the average number of frames required in order to attain frame lock is simply α^{-1}.

Earlier with $p_{c1}p_{b1} = 1$, the acqusition specification required that $p_{rd}p_{sd} \geq 0.2589$. Based upon the μ calculations above, it is therefore very reasonable that without perfect carrier and bit synchronization probabilities, we require that

$$p_{b1}p_{c1} \geq \frac{0.2589}{p_{rd}\, p_{sd}} \tag{9}$$

where of course all probabilities must be ≤ 1.0. Substituting in the previous value for p_{sd} of 0.6486, the final requirement for the carrier recovery and bit synchronization success probabilities is

$$\begin{aligned} p_{b1}\, p_{c1} &\geq \frac{0.40}{p_{rd}} \quad \textit{for } 90 \text{ sec.} \\ &\geq \frac{0.925}{p_{rd}} \quad \textit{for } 45 \text{ sec.} \end{aligned} \tag{10}$$

Since the analysis provided in Appendix IV substantiates that the CP ratio probability of detection p_{rd} should be very good, assuming a p_{rd} value here for discussion purposes of 0.98 is reasonable. Under this assumption combined with assuming that $p_{b1} = p_{c1}$, acquisition may be achieved in less than 90 seconds provided that $p_{c1} \geq 0.639$, and in less than 45 seconds provided that $p_{c1} \geq 0.972$.

In conclusion, acquisition in less than the current 90 second specification should be very attainable. Although acquisition in less than 45 seconds may be overly aggressive, the calculations indicate that this performance may in fact be achievable with the approach advocated. The design guidelines established thus far are

summarized below in Table A5.2.

Table A5.2 System Probability Parameters

CP Ratio Test Frame False Alarm Rate, Noise Only	$\leq 2.7\ 10^{-5}$
CP Ratio Test Frame Detection Probability, E_b/N_o= 6 dB	≥ 0.98
Carrier Recovery Lock Probability	$p_{cl} \geq 0.64$ (90 sec) ≥ 0.972 (target)
Bit Synchronization Lock Probability	$p_{bl} \geq 0.64$ (90 sec) ≥ 0.972 (target)
Bit Error Rate, Uncoded @ E_b/N_o = 3 dB	≤ 0.25

Initial Signal Detection Details

Initial signal detection of the 5 kHz DAMA preamble is based upon the CP ratio test discussed in Appendix IV. As supported by Figures A4.2 and A4.3, the algorithm works well for even very low E_b/N_o situations. From these figures, the CP ratio mean and standard deviation at a CNR of 3 dB (corresponding to E_b/N_o of 6 dB in a rate 1/2 coded system) are 0.7 and 0.03 respectively.

In order to achieve good systems level performance with a low false alarm rate, it is important that the AMST reliably discriminate between signals having CNRs ≥ 3 dB and those having a slightly lower CNR (e.g., 2 dB) since reliable communications is not possible much below a CNR of 3 dB. The approach advocated for the AMST is based upon Markov chain concepts [A5.3] and delayed decision concepts which commonly accompany forward-error correction decoding. A representative Markov chain diagram for the signal detection process in shown in Figure A5.3.

In the context of the material developed in Appendix IV, a CP ratio threshold test is performed once every fifteen 600 sps symbol periods. If the CP ratio exceeds the established threshold, the system state in Figure A5.3 is incremented one to the right. If on the other hand, the ratio test does not exceed the threshold and the test fails for a given group of 15 symbols, the system state is decremented by 2 to the left. The key concept behind this methodology is the association of a higher cost with each failed ratio test compared to the gain associated with a successful test.

In principle, declaration of signal presence may be delayed in

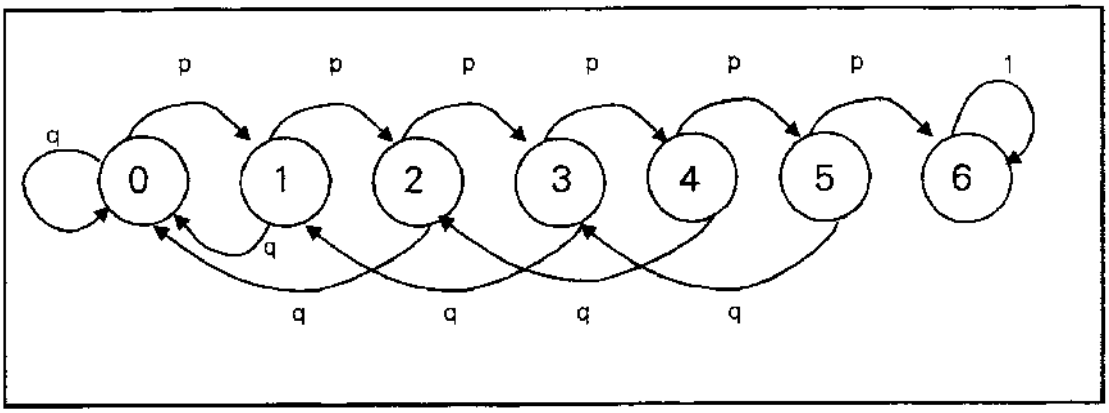

Figure A5.3 Example Markov Chain for the Initial Signal Detection Process.
P is the probability that the CP ratio test exceeds a given threshold and q=1-p.

the algorithm right up until reception of the SOM in order to improve the system false alarm rate. Other elements of the signal acquisition process would of course have to be initiated in advance of the SOM word in order to achieve carrier and symbol synchronization before arrival of the SOM word. Figure A5.3 is only one of many possible state diagram schemes which could be used for the AMST.

The simplified state diagram shown in Figure A5.4 will be used in the AMST where the z operator has been appended to each state transition path for subsequent analysis and the total chain length has been reduced to 5 states which corresponds to 75 symbol periods at 600 sps. The state diagram transfer function for Figure A5.4 can be written as

$$H(z) = \frac{p^4 z^5}{1 - qz - pqz^2 - 2p^2qz^3 + q^2p^2z^4} \qquad (11)$$

Based upon equation (6), the mean number of CP ratio tests performed before signal presence is declared in state 4 is given by

$$\mu = \frac{(1-q-pq-2p^2q+q^2p^2)4p^4 - p^4(-q - 2pq - 6p^2q + 4p^2q^2)}{(1 - q - pq - 2p^2q + q^2p^2)^2} + 1 \qquad (12)$$

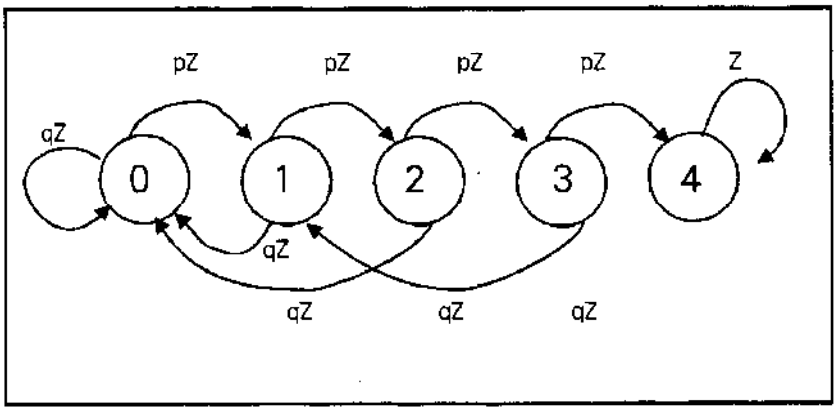

Figure A5.4 AMST Markov Diagram for 5 kHz DAMA Signal Detection

In order to get some idea of the signal level discrimination capability of this approach, the quantity μ was evaluated as a function of CNR in Table A5.3 below. The CP ratio test threshold was established based upon Figure A4.10, an assumed Gaussian distribution for the CP ratio test statistic, and the desire to have a 98% probability of detection on each CP ratio test at a CNR of 3 dB. This translated into a threshold of $A = 0.7 - 2.5\sigma = 0.625$.

At CNRs below approximately 2 dB, the mean time required to recognize the preamble signal presence exceeds the length of the 5 kHz DAMA preamble period. In these cases, the SOM word is never recognized aside from random false alarm occurrences. Even so, the SOM recognition test lowers the would-be false alarm rate to approximately one every 1.5 sec/0.0014 $\approx$ 17.9 minutes for $p = 0.40$ in Table A5.3 which should be very acceptable.

The Markov process described in Figure A5.4 will be implemented in a control processor within the AMST since it requires a very low update rate and can be very easily changed in this form. The CP ratio test threshold will be made variable thereby implementing a form of user-specified squelch whenever desired.

Table A5.3 Mean-Time to Recognize Preamble Presence

CNR, est. dB	CP Ratio Prob p	No. of CP Ratio Tests	Mean Time to Declare
-0.8	0.01	$1.01\ 10^6$	29.2 days
	0.10	11,021	4.6 min.
	0.20	761	19 sec.
	0.30	168.2	4.2 sec.
	0.40	60.7	1.5 sec.
1.0	0.50	29	730 msec
	0.60	16.7	420 msec
	0.70	10.9	270 msec
	0.80	7.9	172 msec
2.2	0.90	6.1	153 msec
	0.95	5.5	138 msec
3.0	0.98	5.2	130 msec
	0.99	5.09	127 msec

Carrier and Symbol Timing Recovery- Initial Synchronization

Following a successful preamble signal detection as described above, the received signal frequency error (with respect to the AMST local oscillator) is estimated as discussed in Appendix IV, and an adjustment to the receiver local oscillator is made to remove the frequency error. Following these steps, some residual carrier frequency error will of course remain present along with an unknown carrier phase. The structure of the preamble may be exploited to speed the remaining portion of the initial carrier synchronization process as described next.

Many methods have been proposed for achieving carrier synchronization for suppressed carrier waveforms. However, most of these methods are either (i) unsuited for offset QPSK type waveforms, (ii) do not exploit the preamble data pattern being used, or (iii) do not work well following integrate-and-dump matched filters as planned for the AMST. The approach taken here is believed to be completely original and results in new error metrics for initial carrier synchronization and initial symbol synchronization which are mutually independent. Since the two error metrics are uncoupled, both carrier and symbol synchronization can be initiated immediately after the initial frequency error process has been completed.

The basis for the initial carrier synchronization method comes from the eye diagrams shown in Figures A1.24b and A1.25b. During the preamble portion of the DAMA waveform, it is very reasonable to represent the received signal less noise at the receiver as

$$r(t) = A\left[\, 1 + j \sin(\omega_s t + \theta) \,\right] e^{j\phi} \qquad (13)$$

where ω_s is the radian/sec symbol rate divided by two, θ is the unknown symbol timing phase, and φ is the unknown carrier phase. Both θ and φ are assumed to be slowly changing with respect to time due to the small uncertainty in the symbol rate and the precision of the initial carrier frequency error removal step which preceded.

If a correlation type receiver were to be used to receive the preamble portion of the DAMA FOW, the receiver would correlate the incoming signal with c(t) which is given by

$$c(t) = 1 - j \sin(\omega_s t) \qquad (14)$$

If we perform the multiplication r(t) c(t) and follow this with a time averaging step to remove frequency components above ω_s, the correlator output is given by

$$d(t) = A\left[\, 1 + \frac{1}{2} \cos(\theta) \,\right] e^{j\phi} \qquad (15)$$

where clearly φ = Arg[d(t)]. Although the unknown symbol timing error θ does affect the amplitude of d(t), it is not coupled with the carrier phase φ which makes this result attractive.

If the receiver's correlation function c(t) is modified to

$$v(t) = 1 - j\, Sign[\, \sin(\omega_s t) \,] \qquad (16)$$

although some mismatch loss will occur, the correlation receiver can be simplified to a matched filter receiver where integrate-and-dump filters are used on the I and Q baseband channels. This choice is adopted for the AMST and algorithms for extracing the carrier and symbol timing phases must be derived.

Rewriting the received signal less noise r(t) in rectangular form gives

$$\begin{aligned} r_i(t) &= A \cos(\phi) - A \sin(\omega_s t + \theta) \sin(\phi) \\ r_q(t) &= A \sin(\phi) + A \sin(\omega_s t + \theta) \cos(\phi) \end{aligned} \qquad (17)$$

Including the integrate-and-dump matched filter operations upon $r_i(t)$ and $r_q(t)$, the processed I and Q baseband samples for the k^{th} dump period are given by

$$I(k) = \int_{(k-1)T}^{kT} A\cos(\phi) - A\sin(\omega_s T + \theta)\sin(\phi)\,dt$$
$$= -\frac{A\pi}{\omega_s}\cos(\phi) + (-1)^k \frac{2A}{\omega_s}\sin(\phi)\cos(\theta) \qquad (18)$$

and

$$Q(k) = \int_{(k-1)T}^{kT} A\sin(\phi) + A\sin(\omega_s t + \theta)\cos(\phi)\,dt$$
$$= \frac{A\pi}{\omega_s}\sin(\phi) - (-1)^k \frac{2A}{\omega_s}\cos(\phi)\cos(\theta) \qquad (19)$$

In this form, it is not immediately apparent that θ and φ can be easily extracted separately. From (18) and (19), it is easy to show however that

$$\phi = Tan^{-1}\left[\frac{Q(k) + Q(k-1)}{I(k) + I(k-1)}\right] \qquad (20)$$

due to the preamble data pattern structure which makes the $(-1)^k$ terms cancel out. This cancellation makes (20) independent of the symbol timing phase θ.

It is equally desirable to form an error metric for the symbol timing error which is itself independent of the carrier phase. From (18) and (19) for slowly changing arguments θ and φ,

$$\cos(\phi) = \frac{\omega_s}{A\pi}\,\frac{I(k) + I(k-1)}{2}$$
$$\sin(\phi) = \frac{\omega_s}{A\pi}\,\frac{Q(k) + Q(k-1)}{2} \qquad (21)$$

Substituting (21) into (18) and simplifying, the symbol timing phase is given by

$$\theta = \cos^{-1}\left[\frac{\pi}{2} (-1)^k \frac{I(k) - I(k-1)}{Q(k) + Q(k-1)} \right] \quad (22)$$

A second equation for the same symbol timing phase can be obtained by similarly substituting (21) into (19) which gives

$$\theta = \cos^{-1}\left[\frac{\pi}{2} (-1)^{(k+1)} \frac{Q(k) - Q(k-1)}{I(k) + I(k-1)} \right] \quad (23)$$

The obvious concern with the results represented by (22) and (23) is the behavior of the equations whenever the denominator quantities become very small. Looking back over the derivation of these results, the $\cos^{-1}$ functions could just as easily have resulted in $\sin^{-1}$ functions, in which case the most important attribute of the formulas is for θ very small. If the small angle approximation for $\sin^{-1}$ is assumed, since only the numerator terms determine the zeros of the functions, the troublesome denominator quantities can be dropped. The final error metric which includes a weighted average to largely compensate for dropping the denominator terms is then given by

$$\theta = \beta \frac{Q(k)\ [\ I(k) - I(k-1)\ ] - I(k)\ [\ Q(k) - Q(k-1)\ ]}{|\ I(k)\ | + |\ Q(k)\ |} \quad (24)$$

where ß is a simple proportionality constant. This is a very nice result because it is reasonably simple and more importantly, it is independent of the unknown carrier phase. The error metric results are summarized in Table A5.4.

Table A5.4 Carrier Phase and Symbol Timing Error Metrics for Initial Pull-In for 5 kHz DAMA

Carrier Phase Error Metric

$$\varepsilon_c = \tan^{-1}\left[\frac{Q(k) + Q(k-1)}{I(k) + I(k-1)} \right] \qquad (25)$$

Symbol Timing Error Metric

$$\varepsilon_s = \frac{Q(k)\ [\ I(k) - I(k-1)\ ] - I(k)\ [\ Q(k) - Q(k-1)\ ]}{|\ I(k)\ | + |\ Q(k)\ |} \qquad (26)$$

Computer simulation was used to expediently assess the performance of these two error metrics including noise as described in the next section.

Computer Evaluation of Initial Pull-In Error Metrics

Computer evaluation of the two error metrics was done using the system block diagram shown in Figure A5.5. Referring to this figure, the transmitter spectral shaping approach developed in Appendix I was used with a N=4 Butterworth filter which had a BT product of 0.80. An arbitrary carrier phase parameter ψ was included to permit easy verification of the independence of the symbol timing error metric upon carrier phase. Some receiver IF filtering was included in the form of a N=4 Butterworth bandpass filter having an RF BT of 4.0. The integrate-and-dump matched filters were implemented for both I and Q channels. The transmitter data pattern was assumed to be given by $I + jQ = 1 + j(-1)^k$.

Results for the symbol timing error metric are presented here first. Several CNR cases were examined in order to substantiate the performance of the proposed error metric. The baseband eye diagram for the I channel is shown in Figure A5.6 assuming a CNR of 10 dB and a random carrier phase ψ of 77 degrees. The accompanying symbol timing error metric output (unaveraged S-curves, again viewed in eye diagram form) is shown in Figure A5.7. The stable locking points near t/T= 0.3 and 1.3 are clearly visible. Given the error metric output, a time-averaged S-curve may be computed or as done in this case, the probability that the error metric output is greater than zero may be calculated as a function of symbol timing error as shown in Figure A5.8. This so-called state-transition probability curve may be used to characterize the closed-loop performance of the symbol timing loop as developed shortly. Similar results for CNRs of 3 dB, 0 dB, and -3 dB are presented in Figures

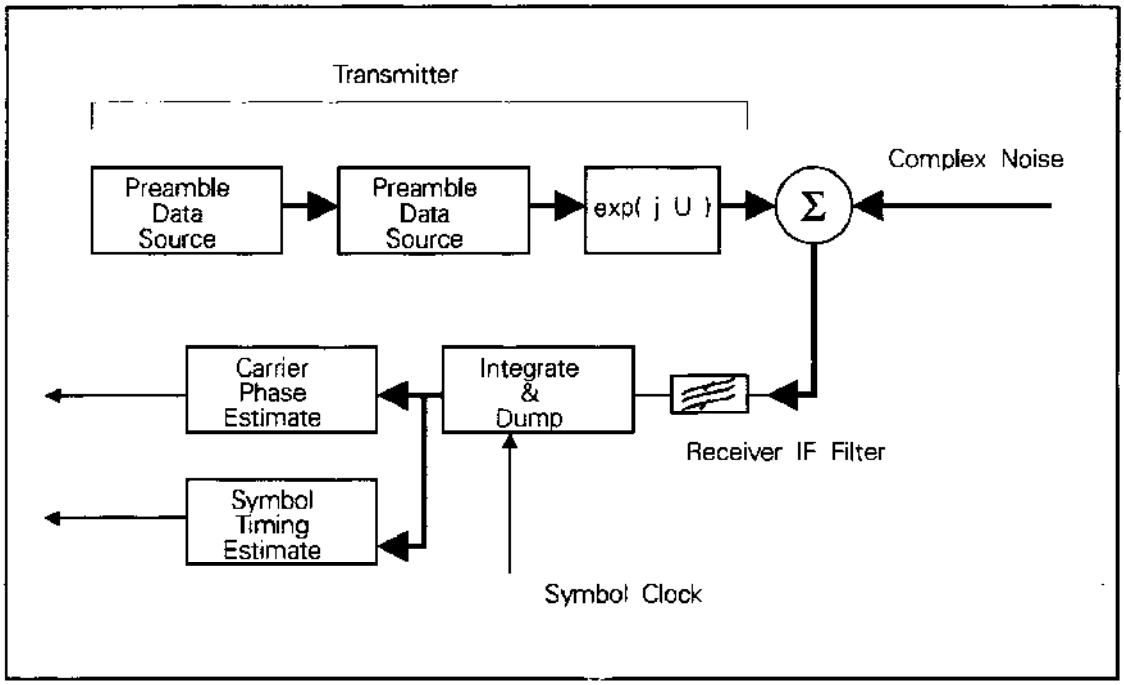

Figure A5.5 Block Diagram for Assessment of Open-Loop Carrier and Symbol Timing Error Metrics

A5.9 through A5.14. Even at the lowest CNR, the symbol timing error metric remains unbiased and no threshold effects are apparent.

The closed-loop performance of the symbol error metric can be evaluated by combining a discrete first-order Markov model with the state-transition probability curves. The discrete model approach is preferred as compared to a continuous model because it more closely represents digital implementations and is mathematically more simple. The Markov modeling approach permits us to examine important closed-loop behavior elements such as mean-time to achieve lock, mean-time to loose lock, and the steady-state tracking error variance. Assume that the symbol timing phase θ can only take on N discrete uniformly spaced values which span the complete range of 0 to 2π. At any time instant, the phase of the locally generated symbol clock can be equivalenced with being in one of the given N Markov states. At each new integrate-and-dump output sample pair, the error metric is then calculated based upon (26). The probability that the error metric calculation is > 0 is again given by the state-transition probability curves for a given CNR. Assuming that the state-transition probability at state k is represented by γ, the probability that we advance the local symbol clock by one state is given by $q = 1 - \gamma$ and the probability that we retard the local symbol clock one state is given by $p = \gamma$. The model described here is a first-order Markov process because only phase changes to immediately adjacent phase states are permitted. A

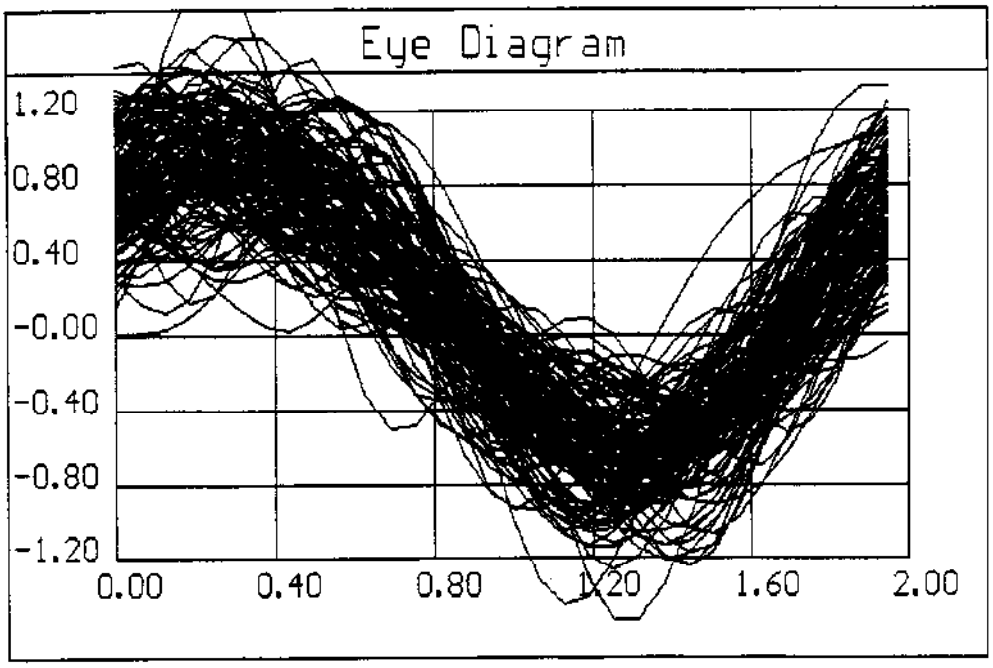

Figure A5.6 Case 1. Eye Diagram for I-Channel Integrate-and-Dump Output. CNR= 10 dB, φ= 77 degrees.

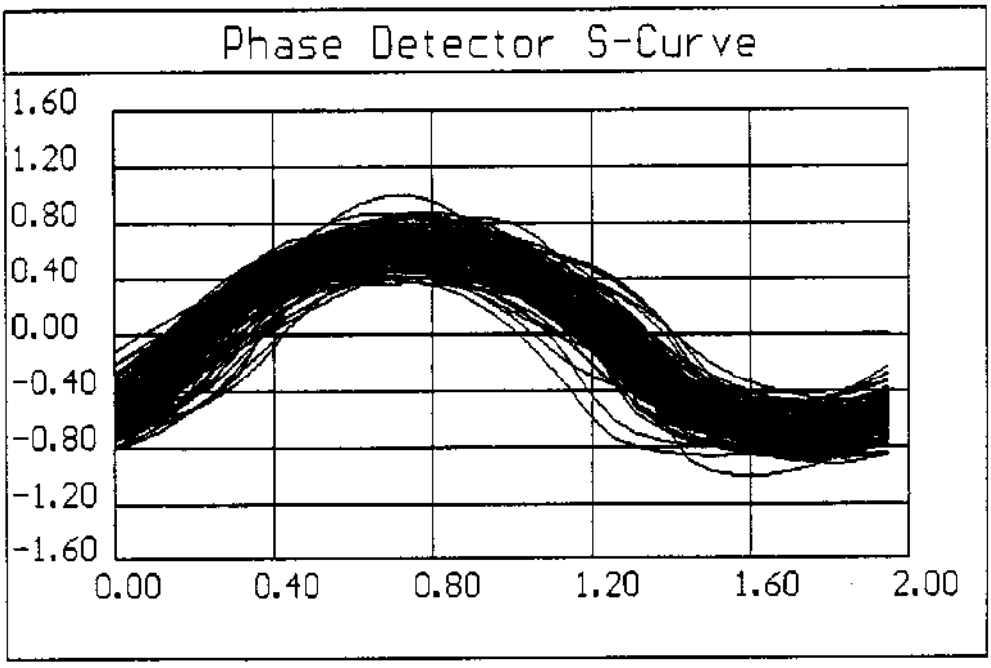

Figure A5.7 Symbol Timing Error Metric Output in Eye Diagram Form for Case 1.

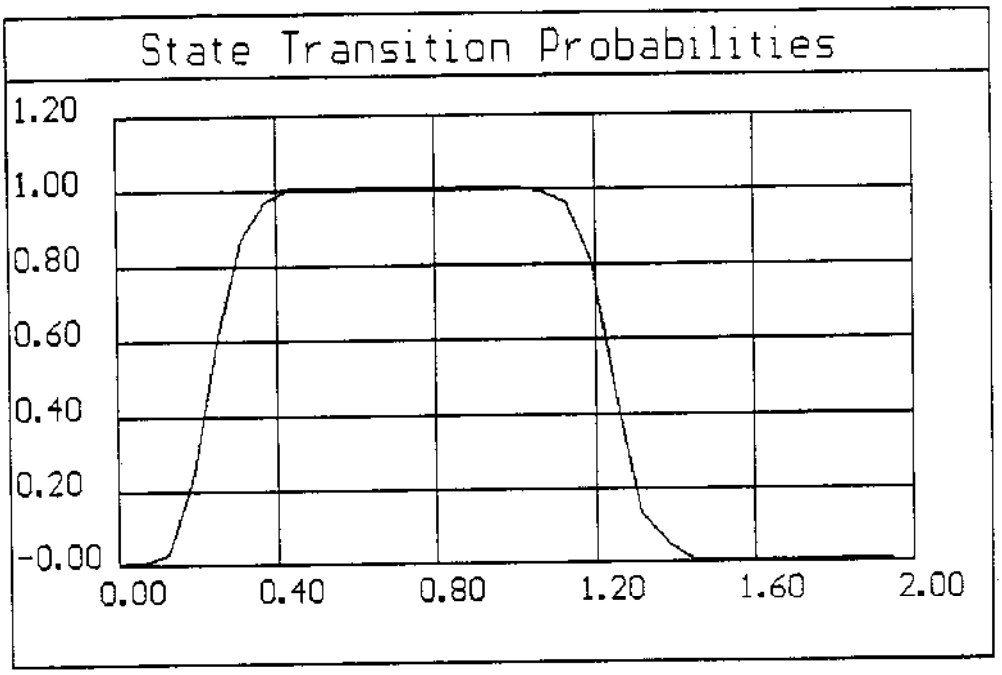

Figure A5.8 Case 1 State-Transition Probability Curve

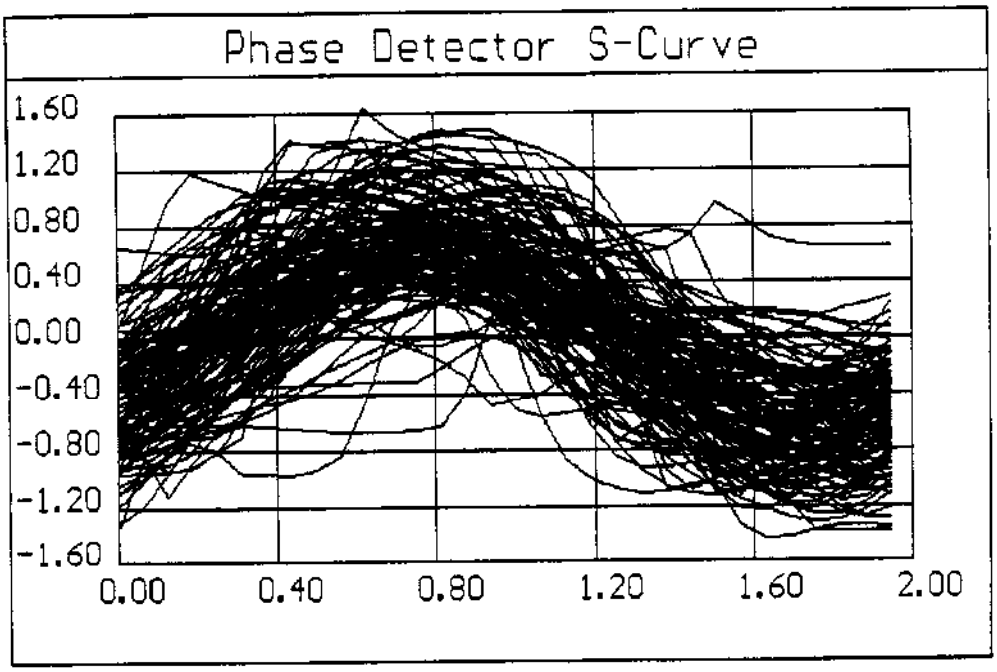

Figure A5.9 Case 2. Symbol Timing Error Metric Output in Eye Diagram Form. CNR= 3 dB, φ= 33 degrees.

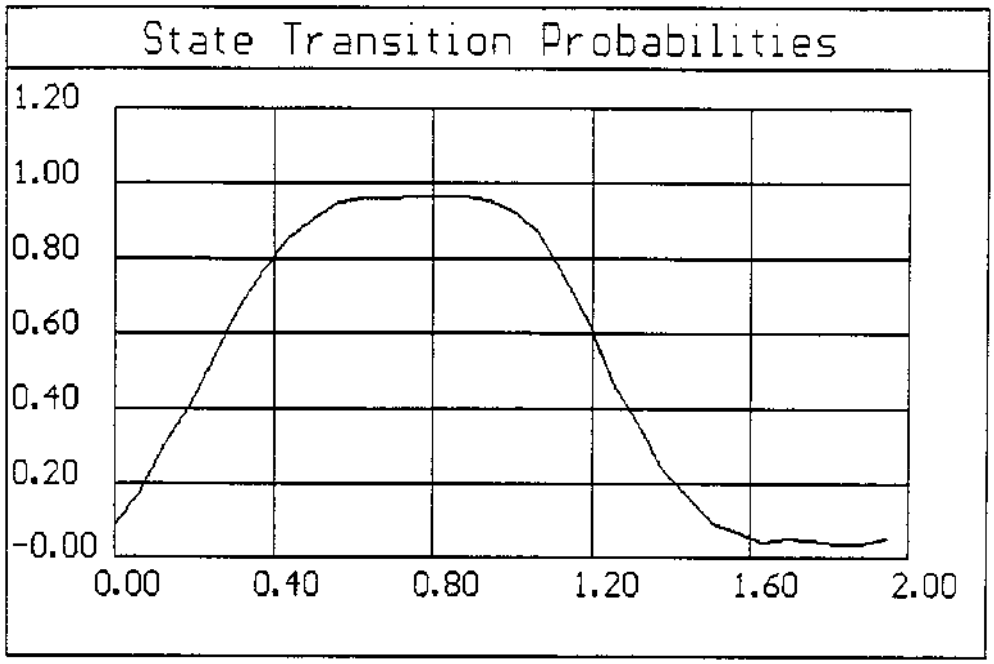

Figure A5.10 Case 2 State-Transition Probability Curve

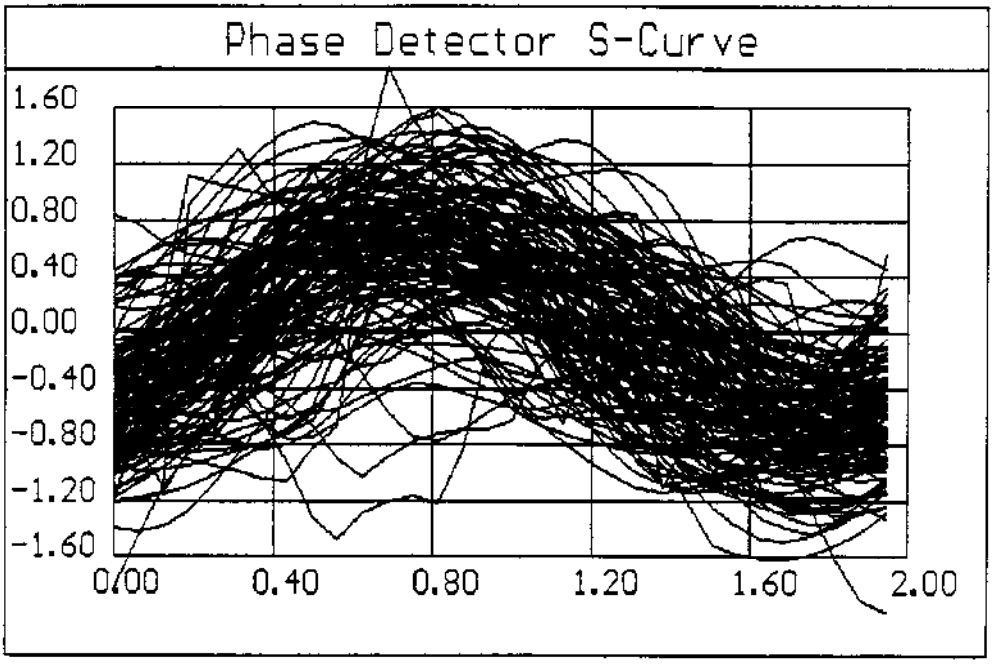

Figure A5.11 Case 3. Symbol Timing Error Metric Output in Eye Diagram Form. CNR= 0 dB

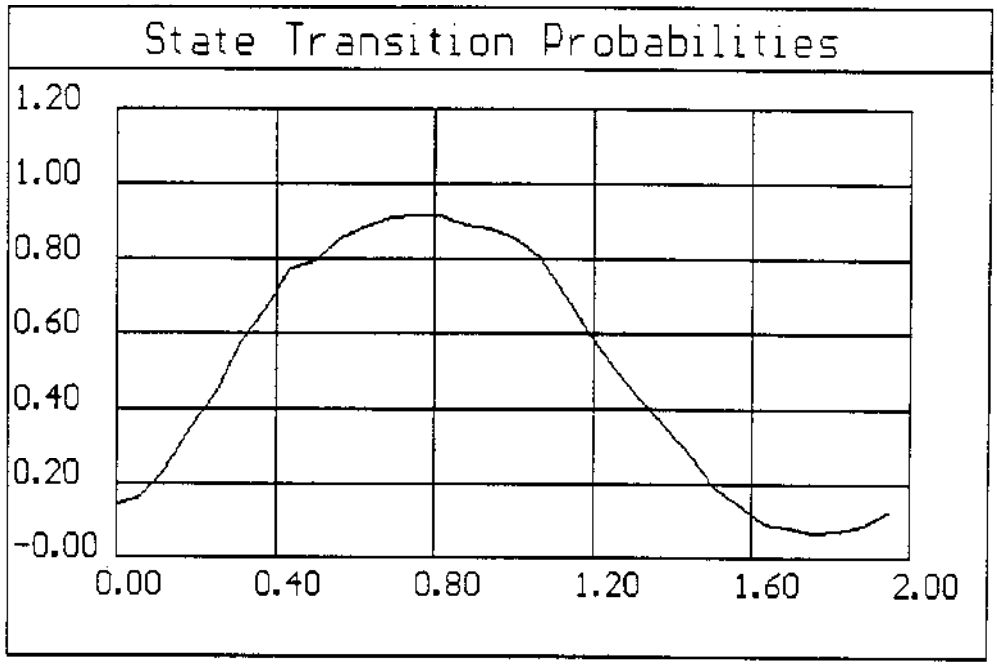

Figure A5.12 Case 3 State-Transition Probability Curve

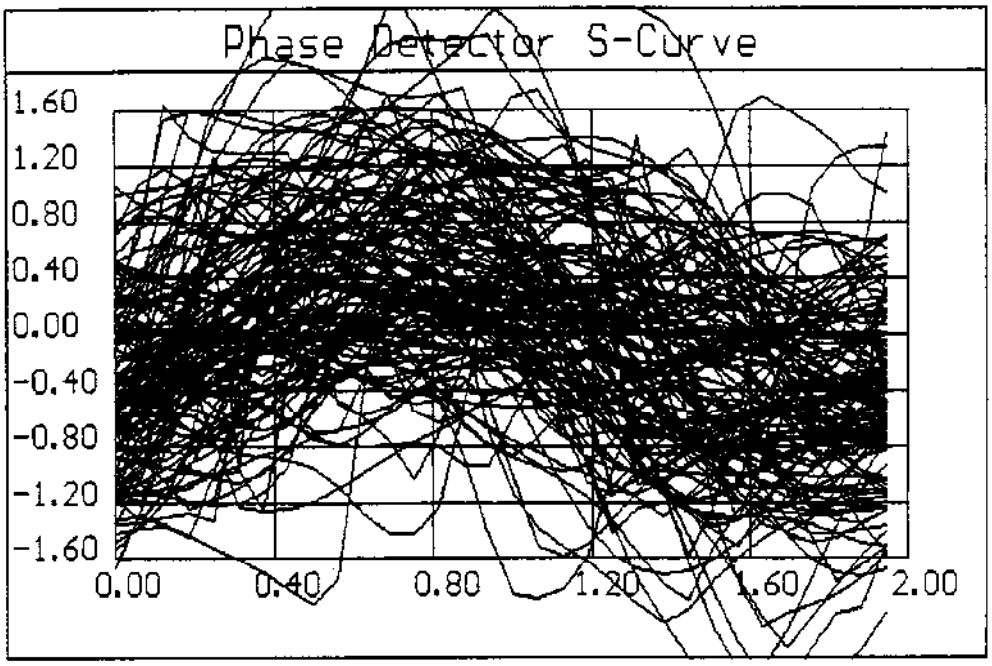

Figure A5.13 Case 4. Symbol Timing Error Metric Output in Eye Diagram Form. CNR= -3 dB

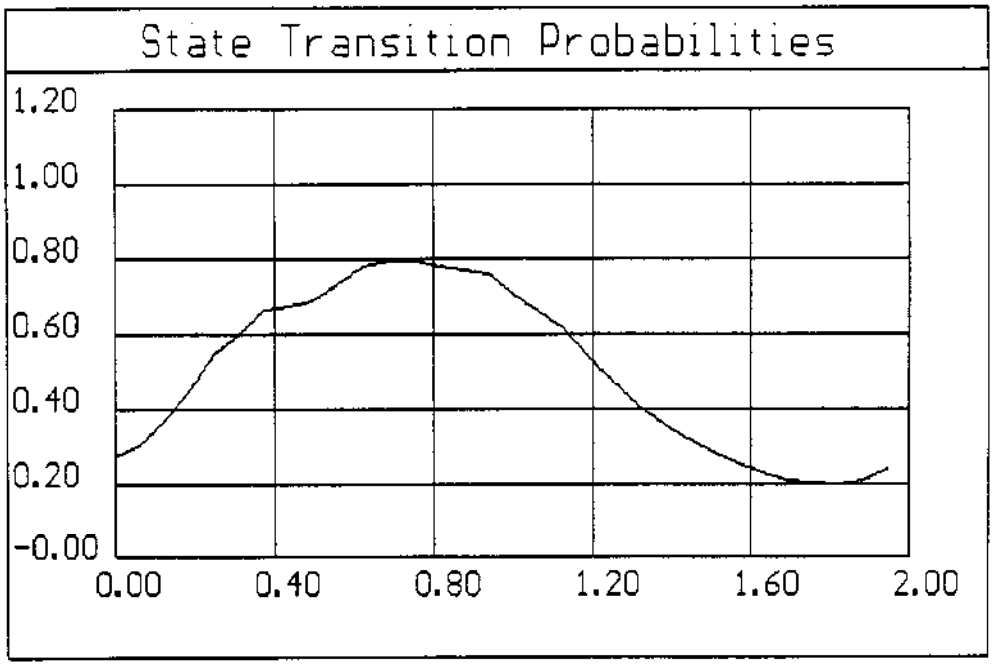

Figure A5.14 Case 4 State-Transition Probability Curve

representative Markov state diagram with N= 51 is shown in Figure A5.15 which can be used to calculate the steady-state tracking error variance. The Markov state diagram must be modified in order to compute the mean-time to loose lock and the (worst case) mean time to acquire lock as shown in Figure A5.16. Although the state diagram could in principle be simply modified for this calculation by adding a fully absorbing state, the computation of the mean time to acquire lock becomes incredibly ill-conditioned numerically. To circumvent this issue, the symmetry of the state transition probability curves is exploited as shown in Figure A5.16.

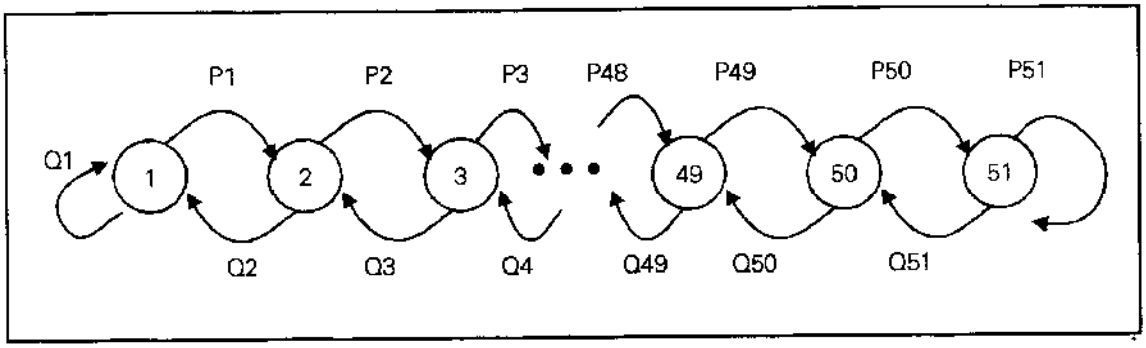

Figure A5.15 First-Order Markov Model for Calculation of Steady-State Tracking Error Variance. N= 51

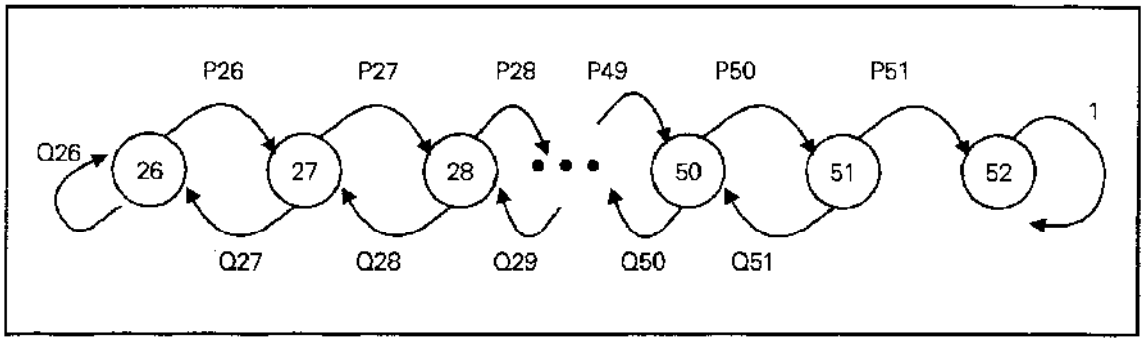

Figure A5.16 First-Order Markov Model for Calculation of Mean-Time to Loose Lock. N= 51

Concentrating on Figure A5.15 and the calculation of the steady-state tracking performance, the transition probabilities for each i^{th} state are given as previously by p_i and q_i where

$$p_i + q_i = 1 \tag{27}$$

which also guarantees that the model adjusts the symbol clock phase every symbol period.

The steady-state tracking error variance may be calculated by recognizing that the steady-state probability of having the local symbol clock phase in state k is

$$S_k = p_{k-1}S_{k-1} + q_{k+1}S_{k+1} \tag{28}$$

where we also have that

$$\begin{aligned} S_1 &= q_1S_1 + q_2S_2 \\ S_N &= p_NS_N + q_{N-1}S_{N-1} \end{aligned} \tag{29}$$

where S_k is the steady-state probability of being in state k. The first recursive equation is satisfied for

$$S_k = \frac{p_{k-1}}{q_k} S_{k-1} \tag{30}$$

Since the clock phase state must occupy one of the N available discrete states,

$$\sum_{k=1}^{N} S_k = 1 \tag{31}$$

Upon substituting (30) into (31), the steady-state probabilities are given by

$$S_1 = \frac{1}{1 + \sum_{k=1}^{N} \left[\prod_{i=1}^{k-1} \left(\frac{p_i}{q_{i+1}} \right) \right]} \tag{32}$$

$$S_k = S_1 \prod_{i=1}^{k-1} \left(\frac{p_i}{q_{i+1}} \right) \tag{33}$$

The mean tracking state number is given by

$$\mu = \sum_{i=1}^{N} i \, S_i \tag{34}$$

and the tracking error variance in steady-state is given by

$$\sigma^2 = \sum_{i=1}^{N} (i - \mu)^2 \, S_i \tag{35}$$

The mean-time to loose lock (or cycle slip) can be found in a similar manner by using Figure A5.16. Let T_k^{N+1} be the mean-time to reach state N+1 given that we begin in state k. Then

$$T_k^{N+1} = p_k T_{k+1}^{N+1} + q_k T_{k-1}^{N+1} + 1 \tag{36}$$

For the end states,

$$T_1^{N+1} = T_2^{N+1} + \frac{1}{p_1} \tag{37}$$

$$T_{N+1}^{N+1} = 0 \tag{38}$$

From (36), the recursive form may be rewritten as

$$T_{k+1}^{N+1} = \frac{T_k^{N+1}}{p_k} - \frac{q_k}{p_k} T_{k-1}^{N+1} - \frac{1}{p_k} \tag{39}$$

Dropping the N+1 superscript and subtracting T_k from each side,

$$T_{k+1} - T_k = T_k \left(\frac{1}{p_k} - 1 \right) - \frac{q_k}{p_k} T_{k-1} - \frac{1}{p_k} \tag{40}$$

$$\therefore \quad T_{k+1} - T_k = \frac{q_k}{p_k} [T_k - T_{k-1}] - \frac{1}{p_k} \tag{41}$$

This recursion may be applied repeatedly starting with state 1 which leads to

$$T_{k+1} - T_k = \sum_{i=1}^{k} \left[\left(\frac{1}{q_i} \right) \prod_{j=1}^{k} \left(\frac{q_j}{p_j} \right) \right] \tag{42}$$

The boundary condition on T_{N+1} can be used to solve for T_1 in closed form as

$$\sum_{k=1}^{N} (T_k - T_{k+1}) - T_1 \tag{43}$$

Therefore,

$$T_1 - \sum_{k=1}^{N} \left\{ \sum_{i=1}^{k} \left(\frac{1}{q_i} \prod_{j=i}^{k} \left(\frac{q_j}{p_j} \right) \right) \right\} \tag{44}$$

If we want to know the mean time to reach state N+1 from an abitrary state α, we may recursively compute (39) as required.

With this information as background, it is simple to argue that if the worst case pull-in time for the symbol tracking loop is to be M symbol periods, then N < 2M is required. Since the symbol timing phase is allowed to only change one increment at each update, there is a direct relationship between the number of Markov states selected and the effective bandwidth of the closed loop.

These equations were evaluated for a number of CNR values and a number of Markov states N in order to investigate the feasibility of initial symbol synchronization using the proposed error metric(%24'24* ^\3 intermediate calculation of the steady-state probabilities given by (32) and (33) were computed and plotted for example in Figure A5.17 for N=129 and CNR= -2 dB where the x-axis represents the width of one symbol period and the y-axis represents the steady-state probability of finding the symbol clock phase at a particular x-axis value (0.5 being optimal).

In order to keep the worst-case pull-in times small, N=65 is most representative for the DAMA acqusition situation being addressed. Under this assumption, the mean-time to acquire lock, the standard deviation of the steady-state tracking error, and the mean-time to loose lock were calculated as a function of CNR and the results are shown in Table A5.5.

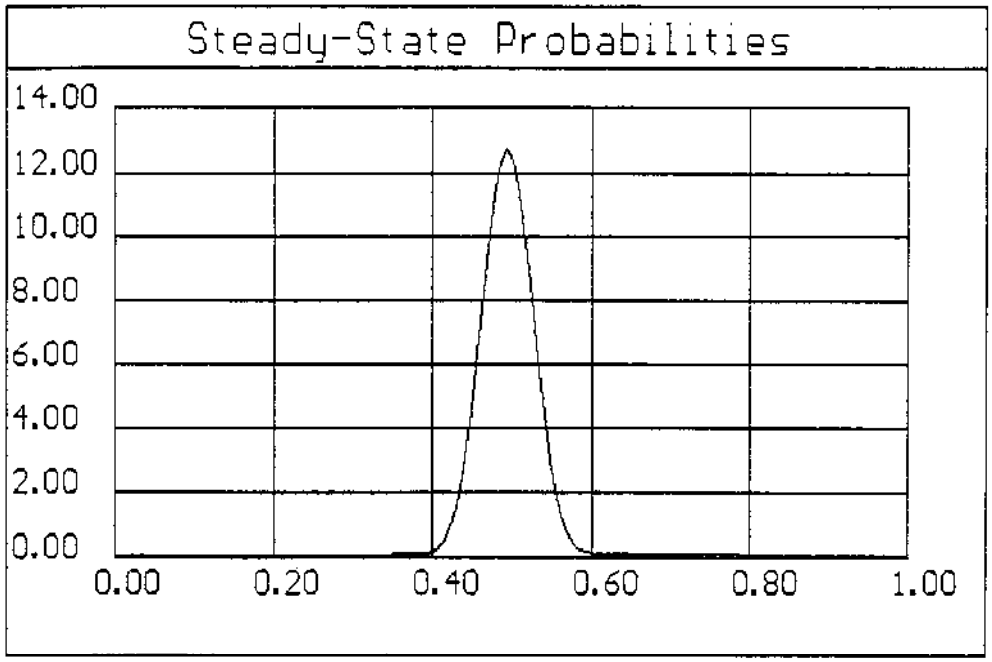

Figure A5.17 Example Calculation of Steady-State Probabilities for N=129, CNR= -2 dB

Table A5.5 First-Order Markov Symbol Tracking Loop Performance Versus CNR

CNR, dB	Mean-Time to Lock, Symbols	S.S. Tracking Std. Dev., Deg.	Mean-Time to Loose Lock, Symbols
0	71.14	13.619	5.9e21
1	59.2	12.04	3.3e24
2	55.4	11.12	1.3e32
3	51.5	10.07	> 1e35
4	51.0	10.6	> 1e35
5	47.4	9.5	> 1e35
6	46.1	9.0	> 1e35
7	44.7	8.8	> 1e35
8	44.2	8.8	> 1e35
9	43.0	8.3	> 1e35
10	41.3	7.8	> 1e35

The mean number of symbols required to achieve lock given in Table A5.5 assumes that the initial starting point for the symbol timing phase is π radians away from the steady-state locking point and is therefore an average worst-case time to achieve lock value. This quantity is plotted versus CNR in Figure A5.18 using the data provided in Table A5.5. This curve could have been made more smooth by employing longer averaging times in the phase detector S-curve calculations but nevertheless still communicates the important elements of the analysis.

Referring again to Table A5.5, the key entry is for a CNR of 3 dB which corresponds to the principle DAMA acquisition requirement at an E_b/N_o of 6 dB with rate 1/2 coding. From the table, the mean-time required to achieve lock is 51 symbol periods which is well withing the remaining preamble time available. The mean-time to loose lock is very large indicating that the quality of the lock is very high. Since the steady-state tracking error is only 10 degrees rms, reasonable bit error rate is achievable in transitioning from acquisition mode to tracking mode. We can therefore conclude that even with a first-order Markov loop implementation, initial symbol timing recovery with the proposed error metric is achievable for the AMST.

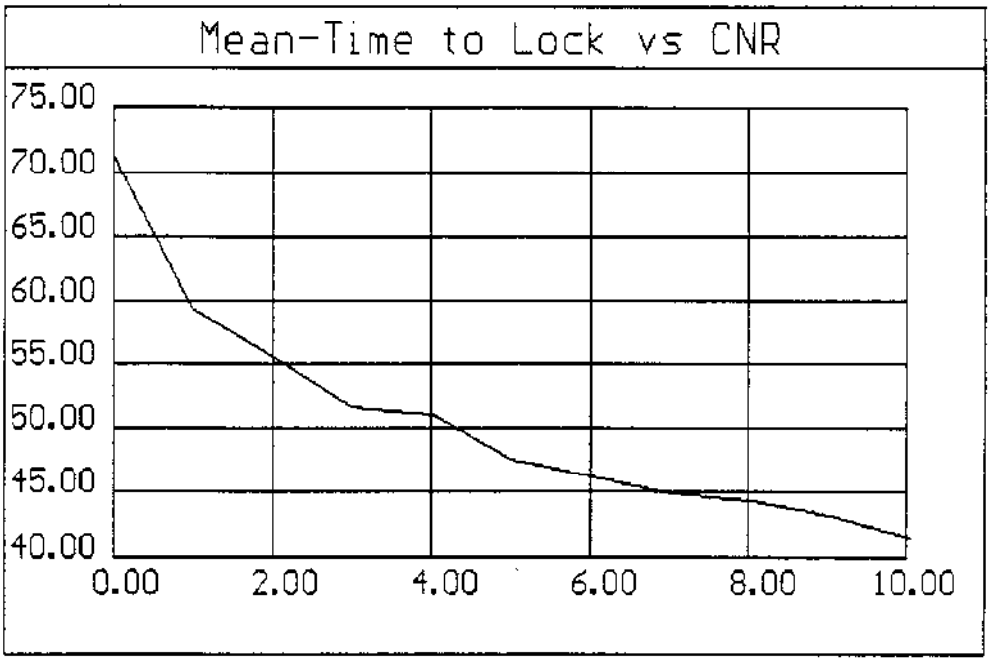

Figure A5.18 Mean-Time to Achieve Lock (Symbol Units) Versus CNR (dB). N=65.

Performance of the Phase Error Metric for Preamble Acquisition

The same type of simulation work was performed in order to investigate the performance of the second error metric during the preamble acquisition phase. Some simplification was made to the error metric (25) as given here

$$\varepsilon_c = Sign[\, I(k) + I(k-1) \,]\; [\, Q(k) + Q(k-1) \,] \qquad (45)$$

It was also noticed that the preamble data pattern is somewhat observable on this error metric output. Recognizing this periodicity, the error metric was only calculated once every two symbol periods. The calculations presented here also reflect averaging of the error metric over all possible symbol timing errors thereby confirming the algorithm's indifference to symbol timing error.

Using this error metric, the average phase detector output versus phase error (i.e., S-curve) and the state transition probability curves were calculated for several CNR values much like the work done for the symbol timing analysis. The results of these calculations for CNR values of 10 dB and 3 dB are shown in Figures A5.19 through A5.21. As shown in these figures, the error metric is unbiased and shows no thresholding effects even at 3 dB CNR. The nearly linear form of (45) is responsible for this latter result.

Since the state transition probability curves near the tracking point are quite steep even at the low CNR value, the steady-state tracking performance will be very good and on par with that observed for the symbol error metric. Compared with Figure A5.8 for the symbol error metric case, the closed-loop Markov state assessment should be even better thereby substantiating the use of this error metric for the AMST acquisition process.

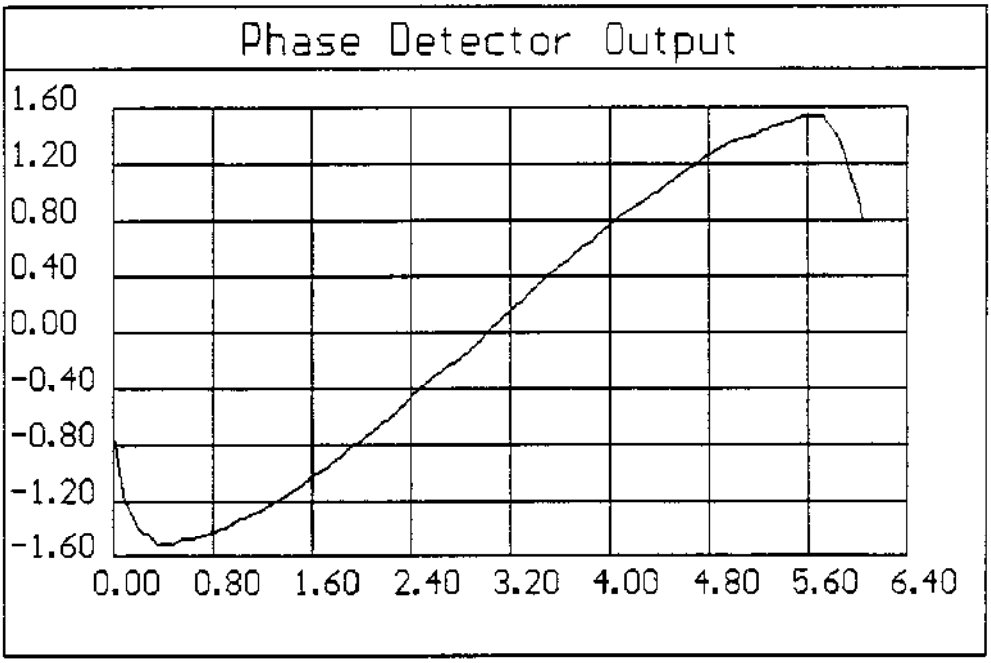

Figure A5.19 Carrier Phase Error Metric S-Curve for CNR = 10 dB

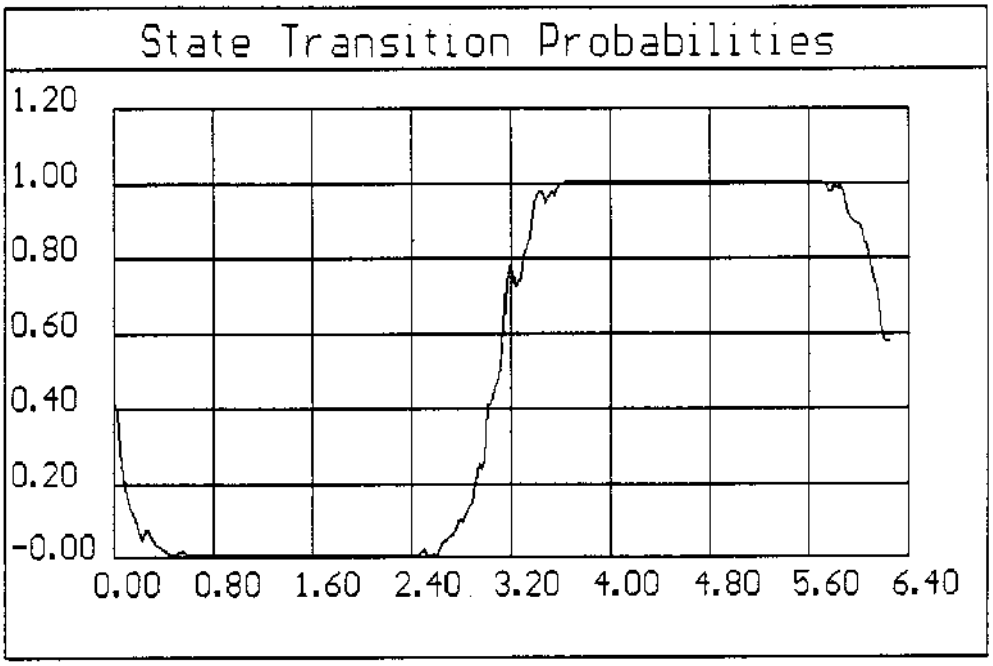

Figure A5.20 Carrier Phase Error Metric State Transition Probability Curve for CNR = 10 dB

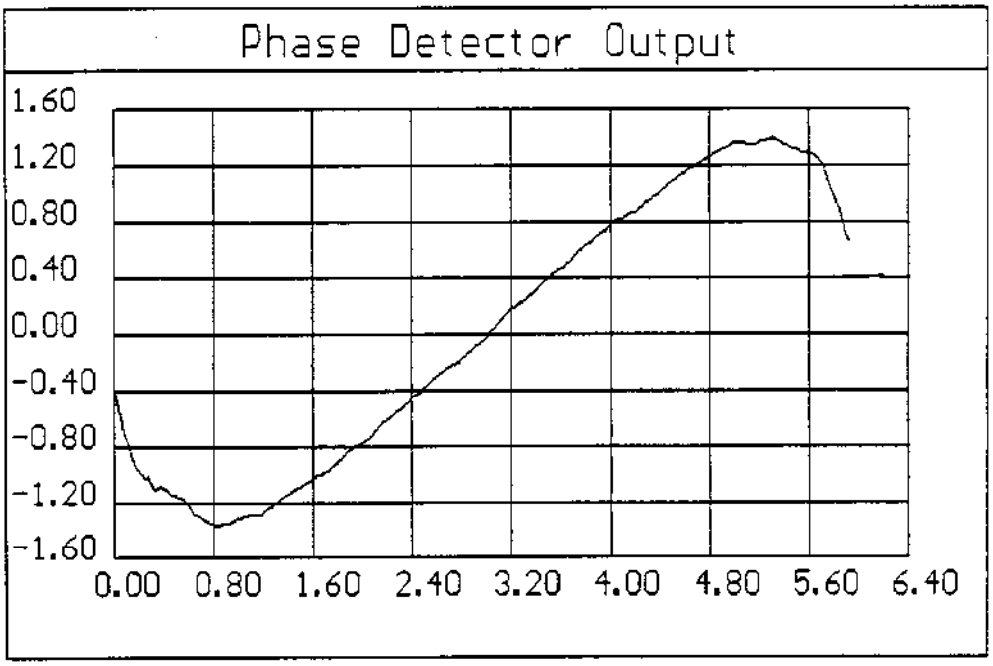

Figure A5.21 Carrier Phase Error Metric S-Curve for CNR = 3 dB

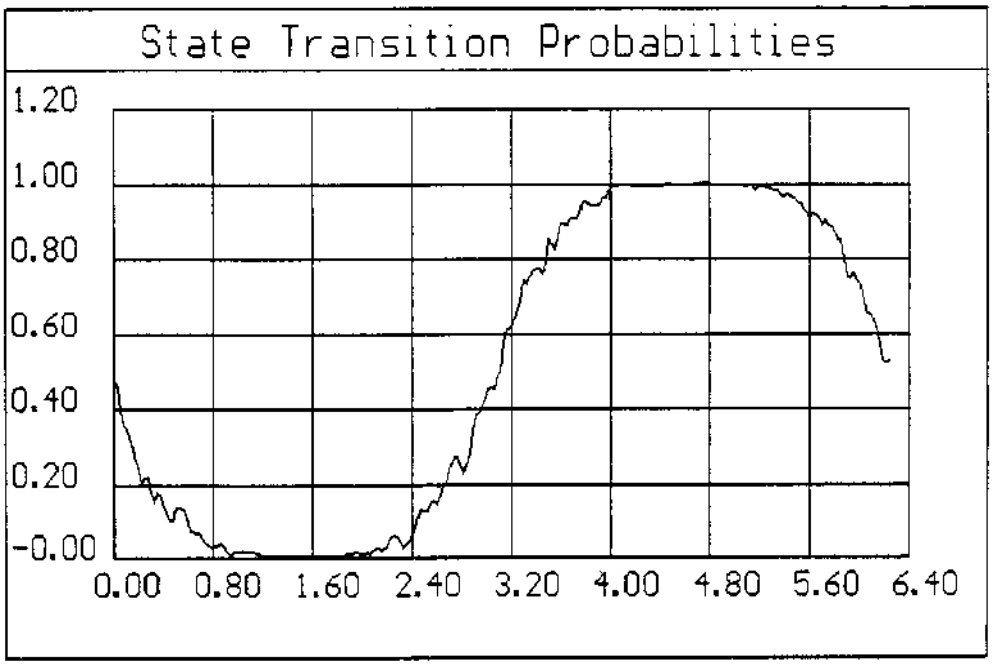

Figure A5.22 Carrier Phase Error Metric State Transition Probability Curve for CNR = 3 dB

Error Metrics for Steady-State 5 kHz DAMA Operation with Random Data

The error metrics which were just investigated are only suitable for the preamble portion of the 5 kHz DAMA waveform and alternate error metrics must be switched over to prior to the SOM unique word arrival which are suitable for operation with random data. Based upon the results presented earlier, there will be plenty of time for changing over to the new error metrics after pull-in of the symbol and carrier loops has occurred.

Due to the baseband symbol shaping used in the transmitter (TOQPSK), the recovered signal constellation at the receiver integrate-and-dump (I&D) outputs consists of the normal points seen with QPSK in addition to other constellation points arising from the shaping. This is most easily observed by examining the TOQPSK waveform shown in Figure A5.23 where the in-phase I and Q channel I&D periods are denoted by I_1 and Q_1, and the mid-phase I and Q channel I&D periods are denoted by I_2 and Q_2.

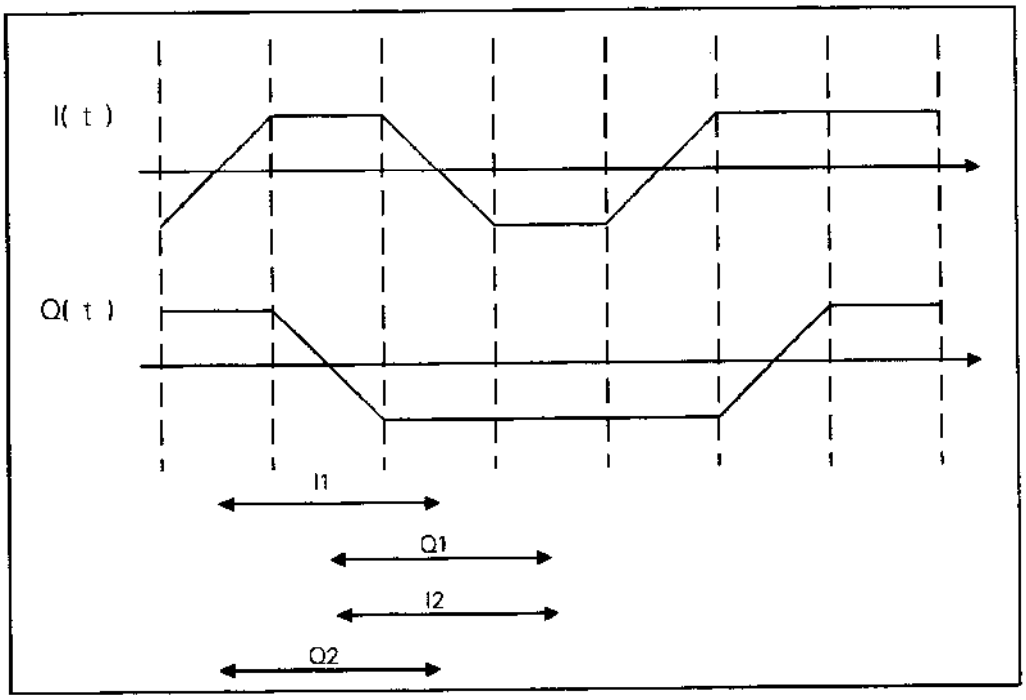

Figure A5.23 TOQPSK Baseband I and Q Channels With Integrate-and-Dump Time Periods Shown

The signal constellation points represented by choosing I_1 and Q_2 for the carrier phase error metric are shown in Figure A5.24 whereas the constellation points using I_1 and Q_1 are shown in Figure A5.25. This latter figure makes it very clear that the I_1,Q_1 choice is best suited for carrier recovery.

Even without noise and bandlimiting effects, the transmit waveshaping introduces a random phase jitter in the receiver having a peak value of 8.1° as shown in Figure A5.25. On the average however, the rms phase jitter is somewhat less at 5.76°. At a symbol rate of 600 sps, a loop bandwidth on the order of 60 Hz is still quite feasible since the resulting closed-loop phase jitter would still be only about 1° rms.

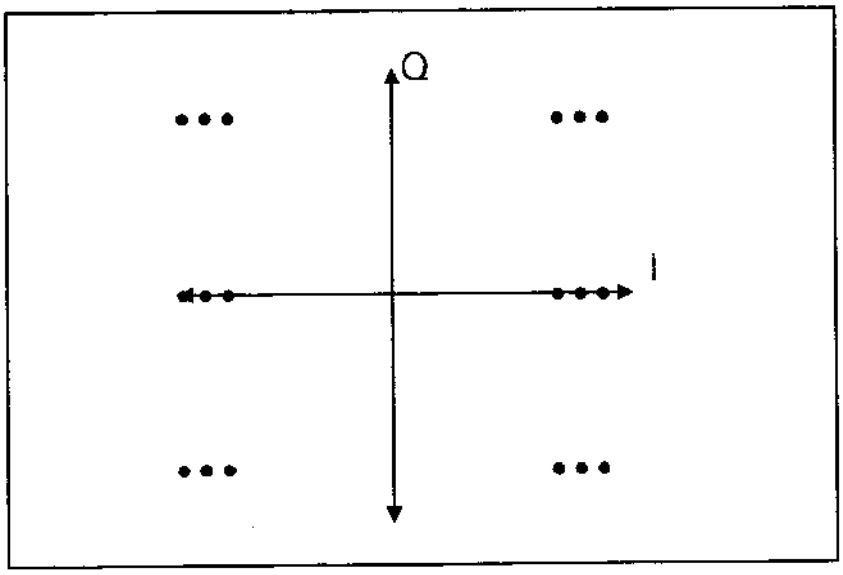

Figure A5.24 Constellation Points Given for I_1 and Q_2 Selected for Error Metric

One possible carrier phase error metric which could be used is the classical fourth-power type in which the phase error estimate is given by

$$\theta_e = 4 \tan^{-1} (Q_1, I_1) \; MOD \; 2\pi \qquad (46)$$

A simplified error metric which avoids the arctagent function can be derived by a slightly different method which calculates the angular error between each observed constellation point (represented by I,Q) and the data decisions made on these I&D output values (represented by D_i,D_q). The exact angular distance between the sample pair value and the decision point value is given by

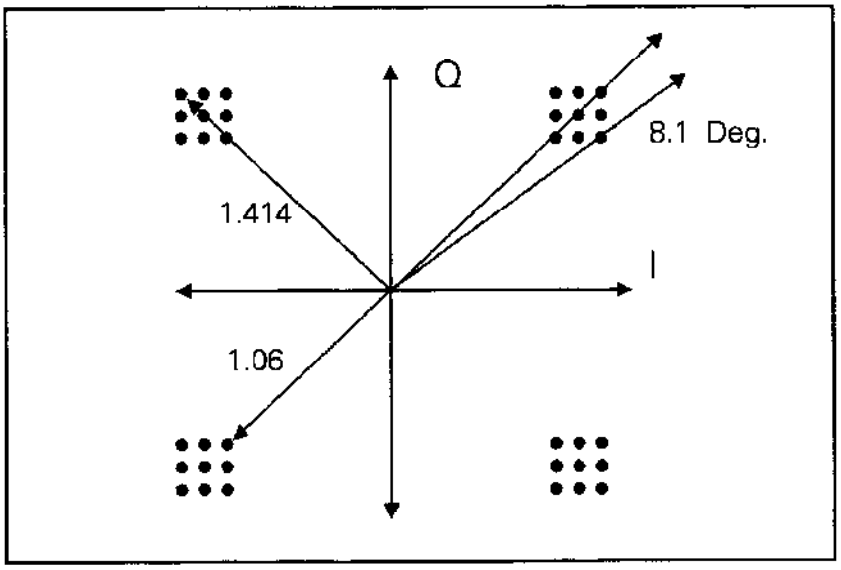

Figure A5.25 Constellation Points for I_1 and Q_1

$$\theta_e = \tan^{-1}\left[\frac{D_q I - D_i Q}{I D_i + Q D_q}\right] \quad (47)$$

which for an error metric, can be easily approximated without introducing any bias by the simplified metric

$$\varepsilon_c = D_q I - D_i Q \quad (48)$$

This formulation avoids both the division operation as well as the arctangent function and is advocated for the AMST.

The proposed symbol timing error metric is based upon tracking the mid-bit transitions shown in Figure A5.23 and is given simply by

$$\varepsilon_s = [\, I_1(k) - I_1(k+1) \,]\, I_2 + [\, Q_1(k-1) - Q_1(k) \,]\, Q_2 \qquad (49)$$

These error metrics were implemented in a computer simulation very similar to the work done earlier in order to evaluate the bit error rate performance of the tracking algorithms. The tracking loop parameters were not optimized but should be representative of the final design choices. The simulations were based upon the system shown in Figure A5.5 where the same filter parameters were used as earlier (spectral shaping: N=4 Butterworth, BT= 0.8), receiver IF: N=4 Butterworth, $B_{RF}T$= 4.0) and staggered integrate-and-dump matched filters were employed. With no noise present in the channel, the recovered signal constellation is as shown in Figure A5.26 where the intersymbol interference effects are clearly apparent. At a CNR of 10 dB (corresponding to E_b/N_o= 13 dB Rate 1/2 coded), the recovered signal constellation is as shown in Figure A5.27, dramatically degrading to the signal constellation shown in Figure A5.28 for a CNR of 3 dB.

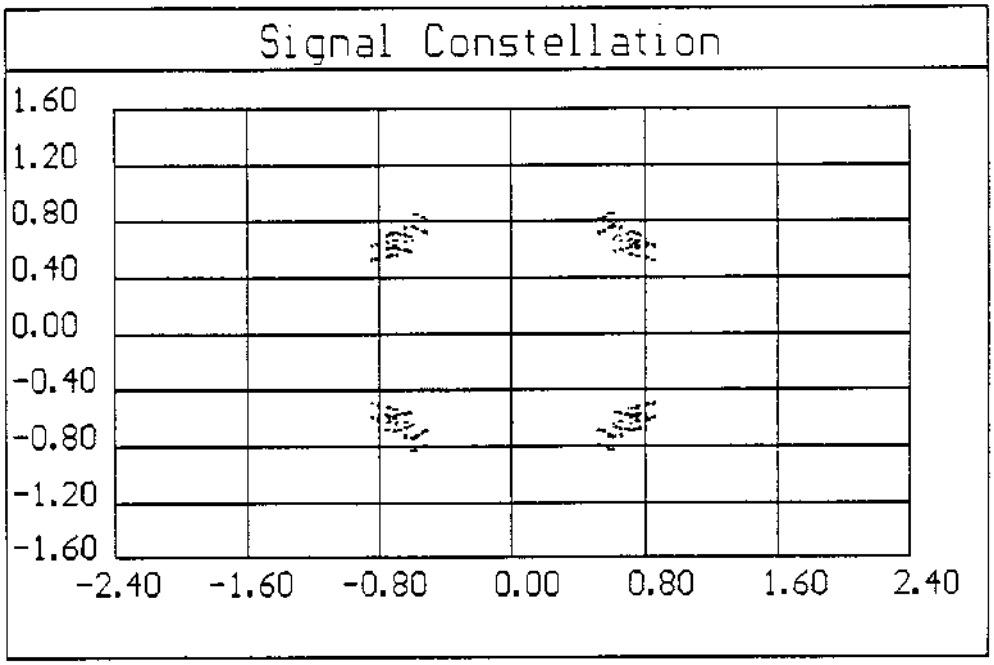

Figure A5.26 Recovered Signal Constellation at the Receiver with No Noise

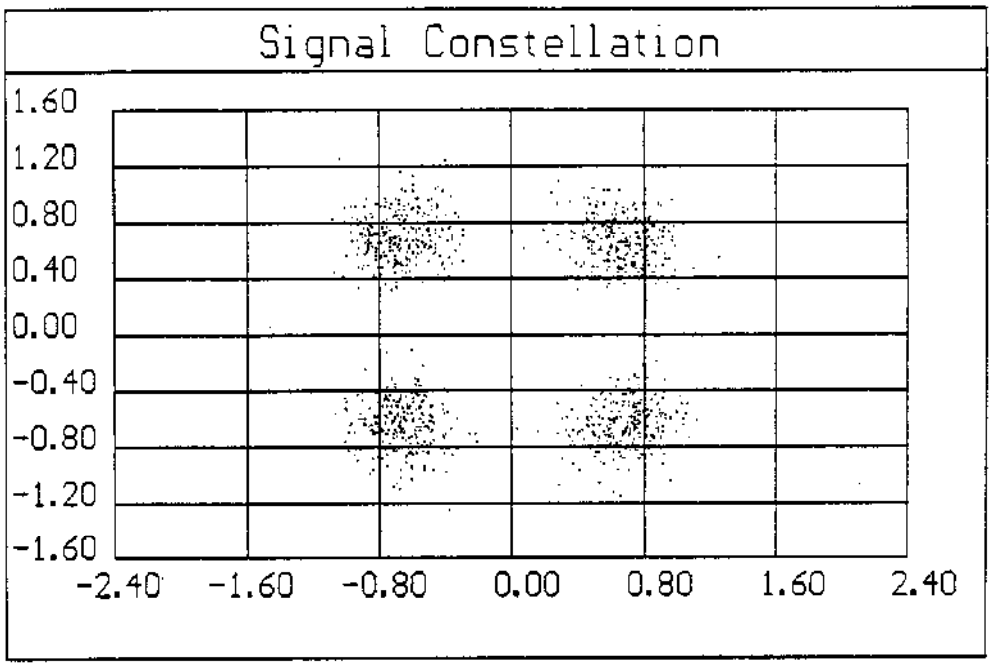

Figure A5.27 Recovered Signal Constellation at the Receiver with CNR= 10 dB

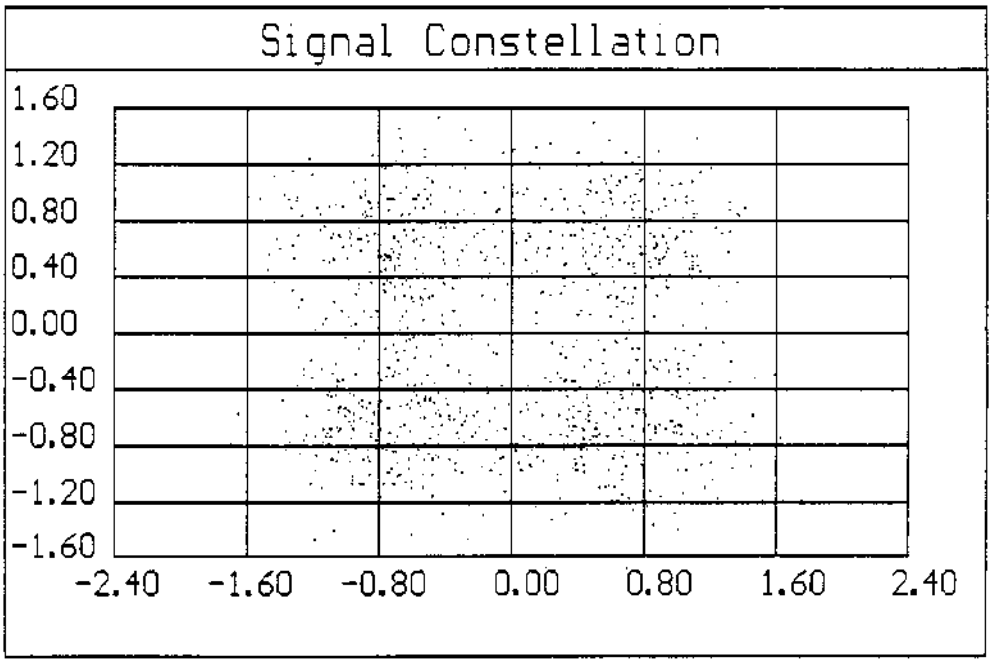

Figure A5.28 Recovered Signal Constellation at the Receiver with CNR= 3 dB

The spectral shaping impact upon the recovered signal spectrum was briefly examined by replacing the shaping filter with an N=2 Butterworth, BT= 1.5 filter thereby essentially removing any significant spectral shaping. The recovered signal constellation in this case is shown in Figure A5.29. Although less intersymbol interference is present, from comparison with Figure A5.26, the additional ISI introduced by shaping is not overly severe.

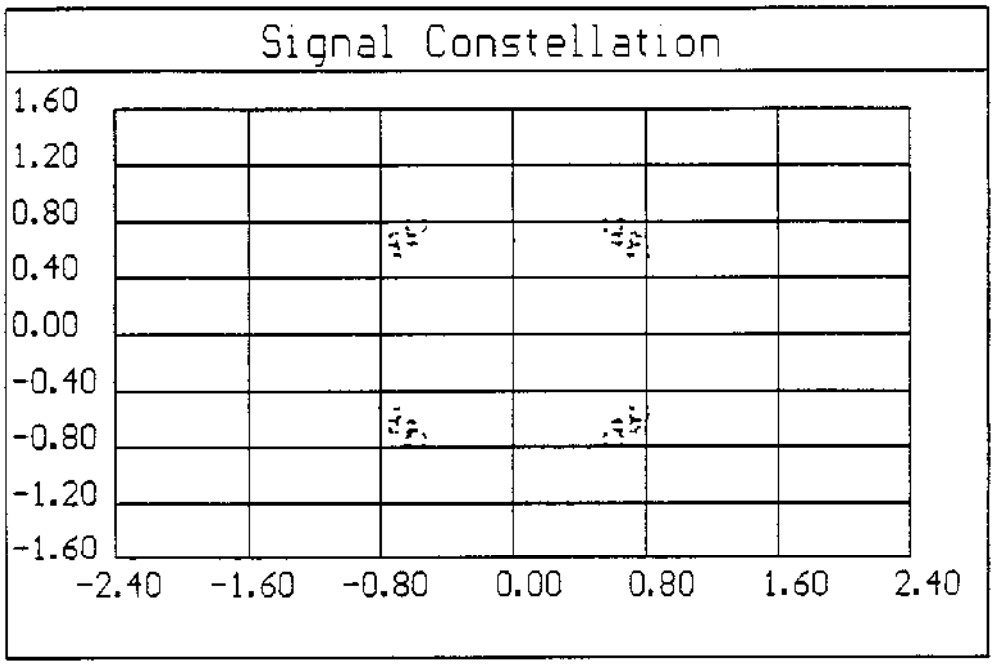

Figure A5.29 Recovered Signal Constellation at the Receiver with No Noise and N=2 Butterworth Transmit Filter

Unlike with the acquisition error metrics. the tracking error metrics are coupled. Computer simulation confirmed that the symbol tracking loop bandwidth should be made at least 2 to 4 times smaller than the carrier tracking loop in order to mitigate any interactions.

As with any low E_b/N_o system, the tracking loops must be designed properly in order to prevent serious bit error rate performance impact due to large tracking variances and/or cycle slipping. This area will receive considerably more attention in Phase II. Evenso, the tracking loop parameters were adjusted to obtain adequate slip performance and the BER calculated by simulation. Only uncoded bit error rate performance is considered here which makes E_b/N_o and CNR synonymous. The simulation results are shown with respect to theory in Figure A5.30. As expected due

to the ISI, the simulated BER points deviate from theory roughly 1.5 dB at BERs in the 10^{-5} vicinity.

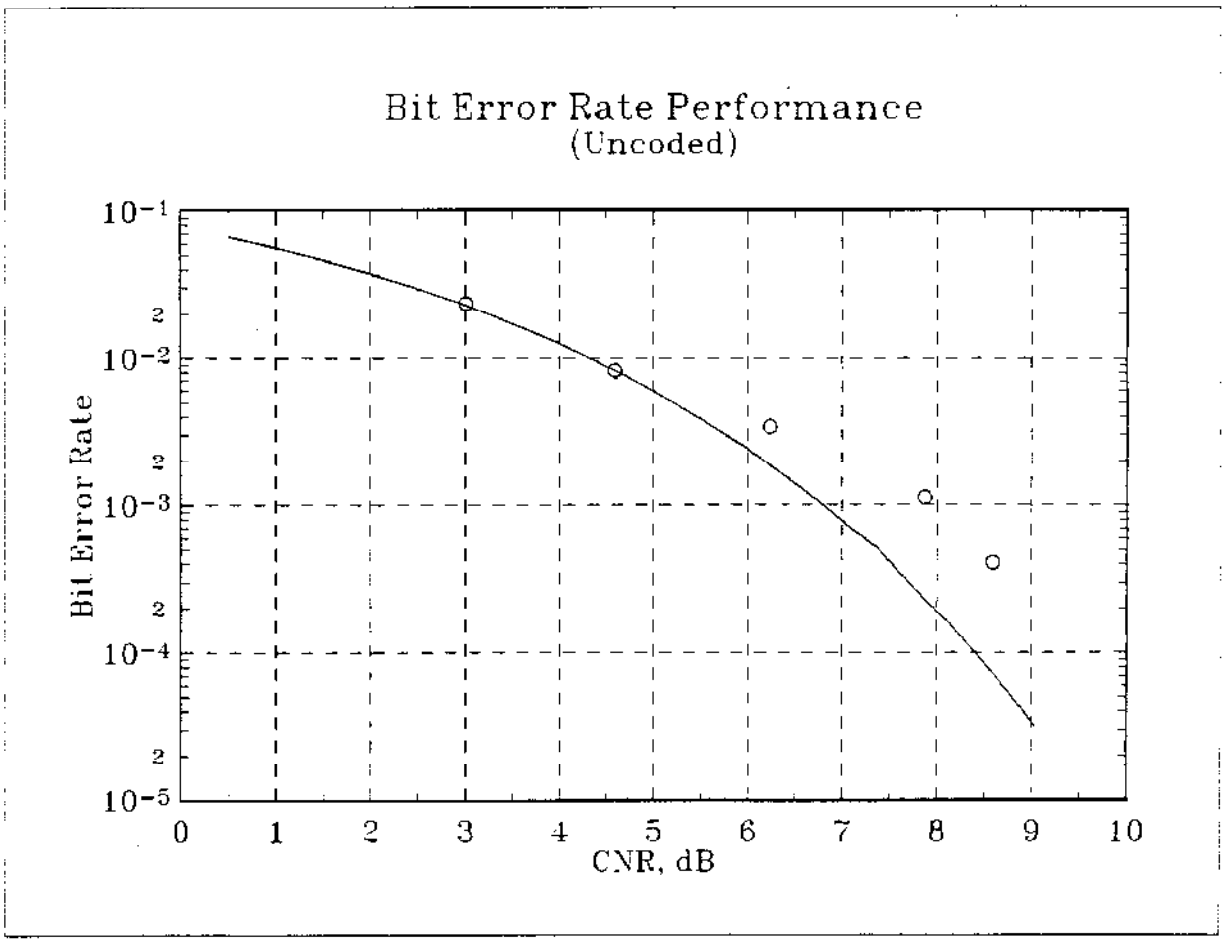

Figure A5.30 Bit Error Rate Performance (Uncoded) in Steady-State

Conclusions

Many new results have been presented in this appendix ranging from methodologies to shorten the initial DAMA net entry time, to new algorithms for implementation of acquisition and tracking modes. Computer simulation results were presented in most cases to substantiate the claims made in the text. In general, most of the key elements necessary to implement a 5 kHz DAMA digital receiver have been addressed and the viability of the proposed approach substantiated.

References

A5.1] Defense Communications Agency, "Technical Interface Specification for the 5 kHz DAMA Waveform," JTC3A Specification 9129, 14 Oct. 1990

A5.2] Meyr, H., G. Ascheid, Synchronization in Digital Communications, Vol. I, John Wiley and Sons, 1990

A5.3] Holmes, J.K., Coherent Spread Spectrum Systems, John Wiley and Sons, 1982

A5.4] Ziemer, R.E., R.L. Peterson, Digital Communications and Spread Spectrum Systems, Macmillan, 1985

A5.5] Spilker, J.J., Digital Communications by Satellite, Prentice-Hall, 1977, p. 448

A5.6] Varanasi, S., S.C. Gupta, "Statistical Analysis of Digital Phase-Locked Loops in Fading Channels," IEEE AES-20, Nov. 1984, pp. 682-692

A5.7] Varanasi, S.V., "Statistical Analysis of Zero-Crossing Sampling Digital Fading Phase-Locked Loops," Ph.D. Dissertation, SMU, 1980

A5.8] Lac, Q.T., "Mathematical Analysis of Digital Phase Locked Loops Over Fading Communication Channels," Ph.D. Dissertation, Northwestern, 1983

A5.9] McBride, A.L., A.P. Sage, "Optimum Estimation of Bit Synchronization," IEEE AES-5, May 1969, pp. 21-32

A5.10] Lindsey, W.C., Synchronization Systems in Communication and Control, Prentice-Hall, 1972

A5.11] Gardner, F.M., Phase-lock Techniques, John Wiley, 1979

A5.12] Franks, L.E., "Carrier and Bit Synchronization in Data Communication - A Tutorial Review," IEEE COM-28, Aug. 1980, pp. 1107-1121

A5.13] Moeneclaey, M., "The Optimum Closed-Loop Transfer Function of a Phase-Locked Loop Used for Synchronization Purposes," IEEE COM-31, April 1983, pp. 549-553

A5.14] , "Synchronization Problems in PAM Systems," IEEE COM-28, Aug. 1980, pp. 1130-1136

A5.15] , "A Simple Lower Bound on the Linearized Performance of Practical Symbol Synchronizers," IEEE COM-31, Sept. 1983, pp. 1029-1032

A5.16] , "A Class of Phase Detector Characteristics for Symbol Synchronizers Yielding Unbiased Estimates," IEEE COM-31, Sept. 1983, pp. 1033-1036

A5.17] , "A Comparison of Two Types of Symbol Synchronizers for Which Self-Noise is Absent," IEEE COM-31, March 1983, pp. 329-334

A5.18] , "The Influence of Four Types of Symbol Synchronizers on the Error Probability of a PAM Receiver," IEEE COM-32, Nov. 1984, pp. 1186-1190

A5.19] , "Two Maximum-Likelihood Symbol Synchronizers with Superior Tracking Performance," IEEE COM-32, Nov. 1984, pp. 1178-1185

A5.20] Waggener, W.N., "A MAP Symbol Synchronizer Implemented with Charge-Coupled Devices," IEEE COM-28, Aug. 1980, pp. 1184-1189

A5.21] Pebbles, P.Z., Communication System Principles, Addison-Wesley Publishing, 1976, p. 265

A5.22] Meyr, H., G. Aschied, Synchronization in Digital Communications, John Wiley & Sons, 1990

A5.23] Hurd, W.J., T.O. Anderson, "Digital Transition Tracking Symbol Synchronizer for Low SNR Coded Systems," IEEE COM-18, April 1970, pp. 141-147

A5.24] Lindsey, W.C., R.C. Tausworthe, "Digital Data-Transition Tracking Loops," JPL Programs Summary, 37-50, Vol. III

A5.25] Simon, M.K., "The Steady-State Performance of a Data-Transition Type of First-Order Digital Phase-Locked Loop," JPL Programs Summary, 37-66, Vol. III

A5.26] Chadwick, H.D., "Estimating the Phase of a Sampled Signal with Minimum Mean-Square Error," JPL Space Programs Summary, 37-62, Vol. III

A5.27] Moeneclaey, M., "A Class of Phase Detector Characteristics for Symbol Synchronizers Yielding Unbiased Estimates," IEEE COM-31, Sept. 1983, pp. 1033-1036

A5.28] Cessna, J.R., D.M. Levy, "Phase Noise and Transient Times for a Binary Quantized Digital Phase-Locked Loop in White Gaussian Noise," IEEE COM-20, April 1972, pp. 94-104

A5.29] Yamamoto, H., S. Mori, "Performance of a Binary Quantized All Digital Phase-Locked Loop with a Ne Class of Sequential Filter," IEEE COM-26, Jan. 1978, pp. 35-45

A5.30] Holmes, J.K., "Performance of a First-Order Transition Sampling Digital Phase-Locked Loop Using Random-Walk Models," IEEE COM-20, April 1972, pp. 119-131

A5.31] Garodnick, J., et al., "Response of an All Digital Phase-Locked Loop," IEEE COM-22, June 1974, pp. 751-763

A5.32] Kumar, R., W.J. Hurd, "A Class of Optimum Digital Phase Locked Loops," Proc. 25th Conf. Decision and Control, 1986, pp. 1632-1634

A5.33] Gupta, S.C., "On Optimum Digital Phase-Locked Lops," IEEE COM, April 1968, pp. 340-344

A5.34] Proakis, J.G., Digital Communication, 2nd Ed., McGraw-Hill, 1989

Appendix VII

AMST Frequency Synthesis

The frequency synthesis function in the AMST is very important because it is an integral part of both transmit and receive operations. This factor makes the power consumption issue particularly acute and was the primary motivation for including the fractional-N loop in the Phase I design proposal [A7.1].

The primary elements of the frequency synthesizer approach advocated in [A7.1] have been retained. Only modifications necessary to accomodate the new radio frequency plan have been made. A top level block diagram of the main frequency synthesizer module is provided in Figure A7.1.

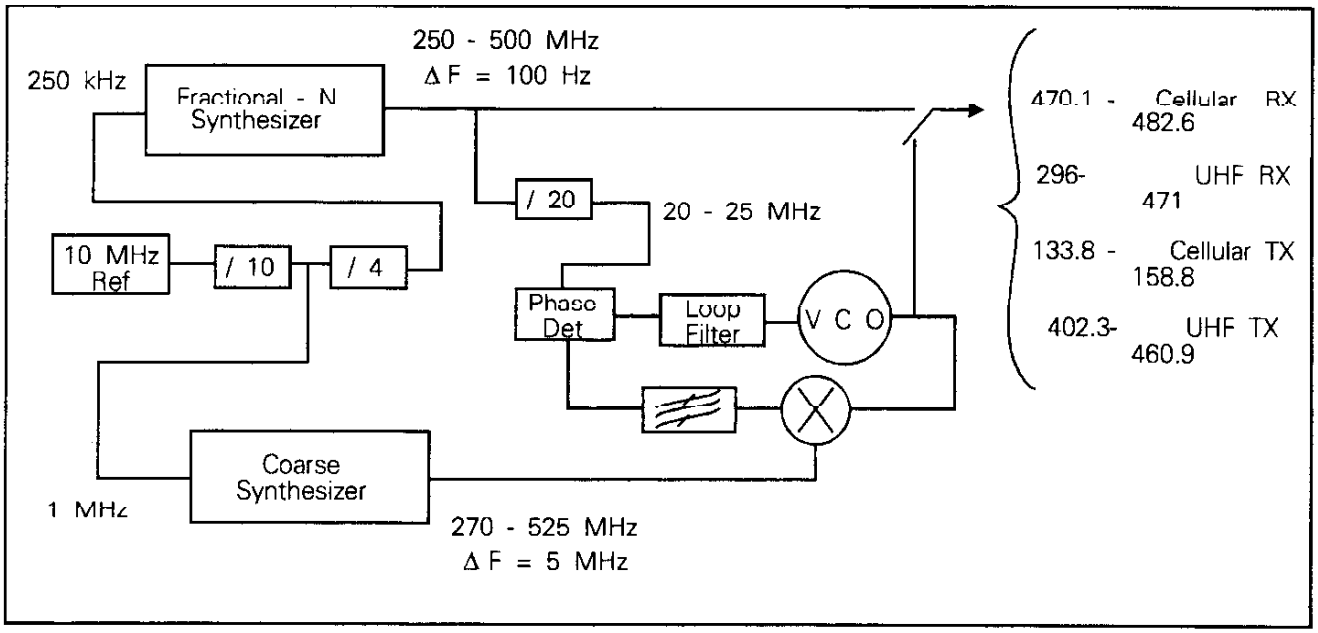

Figure A7.1 Top Level Block Diagram of the AMST Frequency Synthesizer Function

When very low power consumption operation is desired with the AMST (in receive operations primarily), the fractional-N portion of the frequency synthesizer has been designed to run stand-alone and still support the AMST synthesis requirements. Although this mode of operation will result in poorer spurious and phase noise performance, the power savings is very beneficial. The fractional-N portion of the overall frequency synthesizer is expected to consume between 0.5 and 1.0 watt maximum.

The fractional loop is designed based upon the concepts provided in Appendix VIII. Discrete spurious terms will be < -65 dBc and the close-in phase noise will be < -80 dBc/Hz. Switching speed will be < 100 μs worst case. More discussion of the fractional N loop is provided later in this appendix.

The remaining portions of the synthesizer will be operational primarily when stringent cosite operation is required. As discussed in Appendix XII, cosite operation requires very good phase noise performance from the transmit local oscillator (LO) source, and the receive LO function must also be very clean in order to prevent reciprocal mixing problems. To achieve these objectives, the high performance synthesizer consists of three separate phase-locked loops as shown in Figure A7.1.

The coarse frequency synthesizer is designed to have frequency steps of 5 MHz at its output and its close-in phase noise performance will be < -96 dBc/Hz. Since the fractional-N loop output is divided down by a factor of 20, its close-in phase noise level is reduced from 80 dBc/Hz to roughly -106 dBc/Hz thereby making its contribution at the output negligible. Therefore, the output phase noise spectrum from the triple loop configuration is determined primarily by the coarse synthesizer for small offset frequencies and by the summing phase-locked loop for large frequency offsets. Of the three oscillators involved, only the sum loop VCO must be of exceptional quality as far as large offset phase noise is concerned.

The sum loop purposely uses a reference frequency of 20 to 25 MHz in order to simplify the hardware which must be present in order to insure that the sum loop locks to the proper mixer output product. If a lower frequency range were to have been used (e.g., 5 to 10 MHz), additional circuitry would be required. One alternative which is attractive if necessary is the quadricorrelator concept which is given in [A7.2].

Spurious and Phase Noise Requirements for the AMST Frequency Synthesizer

For the symbol rates used in the AMST, the close-in phase noise and discrete spurious requirements are primarily driven by the systems-level bit error rate (BER) requirements, yielding moreso to cosite considerations for larger frequency offsets. Since the cosite performance is heavily dependent upon the receiver preselection filtering and the transmit filtering (Appendix XII), no explicit requirements for phase noise and spurious requirements can be established until the R/T front-end filtering has been designed in detail. It is however possible to establish at least initial guidelines based upon BER performance for close-in phase noise requirements. Of course, the AMST must also satisfy the spurious requirements given in MIL-STD-461.

Over specification of synthesizer spectral requirements has been a common occurrence in many systems present in the field today. This has often resulted from system designer unfamiliarity with RF issues leading ultimately to higher cost and complexity than really required. In principle, this should be avoided in the AMST because over specification also leads to increased power consumption within the radio.

One of the major themes used throughout the AMST concept is the idea of frequency re-use. Every attempt has been made to use the minimum number of LOs in the radio as possible in order to keep cost and internal electromagnetic interference (EMI) issues to a minimum. In this context, the main frequency synthesizer output is used to support both the UHF and cellular receive and transmit functions as shown in Figure A7.2.

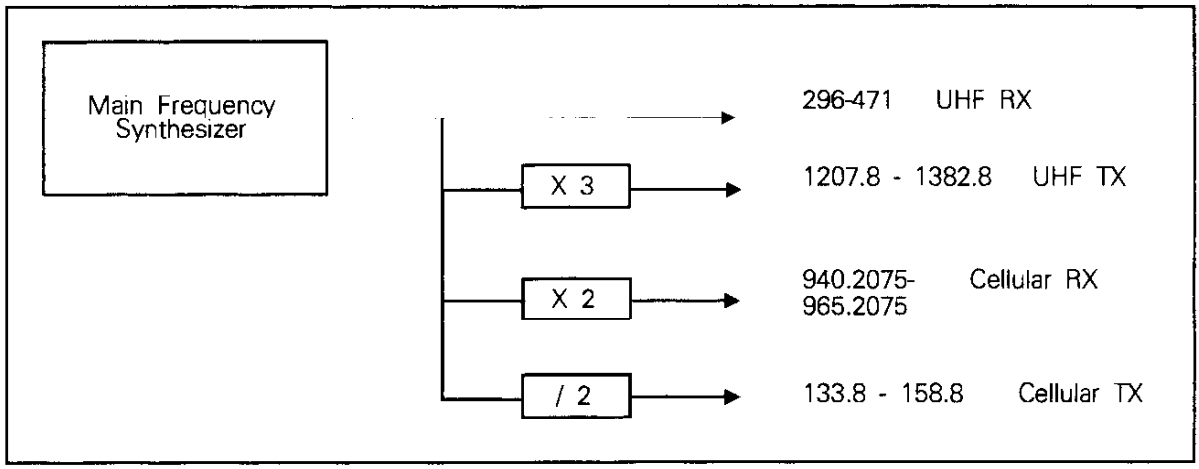

Figure A7.2 Main Frequency Synthesizer Re-Use Within the AMST

Based upon Figure A7.2, the main frequency synthesizer output may be multiplied up by as much as a factor of 3 which increases the output phase noise content by 9.5 dB in order to support the UHF transmit function. Other measures could have been taken to reduce or eliminate this increased noise, but the added hardware required was traded off in favor of this approach.

From a systems perspective, a number of factors serve to reduce the synthesizer phase noise requirements compared to what might normally be specified. These factors include:

- Cosite receiver preselection filtering
- Cosite transmitter post-driver filtering
- Carrier recovery loop tracking
- Waveform selection (e.g., DQPSK)

Each of these issues are elaborated upon next.

Transmit and receive filtering as described in Appendix XII for cosite operation significantly reduce the synthesizer spectral requirements for large frequency offsets. This subject has been addressed as far as possible without actually entering into the detailed design of the filtering elements involved.

Carrier recovery tracking which must be present for all coherent modulation types (e.g., BPSK) will track out much of the phase noise falling within its closed loop bandwidth thereby reducing the phase noise requirements close to the carrier center frequency. If the carrier loop is a classical type 2 having a natural frequency of ω_n and a damping factor of ζ, the effective phase noise spectrum of the receiver's LO is given by

$$\mathcal{L}_{eff}(f) = \mathcal{L}(f) \left[\frac{\omega^4}{(\omega^2-\omega_n^2)^2 + (2\zeta\omega_n\omega)^2} \right] \qquad (1)$$

where $\mathcal{L}(f)$ is the total receiver phase noise associated with frequency translation within the radio.

Phase noise performance for the synthesizer should also consider the type of waveform being utilized as well as the symbol rate employed. Noncoherent communication waveforms such as DQPSK or noncoherent FSK are much more phase noise tolerant than are most coherent waveforms, and these factors should be included.

A number of these forementioned issues are addressed in the balance of this appendix. Much more work will be required in this area to support the detailed design effort which follows in Phase II.

Phase Noise Basics for Digital Communication

The following material provides some of the background which will be needed to fully specify the spurious and phase noise requirements for the AMST frequency synthesizer. Many of the formula have been previously incorporated into computer-aided design tools at ComFocus. These design tools will be utilized during the detailed design elements of Phase II to properly specify the design guidelines for the frequency synthesizer.

To start, several definitions for key quantities must be given:

f — The frequency difference between a specified frequency component and a carrier center frequency f_o, Hz.

$S_\phi(f)$ — The one-sided spectral density of phase fluctuations, one-sided because it is only defined for $0 < f < \infty$. The quantity has units of rad^2/Hz and is measured by passing the signal of interest through a linear phase detector and measuring the power spectral density at the detector output.

$\mathcal{L}(f)$ — The normalized frequency domain representation of phase fluctuations in a 1 Hz bandwidth at an offset of f Hz from the carrier. This quantity has units of Hz^{-1} and is often expressed as dBc/Hz. It is the ratio of the power spectral density in one phase modulation sideband, referred to the carrier frequency on a spectral density basis, to the total signal power. It is a 2-sided spectral density which is defined over the range $-f_o < f < \infty$. For small phase modulation,

$$\mathcal{L}(f) = \frac{S_\phi(f)}{2} \qquad (2)$$

In order to demonstrate these quantities more practically, we can consider a sinusoidal phase noise component at an offset of f Hz having a peak phase deviation of $\Delta\varphi$ radians. The signal may be represented mathematically as

$$s(t) = A\cos\left[\, 2\pi f_o t + \Delta\phi \sin(2\pi f t) \,\right] \qquad (3)$$

For small $\Delta\varphi$, this may be approximated as

$$s(t) \approx A\left\{ \cos(2\pi f_o t) - \frac{\Delta\phi}{2}\left[\cos(2\pi(f-f_o)t) - \cos(2\pi(f+f_o)t) \right]\right\} \quad (4)$$

and the modulation sidebands are clearly apparent. Spectrally, this appears as shown in Figure A7.3.

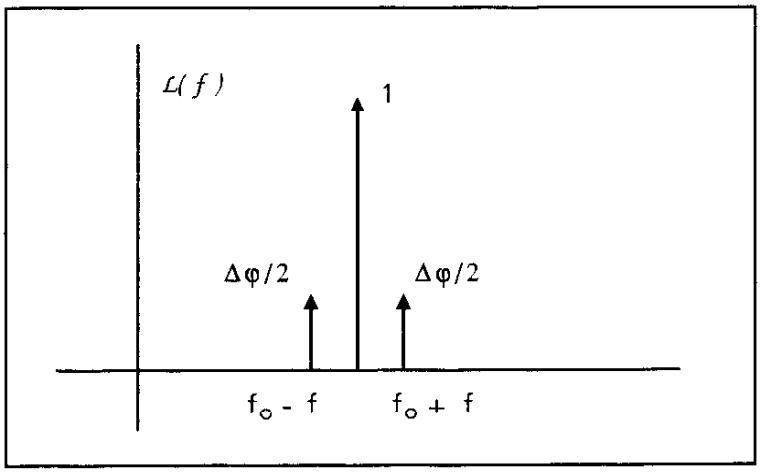

Figure A7.3 Sinusoidal Phase Noise Sidebands

The sidebands are actually 180 degrees out of phase with respect to eachother, each having an amplitude with respect to the carrier of $\Delta\varphi/2$ therefore giving $\mathcal{L}(f) = 20\ \mathrm{Log}_{10}(\ \Delta\varphi/2\ )$ if the signal is assumed to occupy 1 Hz bandwidth. In contrast, passing s(t) through an ideal phase detector results in an output power or variance which given by

$$S_\phi(f) = \mathcal{E}\{[\ \Delta\phi \sin(2\pi f t)\ ]^2\} = \frac{(\Delta\phi)^2}{2} \quad (5)$$

which finally leads to $S_\varphi(f) = \mathcal{L}(f) + 3$ dB as contended earlier.

Given a local oscillator description in terms of a spectral density $\mathcal{L}(f)$ or $S_\varphi(f)$, measures are needed to ascertain the phase noise impact upon the system BER. The performance loss resulting from less than ideal local oscillator phase noise is manifested in three separate terms for coherent communications: (i) a phase modulation (PM) spreading loss, (ii) a coherence loss associated

with the carrier recovery process, and (iii) an additive noise loss associated with the detection process itself.

In order to investigate the PM spreading loss, assume that we have a generalized LO signal which is represented as

$$s(t) = \sqrt{2}\ \cos(\ 2\pi f t + \theta(t)\ ) \tag{6}$$

or in complex form

$$s(t) = \sqrt{2}\ Re[\ e^{j2\pi f t}\ e^{j\theta(t)}\ ] \tag{7}$$

The autocorrelation function of s(t), assuming that $\theta(t)$ is a wide-sense stationary random process, is given by

$$\begin{aligned} R_s(\tau) &= Re\{\ e^{j2\pi f\tau}\ \mathbf{E}[\ e^{j\theta(t)-j\theta(t+\tau)}\ ]\ \} \\ &= Re\{\ e^{j2\pi f\tau}\ [\ 1 - R_\phi(0) + R_\phi(\tau)\ ]\ \} \end{aligned} \tag{8}$$

leading to

$$R_s(\tau) = [\ 1 - R_\phi(0)\ ]\cos(2\pi f\tau) + R_\phi(\tau)\cos(2\pi f\tau) \tag{9}$$

The PM spreading loss is then given by

$$L_{PM} = 10\ Log_{10}[\ 1 - R_\phi(0)\ ] \tag{10}$$

The second term in (9) shows that the phase noise causes an additional cross product term between the incoming signal spectrum and that of the local oscillator. This effect is somewhat less in magnitude than the spreading loss because the output noise spectrum (due to the convolution of the noise and signal spectrums) is significantly wider than the principle term.

The coherence loss occurs because the carrier tracking loop cannot perfectly track the suppressed signal carrier in the presence of noise. Generally, the probability density function for the phase estimation error θ is taken to be the probability density function found by Viterbi for a first-order phase-locked loop which is given by

$$p(\theta) = \frac{e^{\alpha\cos(\theta)}}{2\pi I_o(\alpha)} \tag{11}$$

where α is the signal to noise ratio of the phase reference in the phase recovery loop given by

$$\alpha = \frac{A^2}{N_o D_L} \tag{12}$$

and I_o is the zeroth-order modified Bessel function. For the shaped waveforms (e.g., TOQPSK for 5 kHz DAMA), additional noise results in the system due to intersymbol interference (ISI) which makes the transition probability/Markov analysis approach used in Appendix V must more representative of the true performance.

Given that the probability density function for θ is available, the BER can then be calculated as

$$P_b = \int_{-\pi}^{\pi} P(E|\theta)\ p(\theta)\ d\theta \tag{13}$$

where $P(E|\theta)$ is the marginal probability of a bit error given a carrier reference phase error of θ. All of this work plus the inclusion of the symbol timing errors were partially addressed in Appendix V. In summary, very good carrier loop SNR is needed in order to keep the coherence losses small. The detection loss for a number of waveform types versus loop SNR is shown in Figure A7.4 for an E_b/N_o of 7 dB. For QPSK waveforms, a loop SNR in excess of 22 dB is highly desirable as shown.

Finally, the additive phase noise impairment can be computed based upon the standard E_b/N_o formula such as

$$\begin{aligned} P_b &= Q\left(\sqrt{\frac{2E_b}{N_o}}\right) \quad \textit{for BPSK} \\ &= Q\left(\sqrt{\frac{E_b}{N_o}}\right) \quad \textit{for FSK} \end{aligned} \tag{14}$$

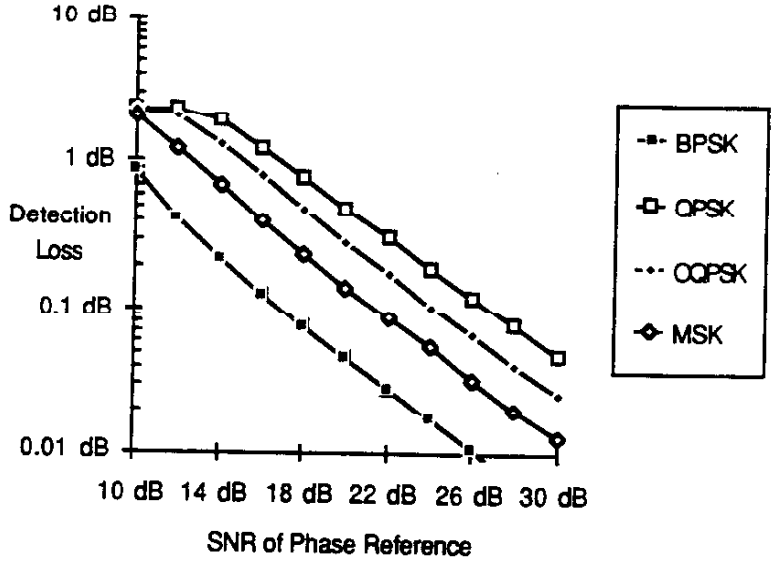

Figure A7.4 Detection Loss Versus Carrier Loop SNR for E_b/N_o = 7 dB [A7.3]

and etc.. Since the receiver detector cannot differentiate between phase noise due to a low E_b/N_o signal and poor LO phase noise performance, any LO phase noise effectively power-adds to the phase noise observed on the incoming signal. Given that the equivalent noise bandwidth of the integrate-and-dump matched filter used for the coherent waveforms is 1/2T Hz, the total integrated phase noise from the carrier loop bandwidth edge to 1/2T Hz should be kept as small as possible.

Noncoherent waveforms are generally more tolerant to low offset phase noise components. Rather than be concerned over the total integrated phase noise, waveforms such as DQPSK look for the change in phase over each symbol period. In this case, the quantity of interest is the accumulated phase due to noise over an individual symbol period which may be calculated as

$$\sigma_\Delta(\tau) = 2 \left[R_\theta(0) - R_\theta(\tau) \right]_{\tau=T} \qquad (15)$$

finally leading to

$$\sigma_\Delta^2 = 8 \int_0^\infty S_\phi(f) \sin^2(\pi f \tau) \, df \qquad (16)$$

Here again, σ_Δ^2 should be small.

In conclusion, more detailed analysis will be required in Phase II to establish phase noise requirements for the different waveforms used. In the short term, the QPSK waveform assumption can be used to ascertain the probable worst case requirements as discussed next.

Requirements

With this material as background, it is possible to finally establish some design guidelines for the AMST close-in phase noise requirements. At present, the most stringent signal constellation in the AMST is for QPSK and this waveform can be assumed to dictate the worst case close-in phase noise requirements for the radio. If we desire that the LO phase noise (actually from all of the radio LOs in the radio combined) contribution degrade the E_b/N_o performance less than 0.05 dB with respect to theory at an operating E_b/N_o of 10 dB, the total integrated phase noise must be less than -30 dBc. The range of integration is from the carrier loop bandwidth edge to the symbol rate. Since this requires that the carrier recovery loop parameters be known first, for the time being, we will take the lower edge to simply be 1.3% of the symbol rate. This is based upon signal reception at a CNR of 3 dB and maintaining a carrier recovery loop SNR of 22 dB which is required to keep the coherence detection losses less than 0.5 dB for QPSK.

If the overall phase noise performance for the frequency synthesizer can be approximated as shown in Figure A7.5, the integration is particularly simple and given as

$$\sigma^2 = \int_{f_L}^{f_H} 2 \, \mathcal{L}(f) \, df$$

$$= 2 \int_{f_L}^{f_H} \frac{L_o}{1 + \left(\frac{f}{f_c} \right)^2} \, df \qquad (17)$$

which simplifies to

$$\sigma^2 = 2L_o\, f_c \left[\tan^{-1}\left(\frac{f_H}{f_c}\right) - \tan^{-1}\left(\frac{f_L}{f_c}\right) \right] rad^2 \qquad (18)$$

For FM reception, normally a residual FM requirement applies. Given the same spectra shown in Figure A7.5, the variance of the residual FM is given by

$$\sigma_f^2 = 2L_o \int_{f_L}^{f_H} \frac{f^2}{1 + \left(\frac{f}{f_c}\right)^2}\, df \qquad (19)$$

$$= 2L_o f_c^2 \left\{ f_H - f_L - f_c \left[\tan^{-1}\left(\frac{f_H}{f_c}\right) - \tan^{-1}\left(\frac{f_L}{f_c}\right) \right] \right\} rad^2$$

These formula may be used to assess the baseline frequency synthesizer design which is presented next.

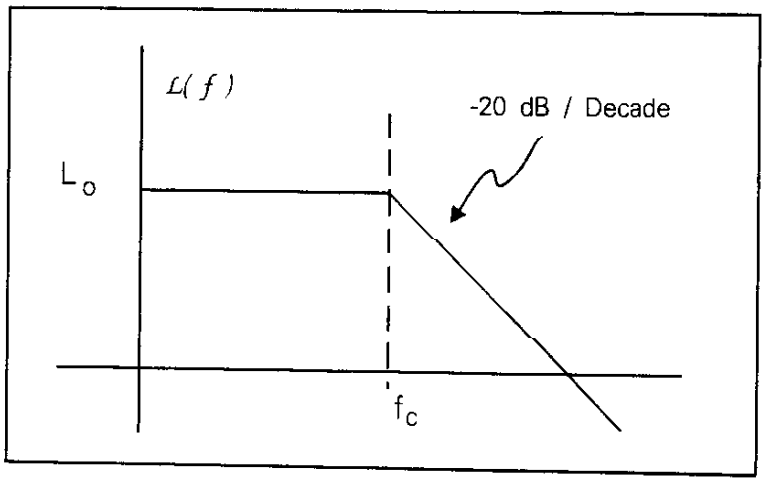

Figure A7.5 Output Phase Noise Approximation

Baseline Frequency Synthesizer Design

The top level description of the frequency synthesizer design is shown in Figure A7.1. Each of the major elements will be described here.

Fractional-N Loop

The fractional-N loop design is again based upon the concepts discussed in Appendix VIII. ComFocus went so far as to completely design the digital portion of the loop in an Actel because originally, a prototype of it had been planned for inclusion in this report. Due to limitations within the Actel device which resulted in the digital portion growing beyond a single Actel device, these plans were tabled. The final digital design consisted of 1 Actel FPGA, 2 PLDs, and 3 external hex counters as shown in Figure A7.6. The analog portion of the loop design was not completed because the final design was more complicated than what could be evaluated within the present contract.

A block diagram for the digital portion of the fractional-N loop representing the circuitry shown in Figure A7.6 is provided below in Figure A7.7. This digital design only includes the necessary complexity to support fractional-N parts as small as 0.001 whereas the final AMST must support smaller fractions. This approach would still have allowed us to fully demonstrate the fractional-N concepts however since even the AMST will only include 3 decades of fractional-N correction circuitry as planned here.

The fractional-N loop uses a reference frequency of 250 kHz which is high by fractional-N loop standards. This choice was made based upon phase noise constraints and was only possible by taking advantage of several key concepts presented in Appendix VIII. Assuming that the fractional-N correction can be done reliably to a level of -60 dBc correction residual, the white noise equivalent noise floor due to the fractional-N process is given roughly by

$$\begin{aligned} Floor &= -60\ dBc - 10\ Log_{10}(\ 250\ kHz\ ) \\ &= -114\ dBc/Hz \end{aligned} \qquad (20)$$

Assuming the typical phase detector noise floor level of -150 dBc/Hz and given that the minimum feedback divider ratio is 1000, the phase detector noise floor reference to the synthesizer output is $-150 + 20\ Log_{10}(1000) = -90$ dBc/Hz. Therefore, any (white) noise arising from the fractional-N process will be completely obscured by the reference noise at the loop output.

Discrete spurious from the fractional-N loop must be kept low also, ideally < -65 dBc. The prototype design provides 3 decades of

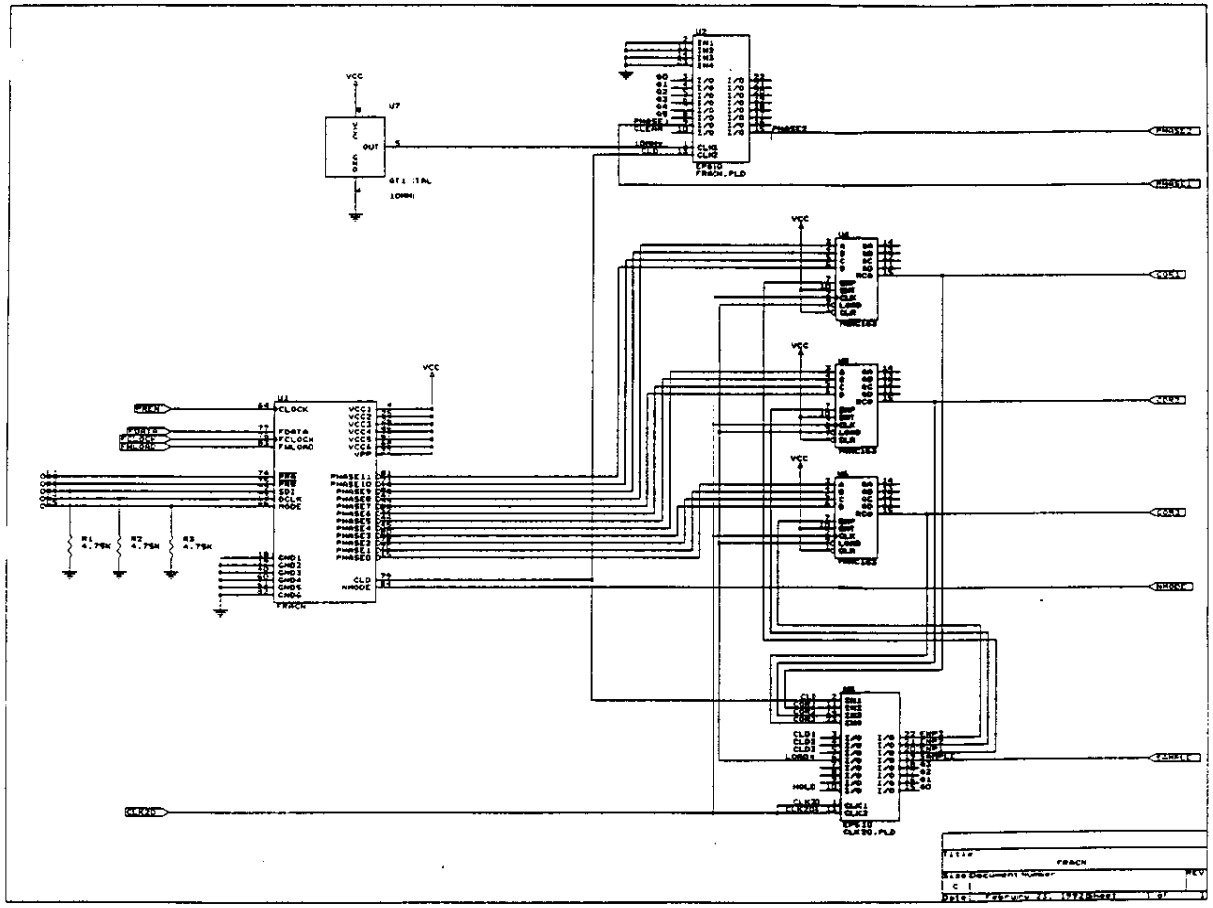

Figure A7.6 Orcad Schematic of Fractional-N Loop Digital Portion

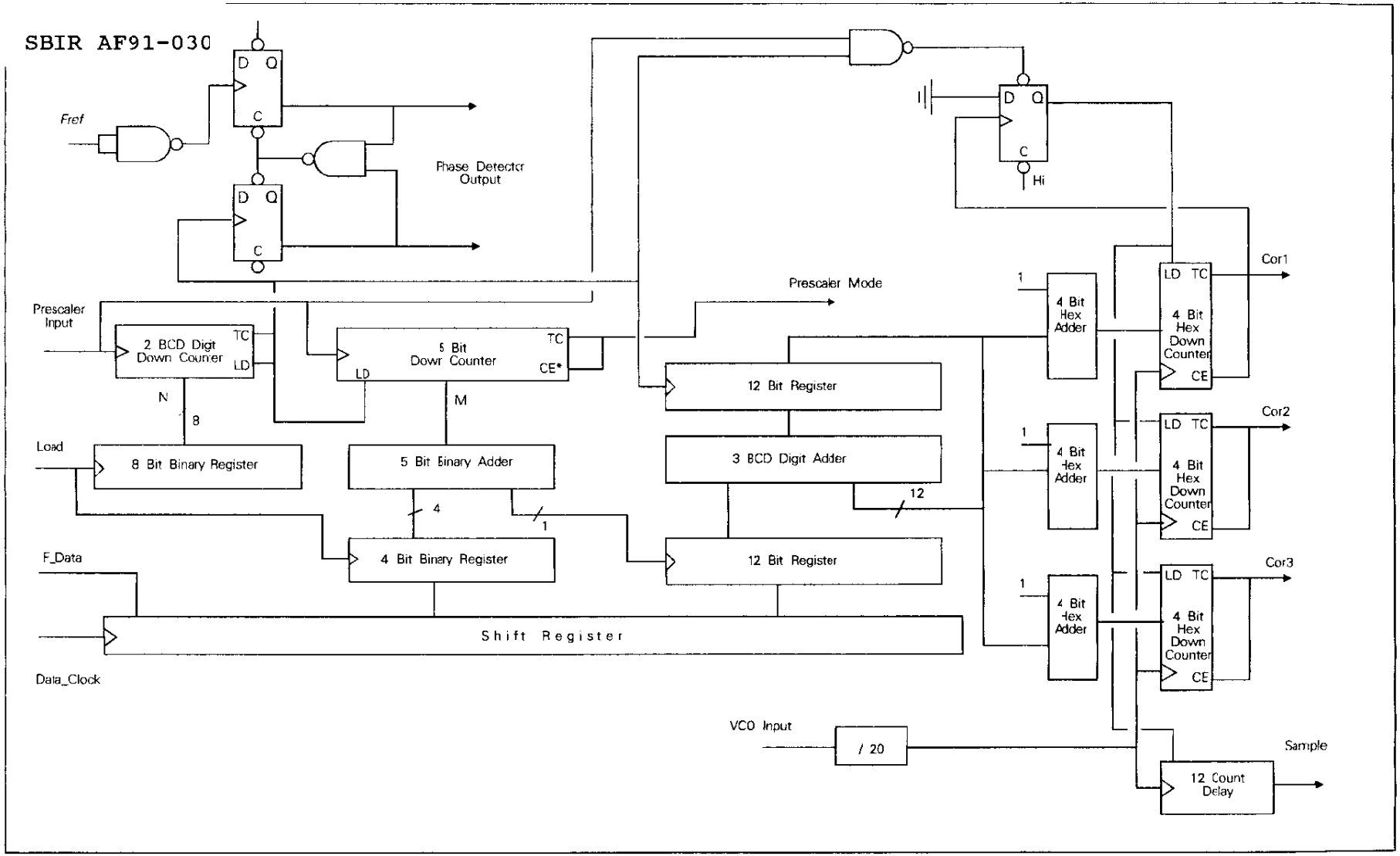

Figure A7.7 Block Diagram for Digital Portion of Fractional-N Loop

fractional-N correction which will attain this objective. The AMST fractional-N loop will also include noise shaping as described in Appendix VIII which will eliminate any real possibility of discrete spurs occuring at the fractional loop output.

The fractional-N loop is configured as a type-1 control loop and utilizes a sample-and-hold phase detector. This architecture is shown in Figure A7.8. It can easily achieve steady-state phase lock to within several degrees of phase within 50 μs. The third-order elliptic filter is used to provide a minimum of 30 dB additional attenuation to the sampling spurs.

Based upon the work provided in [A7.4], the ideal type-1 loop which utilizes a sample-and-hold phase detector has a transient frequency error response which is geometric rather than exponential, the key parameter being the quantity $K = K_d K_v T/N$ where K_d is the phase detector gain in volts per radian, K_v is the VCO sensitivity in radians per second per volt, N is the feedback divider ratio, and T is reference frequency period. In order to have a damped response, ideally $K \leq 1$. K must be less than 2 for stability. Given a step change in N which is equivalent to a step change in VCO output frequency of Δf, the frequency error as a function of sample number index n reduces as

$$f_{err} = \Delta f \left[1 - \frac{K_d K_v}{N} T \right]^n \qquad (21)$$

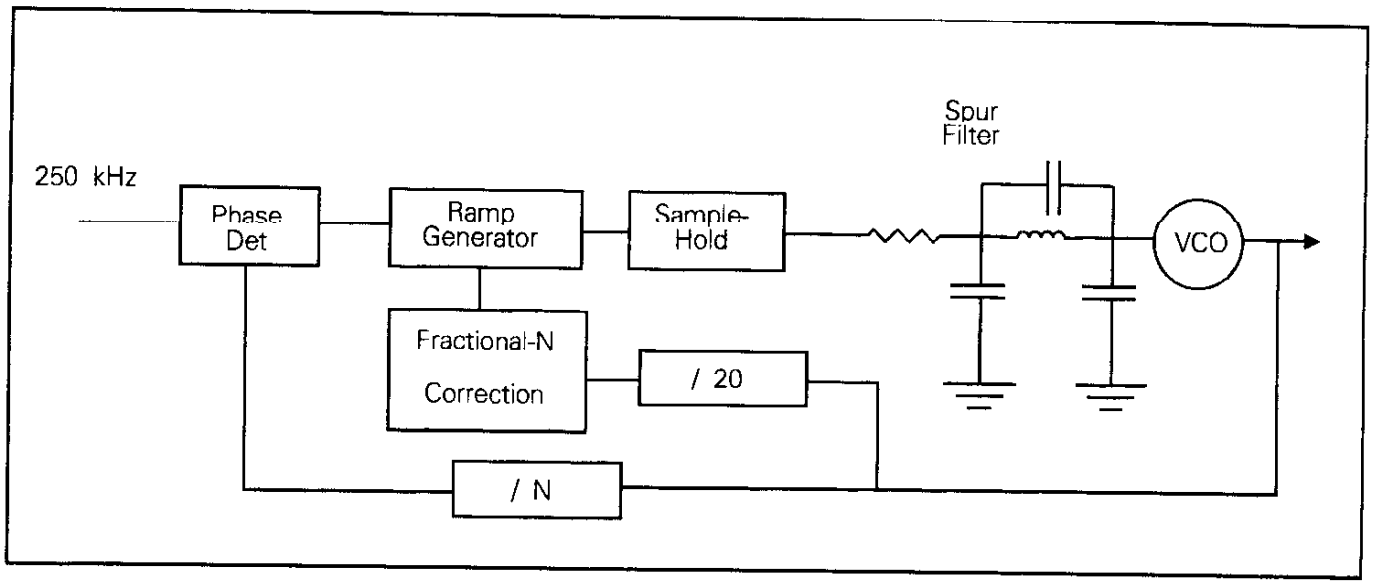

Figure A7.8 Generalized Fractional-N Loop Concept for AMST

If steady-state lock is defined as the point at which less than 5 degrees of phase change occurs over one reference period, the output frequency error must be < 3470 Hz in order to declare lock. Since the fractional loop includes a VCO presetting function, the initial frequency error will be no larger than 25 MHz. Combining these factors with a desired lock up time of 75 μs, n = 18 and therefore K $\geq$ 0.389 is required. Accounting for the change in N, this result leads to a choice for K_d of 1.27 V/rad given that K_v is 25 MHz/V. Assembling these facts together including the elliptic filter, the baseline type-1 design is as shown in Figure A7.9 where the fractional portion has been dropped for simplicity.

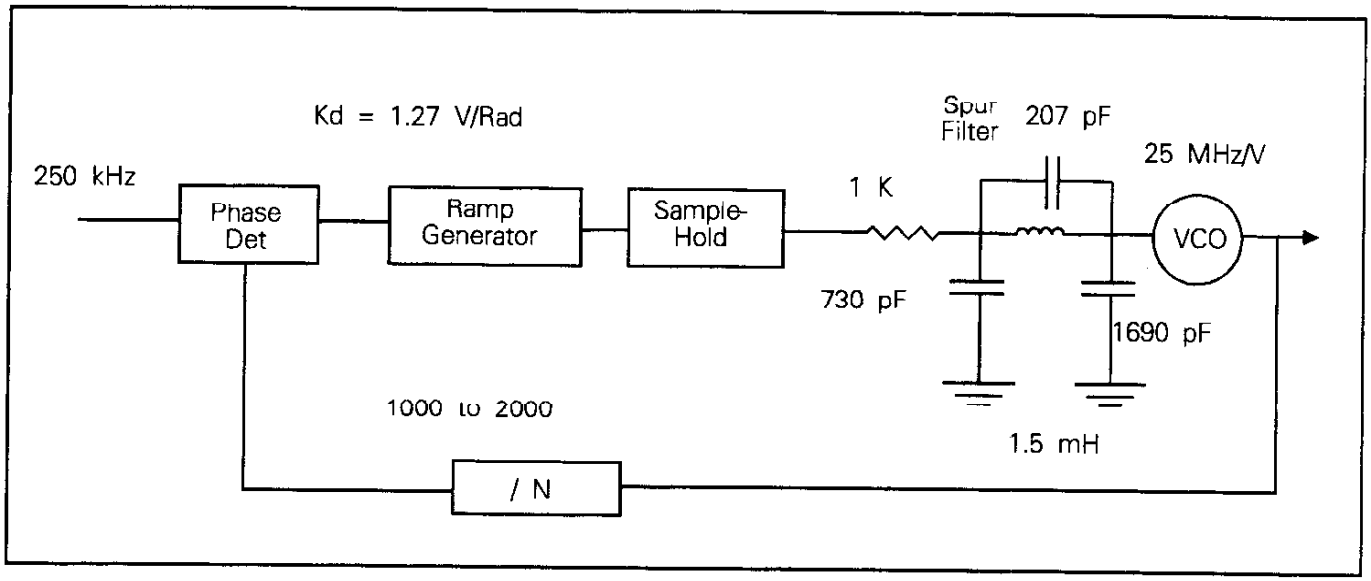

Figure A7.9 Fractional-N Loop Baseline Design

A ComFocus proprietary computer program was used to assess the baseline design shown in Figure A7.9. The transient response of the loop is shown in Figures A7.10 and A7.11 for a step change in output frequency of 25 MHz. Complete phase settling clearly occurs in less than roughly 80 μs. The closed-loop transfer functions are shown in Figures A7.12 and A7.13 assuming a value for N of 1500. Approximately 4 dB of VCO phase noise peaking will occur per Figure A7.12 whereas no evidence of reference noise peaking is present as shown in Figure A7.13. This baseline design therefore meets the switching speed design goals and the phase noise performance is within the guidelines discussed earlier.

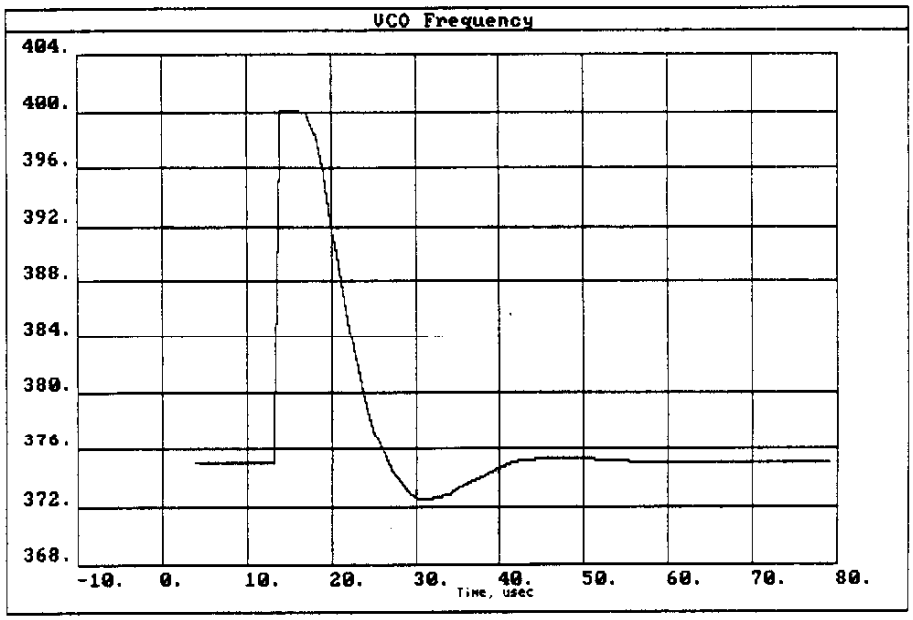

Figure A7.10 VCO Frequency Transient Response of Fractional-N Loop for 25 MHz Step

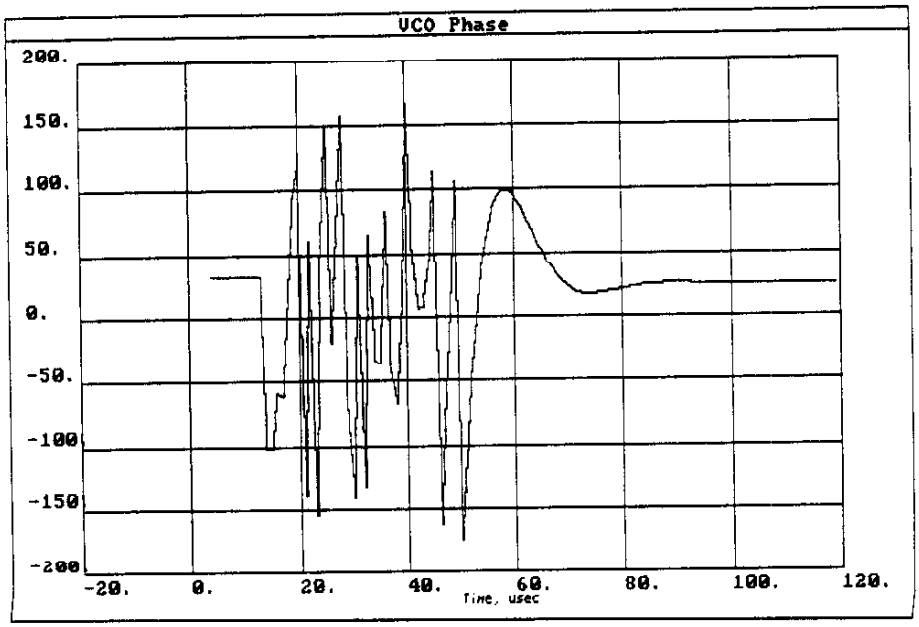

Figure A7.11 VCO Phase Error Transient for Fractional-N Loop and 25 MHz Step

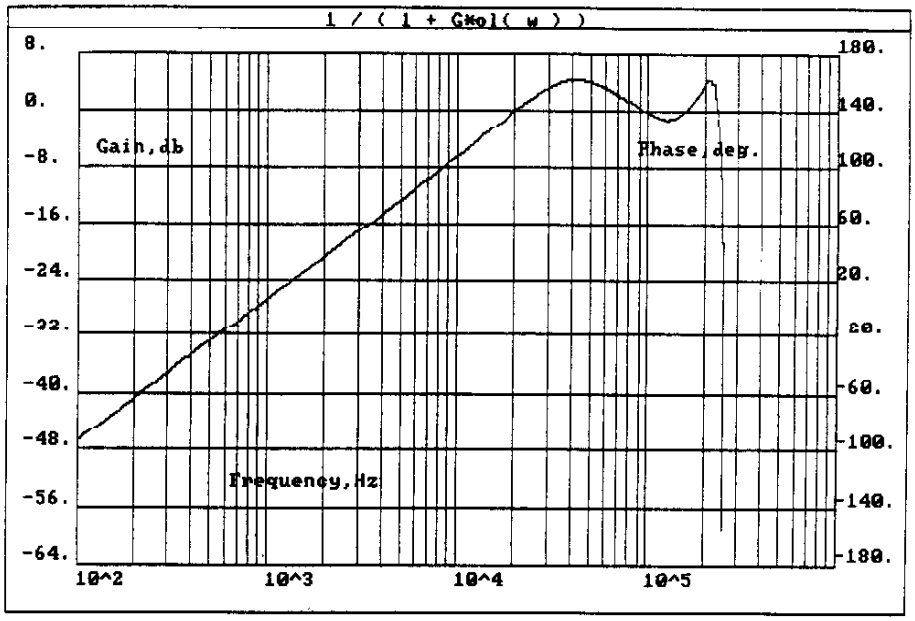

Figure A7.12 Fractional-N Loop VCO Phase Noise Transfer Function (N=1500)

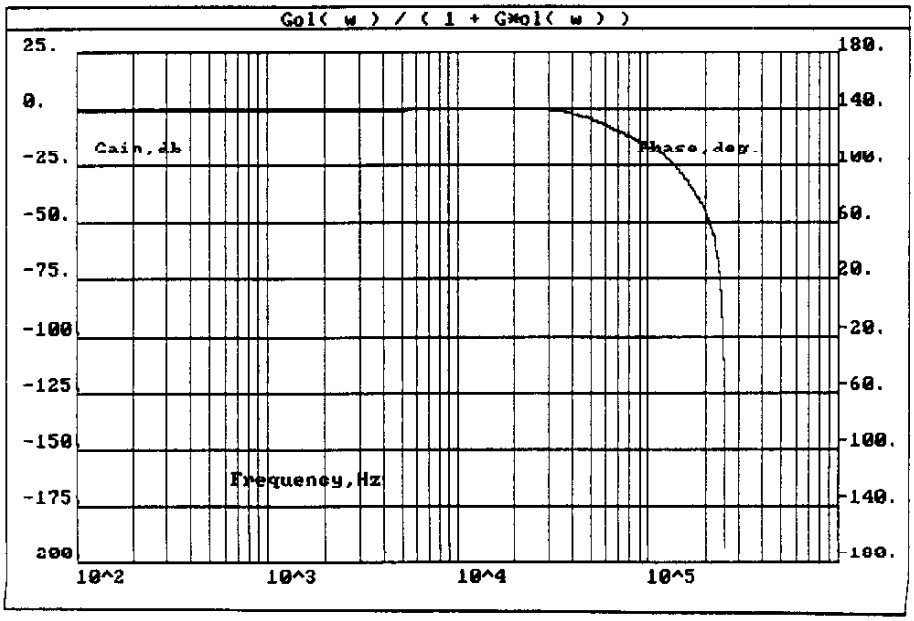

Figure A7.13 Fractional-N Loop Closed-Loop Transfer Function for Reference Noise (N=1500)

Coarse Phase-Locked Loop

The coarse phase-locked loop provides 5 MHz frequency increments at the main synthesizer output as shown in Figure A7.1. It uses a 1 MHz reference rather than a 5 MHz reference in order to permit a 16/17 dual modulus prescaler to be used in the feedback divider which results in lower power consumption. The cost in performance for this choice is higher phase noise.

Worst case, the close-in phase noise at the coarse loop output is anticipated to be -95 dBc/Hz which is still quite good. Large offset discrete spurious and phase noise will of course be cleaned up to some degree by the following sum loop shown in Figure A7.1 also.

The baseline coarse loop design is based upon a fairly traditional type-2 phase-locked loop which utilizes a phase/frequency detector to enhance the pull-in process. The top-level design for this loop is shown in Figure A7.14. A third-order elliptic filter is included in the design to improve suppression of any discrete 1 MHz spurious components an additional 30 dB. The elliptic filter combined with the inherent phase detector balance plus the cleanup action of the sum loop should result in 1 MHz sampling spurs < -90 dBc. The feedback divider ratio ranges from 270 to 525 and the loop parameters were designed such that $\zeta = 0.707$ and $\omega_n/2\pi$ = 80 kHz for N= 270.

The frequency switching performance of this loop was simulated using the same ComFocus proprietary computer program which was used to analyze the fine loop. Consecutive frequency hops from the low frequency extreme to the high and back to the low were simulated, the output frequency versus time being shown in Figure A7.15. Frequency settling clearly occurs well within 50 μs. The larger overshoot at the high frequency extreme results from having the loop critically damped at the other extreme making the loop under damped at the upper extreme. Gain compensation could be added if necessary to make both frequency extremes perform identically but this is unnecessary here.

The real test of synthesizer settling speed is based upon the phase error at the VCO output as shown in Figure A7.16 for the same frequency hop sequence. Worst case settling to steady-state occurs within approximately 60 μs. Gain compensation (if employed) would reduce the worst case settling time to approximately 40 μs.

The open-loop gain function for this loop (N=270) is shown in Figure A7.17. This figure shows a phase margin of 40 degrees and a gain margin of approximately 12 dB. The closed-loop transfer functions which are important for phase noise prediction purposes are shown i Figures A7.18 and A7.19. These predict that the phase noise peaking will be no more that roughly 4 dB. The peaking increases to at most 5 dB for N= 525.

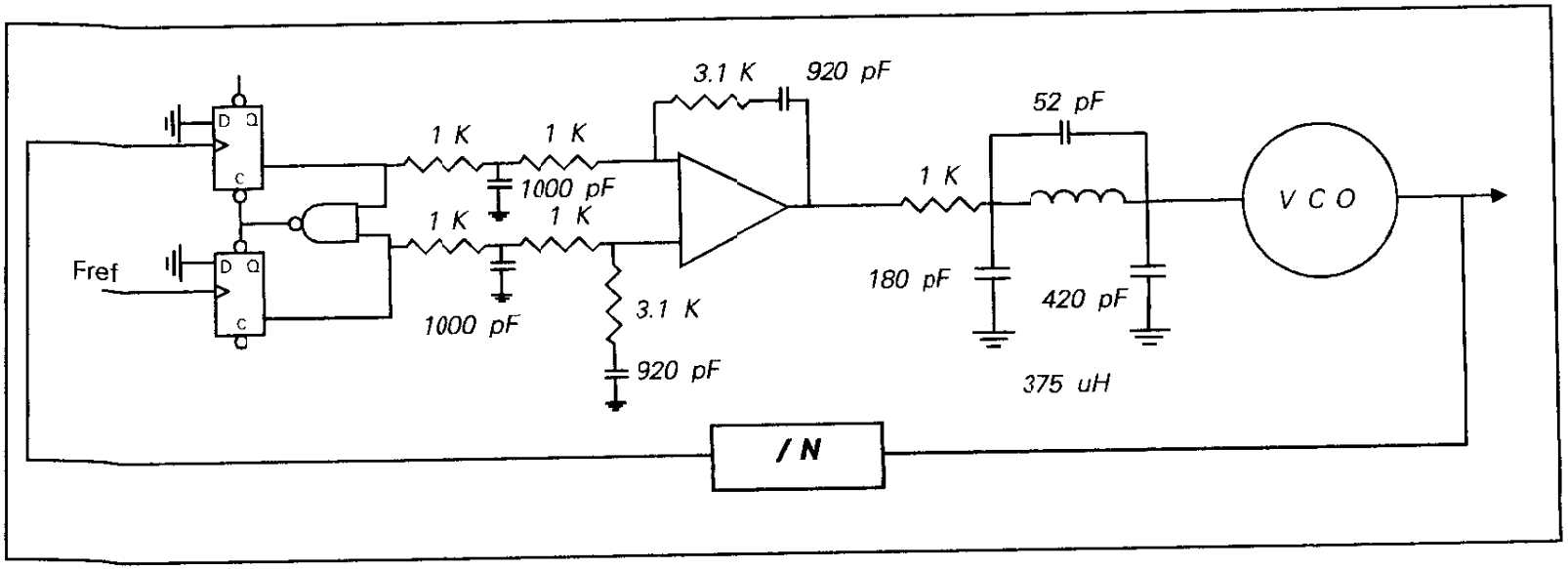

Figure A7.14 Baseline Coarse Phase-Locked Loop Design

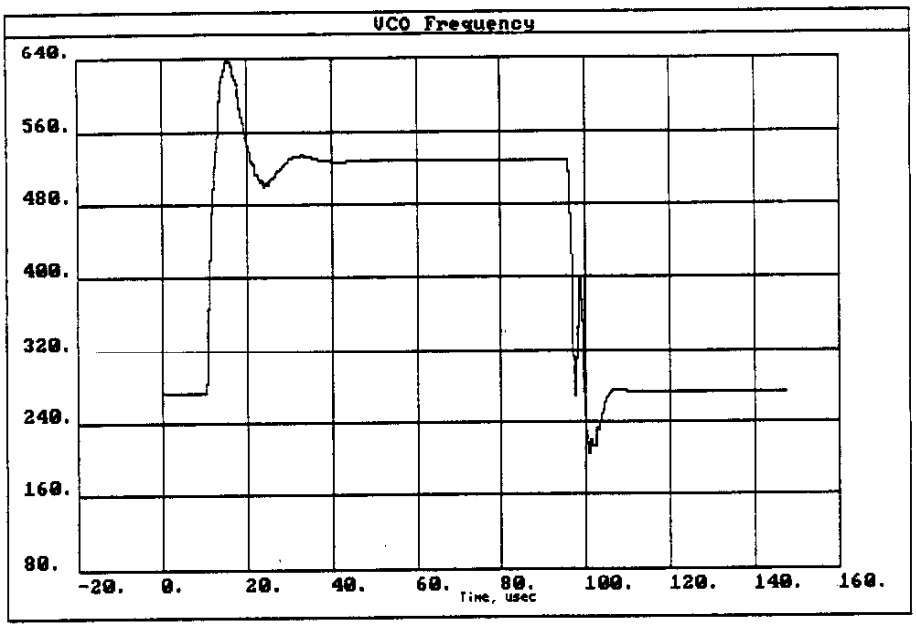

Figure A7.15 Coarse Loop VCO Transient Frequency Error for End-to-End Frequency Hops

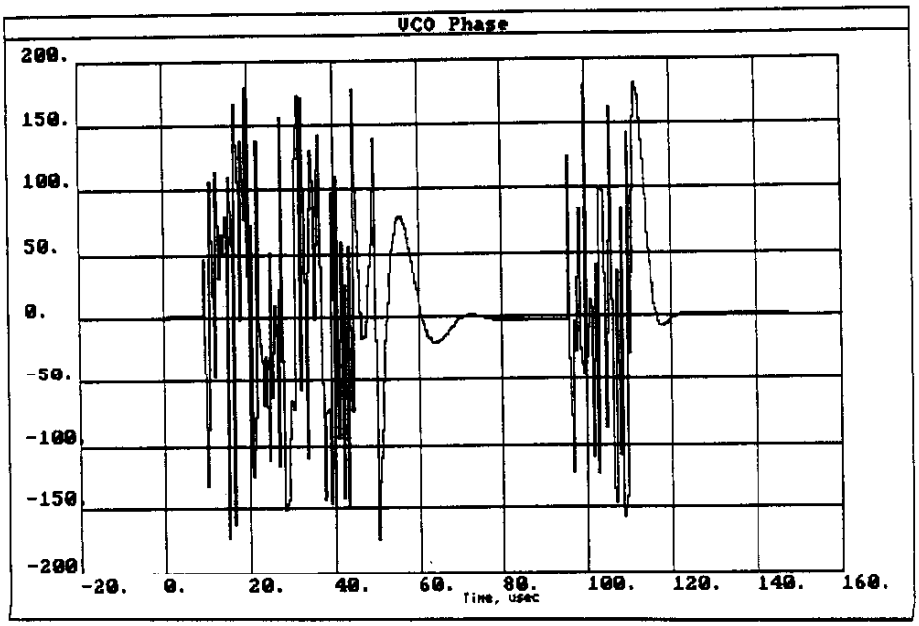

Figure A7.16 Coarse Loop VCO Phase Error for End-to-End Frequency Hops.

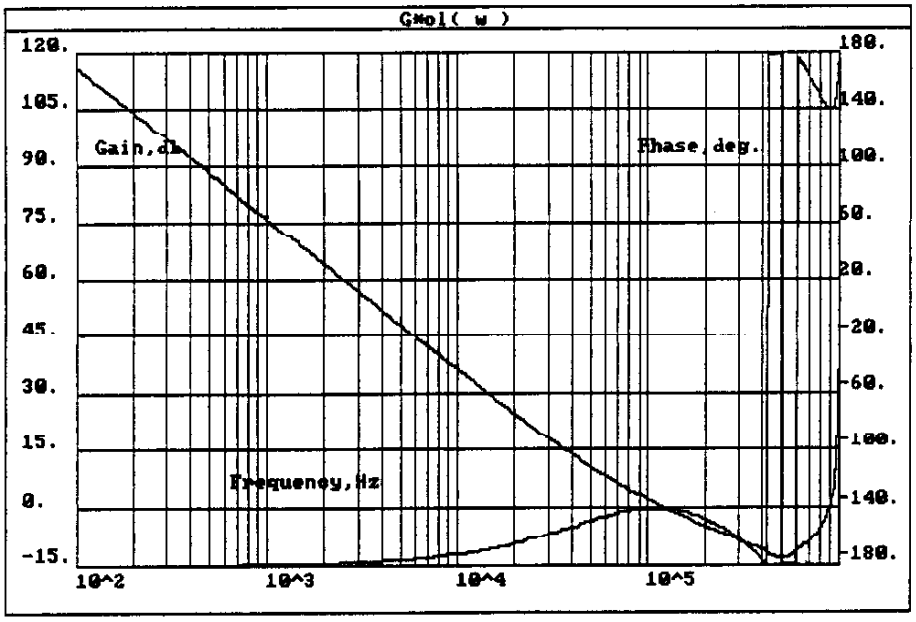

Figure A7.17 Coarse Loop Open-Loop Gain & Phase (N=270)

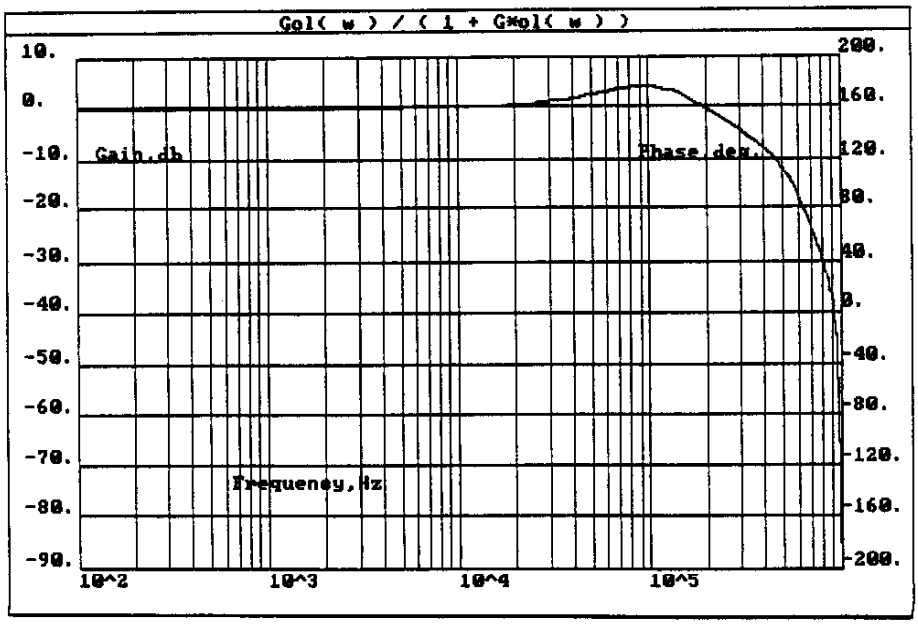

Figure A7.18 Coarse Loop Closed-Loop Transfer Function (N=270) for Reference Node

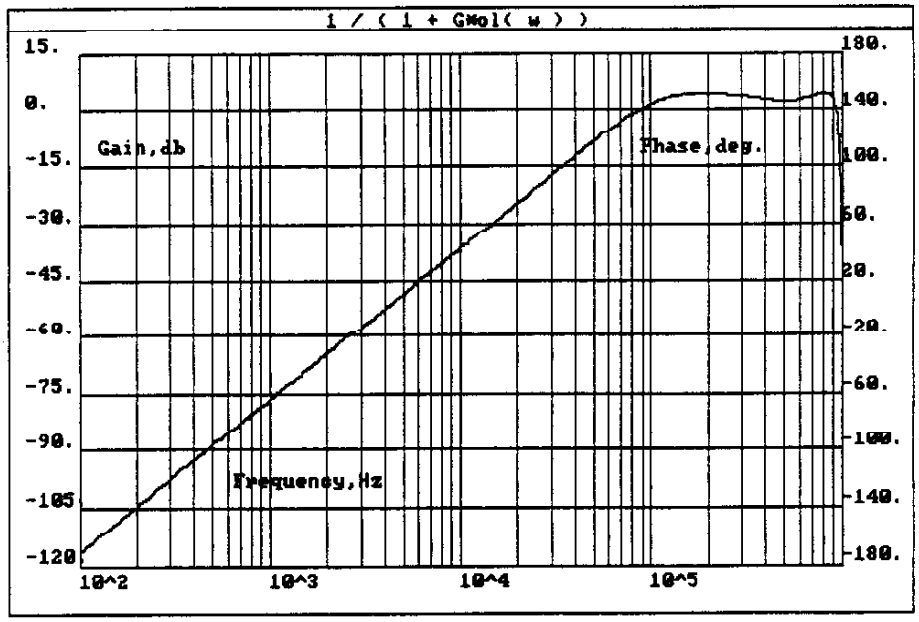

Figure A7.19 Coarse Loop Closed-Loop Transfer Function (N=270) for VCO Node

Sum Loop

The third loop in Figure A7.1 is the sum loop which frequency combines the outputs of the divided down fractional-N loop output with the coarse loop output. N for this loop is always unity. Based upon the switching performance of the coarse loop, a closed-loop bandwidth of 100 kHz for the sum loop will be more than adequate to achieve the desired switching speed objectives. The high reference frequency (20-25 MHz) makes the sampling spur issue trivial to deal with. The VCO tuning voltage will be slaved to the coarse loop VCO to facilitate faster frequency pull-in also. This loop will appear virtually transparent to the coarse and fractional-N loops. Some precautions must be observed in the offset mixing area of this loop, but these issues are well understood.

Overall Phase Noise Performance

An estimate of the overall phase noise performance for the complete main frequency synthesizer is shown in Figure A7.20. The primary contributor is the coarse loop as shown. If a monolithic low power divide-by-N were available for the coarse loop, a reference frequency of 5 MHz could be used there to improve the phase noise performance substantially. Until the preselection and transmit filtering areas have been designed in detail however, this additional performance improvement cannot be substantiated however.

Considering the worst case integrated phase noise for 19.2 kbps BPSK, from Figure A7.20 the integrated phase noise (1 kHz to 20 kHz) is approximately -49 dBc which is 19 dB better than the objective identified earlier. Therefore, as far as BER is considered, the main frequency synthesizer phase noise performance should be quite adequate. Cosite requirements will dictate the remainder of the spectral needs.

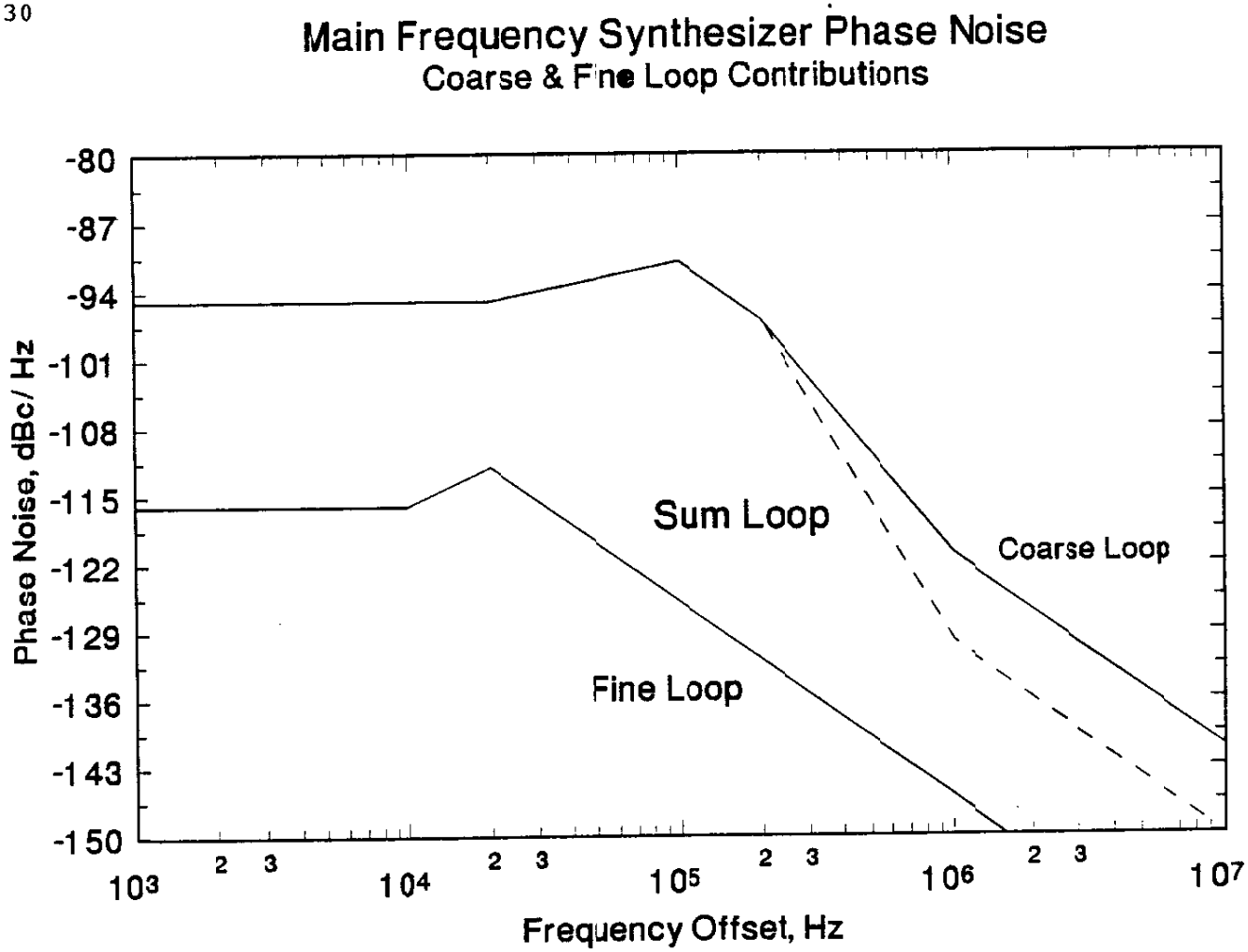

Figure A7.20 Estimated Phase Noise Spectrum for Main Frequency Synthesizer

References

A7.1] ComFocus Corporation, "Advanced Manpack Radio Concept for UHF DAMA Satellite Communications," SBIR Phase I Proposal, 7 January 1991, Topic AF91-030

A7.2] Egan, W.F., Frequency Synthesis by Phase Lock, John Wiley and Sons, 1981

A7.3] Gilmore, R., "Specifying Local Oscillator Phase Noise Performance: How Good is Good Enough?", RF Expo Proceedings, 1991

A7.4] Crawford, J.A., Computer-Aided Frequency Synthesizer Design: A Systems Approach, Artech House, To Be Published

Appendix XIII

AMST Digital Signal Processing

NOTE: This appendix contains a number of ComFocus Proprietary concepts which are very sensitive in that they are being designed into new products at the present time. This fact adds to the importance for complete confidentiality with these ComFocus Proprietary concepts.

Introduction

Digital signal processing (DSP) for the AMST is a very broad subject which covers many areas of specialization. Even though elements of the AMST DSP are discussed in Appendix V for the 5 kHz DAMA waveform, many other details remain to be developed. In partial fulfillment of this objective, a number of specific DSP topics will be addressed within this appendix including:

Demodulation
AM (Line of sight (LOS) applications)
FM (AFSAT FSK, analog cellular, Mobitex)
$\pi/4$-DQPSK (TDMA digital cellular, Federal Std. 1024)

Other
Filtering
Adaptive channel equalization
Specific approach for AMST

Other DSP areas including GPS, CDMA digital cellular, and forward error correction (FEC) topics are addressed in very limited detail in other portions of this report. Even though these topics are certainly important, finite resources require that detailed treatment of them be deferred.

AM Demodulation

Although AM demodulation is not required for UHF SATCOM operation, it is needed for backward compatibility with existing UHF LOS equipments. AM demodulation may be performed using (i) noncoherent envelope demodulation, (ii) coherent synchronous demodulation, or (iii) a ComFocus proprietary coherent synchronous method described shortly.

Noncoherent envelope demodulation may be implemented by using the I and Q bandpass samples (see Appendix III) to implement a standard envelope detector as

$$r_k = \sqrt{I_k^2 + Q_k^2} \qquad (1)$$

where the I_k and Q_k samples are available at a rate of 48 kpairs/sec. Since noise which is also present within the receive bandwidth is also manifested in the r_k output, the I and Q sample stream should be filtered as heavily as possible prior to performing the nonlinear detection function given by (1).

The square root in (1) can be computed by interpolation based upon table lookup, or by recursion as advocated here. The recursion is based upon using the following simple argument. Let

$$y = \sqrt{I^2 + Q^2} \tag{2}$$

and

$$y_1 = y_0 + \Delta y \tag{3}$$

where y_o is an initial estimate for the square root and y_1 is intended to be an improved estimate. Then

$$\begin{aligned} I^2 + Q^2 = V &= (y_0 + \Delta y)^2 \\ V &\approx y_o^2 + 2\Delta y\, y_o \\ \therefore \Delta y &\approx -\frac{V}{2y_0} - \frac{y_0}{2} \end{aligned} \tag{4}$$

This result leads to

$$y_1 = y_0 + \Delta y = \frac{1}{2}\left[y_0 + \frac{V}{y_0} \right] \tag{5}$$

from which the general recursion formula is

$$y_{k+1} = \frac{1}{2}\left[y_k + \frac{V}{y_k} \right] \tag{6}$$

This recursion formula has been used in hand-held calculators for the square root calculation historically. For binary integers, an excellent initial estimate for y is given by $y_o = 2^{k/2}$ where 2^k corresponds to the weight of the maximum nonzero MSB in the value I^2+Q^2. The AM envelope demodulator is shown in Figure A13.1.

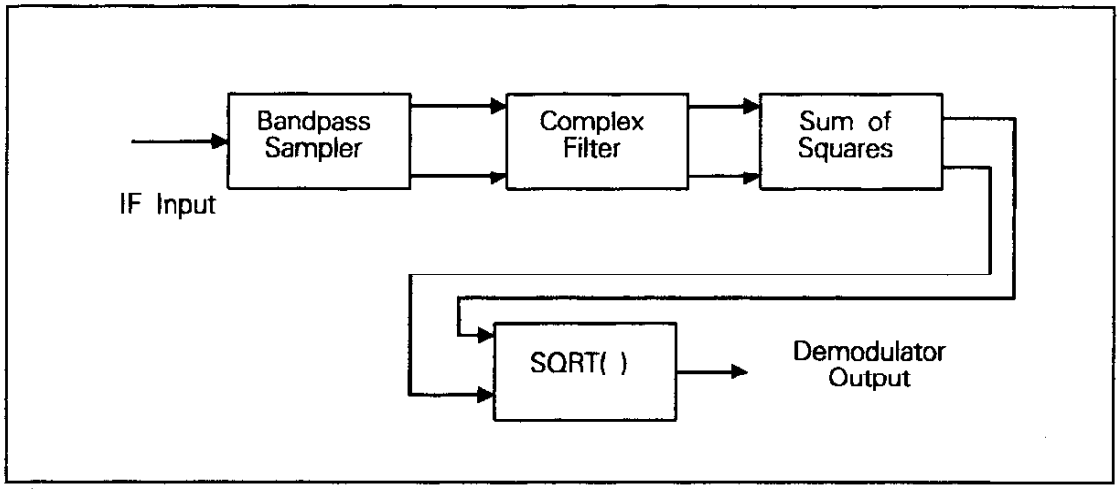

Figure A13.1 Noncoherent Envelope Detection for AM Demodulation

Synchronous AM demodulation is based upon a product detector which utilizes a recovered carrier signal which is phase-locked to the incoming AM signal carrier. A typical synchronous AM detector configuration is shown in Figure A13.2 after [A13.1]. A major advantage of the synchronous AM detector lies in its linear processing of the input signal plus noise signal. Due to this linearity, the noise components may be filtered from the incoming signal either before the detector, or after demodulation at baseband. In sharp contrast, the envelope detector experiences a phenomenon known as squaring loss or small signal supression which results in a thresholding effect for poor input signal-to-noise ratios (SNR). Below this threshold, the demodulator's output SNR degrades approximately 2 dB for every 1 dB decrease in the input SNR. This squaring loss phenomenon is shown in Figure A13.3 where the difference between the two curves is the squaring loss.

One of the potential difficulties in implementing the phase-locked loop portion of the synchronous AM detector is that the closed-loop bandwidth is inherently a function of the input SNR. More often than not, this difficulty is handled by making the closed-loop bandwidth adequately small at low input SNRs such that as the input SNR $\rightarrow \infty$, loop stability is maintained. Unfortunately with the classical type-2 loop which is generally used, this approach leads to a very small loop damping factor at low SNRs

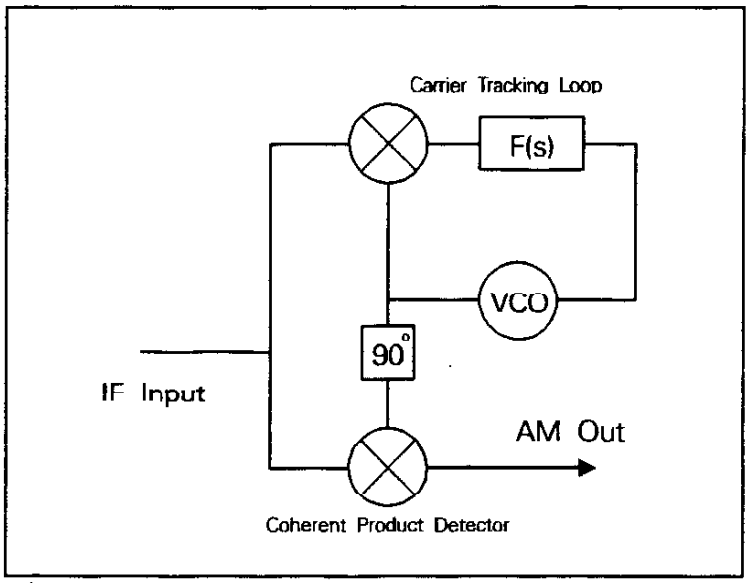

Figure A13.2 Synchronous AM Detector
After [A13.1]

which can potentially degrade the detector's performance due to poor carrier recovery. These issues become less important in the more ideal case where no signal Doppler is present and the VCO in Figure A13.2 can be made a VCXO.

A very effective way in which the small loop damping factor can be mitigated is based upon the following ComFocus Proprietary technique which is in use in a number of ComFocus projects. Recognizing that the loop damping factor and closed-loop phase margin for a classical type-2 loop are closely related by

$$\zeta \approx 0.01\ \varphi_{PM} \qquad (7)$$

for the phase margin expressed in degrees, the loop damping factor can be maintained nearly constant if the loop phase margin can be held constant. Using this concept, it is possible to design a loop filter open-loop gain function which results in this desired behavior over a span of possible closed-loop bandwidths as shown in Figure A13.4.

The normal gain and phase plots for a classical type-2 loop are first shown in Figure A13.4a where the maximum phase margin is only obtainable for one closed-loop bandwidth. Using this proprietary concept in Figure A13.4b however, the phase margin can be made nearly constant over a wide range of closed-loop bandwidths. An example where this technique was actually employed

(for a different application) is shown in Figure A13.5.

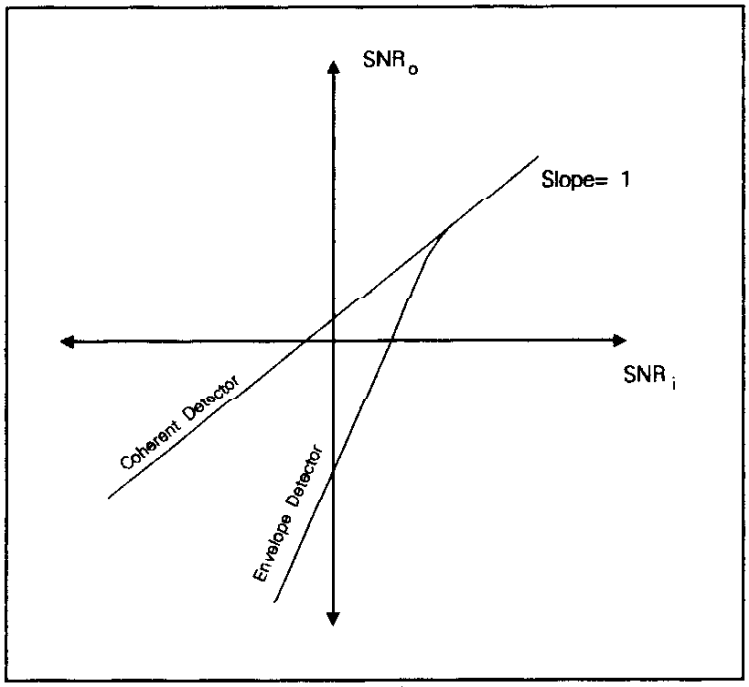

Figure A13.3 Comparison of Coherent and Envelope AM Detection.

Numerical techniques were used to optimize the lead-lag filter feedback time constants in Figure A13.5. For this example, the closed-loop bandwidth can be varied from 100 Hz to over 100 kHz with negligible change in the system phase margin. The open-loop gain and closed-loop gain functions of interest are shown in Figures A13.6 through A13.8. The optimization technique used in this example did not include the additional phase resulting from the post-detection RC filter nor the final output elliptic lowpass filter, so the end results was not a truly equi-ripple phase margin result. By using a variation of this technique in a DSP-implemented synchronous AM detector, exceptional performance should be achievable.

The final technique which will be considered here for AM demodulation is another ComFocus Proprietary technique again utilizing synchronous detection. Normally in AM LOS communications, multipath-induced selective fading is a serious problem. If the transmission material is digital in nature, equalization techniques are available (e.g., decision-feedback equalizer, DFE) which are capable of mitigating the channel impairments. In general, this is

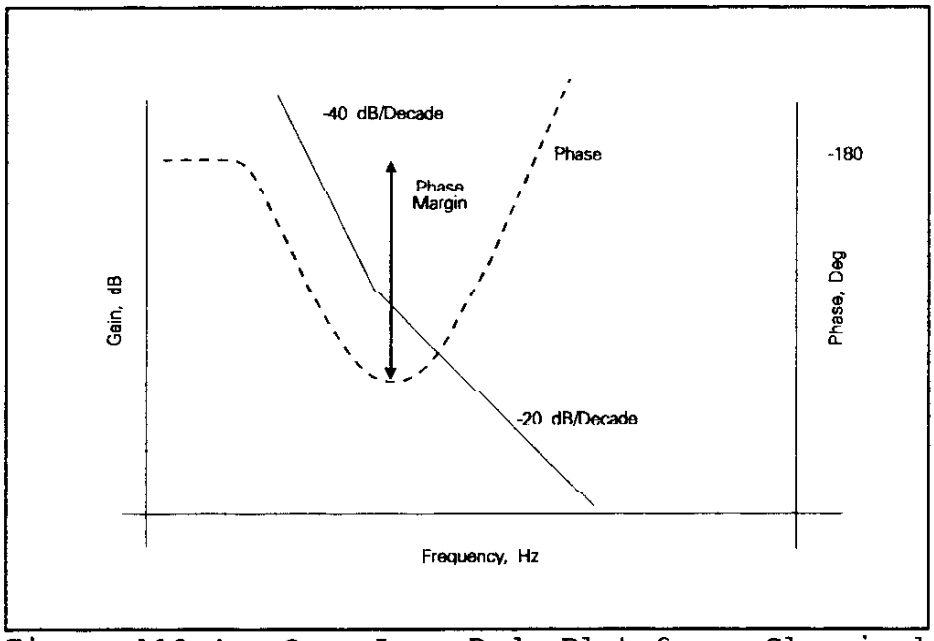

Figure A13.4a Open-Loop Bode Plot for a Classical Type-2 Phase-Locked Loop

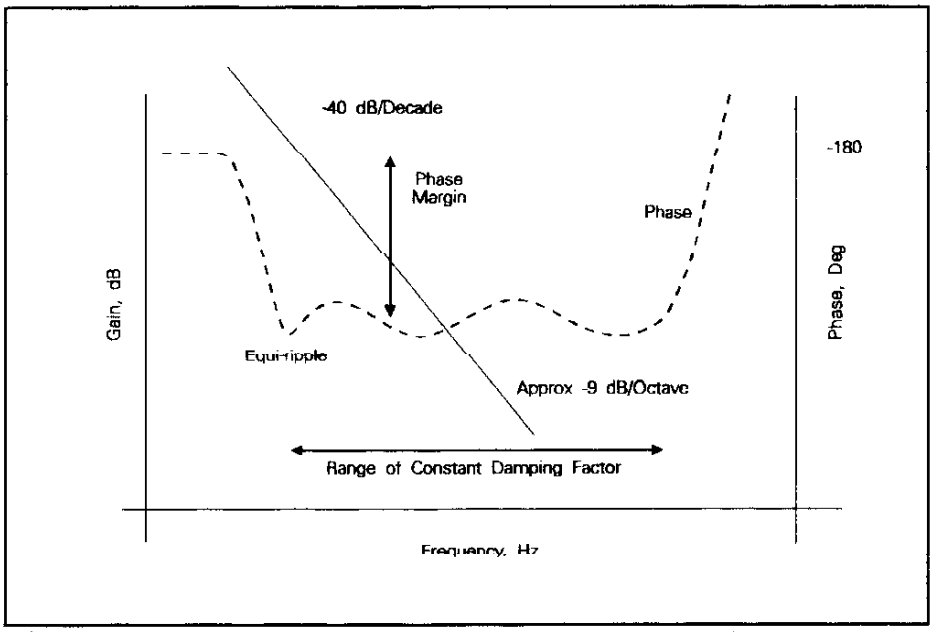

Figure A13.4b Open-Loop Bode Plot for the ComFocus PROPRIETARY Carrier Tracking Phase-Locked Loop

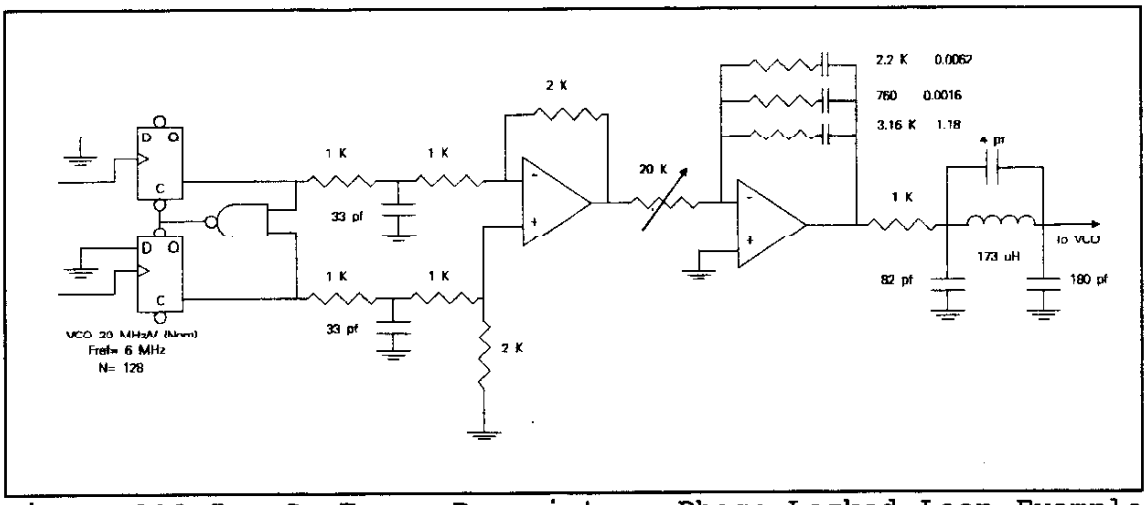

Figure A13.5 ComFocus Proprietary Phase-Locked Loop Example for Enhanced Phase Margin Performance

not true for analog communication such as AM voice which is the situation suited for this proposed approach.

As discussed later in this appendix, the bandpass sampling approach augmented by appropriate filtering can effectively separate the upper and lower sideband portions of a received signal almost perfectly. Since the information carried in the two sidebands of a normal AM signal is completely redundant, this redundancy can be exploited by DSP techniques to implement a two-channel diversity receiver. This technique is being developed for inclusion in a separate ComFocus product at present and no more can be said on this subject for the present time.

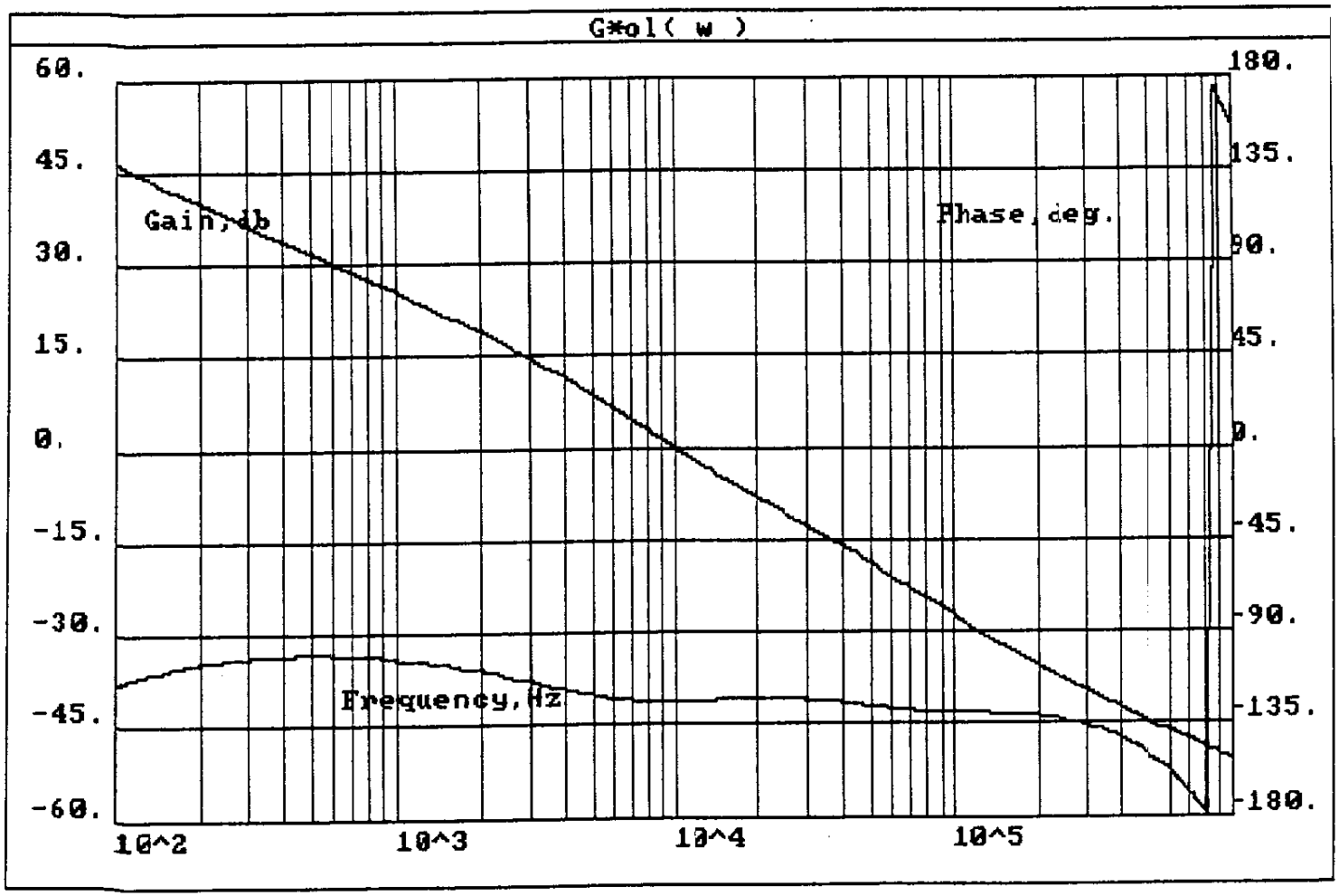

Figure A13.6 Bode Plot for the Proprietary ComFocus Enhanced Phase Margin Approach

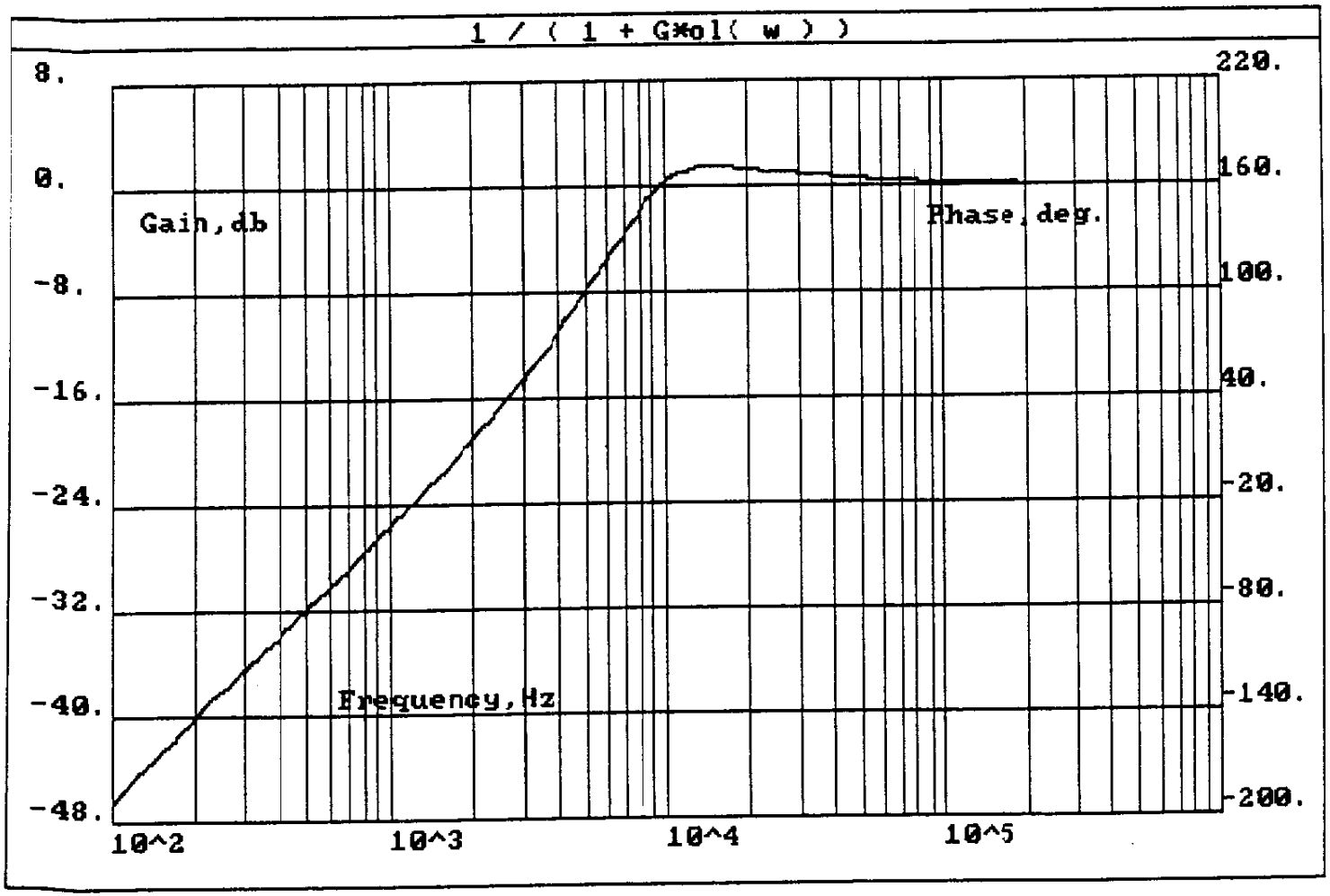

Figure A13.7 Closed-Loop Gain Transfer Function for the Proprietary ComFocus Enhanced Phase Margin Technique

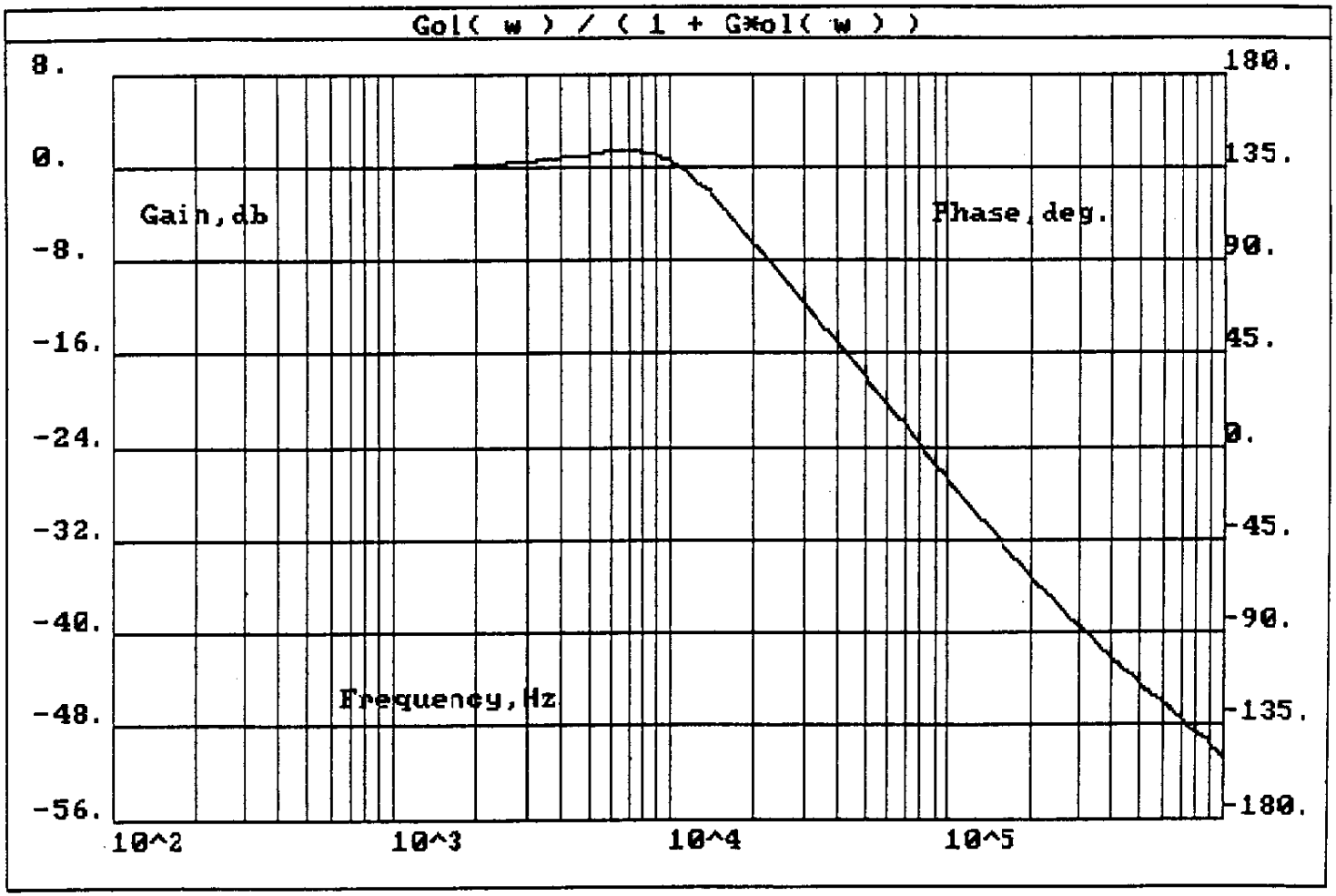

Figure A13.8 Closed-Loop Gain Transfer Furction for the Proprietary ComFocus Enhanced Phase Margin Technique

FM Demodulation

FM demodulation may be performed in a number of ways including coherent phase-locked loop methods and noncoherent frequency discrimination. Phase-locked approaches can benefit from the constant damping factor discussion put forth earlier for the AM synchronous detector. Since feasibility is not a primary issue here, other matters were investigated instead.

FM demodulation will be required in the AMST for AFSAT binary FSK, wideband line-of-sight (LOS) FM, and potentially for demodulating present-day analog FM cellular communications. Satellite channels can benefit from using coherent FM demodulation techniques whereas LOS communications are often corrupted by severe multipath which makes noncoherent FM demodulation much more advantageous.

On the subject of differential versus discriminator detection, a fair amount of discussion has appeared in the literature. A fairly exhaustive treatment has been given in chapter 10 of [A13.2]. Somewhat surprisingly, much of the applicable material from [A13.2] is nearly word for word from [A13.3]. There seems little point in going through many of the details aside from stating a summary position which is applicable for LOS communications. Suffice it to quote:

> "The error-rate performance of differential detection is inferior to that of discriminator detection irrespective of the modulation index" in a fast Rayleigh fading environment [A13.3].

Since the differential approach introduces memory into the demodulator by design which may be very long compared to the channel dynamics (particularly at low data rates), it is not recommended for the AMST LOS modes. Even for slow Rayleigh quasi-static fading, discriminator detection was found to be only ≈0.7 dB inferior to differential detection at 10^{-3} BER [A13.3] and we believe that this difference may be eliminated by what we have to propose later herein.

If complex signal notation is employed, the differential and discriminator outputs may be represented by

$$v(t) = \frac{Re[-jZ^*(t)\dot{Z}(t)]}{|Z(t)|^2} \quad discriminator \tag{10}$$

$$v(t) = Re[-jZ(t)Z^*(t-T)] \quad differential \tag{11}$$

from [A13.2].

The demodulator memory is clearly visible in (9). Although the derivative in (8) requires a time delay as well, it can be made << T.

Although not that practical for the AMST application, several other FM demodulation techniques are worthy of mention [A13.4-7].

Fading is a serious problem in LOS communications which is beyond the scope of this initial study. A number of references have been identified for further study in this area at a later date. [A13.8-17].

Focusing now on noncoherent demodulation, the primary concepts of interest may be found in [A13.18]. This reference goes into substantial detail which will not be repeated here.

Let the received signal be given in terms of its complex envelope form,

$$r(t) = I(t) + jQ(t) \tag{10}$$

Rewriting this in polar form leads to

$$r(t) = \sqrt{I^2(t) + Q^2(t)} \quad \angle \tan^{-1}\left[\frac{Q(t)}{I(t)}\right] \tag{11}$$

Throwing away the amplitude term (e.g., hard-limit, set $\surd = 1$), the instantaneous phase from (11) is

$$\theta(t) = \tan^{-1}\left[\frac{Q(t)}{I(t)}\right] \tag{12}$$

Since frequency is the derivative of phase, the instantaneous frequency is given by

$$\omega(t) = \frac{d\theta}{dt} = \frac{I(t)\dot{Q}(t) - Q(t)\dot{I}(t)}{I^2(t) + Q^2(t)} \tag{13}$$

In terms of discrete samples then

$$\omega(nT_s) = \frac{I(nT_s)\dot{Q}(nT_s) - Q(nT_s)\dot{I}(nT_s)}{I^2(nT_s) + Q^2(nT_s)} \tag{14}$$

If the derivatives can be approximated as finite differences, dropping the nT_s notation in favor of subscripts and taking $T_s = 1$,

$$\dot{Q}_n \approx \frac{Q_n - Q_{n-1}}{2} \tag{15}$$

$$\dot{I}_n \approx \frac{I_n - I_{n-1}}{2} \tag{16}$$

Substituting into (14) produces

$$\omega_k \approx \frac{1}{2} \frac{I_k(Q_k - Q_{k-1}) - Q_k(I_k - I_{k-1})}{I_k^2 + Q_k^2} \tag{17}$$

$$\approx \frac{1}{2} \frac{Q_k I_{k-1} - I_k Q_{k-1}}{I_k^2 + Q_k^2} \tag{18}$$

Aside from the implied division, this is a very nice form for DSP implementation.

If the sampling rate is substantially higher than the maximum information bandwidth being received, these results are directly suitable for DSP implementation. When this is not the case, it is wiser to implement a better estimate of the derivative based upon more than simply two adjacent signal samples.

Assume that the derivative at t=0 is to be estimated. A simple second-order interpolating polynomial which can be used is

$$x(t) = a\,t^2 + bt + c \tag{19}$$

Evaluating (19) at three adjacent sample points gives

$$\begin{aligned} x_{-1} &= a\,T^2 - bT + c \\ x_0 &= c \\ x_1 &= a\,T^2 + bT + c \end{aligned} \tag{20}$$

Solving for the polynomial coefficients,

$$\begin{aligned} c &= x_0 \\ b &= \frac{x_1 - x_{-1}}{2T} \\ a &= \frac{x_1 + x_{-1}}{2} - x_0 \end{aligned} \tag{21}$$

Differentiating (19) at t=0,

$$\dot{x}(0) = b = \frac{x_1 - x_{-1}}{2T} \tag{22}$$

Using this result in (14) leads to the final result (taking T=1)

$$\omega_k = \frac{I_k\left(\frac{Q_{k+1} - Q_{k-1}}{2}\right) - Q_k\left(\frac{I_{k+1} - I_{k-1}}{2}\right)}{I_k^2 + Q_k^2} \tag{23}$$

This result is clearly more complicated than (18) but it should provide significantly better results. Higher order interpolating polynomials may of course be used in (20) if desired.

Assuming that (23) is adopted as the baseline noncoherent FM demodulator, it is instructive to focus further attention on the denominator portion of (23). Although the click-effect is a major noise contributor in conventional digital FM, it does not contribute significantly to errors for low frequency deviation systems. Even so, since it has also been demonstrated [A13.23] that the phase-locked loop improves the FM noise threshold by not tracking many of these "clicks" which would normally appear at the output of a limiter-discriminator, Park's paper [A13.18] should be

seriously considered. Park advocates augmenting the denominator term in (23) and (17) as

$$I_k^2 + Q_k^2 \rightarrow I_k^2 + Q_k^2 + C \qquad (24)$$

where C is a positive constant. This constant prevents the denominator from ever becoming zero which is the source of the noise click problem. This modification is known as the hybrid detector in [A13.18]. Park is less than complete in making any recommendations for the constant C. Its determination will require further investigation.

$\pi/4$-DQPSK for TDMA Digital Cellular

The $\pi/4$-DQPSK waveform which has been adopted for the North American Digital Cellular standard (NADC) [A13.59] is very closely related to traditional differentially encoded QPSK (DQPSK) except that the allowable phase changes for data symbols are restricted to be $\pm 45^\circ$ and $\pm 135^\circ$ rather than integral multiples of 90° [A13.25]. Square-root raised cosine symbol shaping is imposed at the transmitter in order to limit the RF spectrum occupancy to roughly 30 kHz as shown in Figure A13.9. The effective bandwidth is further reduced in the receiver after the signal is passed through an identical square-root raised cosine filter there. Both filters utilize an excess bandwidth parameter α of 0.35. A measured spectrum at the receive filter output is shown in Figure A13.10.

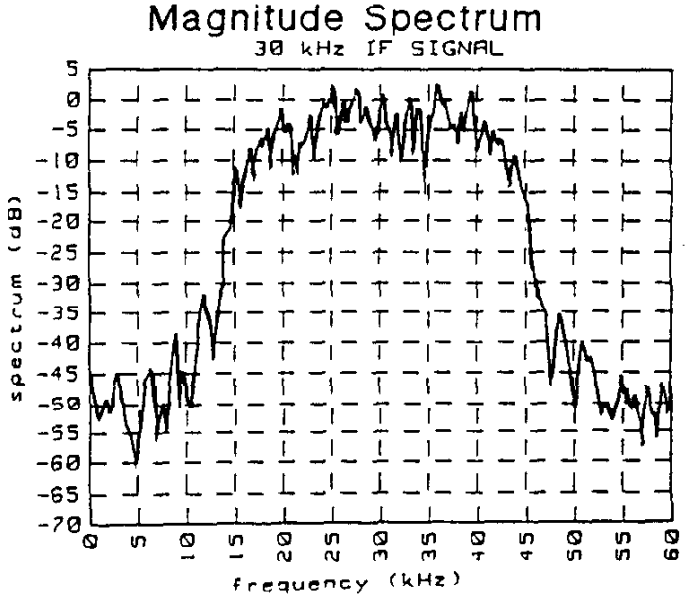

Figure A13.9 Magnitude of $\pi/4$-DQPSK Transmit Spectrum Which Utilizes Root Raised-Cosine Shaping With $\alpha = 0.35$. After [A13.25]

The 30 to 35 kHz bandwidth occupancy is considerably higher than the 25 kHz maximum which must be addressed for UHF SATCOM communications, particularly if the root raised-cosine receive filter is implemented digitally. In this case, the bandwidth occupancy is more like 35 to 40 kHz. Alternatively, the root raised-cosine filter could be implemented at IF with a passive filter.

A number of references sited in Appendix III advocate a required bandpass sampling rate of 4B where B is the total RF

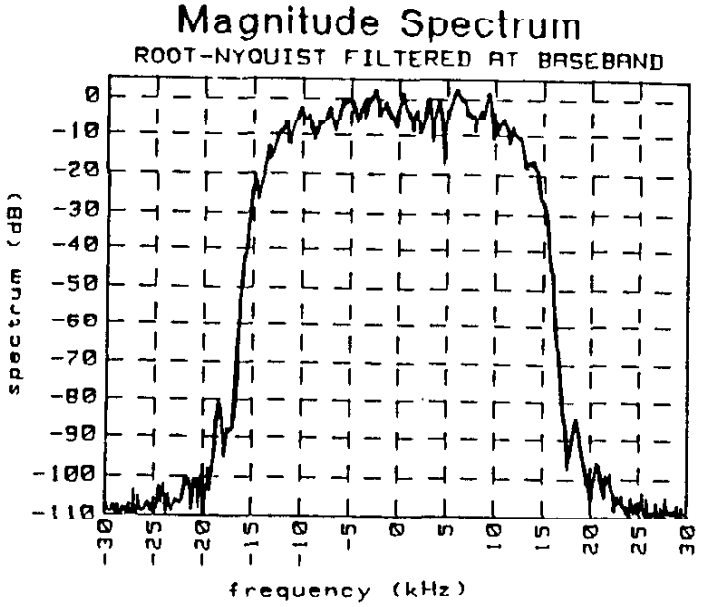

Figure A13.10 Magnitude Spectrum of $\pi/4$-DQPSK Receive Spectrum After Root Raised-Cosine Filtering in the Receiver

bandwidth including guard bands. If applied here, this leads to a required sampling rate of 160 kHz. It is important to recognize that this 4B requirement developed from permitting the Hilbert transform filter to have a very wide stopband which made its realization very simple [A3.5], but also led to a sampling rate which is actually twice that which is dictated by strictly Nyquist reasoning. With proper steps taken in the bandpass sampling area, the planned 97.2 Khz sampling rate will work very well since it represents a sampling rate which is 1.215 times the minimum Nyquist rate even given the 40 kHz information bandwidth mentioned above. This choice also represents an integral number of samples per symbol for the 24.3 ksps data rate which is very advantageous.

There are numerous DSP issues which must be addressed at both the transmit and the receive ends in order to support $\pi/4$-DQPSK communications. At the transmit end, the most significant requirement is for the root raised-cosine baseband filter of I and Q channels which is required. In contrast, the receiver signal processing is much more complex.

One of the major complications in the receiver beyond the need to implement a similar root raised-cosine filter for the I and Q channels is the need for a fairly sophisticated adaptive equalizer [A13.26]. The equalizer is required to combat the potentially severe channel multipath which can occur. Due to the difficulties inherent with the mobile communications channel combined with the fast adaptation required to support TDMA operations, there is

presently substantial research and development effort going on in this area.

The primary difficulty with adaptive channel equalization is that virtually all techniques require some form of initial channel estimate in order to initially converge in the presence of severe multipath (severe enough to cause data eye closure in the receiver). Not only must the receiver decipher the needed equalizer tap weights for the channel, it must also unravel the proper carrier phase, carrier frequency, symbol timing, and AGC level in the process before a tracking mode can be entered. If the symbol timing, carrier phase, and AGC levels can be determined by other means, it can be shown that the least mean-square (LMS) error surface for the equalizer tap weights is quadratic and therefore standard LMS techniques are guaranteed to converge [A13.42,43]. The outstanding questions remain then (i) the means by which these other parameters may be obtained and (ii) whether the LMS approach converges fast enough for the TDMA requirements without some additional open-loop initial channel estimate being performed.

These and other technical issues related to the NADC implementation have been under the scrutiny of the cellular industry for several years and remain areas of intense study. Fortunately from the AMST point of view, the feasibility of the NADC concepts will be proven in that marketplace rather than here. The AMST will simply have to interoperate with the final form of the NADC standard rather than break new technology ground.

The NADC signal frame structure is based upon 40 ms frames where each frame is equally divided up into 6 user slots which each have a length of 6.667 ms. Further user slot details are provided in Figure A13.11. From this figure, it is clear that only 14

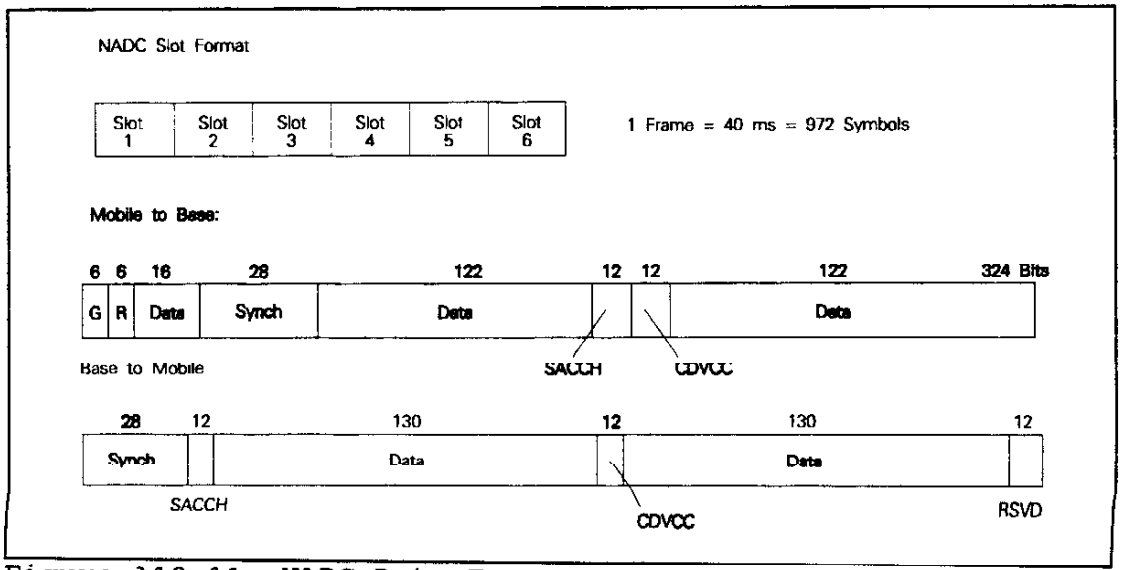

Figure A13.11 NADC Data Frame Format. After [A13.25]

symbols are available at the mobile receiver from which to extract synchronization information prior to the start of data. To what degree the cellular industry equalization approaches confine the synchronization algorithms to the initial synchronization portion of the frame compared to using the data portion in a decision directed manner (or other related techniques) is presently unknown because most equipment developers are being cautious about releasing such details.

Literature directly pertaining to the channel equalization methods slated for use in NADC hardware is presently almost nonexistent because many issues (we believe) are still being resolved in the industry. In this respect, it is interesting to note that while Qualcomm has conducted several extensive field trials with their CDMA system with multiple cell sites and upwards of 100 mobile units in San Diego and to a lesser degree in New York City, this degree of testing has not been done for the NADC mobile system. Qualcomm also plans to have at least one CDMA cell site installed in greater Los Angeles before the end of the year also. Some representative alternatives at least being considered by OEMs (original equipment manufacturers) to addess the equalization issue can be found in [A13.60-70].

Based upon the nature of the cellular communications channel, it is likely that the adaptive equalizer will take the form of a classical decision-feedback equalizer (DFE) or a block-oriented channel estimator such as that proposed in [A13.65]. From a silicon implementation point of view, it is more likely that a DFE architecture will be chosen, a representative demodulator being that shown in Figure A13.12. A number of important functional blocks performing initial signal detection, equalizer training, frame and slot synchronization and AGC have been omitted for brevity.

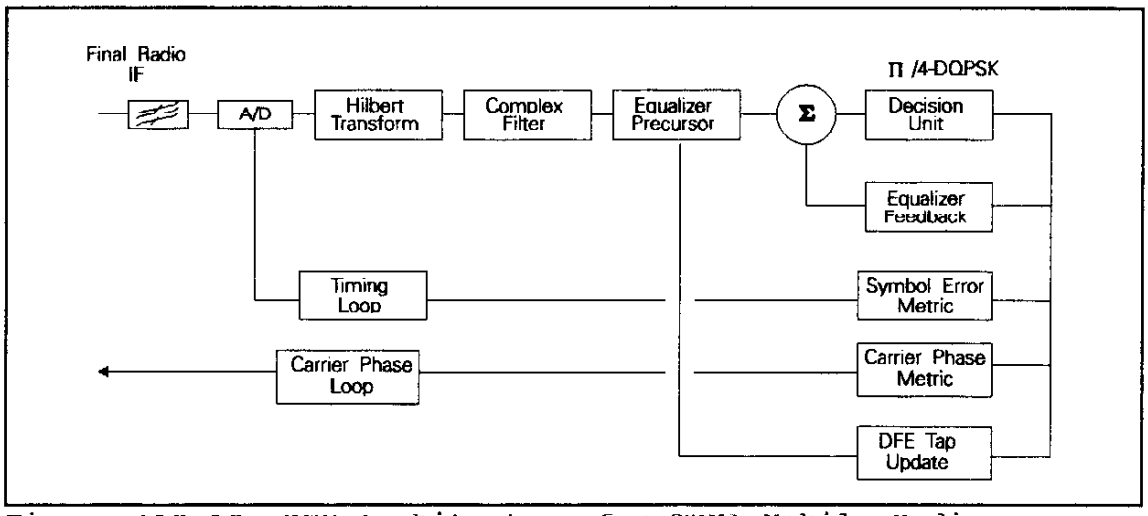

Figure A13.12 DFE Architecture for TDMA Mobile Radio

Referring to Figure A13.12, the complex filter implements the forementioned root raised-cosine filter shape. The precursor portion of the DFE consists of the noncausal taps portion of the equalizer whereas the feedback portion contains all of the causal equalizer taps. Both sets of taps as well as the symbol and carrier phase recovery algorithms are updated based upon the standard LMS algorithms found in the literature[1] [A13.27,42,43]. The DFE approach presented here relies upon a coherent receiver whereas many researchers have primarily constrained their investigations to noncoherent receivers. In these cases, any equalization is done after detection which results in poorer performance generally.

At best, Figure A13.12 represents the potential complexity of a NADC radio receiver even though at this point, it largely based upon conjecture. Fortunately for the AMST, NADC mobile units are planned to be shipped the second or third quarter of this year and the real viability of the NADC concepts confirmed in actual field use.

It is very important to point out that the Japanese digital cellular standard which is largely based upon the NADC does not utilize adaptive equalization for combatting multipath. The approach taken there utilizes very simple switched antenna diversity to deal with multipath which obviously does not entail the complexity of an adaptive equalizer, and since the hardware is much more simple, the power consumption would be less as well. Based upon the power consumption aspect alone, this alternative is worthy of further consideration.

Implementing Filter Functions with DSP

The prospect for implementing the final radio IF filtering digitally rather than at RF is a possible alternative for the AMST due to the substantial advances made recently in digital device technologies. In most cases however, the increased performance possible with this approach is overkill for UHF SATCOM communications since immediately adjacent channel interference problems are generally not too severe. In contrast, line-of-sight communications can benefit greatly from the improved selectivity possible with DSP-based filtering.

For satellite BPSK and QPSK waveforms, almost all digital demodulators use simple integrate-and-dump (I&D) filters for the matched filter function which are very easy to implement. Assuming

---

[1] ComFocus is presently developing a complete QAM receiver for the cable television industry which includes adaptive channel equalization for data rates in excess of 30 Mbps. Although well acquainted with this technology, further details will not be given at this time.

that any adjacent signal which is present is of the same modulation type as the desired signal (for simplicity), it is fairly simple to show that the adjacent channel must be much stronger than the desired signal before the I&D filter does not sufficiently attenuate it. Supporting analysis for this point is somewhat beyond the scope of this present study [A13.71,72], but some results are provided at the end of this appendix.

Generalized Filtering

Any bandpass filter X(f) which has a real time domain impulse response can be represented in terms of an equivalent lowpass filter function H(f) as

$$X(f) = H(f-f_c) + H^*(-f-f_c) \tag{25}$$

where f_c is the center frequency of the filter [A13.68]. The filtering function X(f) must of course be an even function of f in order for the filter impulse response x(t) to itself be real. No such restrictions apply to H(f) however. Given that a signal s(t) is to be filtered using X(f), and assuming that S(f) is also centered about $\pm f_c$, the filtered output W(f) is given by

$$\begin{aligned} W(f) &= \frac{1}{2}\left[S(f-f_c) + S^*(-f-f_c) \right]\left[H(f-f_c) + H^*(-f-f_c) \right] \\ &= \frac{1}{2}\left[S(f-f_c)H(f-f_c) + S^*(-f-f_c)H^*(-f-f_c) \right] \\ &= \frac{1}{2}\left[V(f-f_c) + V^*(-f-f_c) \right] \end{aligned} \tag{26}$$

where the other cross-product terms drop out because the spectra are assumed to not overlap.

By virtue of the receiver bandpass sampling operation discussed in Appendix III, the signal being received is already in complex envelope form. Specifically, the received (real) signal is given by

$$r(t) = I(t)\cos(\omega_o t + \theta) - Q(t)\sin(\omega_o t + \theta) \tag{27}$$

which may be rewritten as

$$r(t) = Re\{ [\, I(t) + jQ(t) \,]\, e^{j(\omega_o t + \theta)} \} \tag{28}$$

Disregarding the carrier term, it suffices to work directly with the pre-envelope form which is given by

$$r_p(t) = I(t) + jQ(t) \tag{29}$$

The arbitrary bandpass filter H(f) may be handled in an analogous manner.

Assume now that H(f) represents a bandpass filter function which has a real time-domain impulse response. In this case, $H(-f) = H^*(f)$. H(f) may be broken down into its real and imaginary parts H_e and H_o which are respectively even and odd functions of f as

$$H(f) = H_e(f) + jH_o(f) \tag{30}$$

in which case

$$\begin{aligned} H_e(f) &= \frac{H(f) + H^*(f)}{2} \\ H_o(f) &= \frac{H(f) - H^*(f)}{2j} \end{aligned} \tag{31}$$

It is straight forward to show that

$$\begin{aligned} h_e(t) &= 2 \int_0^\infty H_e(f) \cos(2\pi f t)\, df \\ h_o(t) &= 2 \int_0^\infty H_o(f) \sin(2\pi f t)\, df \end{aligned} \tag{32}$$

Returning to the general filtering problem for an input signal given in pre-enevelope form, the filtered output in the frequency domain is given by

$$\begin{aligned} Z(f) &= [\, I(f) + jQ(f) \,][\, H_e(f) + jH_o(f) \,] \\ &= [\, I(f)H_e(f) - Q(f)H_o(f) \,] + j\,[\, H_e(f)Q(f) + H_o(f)I(f) \,] \end{aligned} \tag{33}$$

which is shown schematically in Figure A13.13.

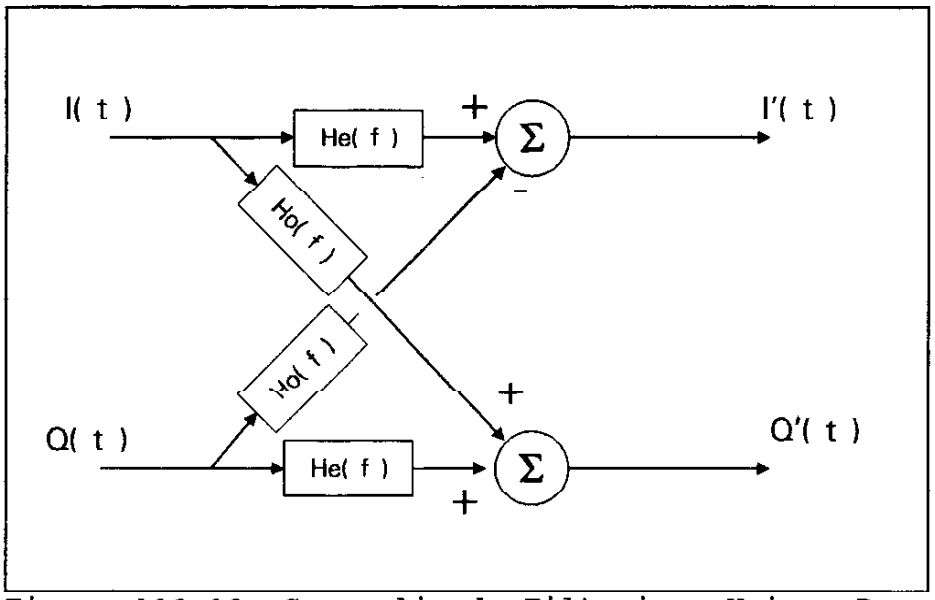

Figure A13.13 Generalized Filtering Using Pre-Enevelope Form

As quickly seen from this figure, if the filter is made symmetric with respect to frequency, $H_o(f)$ is identically zero and the computation load is reduced by slightly more than one-half. This is normally a very worthwhile step to take. If the filter characteristic must be offset from center thereby introducing a nonzero $H_o(f)$, it is much more computationally efficient to rotate I + jQ with exp(jωt) prior to and following the filtering operation as shown schematically in Figure A13.14.

For single sideband (SSB) reception or for the (ComFocus Proprietary) AM diversity scheme mentioned earlier, the desired H(f) results in an impulse response which is no longer real because H(f) is restricted to be a real function of f rather than complex. Again breaking H(f) into even and odd parts (which are both real

now) H_e and H_o, the upper sideband filter case may be represented as shown in Figure A13.15. Normally, some nonzero width D.C. notch is also present to eliminate frequency components very near the would-be carrier. The even and odd portions of H(f) have been accentuated here to illustrate the concept and the complete filtering scheme is shown in Figure A13.16. For SSB reception, both the upper and lower sideband outputs are readily available using only one Hilbert transform filter (i.e., the multiplication by j in the frequency domain).

For AM diversity reception of analog signals, the upper and lower sideband components will be combined based upon a sub-band signal-to-noise ratio (SNR) criterion in order to improve the output SNR in severe selective fading which is very common

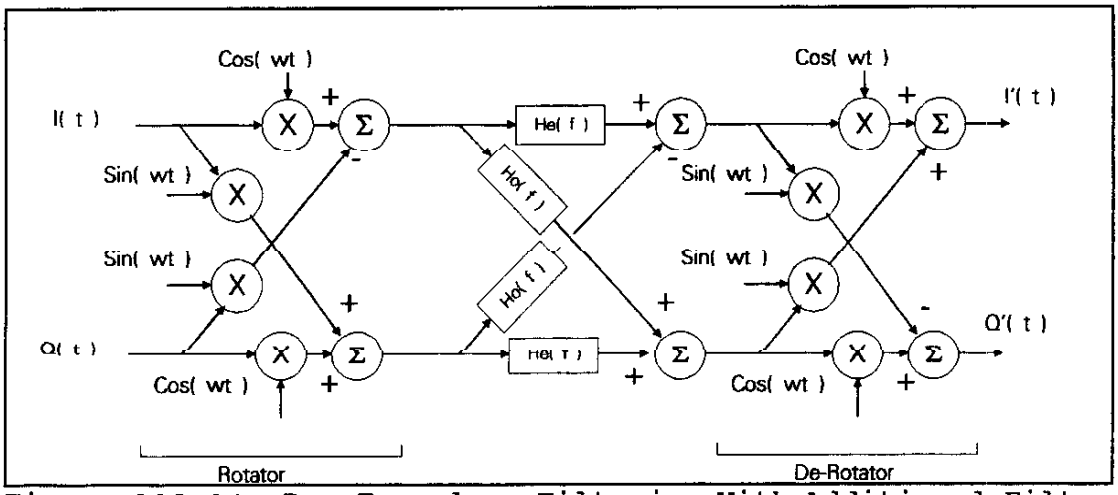

Figure A13.14 Pre-Enevelope Filtering With Additional Filter Offset Capability

for HF channels. This ComFocus Proprietary approach is still under development and no further details will be provided here at this time.

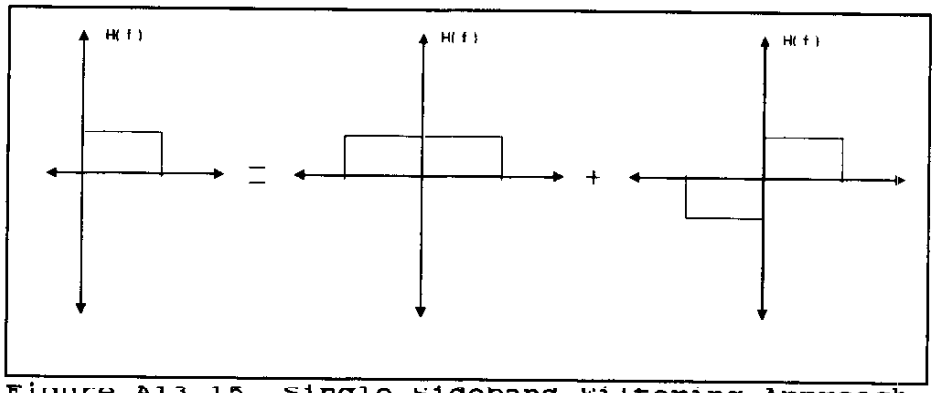

Figure A13.15 Single Sideband Filtering Approach

Digital Filter Implementation

For all practical filter cases envisioned for the AMST, symmetrical bandpass filters should be sufficient. Even single sideband reception may be implemented using a sharp symmetrical filter if the pre- and post-filtering rotation shown in Figure A13.14 is employed. For a normal 2.4 kHz SSB signal, normally the frequency rotation used would be ±1700 Hz.

The detailed implementation of any digital filters is an area which is very technology-choice driven. If the filtering functions are going to be implemented directly in a VLSI chip, one of the most attractive approaches is that of a standard FIR filter topology. It is also possible that the FIR filter could be implemented using the residue number system (RNS) in order to reduce the complexity of the multiply-and-accumulate (MAC) operations. Generally, the conversion to and from RNS is one of its principle drawbacks, but if these functions make use of available prom technology, accomodating 18 to 20 bits of RNS dynamic range is readily achievable. If on the other hand, the filters are to be implemented using a processor-based approach, the large number of MAC steps for the FIR approach may be prohibitive for implementing sharp filters.

Funding levels in the Phase II effort will necessarily focus our attention on the processor implementation route for digital filters rather than on full custom ASIC devices. A number of new digital signal processors are becoming available which boast reasonably low power consumption for supporting the emerging digital cellular markets, notably the device family from AT&T. One processor which has been used on several projects within ComFocus is the Analog Devices ADSP2101 device which delivers about 10 million MAC instructions per second. At the 96 kHz sampling rate defined in Appendix III, and ignoring other processing overhead,

this device is capable of a maximum of 10 MHz/96 kHz ≈ 104 MAC operations per sample, 50 being much more representative given reasonable overhead and loading margin. This translates into only 25 taps per I and Q channel filter which is somewhat small for implementing narrow band filters unless stages of sampling rate decimation are also employed. This simple reasoning illustrates that centrallized processing for intensive computations such as filtering are still very demanding upon the throughput of even the latest processor technology.

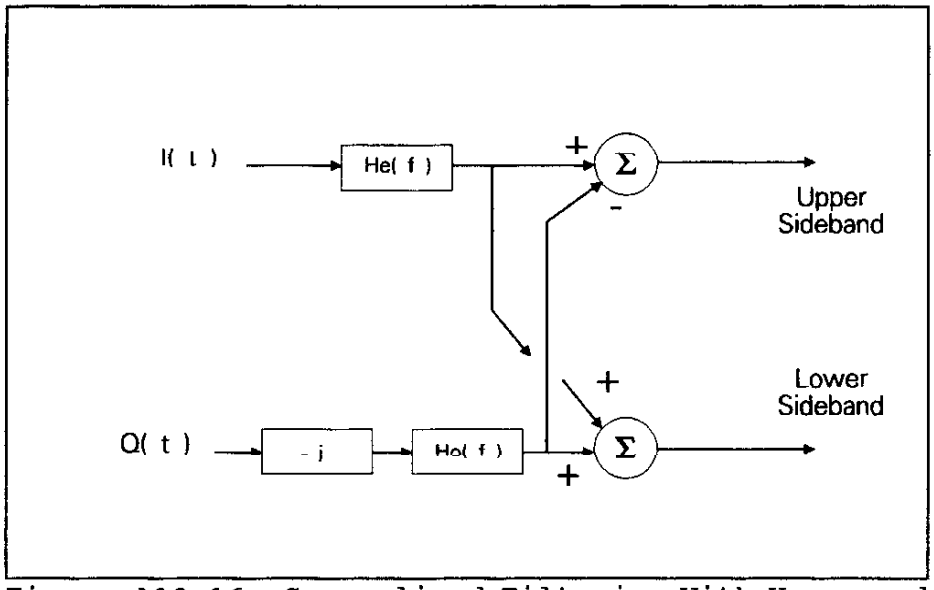

Figure A13.16 Generalized Filtering With Upper and Lower Sideband Spectrum Separation

A compromise between the fully processor-oriented and custom VLSI approach is best suited for the Phase II effort if sophisticated digital filtering is to be included. This is a necessary and desirable step to take before moving into a fully integrated solution regardless. Taking this approach, it is desirable to keep all processor computations constrained to baud rate operations, putting the higher rate calculations into FPGAs wherever possible. The most promising approach developed thus far for an FPGA implementation is based upon a three-modulo RNS representation combined with a clever multiplier implementation known as the Kenyan double and halve algorithm [A13.75].

The fairly low sampling rate (96 kHz) used in the AMST may make the RNS approach an overkill in that the same Kenyan algorithm could be used to implement non-RNS computations. Due to the continuing interest in RNS however, we only address the Kenyan-RNS based approach here.

A Note on RNS

The residue number system is mathematically based upon the Chinese Remainder Theorem (CRT). An RNS is defined by a set of integers (p_1, p_2, ..., p_J) which are pairwise relatively prime. Any integer value N in the range [0,M) where

$$M = \prod_{i=1}^{J} p_i \tag{34}$$

may be uniquely represented in terms of its J residues which are denoted by a_i which are computed as

$$a_i = N \bmod p_i \tag{35}$$

One of the principle advantages of RNS is that all of the arithmetic operations which are closed on the integer set [0,M) may be performed on the residue values alone with no carries or borrows involved. For this reason, RNS has often been referred to in the literature as "carry-free arithmetic."

Given the J residues of an unknown number, the number may be reconstructed as

$$x \bmod M = \left[\sum_{i=1}^{J} (r_i u_i t_i) \bmod p_i \right] \bmod M \tag{36}$$

where

$$t_i = \frac{M}{p_i} \tag{37}$$

and u_i is the multiplicative inverse of t_i which may be also written as

$$(u_i t_i) \bmod p_i = 1 \tag{38}$$

As an example of the RNS approach, consider the pairwise relatively prime factors {15,16,17}. For this case, M= 4080. Assume further that the number to be represented in the RNS is N= 341. From (35), the three residues are 341 mod 15= 11, 341 mod 16= 5, and 341 mod 17= 1. The U_i needed to compute the inverse RNS may be calculated using Euclid's algorithm.

Euclid's algorithm states that if two positive integers a and b (a<b) are relatively prime (i.e., their greatest common divisor (GCD) is 1), then there exist two integers c and d such that ca + db = 1. In general, if the GCD of a and b is r, then there exist two integers c and d such that ca + db= r. The $\{u_i\}$ can be determined by the fact that t_i and p_i are relatively prime in which case we must have that

$$c\,t_i + d\,p_i = 1 \tag{39}$$

By choosing $u_i = c$, the defining relationship (38) is satisfied.

The recursive form of Euclid's algorithm is given by

$$c^k\,t_i + d^k\,p_i = r^k$$

$$c^{-1} = 0 \quad d^{-1} = 1$$

$$c^0 = 1 \quad d^0 = 0$$

for $k > 0$:

$$r^k = r^{k-2} - \left\lfloor \frac{r^{k-2}}{r^{k-1}} \right\rfloor r^{k-1} \tag{40}$$

$$c^k = c^{k-2} - \left\lfloor \frac{r^{k-2}}{r^{k-1}} \right\rfloor r^{k-1}$$

$$d^k = d^{k-2} - \left\lfloor \frac{r^{k-2}}{r^{k-1}} \right\rfloor r^{k-1}$$

where the stop condition is reached when $r^n = 0$. Integral equations of the form given in (40) are known as Diophantine equations, a nice introduction to the subject being available in [A13.74].

RNS in the AMST Context

The most promising RNS-based architecture explored thus far for the AMST is based upon the Kenyan double-and-halve algorithm

used in a 3 moduli RNS system where the pairwise prime factors are given by { $2^N - 1$, 2^N, $2^N + 1$ }; This choice of relatively prime factors has a number of nice properties associated with it [A13.76-78]. For the AMST, an N value of 5 provides a more than adequate dynamic range of nearly 15 bits. The conversion from binary to RNS can be done completely within table lookup PROM since the input value dynamic range will be no more than approximately 10 bits (i.e., 1 K address space). The conversion from RNS back to binary may be implemented again in PROM or directly using N and (N+1) bit adders which is more compact [A13.76].

The multiplication between a multiplicand A and a multiplier B may be performed using the following simple procedure [A13.75]:

> Repeatedly halve the multiplicand (discarding remainders) and double the multiplier until the former is 1. For every odd multiplicand, add the respective multiplier to an accumulated sum.

This procedure is particularly simple for binary-based multiplier implementations as shown in Figure A13.17. Some additional circuitry is of course required here to orchestrate loading, shifting, and clearing, but this circuitry is common for all the multiplier blocks involved. If the maximum length of the multiplicand (and multiplier) is 10 bits, one multiply operation will require roughly 10 clock cycles. Given a bandpass sampling rate of 96 kHz, the clock speed would only be 0.96 MHz which is ideal for very low power consumption.

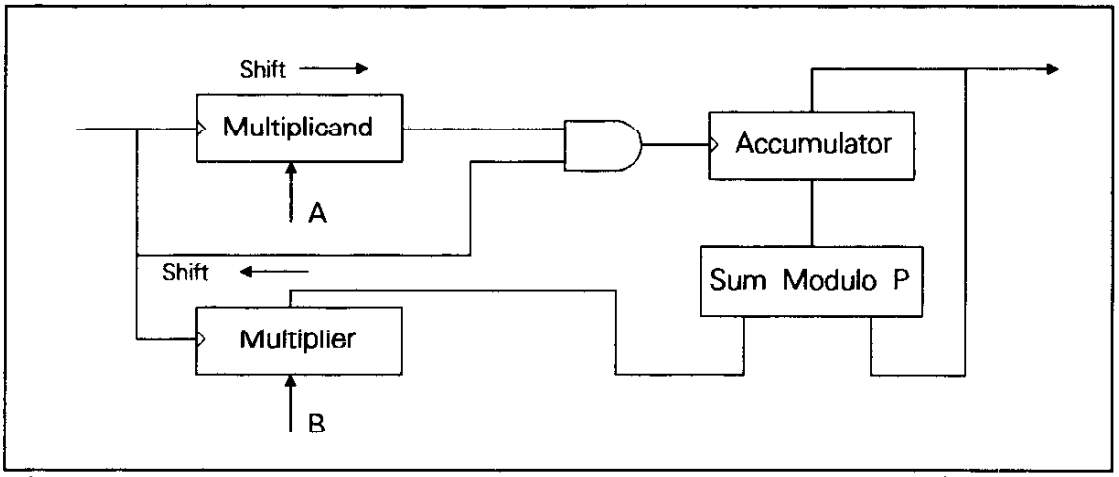

Figure A13.17 Kenyan Double and Halve Algorithm for Mutliplier Implementation

It is very important to size the multiplier block in terms of available field programmable gate array (FPGA) technology such as that from Actel since semi-custom and custom gate array approaches will be too expensive to undertake in the Phase II effort. For the N=5 RNS moduli case, both shift registers and the accumulator are 5 bits wide as well as the modulo p_i adder. Assuming that the modulo p_i adder is about twice as complex as a normal binary adder and including a 10% overhead factor, one multiplier requires approximately 56 modules of an Actel device. The largest Actel presently available has 1232 modules which theoretically makes it possible to put 22 such multipliers in one Actel. Accounting for the normal pipeline delay registers which must accompany a systolic FIR filter structure and the fact that 3 moduli calculations must be performed, approximately 5 filter MAC stages are possible in one Actel device. Therefore, to implement a 25 tap FIR filter for both the I and Q channels would require approximately 10 Actels. Even with the RNS route, a practical end solution is only attractive if VLSI is admitted to the solution process.

If on the other hand, it is of value to simply evaluate the FIR approach in general, off-the-shelf FIR devices are available from a number of vendors including LSI Logic and Zoran. In general, these devices require substantial power and the equivalent gate counts are very high. These are factors which make the off-the-shelf approach unsuitable for use beyond technology demonstration for the most part.

Before leaving the RNS subject, it is insightful to compare the RNS approach just described with that achievable using straight binary implementations such as the Zoran or LSI Logic devices. Straight binary implementation of an 8x8 2's compliment mutliplier in the Actel device requires 235 modules. In order to prevent overflow, the input operands must be limited to 4 bit values and then sign extended to 8 bits. One Actel device can therefore host a maximum of 8 multipliers with a maximum dynamic range of only 8 bits. In contrast, an Actel based upon the RNS approach can host approximately 7 multipliers with a dynamic range of 16 bits. In this comparison, the superiority of the RNS based approach is quite clear.

In conclusion, even though a 3 moduli based RNS approach as described can provide enhanced capabilities as compared to binary approaches, the required hardware is still quite complex. Aside from possibly the root raised-cosine filtering and adaptive equalization required for NADC, all of the AMST performance objectives can be met using traditional IF filtering combined with I&D baseband matched filters. Therefore, inclusion of a digitally implemented programmable filter in the AMST does not appear necessary at this time. Even though digital filtering is required for the TOQPSK spectral shaping developed in Appendix IV, since the sampling rate need only be 4x the maximum symbol rate of 3000 sps or 12 kHz, a processor-based filtering approach is well suited. The fact that processing requirements are generally lower in the

transmit mode than for receive mode is a further benefit as well.

Bit Error Rate Performance in the Presence of Adjacent Channel Interference

A simulation based analysis of the BER performance achievable when only IF filtering combined with baseband I&D matched filtering is presented here. This investigation is by no means exhaustive, but it does support the premise that adequate performance is achievable in the presence of fairly strong adjacent channel interference without resorting to more sophisticated digital filtering techniques.

Only the 5 kHz DAMA waveform is considered in the analysis and the spectral shaping shown in Figure A1.25a is assumed. The adjacent channel interferer is assumed to also be a 5 kHz DAMA waveform with the same spectral shaping offset 5 kHz from the desired signal.

Two RF filter bandwidths are considered here, one with an RF bandwidth of 1.5x the symbol rate (3000 sps) and the second 2.0x the symbol rate. The filters are assumed to be N=4 Butterworth in nature. The recovered signal constellations for these two filter cases with infinite CNR and no adjacent channel interference are shown in Figures A13.18 and A13.19. Slightly more ISI is visible in Figure A13.18 due to the narrower IF filter being employed. The recovered signal constellations are shown for a number of adjacent channel interference levels in Figures A13.20 through A13.29. The impact of the interferer only becomes clearly recognizable here for interferer levels on the order of 15 dB stronger than the desired signal.

One of the better perspectives on the adjacent channel performance is based upon the actual BER versus interferer level. A number of cases were examined and the results are shown below.

Table A13.1 BER Versus Interferer Level

CNR= 10 dB
IF Filter Bandwidth = 1.5 x Symbol Rate (4500 Hz)
Adjacent Interferer +5 kHz Relative to Desired Signal

Interferer Level wrt Desired	BER
+ 10 dB	0.00041
+ 15	0.0033
+ 17	0.012
+ 20	0.054

The BER performance degraded rapidly for interferer levels above 20

dB. Some of this degradation was no doubt due to increased tracking variance in the symbol and carrier tracking loops but these results are nonetheless representative.

In conclusion, the performance of the IF filter/baseband I&D filter is very robust for adjacent channel performance, particularly where the spectral occupancy has been addressed as assumed here. This approach will be adopted for the AMST signal processing.

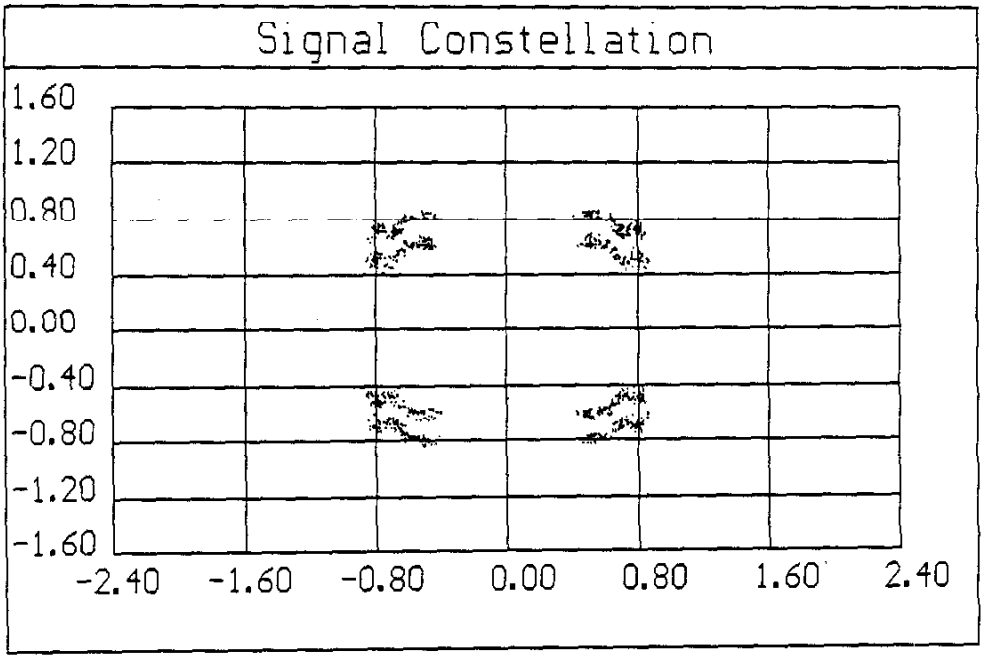

Figure A13.18 Recovered Signal Constellation At CNR= ∞, RF Filter Bandwidth 1.5xSymbol Rate, No Adjacent Channel Interference

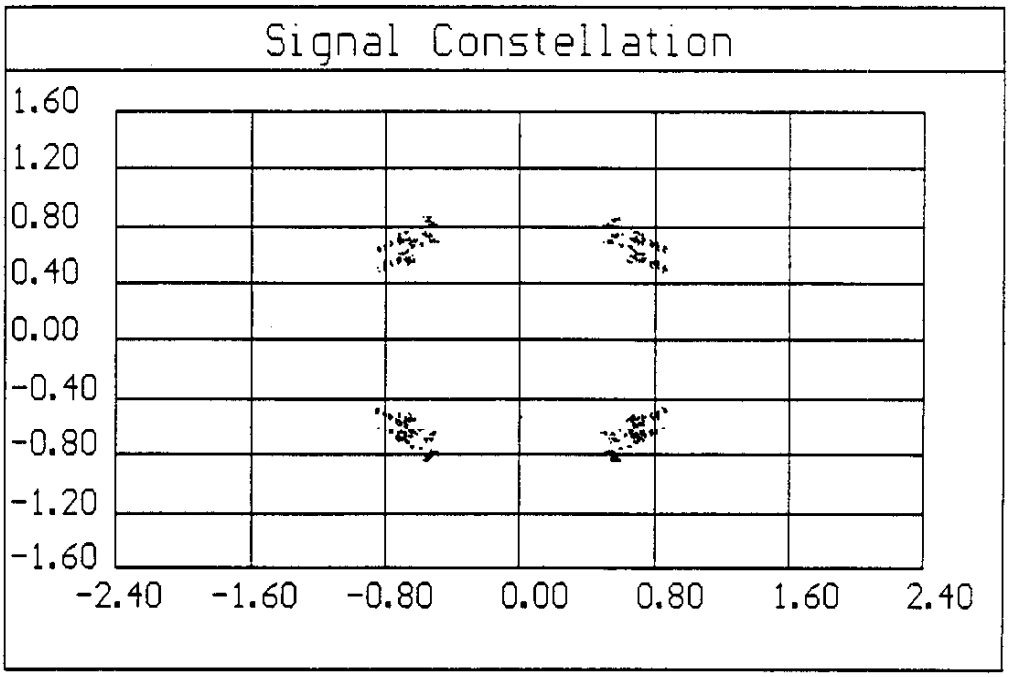

Figure A13.19 Recovered Signal Constellation At CNR= ∞, RF Filter Bandwidth 2.0xSymbol Rate, No Adjacent Channel Interference

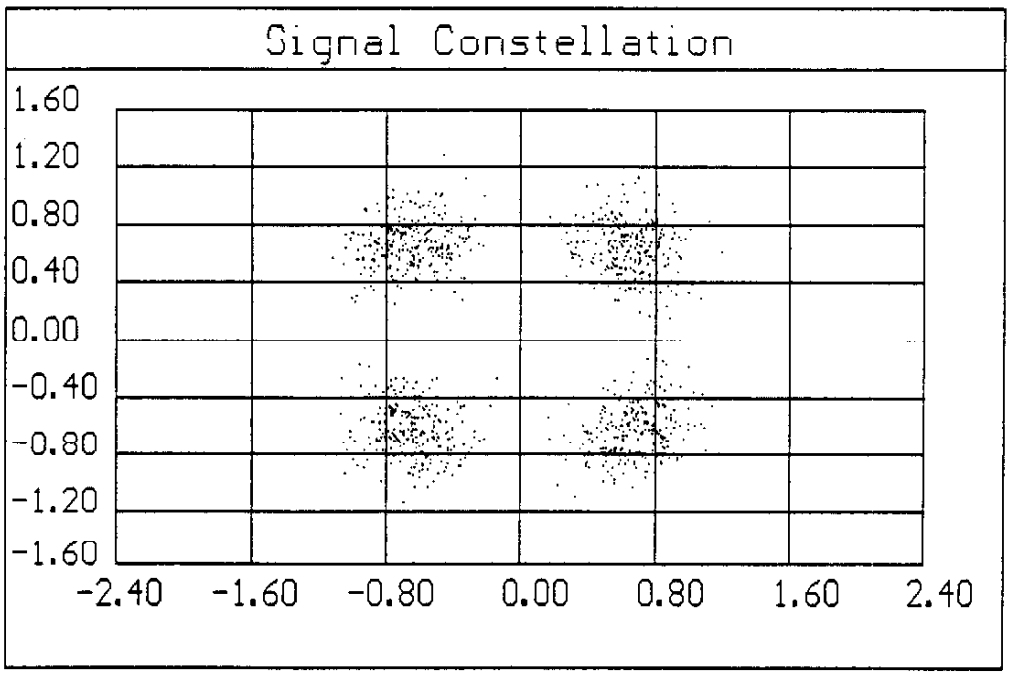

Figure A13.20 Recovered Signal Constellation At CNR= 10 dB, RF Filter Bandwidth 1.5xSymbol Rate, No Adjacent Channel Interference

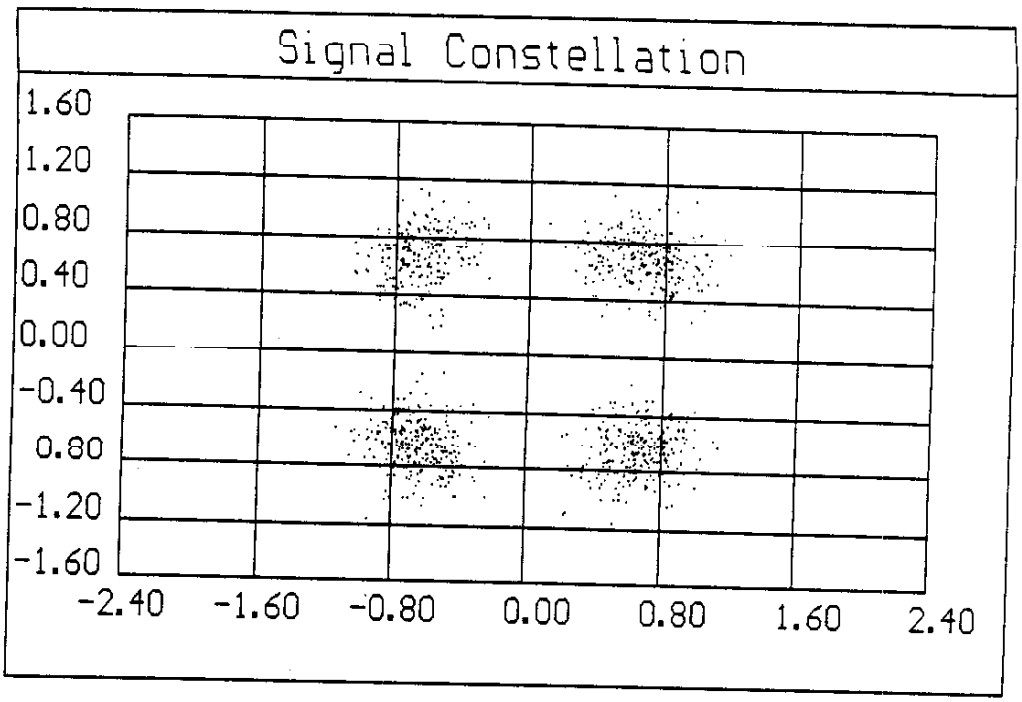

Figure A13.21 Recovered Signal Constellation At CNR= 10 dB, RF Filter Bandwidth 2.0xSymbol Rate, No Adjacent Channel Interference

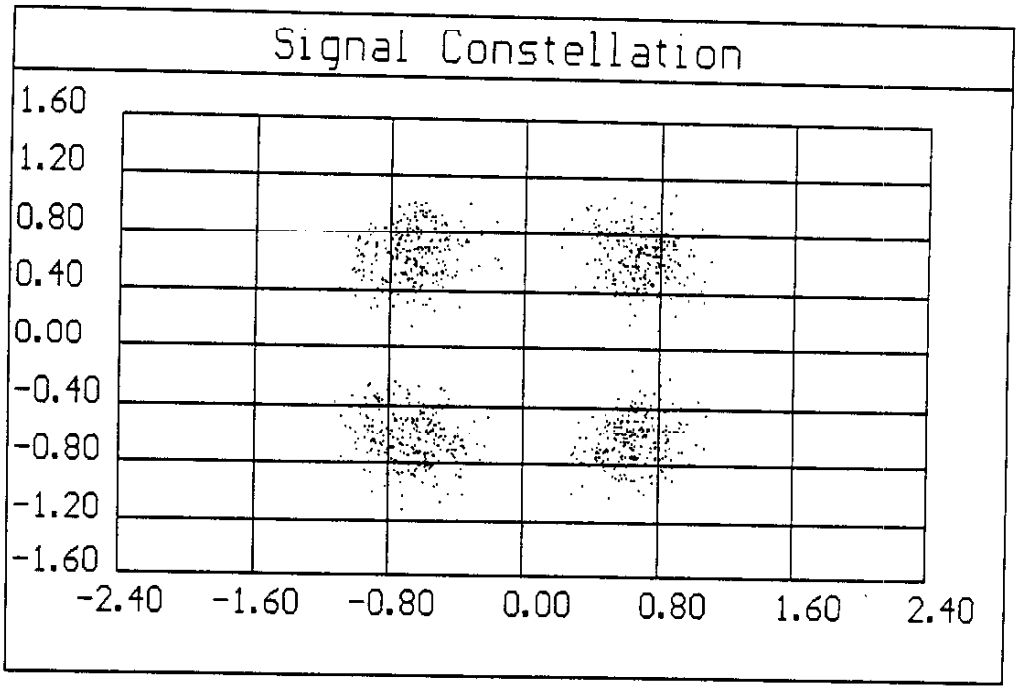

Figure A13.22 Recovered Signal Constellation At CNR= 10 dB, RF Filter Bandwidth 1.5xSymbol Rate, Adjacent Channel Interference at + 0 dB

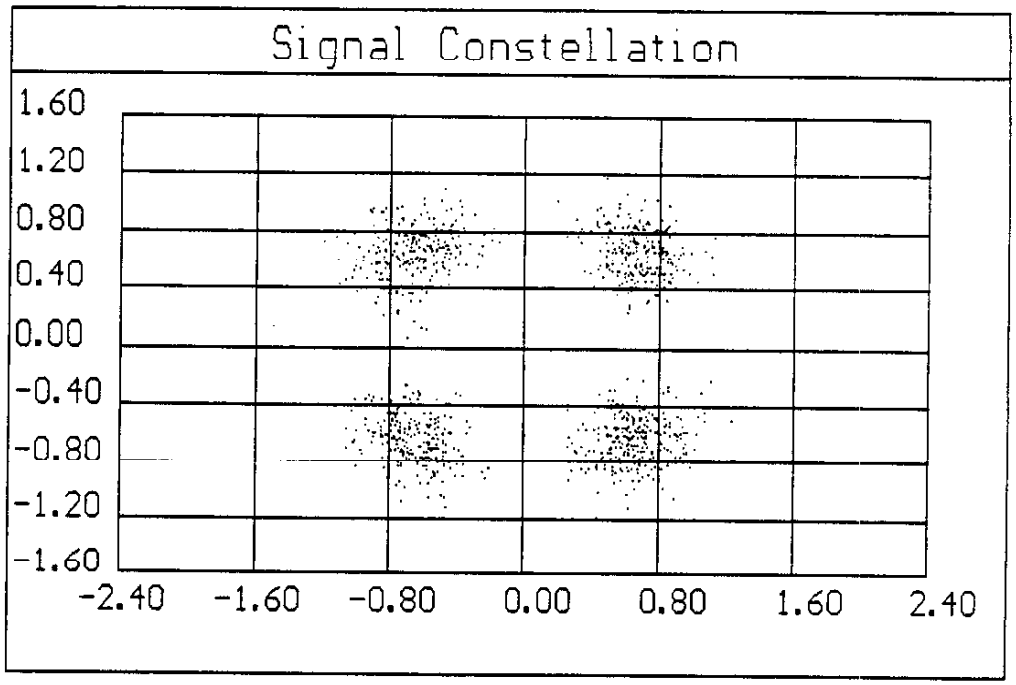

Figure A13.23 Recovered Signal Constellation At CNR= 10 dB, RF Filter Bandwidth 2.0xSymbol Rate, Adjacent Channel Interference at + 0 dB

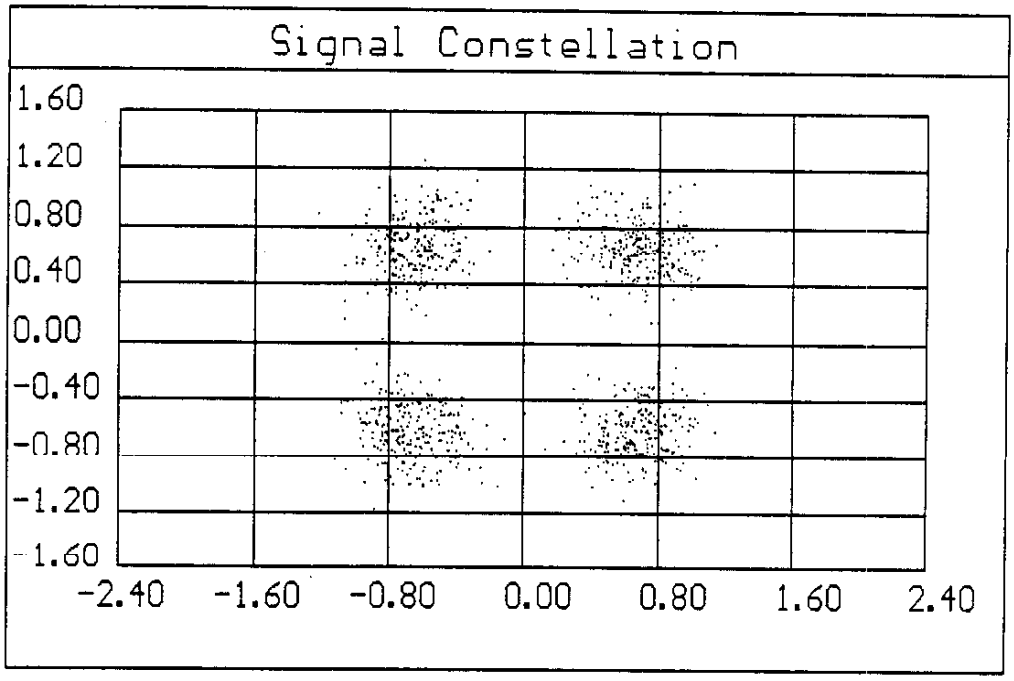

Figure A13.24 Recovered Signal Constellation At CNR= 10 dB, RF Filter Bandwidth 1.5xSymbol Rate, Adjacent Channel Interference at + 5 dB

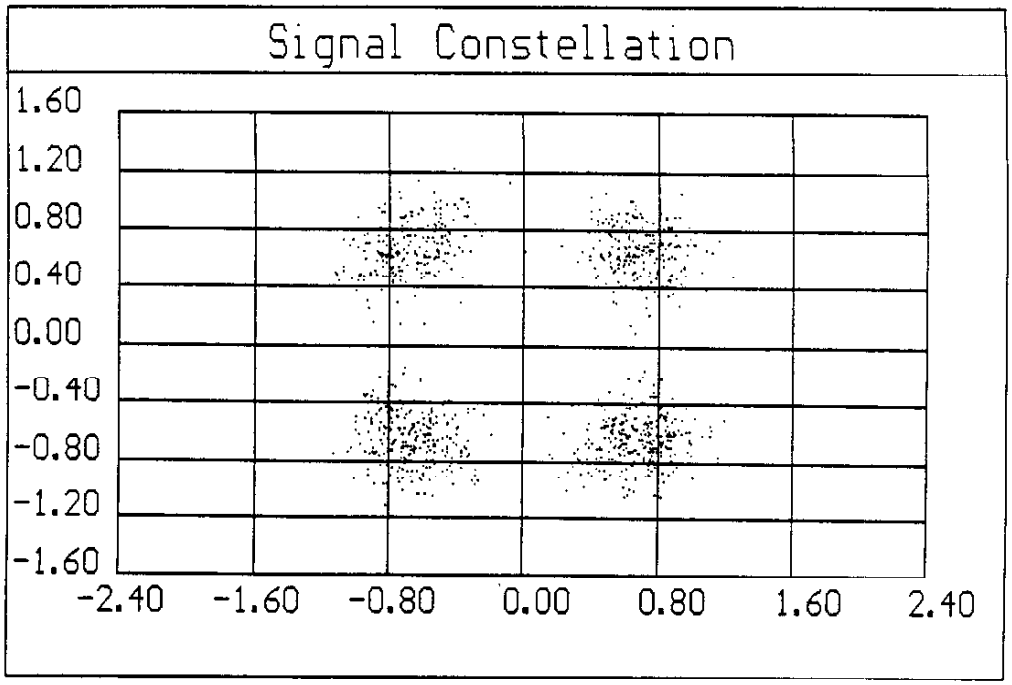

Figure A13.25 Recovered Signal Constellation At CNR= 10 dB, RF Filter Bandwidth 2.0xSymbol Rate, Adjacent Channel Interference at + 5 dB

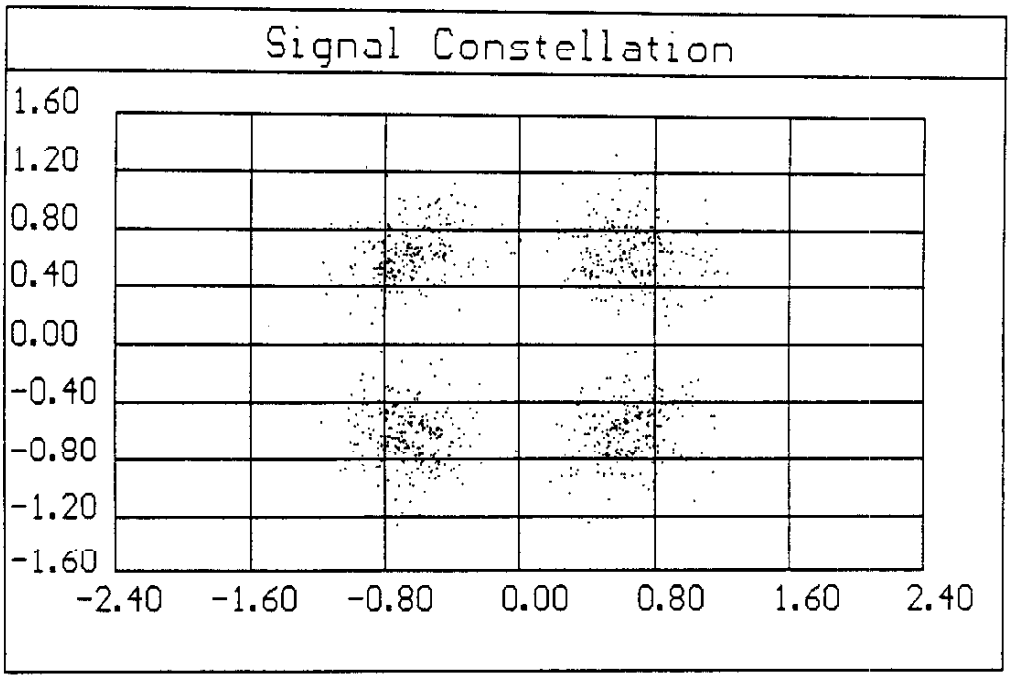

Figure A13.26 Recovered Signal Constellation At CNR= 10 dB, RF Filter Bandwidth 1.5xSymbol Rate, Adjacent Channel Interference at + 10 dB

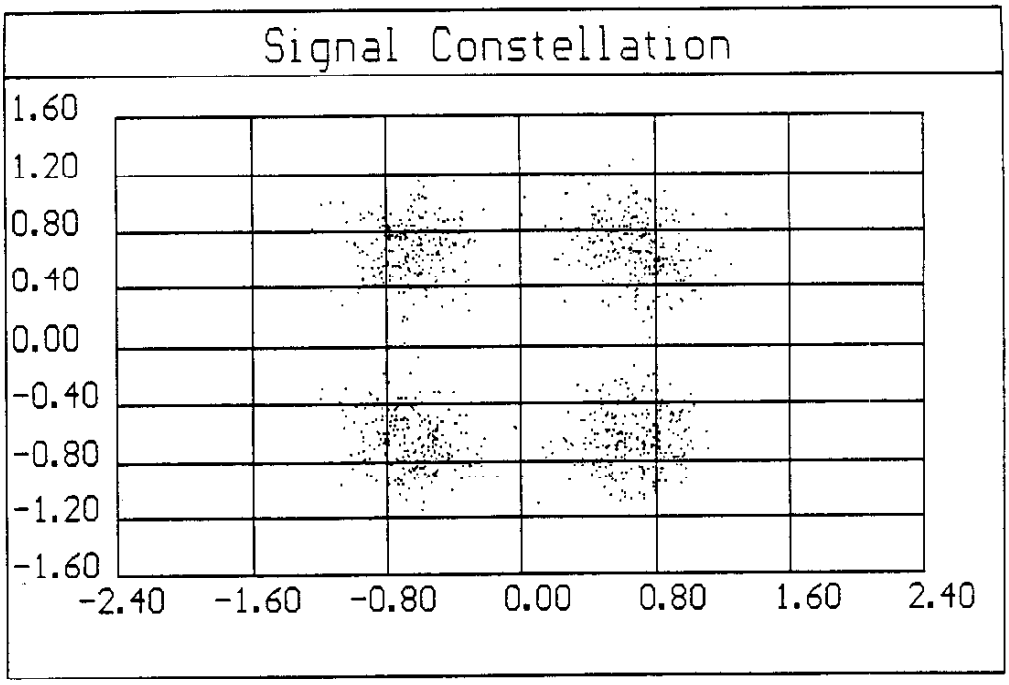

Figure A13.27 Recovered Signal Constellation At CNR= 10 dB, RF Filter Bandwidth 2.0xSymbol Rate, Adjacent Channel Interference at + 10 dB

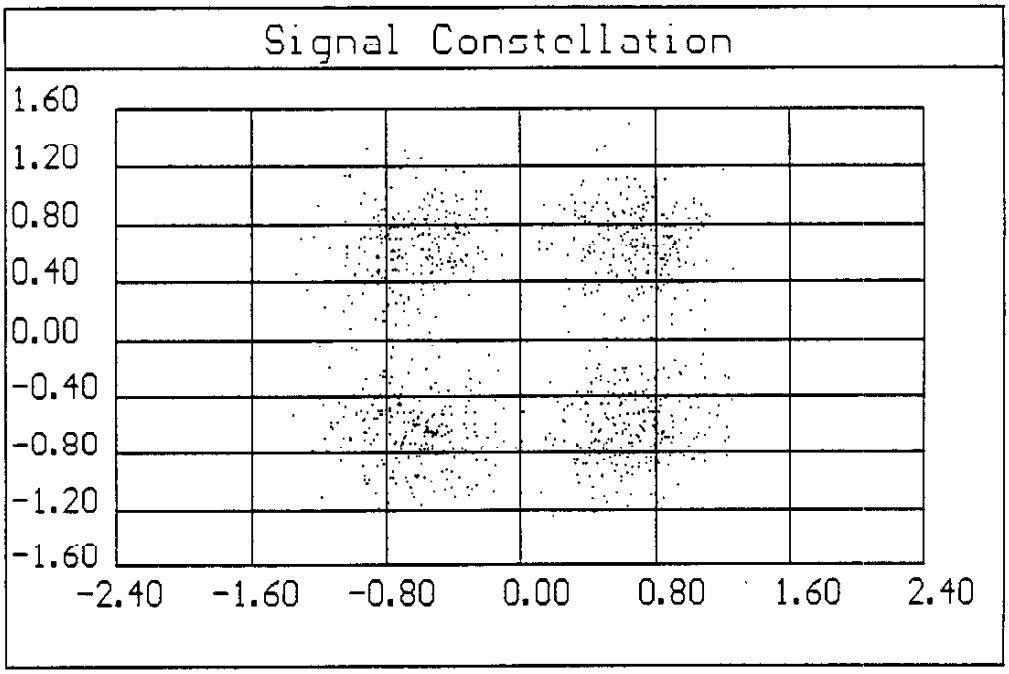

Figure A13.28 Recovered Signal Constellation At CNR= 10 dB, RF Filter Bandwidth 1.5xSymbol Rate, Adjacent Channel Interference at + 15 dB

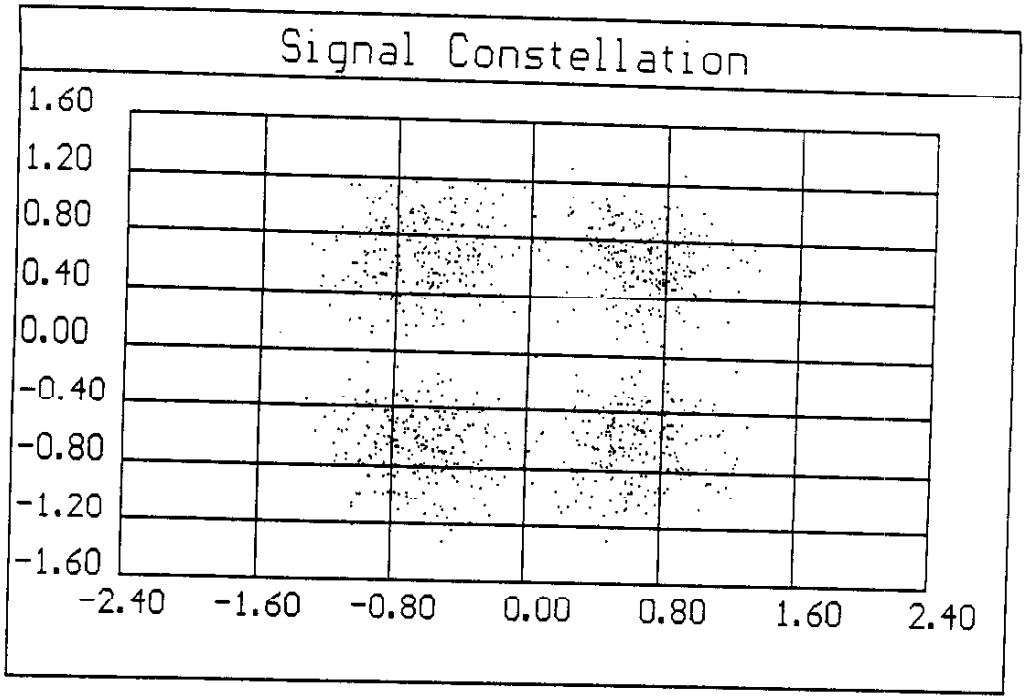

Figure A13.29 Recovered Signal Constellation At CNR= 10 dB, RF Filter Bandwidth 2.0xSymbol Rate, Adjacent Channel Interference at + 15 dB

References

A13.1] Gardner, F.M., Phaselock Techniques, 2nd Ed., John Wiley and Sons, 1979, page 168

A13.2] Feher, K., Advanced Digital Communications, Prentice-Hall, 1987

A13.3] Hirade, K., et al., "Error-Rate Performance of Digital FM with Differential Detection in Land Mobile Radio Channels," IEEE VT-28, Aug. 1979, pp. 204-212

A13.4] Klapper, J., "A New Family of Low-Delay FM Detectors," Proc. NTC, 1975, pp. 34-6 through 34-10, Patent Awarded Dec. 10, 1974, No. 3,854,099

A13.5] Ray, S.R., "Zero-Crossing-Based Approximate Demodulation of Wide-Deviation FM," IEE Proc., Part F, Feb. 1984, pp. 47-51

A13.6] Suzuki, H., "Optimum Gaussian Filter for Differential Detection of MSK," IEEE COM-29, June 1981, pp. 916-918

A13.7] Scott, R.E., C.A. Halijak, "The SCEM-Phase-Lock Loop and Ideal FM Discrimination," IEEE COM-, March 1977, pp. 390-392

A13.8] Aguirre, S., S. Hinedi, "Two Novel Automatic Frequency Tracking Loops," IEEE AES-25, Sept. 1989, pp. 749-760

A13.9] Turner, S.E., "Multipath Interference in FM Data Transmission," RF Design, Dec. 1988, pp. 26-47

A13.10] Iwanami, Y., T. Ikeda, "An Adaptive Control Method of a Digital Signal Processing DPLL FM Demodulator Under a Fading Environment," Globecom 1987, pp. 34.2.1-34.2.6

A13.11] Varanasi, S., S.C. Gupta, "Statistical Analysis of Digital Phase-Locked Loops in Fading Channels," IEEE AES-20, Nov. 1984, pp. 682-692

A13.12] Davis, B., "FM Noise with Fading Channels and Diversity," IEEE COM-19, Dec. 1971, pp. 1189-1200

A13.13] Dharamsi, M.T., S.C. Gupta, "Performance of Quasi=Optimum Digital FM Demodulators for Fading Channels," Comp. & Elect. Engng, Pergamon Press, 1975, pp. 175-193

A13.14] , "Performance Analysis of Digital FM Demodulators for Fading Channels in the Threshold Region," Comput & Elect. Engrg., Vol. 3, Pergamon Press, 1976, pp. 203-208

A13.15] Shein, N.P., "An Approximate Formula for MFSK Symbol Error Probability in Fast Rayleigh Fading," Milcom 1988, pp. 5.5.1-5.5.7

A13.16] Varanasi, S.V., "Statistical Analysis of Zero-Crossing Sampling Digital Fading Phase-Locked Loops," Ph.D. Dissertation, SMU, 1980

A13.17] Lac, Q.T., "Mathematical Analysis of Digital Phase Locked Loops Over Fading Communication Channels," Ph.D. Dissertation, Northwestern, 1983

A13.18] Park, J.H., "An FM Detector for Low S/N," IEEE COM-18, April 1970, pp. 110-118

A13.19] Rife, D.C., R.R. Boorstyn, "Single-Tone Parameter Estimation from Discrete-Time Observations," IEEE IT-20, Sept. 1974, pp. 591-598

A13.20] Abatzoglov, T.J., "A Fast Maximum Likelihood Algorithm for Frequency Estimation of a Sinusoid Based on Newton's Method," IEEE ASSP-33, Feb. 1985, pp. 77-89.

A13.21] Ziemer, R.E., R.L. Peterson, Digital Communications and Spread Spectrum Systems, Macmillan, 1985

A13.22] Juntti, J., et al., "Digital FSK Receivers Implemented by the TMS3210 Signal Processor," IEEE 88CH 2607-0, 1988

A13.23] Hess, D.T., "Equivalence of FM Threshold Extension Receivers," IEEE Com-, Oct. 1968, pp. 746-748

A13.24] Hirono, M., et al., "Multi-level Decision Method for Bandlimited Digital FM with Limiter-Discriminator Detection," IEEE VT-33, Aug. 1984, pp. 114-122

A13.25] Hoover, D., "Testing North American Dual-Mode Cellular, Japan Digital Cellular Transceivers," RF Expo East Proc., Oct. 1991, Orlando Florida, pp. 143-163

A13.26] Feher, K., "Modems for US Digital Cellular and Emerging Digital Mobile Radio Systems," ICC, 1991

A13.27] Proakis, J.G., Digital Communications, McGraw-Hill Book, 1989

A13.28] Levenberger, K.J., "Digital Radio Systems Examined- Part II, Modulation and Transmission Characteristics," MSN, Feb. 1986

A13.29] Hinedi, S., W.C. Lindsey, "Intersymbol Interference Effects on BPSK and QPSK Carrier Tracking Loops," IEEE COM-38, Oct. 1990

A13.30] Schollmeier, G., "Carrier and Timing Recovery in Data Receivers with Adaptive Equalization," Conf. Rec. Int. Conf. Commun., June 1977, pp. 96-99

A13.31] Leclert, A., P. Vandamme, "Universal Carrier Recovery Loop for QASK and PSK Signal Sets," IEEE COM-31, Jan. 1983, pp. 130-136

A13.32] Kim, H.J., et al., "The N-Phase Digital Tanlock Loop for Tracking Suppressed Carrier N-ary PSK Signals," IEEE COM-33, Sept. 1985

A13.33] Matyas, R., P.J. McLane, "Decision-Aided Tracking Loops for Channels with Phase Jitter and Intersymbol Interference," IEEE Trans. COM-22, Aug. 1974

A13.34] Mordi, S., H. Sari, "Analysis of Four Decision Feedback Carrier Recovery Loops in the Presence of Intersymbol Interference," IEEE COM-33, June 1985

A13.35] Meyers, M.H., L.E. Franks, "Joint Carrier Phase and Symbol Timing Recovery for PAM Systems," IEEE COM-28, Aug. 1980

A13.36] Cupo, R.L., R.D. Gitlin, "Adaptive Carrier Recovery Systems for Digital Data Communications Receivers," IEEE J. Selected Areas Comm., Dec. 1989

A13.37] Sari, H., S. Moridi, "New Phase and Frequency Detectors for Carrier Recovery in PSK and QAM Systems," IEEE COM-36, Sept. 1988

A13.38] Glisic, S.G., M.D. Pajkovic, "Symbol Synchronization for Digital Signals with Multisegment Trajectory: Digital Data Transition Tracking Loop," IEEE COM-38, Setp. 1990

A13.39] Qureshi, S., "Adaptive Equalization," IEEE Com. Magazine, March 1982

A13.40] Ungerboeck, G., "Fractional Tap-Spacing Equalizer and Consequences for Clock Recovery in Data Modems," IEEE COM-24, Aug. 1976

A13.41] Fihel, A., H. Sari, "Performance of Reduced Bandwidth 16-QAM with Decision Feedback Equalization," IEEE COM-35, July 1987

A13.42] Falconer, D.D., "Jointly Adaptive Equalization and Carrier Recovery in Two-Dimensional Digital Communication Systems," BSTJ, March 1976

A13.43] _____, "Analysis of a Gradient Algorithm for Simultaneous Passband Equalization and Carrier Phase Recovery," BSTJ, April 1976

A13.44] Citlin, R.D., S.B. Weinstein, "Fractionally-Spaced Equalization: An Improved Digital Transversal Equalizer," BSTJ, Feb. 1981

A13.45] D'Avella, R., et al., "An Adaptive MLSE Receiver for TDMA Digital Mobile Radio, "IEEE J. Sel. A. of Comm., Jan. 1989

A13.46] Hamied, K.A., et al., "A New Channel Estimator for Fast Start-Up Equalization," IEEE COM-39, Feb. 1991

A13.47] Porat, B., B. Friedlander, "Blind Equalization of Digital Communication Channels Using High-Order Moments," IEEE Trans. on Sig. Proc., Vol. 39, Feb. 1991

A13.48] Godard, D.N., "Self-Recoverying Equalization and Carrier Tracking in Two-Dimensional Data Communication Systems," IEEE COM-28, Nov. 1980

A13.49] Ling, F., "On Training Fractionally Spaced Equalizers Using Intersymbol Interpolation," IEEE COM-37, Oct. 1989

A13.50] Milutinovic, V.M., "A Microprocessor-Oriented Algorithm for Adaptive Equalization," IEEE COM-33, June 1985

A13.51] Kappes, J.M., "An Adaptive Equalizer for 120 Mbps QPSK Transmission," Comsat Tech. Rev., Spring 1987

A13.52] Murata, T., et al., "Practical TV Ghost Canceller Using 2-State CCD Transversal Filter," IEEE Trans. Consum. Elec., Aug. 1983

A13.53] Murakami, J., et al., "Ghost Clean System", IEEE Trans. Consum. Elec., Aug. 1983

A13.54] Bessai, H.J., W. Lorek, "Influence of Coding and Hardware Imperfections on the Bit Error Structure of Multilevel QAM Signals," IEEE COM-37, June 1989

A13.55] Kohno, R., et al., "Design of Automatic Equalizer Including a Decoder of Error Correcting Code," IEEE COM-33, Oct. 1985

A13.56] Sexton, T.A., K. Pahlavan, "Channel Modeling and Adaptive Equalization of Indoor Radio Channels," IEEE J. Selected Areas Comm., Jan. 1989

A13.57] Seshadri, N., "Joint Data and Channel Estimation Using Fast Blind Trellis Search Techniques"

A13.58] Chang, R.W., R. Srinivasagopalan, "Carrier Recovery for Data Communication Systems with Adaptive Equalization," IEEE COM-28, Aug. 1980

A13.59] Electronics Industries Association Specification IS-54, "Dual-Mode Subscriber Equipment-Network Equipment Compatibility Specification," EIQ Project Number 2215, January 1990

A13.60] Doherty, J.F., "Decision Feedback Equalization of Data with Spectral Nulls," Milcom 1990

A13.61] Newson, P., B. Mulgrew, "Adaptive Channel Identification and Equalization for GSM European Digital Mobile Radio," ICC 1991

A13.62] Dohergy, J.F., "Equalization for Mobile Communications Channels," Milcom 1990

A13.63] Bune', P.A.M., "A Low-Effort DSP Equalization Algorithm for Wideband Digital TDMA Mobile Radio Receivers," ICC 1991

A13.64] Cavers, J.K., "An Analysis of Pilot Symbol Assisted QPSK for Digital Mobile Communications," Globecom 1990

A13.65] Lo, N.W.K., et al., "Channel Interpolation for Digital Mobile Radio Communications," ICC 1991

A13.66] Feher, K., "Modems for U.S. Digital Cellular and Emerging Digital Mobile Radio Systems," ICC 1991

A13.67] D'Aria, G., et al., "Fast Adaptive Equalizers for Narrow-Band TDMA Mobile Radio," IEEE Trans. on Veh. Tech., May 1991

A13.68] Proakis, J.G., "Adaptive Equalization for TDMA Digital Mobile Radio," IEEE Trans. on Veh. Tech., May 1991

A13.69] Balaban, P., J. Salz, "Dual Diversity Combining and Equalization in Digital Cellular Mobile Radio," IEEE Trans on Veh. Tech., May 1991

A13.70] Sollenberger, N.R., et al., "Architecture and Implementation of an Efficient and Robust TDMA Frame Structure for Digital Portable Communications," IEEE Trans. on Veh. Tech., Feb. 1991

A13.71] Glave, F.E., A.S. Rosenbaum, "An Upper Bound Analysis for Coherent Phase-Shift Keying with Cochannel, Adjacent Channel, and Intersymbol Interference," IEEE COM, June 1975

A13.72] Rosenbaum, A.S., "Binary PSK Error Probabilities with Multiple Cochannel Interferences," IEEE COM, June 1970

A13.73] Feher, K., Advanced Digital Communications, Prentice-Hall, 1987, Chapter 9

A13.74] Kurosaka, R.T., "Diophantine Equations," Byte, March 1986, pp. 343-350

A13.75] Reichbom-Kjennerud, G., "Novel Methods of Integer Multiplication and Division," Byte, June 1983

A13.76] Bi, G., "Fast Conversion Between Binary and Residue Numbers," Electronic Letters, 1988

A13.77] Ibrahim, K.M., S.N. Saloum, "An Efficient Residue to Binary Converter Design," IEEE Cir. Sys., Sept. 1988

A13.78] IEEE Press, Residue Number System Arithmetic

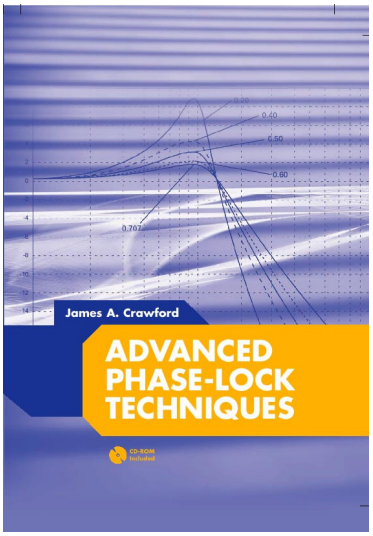

Advanced Phase-Lock Techniques

James A. Crawford

2008

Artech House

510 pages, 480 figures, 1200 equations
CD-ROM with all MATLAB scripts

ISBN-13: 978-1-59693-140-4
ISBN-10: 1-59693-140-X

Chapter	Brief Description	*Pages*
1	*Phase-Locked Systems—A High-Level Perspective* An expansive, multi-disciplined view of the PLL, its history, and its wide application.	26
2	*Design Notes* A compilation of design notes and formulas that are developed in details separately in the text. Includes an exhaustive list of closed-form results for the classic type-2 PLL, many of which have not been published before.	44
3	*Fundamental Limits* A detailed discussion of the many fundamental limits that PLL designers may have to be attentive to or else never achieve their lofty performance objectives, e.g., Paley-Wiener Criterion, Poisson Sum, Time-Bandwidth Product.	38
4	*Noise in PLL-Based Systems* An extensive look at noise, its sources, and its modeling in PLL systems. Includes special attention to 1/*f* noise, and the creation of custom noise sources that exhibit specific power spectral densities.	66
5	*System Performance* A detailed look at phase noise and clock-jitter, and their effects on system performance. Attention given to transmitters, receivers, and specific signaling waveforms like OFDM, M-QAM, M-PSK. Relationships between EVM and image suppression are presented for the first time. The effect of phase noise on channel capacity and channel cutoff rate are also developed.	48
6	*Fundamental Concepts for Continuous-Time Systems* A thorough examination of the classical continuous-time PLL up through 4^{th}-order. The powerful Haggai constant phase-margin architecture is presented along with the type-3 PLL. Pseudo-continuous PLL systems (the most common PLL type in use today) are examined rigorously. Transient response calculation methods, 9 in total, are discussed in detail.	71
7	*Fundamental Concepts for Sampled-Data Control Systems* A thorough discussion of sampling effects in continuous-time systems is developed in terms of the *z*-transform, and closed-form results given through 4^{th}-order.	32
8	*Fractional-N Frequency Synthesizers* A historic look at the fractional-N frequency synthesis method based on the U.S. patent record is first presented, followed by a thorough treatment of the concept based on Δ-Σ methods.	54
9	*Oscillators* An exhaustive look at oscillator fundamentals, configurations, and their use in PLL systems.	62
10	*Clock and Data Recovery* Bit synchronization and clock recovery are developed in rigorous terms and compared to the theoretical performance attainable as dictated by the Cramer-Rao bound.	52